UNIVERSIDAD COMPLUTENSE DE MADRID

FACULTAD DE CIENCIAS FÍSICAS
Departamento de Física de la Tierra, Astronomía y Astrofísica II

TESIS DOCTORAL

A new martian radiative transfer model: applications using in situ measurements

Un nuevo modelo de transferencia radiativa en Marte: aplicaciones utilizando medidas in situ

MEMORIA PARA OPTAR AL GRADO DE DOCTOR

PRESENTADA POR

Álvaro Vicente-Retortillo Rubalcaba

Directores

Francisco Valero Rodríguez
Luis Vázquez Martínez
Germán Martínez Martínez

Madrid, 2017

UNIVERSIDAD COMPLUTENSE DE MADRID

FACULTAD DE CIENCIAS FÍSICAS

Departamento de Física de la Tierra, Astronomía y Astrofísica II

TESIS DOCTORAL

A NEW MARTIAN RADIATIVE TRANSFER MODEL: APPLICATIONS USING IN SITU MEASUREMENTS

UN NUEVO MODELO DE TRANSFERENCIA RADIATIVA EN MARTE: APLICACIONES UTILIZANDO MEDIDAS IN SITU

Memoria para optar al grado de doctor con Mención Internacional

Presentada por:

Álvaro de Vicente-Retortillo Rubalcaba

Directores de tesis:

Prof. Francisco Valero Rodríguez[1]

Prof. Luis Vázquez Martínez[1]

Dr. Germán Martínez Martínez[2]

[1]Universidad Complutense de Madrid

[2]University of Michigan

Madrid, 2017

A NEW MARTIAN RADIATIVE TRANSFER MODEL: APPLICATIONS USING IN SITU MEASUREMENTS

UN NUEVO MODELO DE TRANSFERENCIA RADIATIVA EN MARTE: APLICACIONES UTILIZANDO MEDIDAS IN SITU

PhD. Thesis

Author:

Álvaro de Vicente-Retortillo Rubalcaba

Advisors:

Prof. Francisco Valero Rodríguez[1]

Prof. Luis Vázquez Martínez[1]

Dr. Germán Martínez Martínez[2]

[1]Universidad Complutense de Madrid

[2]University of Michigan

Madrid, 2017

La presente Tesis Doctoral se ha realizado gracias a la concesión por parte del Ministerio de Economía y Competitividad (MINECO) de la ayuda predoctoral de Formación de Personal Investigador (FPI) con referencia BES-2012-059241, asociada al proyecto "Participación Científica en la Misión a Marte MEIGA-METNET-PRECURSOR" (AYA2011-29967-C05-02). Durante la elaboración de la misma se han realizado tres estancias en la University of Michigan, Ann Arbor, Estados Unidos, gracias a la concesión por parte del MINECO de tres ayudas a la movilidad predoctoral para la realización de estancias breves en centros de I+D españoles y extranjeros. La duración de las estancias realizadas ha sido de 94 días (2014), 96 días (2015) y 95 días (2016).

The research activity associated to the development of this PhD. Thesis has been funded by the Spanish Ministry of Economy and Competitiveness (MINECO) through the predoctoral research FPI (Training of Researchers) grant BES-2012-059241, associated with the project "Participación Científica en la Misión a Marte MEIGA-METNET-PRECURSOR" (AYA2011-29967-C05-02). The candidate has performed three stays at the University of Michigan, Ann Arbor, USA, funded by MINECO through three predoctoral mobility grants for short stays in foreign research institutions. The duration of these stays has been 94 days (2014), 96 days (2015) and 95 days (2016).

To my parents

To Marta

Acknowledgements

During the last months, I have frequently imagined myself writing these acknowledgements. Now that the moment to write them has arrived, I have to admit that it is not easy at all, mainly because of the difficulties to express with words my immense gratefulness to each person that has been important not only in the development of this thesis, but in my life.

I thank the Spanish Ministry of Economy and Competitiveness (MINECO) for the financial support through the predoctoral research FPI (Training of Researchers) grant BES-2012-059241, associated with the project "Participación Científica en la Misión a Marte MEIGA-METNET-PRECURSOR" (AYA2011-29967-C05-02), and through three predoctoral mobility grants (EEBB-I-14-09122, EEBB-I-15-09985 and EEBB-I-16-11223) for short stays at the University of Michigan.

I am extremely grateful to my advisors: Prof. Francisco Valero, Prof. Luis Vázquez and Dr. Germán Martínez. Thank you for giving me the opportunity of performing research in this fascinating world of Mars exploration. Thank you for getting me involved in exciting present and future missions to Mars: the initial frame was the project associated with the MetNet mission; in 2014, being part of the Mars Science Laboratory Team became a reality; and now we are starting to collaborate in Mars 2020 and ExoMars missions. Thank you for your excellent advices: without them, the current situation would be very different. Thank you very much for your complete support from the very first minute, which has allowed me to grow as a researcher. I am convinced that I have had the privilege of having the best advisors that I could have imagined.

I also really want to thank Prof. Nilton Renno for the hospitality and for the excellent suggestions in the analysis of REMS data during my stays at the University of Michigan. Thank you for the financial support for the publication of the paper published in *Geophysical Research Letters.*

I want to thank the Instituto de Matemática Interdisciplinar for the financial support for the publication of the paper published in *Journal of Space Weather and Space Climate*.

I am also extremely grateful to my family, for all what I have received from each of you. I have to give special thanks to my parents. Thank you for all the decisions that you have made having in mind that they were the best for me, in any aspect. Thank you for having been always there, enjoying the good moments and listening to me and giving your most sincere advice whenever I felt there were problems around. Thank you for supporting my decisions. Thank you to my sister and my brother, for all the moments that we have spent together. Thank you to my grandparents, aunts and uncles. Special thanks to Raquel and Salva: those summers in Germany and England come now to my mind, as well as our special dinners every time there is something important to celebrate. Thank you (and also to Paloma) for your advices and interest in my future professional career (as you see, I am following your advice probably more than what you expected some years ago …)

Thank you very much to my friends. Special thanks to Jorge, for being always there since we were three years old; thank you for all the time we have spent together. I have realized that distance is not a problem for real friends. Thank you to Nacho and Martazu, not only for the great plans in the recent years, but also for some very interesting conversations. Thank you to Saioa. Thank you for being there, sharing the bureaucratic processes during the bachelor's degree, master's degree and during the PhD studies; thank you also for the daily lunches at the University. Thank you also to Fernando, with whom I have shared uncountable hours working on laboratory reports and studying during the bachelor's degree.

I also want to thank my office partners in Madrid. Thank you to Marisa, Álvaro, Lara and Antonio. It has been great to share the working hours with you. Thank you also to Sergio, for addressing my questions regarding the final steps of the thesis.

Thank you very much to my office partners in Ann Arbor. Thank you to Erik, Harvey and Cauê. Thank you very much for your excellent hospitality. It has been a pleasure to work and make plans after work with you during my stays in Michigan.

Finally, Marta, I cannot be more grateful to you. Thank you for listening every day to my progress on the thesis, celebrating with me the good news and giving me all your support during the difficult moments. Thank you for living this process of the thesis as if it were yours. Thank you so much for so many things, especially for changing my life and for helping me to become a better person.

Contents

Acknowledgements…………………………………………………………………..ix

Abstract…………………………………………………………………………..xiii

Resumen……………………………...………………………………………….xvii

List of publications and contributions……………………………………………xxi

Abbreviations…………………………………………………………………….xxv

I. Introduction, State of the Art and Contribution of this Work…………………1

1. Introduction……………………………………………………………………..3
2. Studies of solar radiation on Mars: Motivation and state of the art…………15
3. Contribution of this work……………………………………………………...29

II. Results…………………………………………………………………………...31

4. A model to calculate solar radiation fluxes on the Martian surface…………33
5. Seasonal and interannual variability of solar radiation at Spirit, Opportunity and Curiosity landing sites……………………………………………………47
6. A new Monte Carlo radiative transfer model to determine dust aerosol particle size at Gale Crater……………………………………………………………..65
7. Determination of dust aerosol particle size at Gale Crater using REMS UVS and Mastcam measurements …………………………………………………75

III. Discussion……………………………………………………………………..89

8. Discussion……………………………………………………………………..91

IV. Conclusions…………………………………………………………………103

9. Conclusions…………………………………………………………………...105

V. Future Research …………………………………………………………...111

10. Generation of UV radiation data products at Gale Crater by correcting REMS UV data from dust deposition and sensor's angular response ……….. ……………………………………………………………………...113
11. Studies associated with Mars 2020 MEDA instrument……………………125

Bibliography…………………………………………………………………….131

Abstract

Introduction

The study of the radiative environment at the Martian surface is paramount to understand and better characterize the physical processes of the atmosphere and the climate of the planet, as well as to determine the biological impact of ultraviolet radiation. These two objectives are a priority in current and future Mars missions due to their implications in the preparation for the human exploration of the planet.

Due to the importance of solar radiation, accurate radiative transfer models are needed. Accuracy is particularly important for the calculation of the solar radiances and fluxes at the surface, which are key quantities to characterize the radiative environment at the surface and to maximize the scientific return of the missions to Mars.

Accurate simulations of the solar radiation at the Martian surface require not only comprehensive and validated radiative transfer models, but also an accurate knowledge of the radiative properties of the atmospheric components, suspended dust being especially important. The combination of model results and solar radiation measurements from the Martian surface can allow the retrieval of the dust aerosol properties.

The Ultraviolet Sensor (UVS) of the Rover Environmental Monitoring Station (REMS) on board the Mars Science Laboratory (MSL) mission has been measuring solar radiation at the surface of Mars for the first time in six bands between 200 and 380 nm. These measurements can provide information about the properties and temporal variability of the suspended dust. The spectral range of this sensor will be extended in future missions, such as MetNet, which will contain a Solar Irradiance Sensor (MetSIS). Other future missions, such as ExoMars 2020 and Mars 2020, will also carry a Radiation and Dust Sensor (RDS).

Objectives

The main objectives of this work are:

1. Development of new comprehensive radiative transfer models to calculate the solar radiation that reaches the Martian surface. The models should be accurate and should have different levels of complexity so that the most suitable model can be selected for each particular investigation.
2. Development of novel techniques to retrieve dust aerosol properties from solar radiation measurements from present and future Mars missions. In particular, these methodologies should be applicable to REMS UVS measurements of the MSL mission and to future measurements, such as MetSIS data of the MetNet mission.
3. Characterization of the radiative environment at the landing sites of the various missions to Mars.

4. Determination of the seasonal and interannual variability of dust aerosol particle size at Gale Crater for the first time.

Results

In the context of Objective 1, we have developed radiative transfer models following two approaches: the delta-Eddington approximation and the Monte Carlo method. The first model (COMIMART) includes state-of-the-art radiative properties for dust, water ice clouds and gas molecules as a function of wavelength. Due to its versatility, the model can be used to calculate the solar radiation fluxes in any spectral region of the shortwave range under the wide range of scenarios that can be found in the Martian atmosphere. We have developed two versions of a radiative transfer model that relies on the Monte Carlo method. These versions enable the simulation of radiances and fluxes at the Martian surface. The first version (COMIMART-MCF) is suitable for flux calculations, and the second one (COMIMART-MCR) is optimized for radiance calculations.

In the context of Objective 2, we have developed techniques to retrieve dust aerosol properties (opacity and dust particle size) from solar radiation measurements of present (MSL) and future (MetNet) missions to Mars. We have proposed two methods to retrieve opacity from MetSIS measurements: the first one relies on the measurements of one single channel, and the second one on the ratio between the measurements of two channels in spectral regions with different dust radiative properties. Moreover, the combination of the two methods can provide information on dust aerosol particle size. We have also presented novel techniques to estimate opacity and to determine dust aerosol particle size from REMS UVS measurements. Opacity is estimated by comparing measurements when the solar disk moves from the blocked to the unblocked region of the field of view (FOV) of the photodiodes. Particle size is retrieved by analyzing the measurements when the Sun is in the blocked region of the FOV.

In the context of Objective 3, we have used COMIMART and values of atmospheric opacity derived from observations performed by landed missions on Mars to characterize the seasonal and interannual variability of the radiative environment at the locations of those missions. Especial attention has been devoted to the radiative environment at the locations of the Mars Exploration Rovers (MER) and MSL, where the behavior of the direct and diffuse components has also been analyzed. The values of the shortwave fluxes have been used to study their correlation with other meteorological and environmental variables, and ultraviolet fluxes have been provided due to their biological implications and to enable the study of its potential correlation with methane concentrations.

In the context of Objective 4, we have developed a new methodology to calculate the seasonal and interannual variability of dust aerosol particle size at Gale Crater during the first 1413 sols (more than two Martian years) of the MSL mission for the first time. REMS UVS and Mastcam measurements have been used in this study. Dust aerosol particle size varies significantly with season: effective radii of the size distribution range from ~0.6 during the low opacity season to ~2 μm around the events of enhanced opacity during dusty season. Although the seasonal cycles during the two first Martian years of the mission are similar, interannual variability also exists. Results have been used to improve the estimation of the ultraviolet fluxes at Gale Crater.

Conclusions

To conclude, we enumerate the main contributions of this work:

We have developed a new comprehensive radiative radiative transfer model with updated wavelength-dependent radiative properties of dust, water ice clouds and gas molecules of the Martian atmosphere. The results of the model have been used to characterize the radiative environment at the Martian surface, to study the effect of solar insolation on meteorological variables, to assess the biological impact of the ultraviolet radiation at the Martian surface, and have been provided to study the potential correlation between ultraviolet radiation and methane concentrations.

We have developed techniques to retrieve dust opacity and dust aerosol particle size from solar radiation measurements performed on the Martian surface. Some of these techniques have been applied to estimate dust opacity and to determine dust aerosol particle size from REMS UVS measurements. We have also provided additional methods to retrieve atmospheric opacity and to estimate dust aerosol particle size from MetSIS measurements.

Finally, we have determined for the first time the seasonal and interannual variability of dust aerosol particle size at Gale Crater. These results are important in several contexts due to their implications on the ultraviolet environment at the surface, on dust aerosol atmospheric transport and on the atmospheric heating rates, which in turn affect the thermal and dynamical fields of the atmosphere. Moreover, the developed technique for this investigation is expected to be useful for the analysis of future solar radiation measurements performed by ExoMars 2020 and Mars 2020.

Resumen

Introducción

El estudio del entorno radiativo en la superficie marciana es fundamental para la comprensión y para una mejor caracterización de los procesos físicos de la atmósfera y el clima del planeta, así como para determinar el impacto biológico de la radiación ultravioleta. Estos dos objetivos son prioritarios en las misiones actuales y futuras a Marte debido a sus implicaciones en la preparación para la exploración humana del planeta.

Debido a la importancia de la radiación solar, es necesario poder contar con modelos de transferencia radiativa precisos. Esta precisión es especialmente importante en el cálculo de las radiancias y de los flujos solares en la superficie, los cuales son cantidades fundamentales para caracterizar el entorno radiativo en la superficie y para maximizar el retorno científico de las misiones a Marte.

Las simulaciones precisas de la radiación solar en la superficie marciana no sólo requieren modelos de transferencia radiativa detallados y validados, sino también un conocimiento exacto de las propiedades radiativas de los componentes atmosféricos, entre los que el polvo en suspensión es particularmente importante. La combinación de los resultados de los modelos y de las medidas de radiación solar desde la superficie marciana permiten la obtención de las propiedades del polvo en suspensión.

El sensor de radiación ultravioleta (UVS) de REMS (Rover Environmental Monitoring Station), a bordo de la misión MSL (Mars Science Laboratory) ha estado midiendo la radiación solar en superficie por primera vez en seis bandas entre 200 y 380 nm. Estas medidas pueden proporcionar información sobre las propiedades y la variabilidad temporal del polvo en suspensión. El rango espectral de este sensor se verá ampliado en misiones futuras, tales como MetNet, que contará con un Sensor de Irradiancia Solar (MetSIS). Otras misiones futuras, tales como ExoMars 2020 y Mars 2020, también contarán con un RDS (Radiation and Dust Sensor).

Objetivos

Los principales objetivos de este trabajo son:

1. Desarrollo de nuevos modelos de transferencia radiativa para calcular la radiación solar que llega a la superficie marciana. Estos modelos deberán ofrecer resultados exactos y deberán poseer diferentes grados de complejidad, de manera que se pueda seleccionar el modelo más adecuado para cada investigación.
2. Desarrollo de técnicas novedosas para obtener las propiedades del polvo en suspensión a partir de medidas de radiación solar de misiones a Marte actuales y futuras. Estas metodologías deberán ser aplicables a las medidas del sensor de radiación

ultravioleta de REMS de la misión MSL ya medidas futuras, tales como las de MetSIS, de la misión MetNet.

3. Caracterización del entorno radiativo en los lugares de aterrizaje de las misiones a Marte.

4. Determinación de la variabilidad estacional e interanual del tamaño de las partículas de polvo en suspensión en el cráter Gale por primera vez.

Resultados

En el contexto del Objetivo 1, hemos desarrollado modelos de transferencia radiativa siguiendo dos enfoques: la proximación delta-Eddington y el método de Monte Carlo. El primer modelo (COMIMART) incluye las propiedades radiativas del polvo, de las nubes de hielo y de las moléculas de gas. Estas propiedades constituyen el estado del arte en la materia. Debido a su versatilidad, el modelo puede ser utilizado para calcular los flujos radiativos en cualquier región espectral del rango de longitudes de onda corta bajo el amplio abanico de escenarios que pueden darse en la atmósfera de Marte. Hemos desarrollado dos versiones de un modelo de transferencia radiativa basado en el método de Monte Carlo. Estas versiones permiten la simulación de radiancias y flujos en la superficie marciana. La primera versión (COMIMART-MCF) es adecuada para el cálculo de flujos, y la segunda (COMIMART-MCR) está optimizada para el cálculo de radiancias.

En el contexto del Objetivo 2, hemos desarrollado técnicas para obtener las propiedades del polvo en suspensión (opacidad y tamaño de las partículas) a partir de medidas de radiación solar de misiones actuales (MSL) y futuras (MetNet). Hemos propuesto dos métodos para obtener la opacidad a partir de las medidas de MetSIS: el primero se basa en las medidas de un canal, mientras que el segundo se basa en el cociente de medidas en dos canales en regiones espectrales con diferentes propiedades radiativas. La combinación de ambos métodos puede proporcionar información sobre el tamaño de las partículas de polvo en suspensión. También hemos presentado metodologías novedosas para estimar la opacidad y para determinar el tamaño de las partículas de polvo en suspensión a partir de las medidas del sensor de radiación ultravioleta de REMS. La opacidad se estima comparando medidas cuando el Sol pasa de una zona bloqueada del campo de visión del sensor a otra sin bloquear. El tamaño de las partículas de polvo se obtiene analizando las medidas cuando el Sol está en la región bloqueada del campo de visión.

En el contexto del Objetivo 3, hemos utilizado COMIMART y las medidas de opacidad de las misiones que han operado en la superficie de Marte para caracterizar la variabilidad estacional e interanual del entorno radiativo en las coordenadas de dichas misiones. Se ha dedicado una especial atención al entorno radiativo en los lugares de aterrizaje de los Mars Exploration Rovers (MER) y de MSL, donde el comportamiento de las componentes directa y difusa de la radiación ha sido analizado también. Los valores del flujo de onda corta se han utilizado para estudiar su correlación con otras variables meteorológicas y ambientales, y los flujos de radiación ultravioleta han sido proporcionados debido a sus implicaciones biológicas y para permitir el estudio de su correlación con las concentraciones de metano.

En el contexto del Objetivo 4, hemos desarrollado una nueva metodología para calcular la variabilidad estacional e interanual del tamaño de las partículas de polvo en suspensión en el cráter Gale durante los primeros 1413 días marcianos (más de dos años marcianos) de la misión MSL por primera vez. El tamaño de las partículas de polvo en suspensión varía con la época del año: los radios efectivos de la distribución de tamaños de las partículas oscilan entre ~0.6 µm durante la época de baja opacidad y ~2 µm en torno a los eventos de alta opacidad durante la estación con alto contenido en polvo. A pesar de que los ciclos estacionales durante los dos primeros años de la misión son similares, existe variabilidad interanual. Los resultados han sido utilizados para mejorar la estimación de los flujos de radiación ultravioleta en el cráter Gale.

Conclusiones

Para concluir, enumeramos las aportaciones fundamentales de este trabajo:

Hemos desarrollado un nuevo y detallado modelo de transferencia radiativa con propiedades radiativas espectrales actualizadas del polvo, del hielo y de las moléculas de gas presentes en la atmósfera de Marte. Los resultados del modelo se han utilizado para caracterizar el entorno radiativo en la superficie de Marte, para estudiar el efecto de la radiación solar en las variables meteorológicas, para estudiar el impacto biológico de la radiación ultravioleta en superficie, y han sido proporcionados para estudiar la correlación entre la radiación ultravioleta y las concentraciones de metano.

Hemos desarrollado técnicas para obtener la opacidad y el tamaño de las partículas de polvo en suspensión a partir de medidas de radiación solar en la superficie de Marte. Algunas de estas técnicas se han aplicado para la estimación de la opacidad y para la determinación del tamaño de las partículas de polvo a partir de las medidas de radiación ultravioleta de REMS. Hemos proporcionado métodos adicionales para obtener la opacidad de la atmósfera y para estimar el tamaño de las partículas de polvo en suspensión a partir de las medidas de MetSIS.

Finalmente, hemos determinado por primera vez la variabilidad estacional e interanual del tamaño de las partículas de polvo en suspensión en el cráter Gale. Estos resultados son importantes en varios contextos debido a sus implicaciones en el entorno de radiación ultravioleta en superficie, en el transporte atmosférico de los aerosoles y en las tasas de calentamiento atmosféricas, que a su vez afectan a los campos térmicos y dinámicos de la atmósfera. Más aún, se espera que la técnica desarrollada para esta investigación sea útil para analizar futuras medidas de radiación solar llevadas a cabo por ExoMars 2020 y por Mars 2020.

List of Publications and Contributions

Articles:

6. **Vicente-Retortillo, A.**, Martínez, G.M., Renno, N.O., Lemmon, M.T., and de la Torre-Juárez, M. Determination of dust aerosol particle size at Gale Crater using REMS/UVS and Mastcam measurements, *Geophysical Research Letters*, 44, doi:10.1002/2017GL072589, 2017.

5. Martinez, G.M., Newman, C., **Vicente-Retortillo, A.**, Fischer, E., Renno, N.O., Richardson, M., Gómez-Fairén, A., Guzewich, S.D., Haberle, R.M., Kemppinen, O., Lemmon, M.T., Smith, M.D., de la Torre-Juárez, M. and Vasavada, A. Characterization of the modern Martian climate near the surface: A review of in-situ data from Viking to Curiosity, *Space Science Reviews*, doi:10.1007/s11214-017-0360-x, 2017.

4. **Vicente-Retortillo, A.**, Lemmon, M.T., Martínez, G. M., Valero, F., Vázquez, L. and Martín, M. L. Seasonal and interannual variability of solar radiation at Spirit, Opportunity and Curiosity landing sites. *Física de la Tierra* (invited), 28, 111-117, 2016.

3. Martínez, G. M., de la Torre-Juárez, M., **Vicente-Retortillo, A.**, Kemppinen, O., Renno, N. and Lemmon, M. Analysis of the environmental conditions at Gale Crater from MSL/REMS measurements. *Física de la Tierra*, 28, 163-179, 2016.

2. Martínez, G. M., Fischer, E., Renno, N.O., Sebastián, E., Kemppinen, O., Bridges, N., Borlina, C., Meslin, P.-Y., Genzer, M., Harri, A.-M., **Vicente-Retortillo, A.**, Ramos, M., de la Torre-Juárez, M., Gómez, F., Gómez-Elvira, J., and the REMS team. Likely Frost Events at Gale Crater: Analysis from MSL/REMS measurements. *Icarus*, 280, 93-102, doi: 10.1016/j.icarus.2015.12.004, 2016.

1. **Vicente-Retortillo, A.**, Valero, F., Vázquez, L. and Martínez, G.M. A model to calculate solar radiation fluxes on the Martian surface. *Journal of Space Weather and Space Climate*, 5, A33, doi: 10.1051/swsc/2015035, 2015.

Oral presentations:

6. **Vicente-Retortillo, A.**, G. M. Martínez, N. O. Renno, M. T. Lemmon, M. de la Torre-Juárez. Variability of Dust Aerosol Particle Size at Gale Crater using Mastcam and REMS UV Measurements. Sixth International Workshop of the Mars Atmosphere: Modelling and Observations, January 17-20 2017, Granada, Spain.

5. Martínez, G. M., **A. Vicente-Retortillo**, A. G. Fairén, E. Fischer, M. Genzer, S. D. Guzewich, R. M. Haberle, A.-M. Harri, O. Kemppinen, M. Lemmon, C. Newman, N. Renno, M. Richardson, M. D. Smith, M. Torre-Juárez, A. R. Vasavada. An Overview of the Dust, CO_2 and Water Cycles on Mars as Revealed from In-Situ Environmental

Data from the Viking to the Curiosity Rover. Sixth International Workshop of the Mars Atmosphere: Modelling and Observations, January 17-20 2017, Granada, Spain.

4. **Vicente-Retortillo, A.**, G. M. Martínez, N. O. Renno, M. T. Lemmon, E. Mason, M. de la Torre-Juárez. Temporal evolution of UV opacity and dust particle size at Gale Crater from MSL/REMS measurements. DPS 48/ EPSC 11, October 17-21 2016, Pasadena, California, USA.

3. Martínez, G. M., **A. Vicente-Retortillo**, O. Kemppinen, E. Fischer, A. Fairén, S. D.Guzewich, R. M. Haberle, H. Kahanpää, M. Lemmon, C. Newman, N. Renno, M. Richardson, M. D. Smith, M. de la Torre-Juárez, A. Vasavada. Interannual, seasonal and diurnal Mars surface environmental cycles observed from Viking to Curiosity. DPS 48/ EPSC 11, October 17-21 2016, Pasadena, California, USA.

2. Vázquez-Poletti, J. L., I.M. Llorente, M.P. Velasco, **A. Vicente-Retortillo**, C. Aguirre, R. Caro-Carretero, F. Valero, L. Vázquez. Martian Computing Clouds: A Two Use Case Study. The Seventh Moscow Solar System Symposium, October 10-14, 2016, Moscow, Russia.

1. **Vicente-Retortillo, A.** Characterization of solar radiation on Mars with the Monte-Carlo method. IX Workshop of Young Researchers in Mathematics, 21-23 September 2015, Madrid, Spain.

Poster presentations:

15. **Vicente-Retortillo, A**., G. M. Martínez, N.O. Renno, M. T. Lemmon and M. de la Torre-Juárez. Dust aerosol particle size at the Mars Science Laboratory landing site. EGU General Assembly 2017, April 23-28 2017, Vienna, Austria.

14. Martínez, G., M., **A. Vicente-Retortillo**, N. O. Renno and J. Gómez-Elvira. Correction of MSL/REMS UV data from dust deposition and sensor's angular response. EGU General Assembly 2017, April 23-28 2017, Vienna, Austria.

13. Martínez, G., M., **A. Vicente-Retortillo**, N. O. Renno and J. Gómez-Elvira. Generation of UV radiation data at Gale crater by correcting REMS UV measurements from dust deposition and sensor's angular response. 48th Lunar and Planetary Science Conference, March 20-24 2017, The Woodlands, Texas, USA.

12. Webster, C.R., P. R. Mahaffy, S. K. Atreya, G. Martinez, **A. Vicente-Retortillo** and the MSL Science Team. Low Background Levels of Mars Methane at Gale Crater Indicate Seasonal Cycle: Updated Results from TLS-SAM on Curiosity. 2016 AGU Fall Meeting, 12-16 December 2016, San Francisco, California, USA.

11. de la Torre Juarez, M., J. Gomez-Elvira, S.D. Guzewich, M.T. Lemmon, G. Martinez, E. Mason, S. Navarro, C.E. Newman, M.D. Smith, **A. Vicente Retortillo**. Influence of the atmospheric opacity cycle on the near surface environment of Gale Crater on Mars. DPS 48/ EPSC 11, October 17-21 2016, Pasadena, California, USA.

10. **Vicente-Retortillo, A.**, G. M. Martínez, N. O. Renno, M. T. Lemmon, E. L. Mason, M. de la Torre-Juárez. A Novel Technique to Calculate UV Opacity at Gale Crater from MSL/REMS Measurements. EGU General Assembly 2016, April 17-22 2016, Vienna, Austria.

9. Martinez, G., T. McConnochie, N. Renno, P.-Y. Meslin, E. Fischer, **A. Vicente-Retortillo**, C. Borlina, O. Kemppinen, M. Genzer, A.-M. Harri, M. de la Torre-Juárez, M.-P. Zorzano, J. Martin-Torres, N. Bridges, S. Maurice, O. Gasnault, J. Gomez-Elvira, R. Wiens. Diurnal variation of atmospheric water vapor at Gale crater: Analysis from ground-based measurements. EGU General Assembly 2016, April 17-22 2016, Vienna, Austria.

8. Martínez, G. M., T. McConnochie, N. O. Renno, P.-Y. Meslin, E. Fischer, **A. Vicente-Retortillo**, C. S. Borlina, O. Kemppinen, M. Genzer, A-M. Harri, M. de la Torre-Juárez, M. P. Zorzano, J. M. Torres, N. Bridges, S. Maurice, O. Gasnault, J. Gómez-Elvira, R. Wiens and the REMS Team. Diurnal variation of near-surface atmospheric water vapor at Gale Crater: Analysis from REMS and Chemcam measurements. 47th Lunar and Planetary Science Conference, March 21-25 2016, The Woodlands, Texas, USA.

7. **Vicente-Retortillo, A.**, G. M. Martínez, N. O. Renno, M. T. Lemmon, E. L. Mason, M. de la Torre-Juárez. UV Opacity at Gale Crater from MSL/REMS Measurements. 2015 AGU Fall Meeting, December 14-18 2015, San Francisco, California, USA.

6. Martínez, G. M., E. Fischer, N. O. Renno, E. Sebastián, O. Kemppinen, N. Bridges, C. S. Borlina, P-Y. Meslin, M. Genzer, A-H. Harri, **A. Vicente-Retortillo**, M. de la Torre-Juárez, M. Ramos, F. Gómez, J. Gómez-Elvira. Analysis of likely Frost Events and day-to-night Variability in near-surface Water Vapor at Gale. 2015 AGU Fall Meeting, December 14-18 2015, San Francisco, California, USA.

5. Mason, E.L., M. Lemmon, M. de la Torre-Juárez, **A. Vicente-Retortillo**, G. M. Martínez. Constraining Atmospheric Particle Size in Gale Crater Using REMS UV Measurements and Mastcam Observations at 440 and 880 nm. 2015 AGU Fall Meeting, December 14-18 2015, San Francisco, California, USA.

4. **Vicente-Retortillo, A.**, F. Valero, L. Vázquez, G. M. Martínez. An approach to calculate solar radiation fluxes on the Martian surface. The Fifth Moscow Solar System Symposium, 13-18 October 2014, Moscow, Russia.

3. **Vicente-Retortillo, A.**, F. Valero, L. Vázquez, G. M. Martínez. An approach to calculate solar radiation fluxes on the Martian surface. European Planetary Science Congress 2014, 7-12 September 2014, Cascais, Portugal.

2. **Vicente-Retortillo, A.**, F. Valero, L. Vázquez, M. L. Martín. Estimation of solar radiation in the atmosphere of Mars under different scenarios from an adapted 1-D radiative transfer model. Planet Mars IV Workshop, 20-25 October 2013, Les Houches, France.

1. Vázquez, L., S. Jiménez, F. Valero, **A. Vicente-Retortillo**, M. L. Martín, J. J. Jiménez, F. J. Álvarez-Ríos, I. Arruego, V. Apéstigue, J. M. Oter. Solar Irradiance Sensor (SIS) DREAMS-EDM ExoMars 2016. The Fourth Moscow Solar System Symposium, 14-18 October 2013, Moscow, Russia.

Abbreviations

ASTM: American Society for Testing and Materials

ATS: Air Temperature Sensor

AU: Astronomical Unit

COMIMART: COmplutense and MIchigan MArs Radiative Transfer model

COMIMART-MCF: COmplutense and Michigan MArs Radiative Transfer model using the Monte Carlo method for Flux calculations

COMIMART-MCR: COmplutense and Michigan MArs Radiative Transfer model using the Monte Carlo method for Radiance calculations

CRISM: Compact Reconnaissance Imaging Spectrometer for Mars

ESA: European Space Agency

FOV: Field Of View

HS: Humidity Sensor

IMP: Imager for Mars Pathfinder

IRIS: Infrared Interferometer Spectrometer

IRTM: Infrared Thermal Mapper

ISRU: In-Situ Resource Utilization

LMST: Local Mean Solar Time

LTST: Local True Solar Time

MARCI: MARs Color Imager

MCS: Mars Climate Sounder

MEDA: Mars Environmental Dynamics Analyzer

MEPAG: Mars Exploration Program Analysis Group

MER: Mars Exploration Rover (MER-A: Spirit; MER-B: Opportunity)

MetSIS: Solar Irradiance Sensor of the MetNet mission

MGS: Mars Global Surveyor

Mini-TES: Mini Thermal Emission Spectrometer

MMPM: Mars MetNet Precursor Mission

MNL: MetNet Lander

MODTRAN: MODerate resolution atmospheric TRANsmission

MOLA: Mars Orbiter Laser Altimeter

MOXIE: Mars Oxygen ISRU Experiment

MPF: Mars Pathfinder

MRO: Mars Reconnaissance Orbiter

MSL: Mars Science Laboratory

MY: Mars Year

NASA: National Aeronautics and Space Administration

NIR: Near Infrared

PDS: Planetary Data System

PHX: Phoenix

PIXL: Planetary Instrument for X-ray Lithochemistry

PS: Pressure Sensor

RDS: Radiation and Dust Sensor

REMS: Rover Environmental Monitoring Station

RIMFAX: Radar Imager for Mars' subsurFAce eXperiment

SAM: Sample Analysis at Mars

SHERLOC: Scanning Habitable Environments with Raman & Luminescence for Organics and Chemicals

SSI: Surface Stereo Imager

TES: Thermal Emission Spectrometer

THEMIS: THermal EMission Imaging System

TIRS: Thermal Infrared Sensor

TLS: Tunable Laser Spectrometer

TOA: Top Of the Atmosphere

UV: Ultraviolet

UVS: Ultraviolet Sensor

VL: Viking Lander

WS: Wind Sensor

Part I

Introduction, State of the Art and Contribution of this Work

Chapter 1. Introduction

This chapter is divided into two sections. The first one is devoted to the history of Mars exploration during the pre-telescopic, telescopic and spacecraft eras. The second one is devoted to a general introduction to Mars, focusing on planetary, atmospheric and topographic features.

1.1. Mars exploration

This first section is devoted to the history of Mars exploration. Humankind has always shown big interest in everything that surrounds it, and has made important efforts trying to improve the knowledge of each existing object. The existence of Mars has been known for many centuries, leading to the fascinating history of the exploration of the Red Planet. This section is divided into three subsections describing the progress in the knowledge of Mars in the different stages: pre-telescopic, telescopic and spacecraft eras. An excellent and detailed description of the advances in Mars exploration can be found in Sheehan (1996).

1.1.1. The pre-telescopic era

Although it is not known when Mars was first observed, the ancient civilizations were already familiarized with the Red Planet. It was named the Red One by the Egyptians, and the Star of Death by the Babylonians. The Greeks and the Romans associated it with the god of war: Ares for the Greeks and Mars for the Romans.

Mars was identified by the ancient Greeks as one of the five planets (“wandering stars”, as they were called) known back at that time. In the fourth century B. C., Eudoxus of Cnidus developed a model using 27 spheres centered on the Earth that could explain the retrograde motions of Mars, but it failed to explain the observed changes in the brightness of the planets.

An explanation to these variations arose by 250 B.C., when Aristarchus of Samos developed a heliocentric system, considering the Earth as another planet traveling around the Sun following a circular orbit with a period of one year. However, the famous astronomers that came after him, such as Apollonius and Hipparchus, did not follow his ideas, which were too advanced for their time, and returned to the geocentric model.

In the second century A. D., Claudius Ptolemy developed in Alexandria a system which was successful in calculating the observed motions of the planets. This geocentric model remained virtually unaltered for many centuries.

Fourteen centuries later, Nicolaus Copernicus returned to the heliocentric system, and the idea that the observed retrograde motions of the planet reflected the own motion of our planet in its orbit emerged again.

Tycho Brahe, one of the best observers in history, observed that the distance between the Earth and Mars could be significantly smaller than that between our planet and the Sun. This fact could not be explained with the model developed by Ptolemy, but it was consistent with the system of Copernicus. However, not completely convinced of the latter, he developed an intermediate approach: The planets (except ours) moved around the Sun, which in turn moved around the Earth, which remained in the center of the system, named Tychonic.

At the beginning of the seventeenth century, Kepler, who supported the heliocentric system, found that the planetary orbits could not be circular. He analyzed in detail the observations performed by Brahe and stated that the orbits of the planets were elliptical. Furthermore, he was able to calculate the mean distance between Mars and the Sun with respect to that between the star and our planet, which can be obtained from his Third Law, which states that the ratio between the square of the period of the orbit and the cube of the mean distance to the Sun is constant. Since the Martian year is 687 days long, the mean distance between the Sun and Mars is 1.52 times the distance between the star and the Earth.

In 1609, the first observations of the sky using telescopes were performed, starting a new era on Mars exploration.

1.1.2. The telescopic era

Around 1609-1610, Galileo Galilei made the first observations of Mars with his telescope. However, this instrument could magnify objects only 20 times and aberrations also affected the quality of the observations. For these reasons, very little information could be obtained about Mars.

In 1636, Francesco Fontana made the first drawings of Mars based on his observations using a telescope. These drawings contained features that did not reflect the actual appearance of Mars, but defects in the optical system he used.

Christiaan Huygens observed in 1659 the first albedo feature of the Martian surface, the dark spot known as Syrtis Major (centered around 8.4º N, 69.5º E). Moreover, when three days after he observed Mars again, he found a very similar picture to that in the previous observation; therefore, he concluded that Mars seemed to have a rotation period of 24 hours.

Seven years later, Giovanni Domenico Cassini also observed some spots, which he included in his drawings. Also, by performing observations at the same hour, he realized that he could observe the same regions of the planet every 37 days. From these observations he calculated that the Martian day lasted 24 hours and 40 minutes.

At the same time, Robert Hooke had to take advantage of the few occasions that the atmosphere gave him to perform high quality observations of Mars. He included in his drawings Syrtis Major and other features of the Martian surface.

Returning to Huygens, in 1672 he made a new drawing of Mars. In this occasion it not only clearly showed Syrtis Major, but also the southern polar cap. He also thought about possible life on Mars, but he could only say that temperatures should be lower than on Earth due to its larger distance to the Sun, but he believed that those lower temperatures would not be a problem for the living organisms of the planet, who would have been adapted to those hard conditions.

Giacomo Filippo Maraldi performed observations from which he also calculated the duration of the Martian day, agreeing with the value provided by his uncle, Cassini. He also observed both polar regions of Mars, and in 1719 he observed that the extension of the bright region of the southern polar cap suffered variations.

An explanation to this behavior was provided by Friedrich Wilhelm Herschel, who stated, after his observations in 1783, that the bright regions are due to the intense reflection of the light by icy surfaces, and that the variations in the size of these regions are caused by variations in their exposition to the light of the Sun.

Herschel also stated that Mars had atmosphere, because he could observe changes in partial bright belts that could only explained by the variable disposition of clouds in the Martian atmosphere.

Years later, in 1787, Johann Hieronymus Schröter performed observations of Mars, and he always remained in the idea that the spots on Mars were continuously changing even in temporal windows of one hour, and that, therefore, all he could observe were clouds over the planet. He also made detailed observations of the polar caps, which he considered to be formed by very bright atmospheric precipitation. Finally, considering the features of the orbit and the obliquity of the axis, he stated, as Herschel did, that Mars was the most similar planet to ours.

In1812, the optician Joseph Fraunhofer developed a refractor which enabled clear images of Mars. Ten years later, Georg Karl Friedrich Kunowsky used a Fraunhofer refractor to perform Mars observations, and he arrived to the conclusion that the spots were fixed and, therefore, there were features of the Martian surface.

Wilhelm Beer and Johann Heinrich Mädler stated with absolute confidence after their observations in 1830 that those spots were, in fact, fixed. They also made several measurements of the rotation period of the planet, providing a final value of 24 hours, 37 minutes and 24 seconds. They also performed detailed observations of the southern polar cap, observing its retreat in the Martian southern summer, which supported the idea that the bright regions were caused by ice or snow.

Seven years later they observed the northern polar cap, and they found differences in the behavior of the two polar caps: the retreat of the southern one was faster and the covered area at the minimum in extension was significantly lower in the Southern Hemisphere. This, as it will be discussed later, is explained by the different behavior of the seasons in the Northern and Southern Hemispheres. Three years later, Mädler drew the first map of Mars.

In 1858, Angelo Secchi observed Syrtis Major, but it appeared blue to him. The astronomer named it therefore “Atlantic Canale”, and he stated that the existence of seas and continents on Mars was “conclusively proved”.

Four years later, J. Norman Lockyer also observed the spots on the Martian surface and he also considered them as seas due to their greenish appearance in his observations. Therefore, the presence of continents and seas on Mars became an extended idea.

However, John Phillips, a professor of Oxford, remained skeptic about this idea: He noticed that, if there were seas on Mars, the specular reflection of the Sun should appear on them.

In 1864, Mars was observed by Rev. William Rutter Dawes, who made drawings of the planet which were considered to be clearly better than any others due to the achieved level of detail.

The new detailed maps required an improvement in the nomenclature of the regions of the planet: In 1867, Richard Anthony Proctor made an attempt, with a wide number of regions identified as “Seas” or as “Continents” or “Lands”.

Ten years later, Asaph Hall observed two satellites around Mars and he named them Phobos and Deimos. From the observations of the motion of these satellites, Hall was able to determine the mass of Mars: He stated that the ratio between its mass and that of our planet is 0.1076, which differs in roughly 0.2% from the actual value. In that year, Nathaniel Green was able to identify morning and evening clouds on Mars.

Notwithstanding, the largest step in Martian research in 1877 was given by Giovanni Virginio Schiaparelli. Based on the latitudes and longitudes of 62 identifiable features of the Martian surface, he developed a map which was clearly better than the previous ones. Some of the features shown in previous maps did not appear in his, and he could observe some features which had not been identified before. For this reason, he worked on a new nomenclature for Mars regions, giving names used by the ancient Greeks. These names are still used nowadays.

This new map also showed his *canali*, which could be translated to English as “channels” or “canals”. Instead of “channels”, which reflected more accurately the ideas of Schiaparelli, the term “canals” was adopted, with famous consequences in the next decades.

Finally, Schiaparelli also noticed that the visibility of different regions suffered temporal and spatial variations, which was consistent with the typical events of enhanced dust content during the season around the perihelion.

In 1892, Camille Flammarion finished the first volume of a compilation of the observations of Mars up to that date. He believed that the dark and brighter regions of Mars indicated seas and continents, respectively. Moreover, he thought that the reddish color could be caused by vegetation. He also analyzed in the book the controversial topic regarding the *canali*, stating that it was not possible to deny that those “canals” could form a circulation system on a planetary scale developed by the inhabitants of the planet.

In the same decade, this theory regarding the canals was also supported by Percival Lowell, who wrote that the canals were developed by the inhabitant of the planet to transport water from the polar caps to other locations lacking from this necessary resource.

Schiaparelli left the door open to this possibility because he saw indicators of intelligent life in that network of canals. However, he was always very careful in his asseverations, saying that he was not sure about the actual origin of the canals.

The theory of the *canali* was not embraced by all the community. Edward Emerson Barnard was able to perform observations that magnified by more than one thousand times the apparent size of the planet, and he could not see the canals as straight lines.

In 1894, Edward Walter Maunder wrote that observations could be not revealing the real features of the Martian surface, and that the canals could be chains of dots. A experiment was made in which a number of boys had to reproduce drawings with markings made of small dots; since the drawings were shown from a certain distance, the boys interpreted those markings as canals.

In 1906, the book *Mars and Its Canals*, written by Lowell and based on his observations, became published. In the book he mentioned the pictures made by his assistant Lampland, showing some of the canals. However, the pictures were extremely small (slightly above half a centimeter), and many observers thought that no certain conclusion about the canals could be extracted from them.

Alfred Russell Wallace responded to the asseverations that appeared in Lowell’s book writing the book *Is Mars Habitable?* He mentioned that it would not be really intelligent to build such a network of canals to distribute water across the planet because all the water would be evaporated or would be absorbed by the soil within some kilometers from their source. Still, Lowell’s theory remained widely accepted.

In 1909, Eugène M. Antoniadi conducted some of the best observations of the planet before the spacecraft era. He considered that the canals were completely natural due to their irregular and lacking of geometry appearance.

Although the new findings showed the very natural appearance of the *canali*, the question regarding how a large number of observers could have seen them as straight lines remained. The controversial existence of the canals was finally disproved, the explanation being that they were the result of incomplete perceptions.

During the part of the twentieth century prior to the spacecraft era, new studies and findings about the Martian atmosphere became possible.

In 1947, Gerard Peter Kuiper detected carbon dioxide in the Martian atmosphere, concluding that it contained two times the amount of this gas on Earth. However, the relative abundance of carbon dioxide was not well known, and in 1950 it was estimated to represent a 0.25% of the atmosphere.

Regarding the atmospheric pressure, Lowell published in 1909 an estimation of it based on the estimated albedo and on the known mass of the planet. The result was that the mean pressure on Mars was roughly an 8.7% that on the Earth at the sea level.

Although this number was reduced in 1963 to a maximum of 25 hPa, it was still overestimated. The reason for this is, as it will be shown in the next sections, that dust is present in the Martian atmosphere, increasing its reflective power, and thus leading to wrong values of the pressure when estimated from albedo values under the assumption of a clear atmosphere.

1.1.3. The spacecraft era

The spacecraft era began in 1957, when the Soviet Union launched the *Sputnik 1*, the first artificial satellite orbiting around the Earth. Three years later, in 1960, the Soviets launched the first probes to Mars, but all of them failed. The mission that came closest to success was Mars 1, which was launched in 1962 but lost communications with the Earth on March 21, 1963, when it was 106 million of kilometers away.

The first successful mission was *Mariner 4*, launched by the United States on November 28, 1964. The images obtained by the spacecraft were shocking: There was no vegetation at all, and it seemed that the surface had been dead and unchanged for very long periods of time. Also, *canali* were not observed; instead, the surface presented a high number of craters. This mission allowed a new indirect estimation of the atmospheric pressure, resulting to be between 4 and 6.1 hPa which, combined with the estimated partial pressure of carbon dioxide, allowed to conclude that CO_2 must be the main component of the Martian atmosphere

Days after the launch of *Mariner 4*, the Soviet Union launched *Zond 2*, but communications were lost again before reaching the Red Planet.

Five years later, in 1969, the United States launched *Mariner 6* and *Mariner 7*. The two missions were successful, and a total of 58 pictures were obtained by them, multiplying roughly by ten the size of the region covered by *Mariner 4*, which was around 1% of the planet. The low atmospheric pressure on Mars was confirmed, and the measured temperature of the polar cap was -123ºC, which supported the extended idea that the polar caps were composed of frozen carbon dioxide.

Two more missions were programmed in 1969 by the Soviet Union, but both failed at launch.

In 1971, a total of five missions to Mars were scheduled: Two by the United States (*Mariner 8* and *Mariner 9*) and three by the Soviet Union (*Kosmos 419*, *Mars 2* and *Mars 3*). Two of them, *Mariner 8* and *Kosmos 419*, failed at launch. *Mars 2* and *Mars 3* consisted, in turn, of landers and orbiters. The lander of *Mars 2* crashed on the Martian surface, and its counterpart of *Mars 3* landed softly but transmission stopped after few seconds.

When the three successful missions arrived to Mars, a planet-encircling dust storm was taking place. The orbiters of the Soviet Union had been programmed to take pictures automatically, and therefore could not wait until the dissipation of the dust storm; for this reason, there was very little information in those photos, besides the existence of the dust storm. However, the orbiters were able to perform some useful measurements of the surface temperature at different locations and times of the day.

The most successful mission of the five candidates was clearly *Mariner 9*, which arrived at Mars on May 30, 1971, and lasted until October 27, 1972. During its mission, the spacecraft acquired more than seven thousand pictures of the Martian surface. In these pictures it was possible to see features that looked like outflow channels and valley networks, which suggested that water could have run on the Martian surface in the past.

In 1973, the Soviet Union launched four missions to Mars: *Mars 4, Mars 5, Mars 6* and *Mars 7*. Probably the most successful one was *Mars 5*, which returned data from orbit, but it only lasted nine days.

Two years later, the United States launched two missions: *Viking 1* and *Viking 2*. In turn, each mission had an orbiter and a lander. The landers were the first ones to successfully operate on Mars. Biological experiments were performed on board these landers, but the results remain inconclusive. They also carried meteorological instruments, but the results derived from this kind of measurements are beyond the goals of this historical introduction. The four elements of the Viking performed successfully much longer than expected: Orbiter 2 terminated operations on July 25, 1978; Lander 2 on April 11, 1980; Orbiter 1 on August 17, 1980; and finally Lander 1 on November 13, 1982.

In 1992, the National Aeronautics and Space Administration (NASA) of the United States launched *Mars Observer*, which was designed to expand the information acquired during the Viking missions. Unfortunately, the mission failed three days before arriving to the Martian orbit.

Four years later, the Mars 96 mission of the Russian Federal Space Agency failed at launch. However, in the same year, NASA launched successfully three missions: the orbiter Mars Global Surveyor, the lander Mars Pathfinder and the rover Sojourner. The landed missions finished on September 27, 1997 due to a failure in communication. After extended missions, the termination of Mars Global Surveyor occurred on November 5, 2006, when contact was lost.

In 1998, Japan launched *Nozomi*, also known as *Planet-B*, but it did not arrive to Mars. On the same year, NASA launched the Mars Climate Orbiter, but this mission also failed. In 1999, NASA launched the Mars Polar Lander and the mission Deep Space 2, but both of them were declared a failure.

The first mission that arrived to Mars in the current millennium was the 2001 Mars Odyssey, which has been active for more than 15 years at the time of this writing.

Two years later, in 2003, the European Space Agency made a very successful entrance in the history of Mars exploration with Mars Express mission. This mission consisted of an orbiter and a lander. The lander, Beagle 2, failed after landing, but the Orbiter remains operational more than 13 years after its arrival to Mars.

In the same year, NASA launched two rovers: MER-A (*Spirit*) and MER-B (*Opportunity*). Both missions have successfully operated on the Martian surface. Spirit terminated operations on March 22, 2011, but MER-B remains being operational, providing atmospheric opacity values that have allowed the characterization of the radiative environment at its location for more than seven Martian years, as it will be shown as part of the results of this work (Chapter 5).

NASA made two more launches in the decade of the 2000s: Mars Reconnaissance Orbiter and the Phoenix lander. The orbiter was launched in 2005 and it has been operational for more than ten years, whereas the successful landed mission launched on August 4, 2007, finished operations on November 10, 2008.

In 2011, the Phobos-Grunt mission, a sample return mission to the Martian moon Phobos, suffered a failure after launch by the Russian Federal Space Agency.

On November 26, 2011, NASA launched the MSL mission: The rover, *Curiosity*, arrived at Mars on August 6, 2012, and it is still operational. Its measurements, particularly those of the ultraviolet radiation, have enabled the aerosol studies shown as results of this thesis (Chapter 7).

In 2013, India joined Mars exploration by successfully launching the Mars Orbiter Mission on November 5, and which has been operating for more than two years. NASA launched in the same month the MAVEN mission, which became a new success, and it remains operational.

More recently, the ExoMars Trace Gas Orbiter (European Space Agency (ESA) and Russian Federal Space Agency) and the lander Schiaparelli (ESA) were launched on March 14, 2016. The lander crashed on the surface, but it collected useful data during the landing attempt. The Trace Gas Orbiter arrived to Mars on October 19, 2016, and its main science activities belong to the future.

Several missions are planned to be launched in the next years. These missions of the near future are InSight and Mars 2020 (NASA), ExoMars Surface Platform and ExoMars Rover (Russian Federal Space Agency and European Space Agency), Emirates Mars Mission Hope (United Arab Emirates) and the Chinese Mars Mission. Finally, extending the temporal horizons, MetNet is a proposed mission by Finland, Russia and Spain with the ambitious objective of developing a meteorological network on the Martian surface. Chapter 4 of this thesis is related with MetSIS, the Solar Irradiance Sensor of the MetNet mission.

1.2. An Introduction to Mars

This section is devoted to a presentation of the general features of Mars. The main planetary, atmospheric and topographic features are described in Subsections 1.2.1, 1.2.2 and 1.2.3, respectively.

1.2.1. Planetary Features

Table 1.1 provides a comparison between the main planetary parameters for Mars and Earth. In some aspects, both planets are very similar. The Martian mean solar day (hereinafter referred to as *sol*) has a duration of 24 hours, 39 minutes and 35 seconds, differing in less than a 3% from the solar day on Earth. The obliquity of Mars is only slightly larger than its counterpart on Earth. Therefore, on average, the amount of incoming solar radiation is larger at tropical latitudes than at the poles, as on Earth. The similar obliquity also implies that there are seasonal variations on Mars, and these differences between winter and summer become strong at high- and mid-latitudes.

Parameter	**Mars**	**Earth**
Solar day (s)	88775	86400
Year length (sols)	668.6	365.24
Year length (Earth days)	686.98	365.24
Planetary obliquity (°)	25.19	23.93
Mean orbital radius (10^{11} m)	2.28	1.50
Solar constant (W/m^2)	589	1367
Orbital eccentricity	0.0934	0.017
Distance from Sun (AU)	1.38-1.67	0.98-1.02
L_s of perihelion (°)	251	281
Surface pressure (hPa)	6-10	1013

Table 1.1. Main planetary parameters for Mars and Earth.

Month	**L_s range (°)**	**Duration (sols)**
1	0-30	61.2
2	30-60	65.4
3	60-90	66.7
4	90-120	64.5
5	120-150	59.7
6	150-180	54.4
7	180-210	49.7
8	210-240	46.9
9	240-270	46.1
10	270-300	47.4
11	300-330	50.9
12	330-360	55.7

Table 1.2. Description of the Martian months. $L_s = 180^o$ indicates the Southern Hemisphere Spring Equinox and the beginning of the perihelion season, which is 75 sols shorter than the aphelion season ($L_s = 0 – 180^o$).

In contrast, there are significant differences between the two planets in other aspects. The duration of the Martian year is almost twice as long as on Earth, lasting approximately 669 sols (or 687 days). The Martian year is divided into 12 *months*, defined as the time associated with a change of 30º in solar longitude (L_S). Table 1.2 shows the main features of these months. The mean distance between the Sun and Mars is 1.52 Astronomical Units (AU). Thus, the amount of solar radiation reaching the planet is significantly lower than in ours; in fact, the solar constant is 589 W/m^2, which represents a 43% of its value on Earth. Moreover, the eccentricity of the Martian orbit is more than 5 times larger than that of Earth. Thus, while the Earth remains at distances between 0.98 and 1.02 AU from the Sun, the distance between the Sun and Mars varies from 1.38 to 1.67 AU. Since the perihelion on Mars occurs during the southern summer (L_s = 251º, see table 1.2), the Southern Hemisphere has warmer and shorter summers and colder and longer winters than the Northern Hemisphere.

1.2.2. Atmospheric features

The Martian atmosphere is significantly different from that of our planet. Surface temperatures on Mars are typically lower than on Earth due to the larger distance to the Sun and to the small greenhouse effect of its atmosphere. The absence of oceans and lakes causes a rapid response of the surface to solar insolation, leading to a large range of temperatures, which can be below 150 K and above 300 K.

The pressure at the surface is typically between 6 and 10 hPa (Martínez et al., 2017), which is less than 1% of the mean surface pressure on Earth (1013 hPa). The seasonal variability of the surface pressure is caused by the CO_2 cycle: during the polar winter, temperatures can be below the freezing point of the carbon dioxide (which is the major constituent of the Martian atmosphere, as shown in table 1.3), which causes the condensation of a significant fraction of the Martian atmosphere.

Another key feature of the Martian atmosphere due to its biological implications is the low concentration of H_2O, of the order of precipitable microns. Moreover, atmospheric pressures and temperatures are typically below the triple point of water, and therefore ice directly sublimates. However, due to the low temperatures of the Martian atmosphere and surface, condensates (water ice clouds, fog and frost) can appear despite the low concentration of H_2O.

Gas	**Volume mixing ratio (%)**	
	Mars	**Earth**
CO_2	96.0	0.04
Ar	1.93	0.934
N_2	1.89	78.1
O_2	0.145	20.9
CO	<0.1	10^{-6}

Table 1.3. Volume mixing ratio of the 5 main gases of the Martian atmosphere as measured by the Sample Analysis at Mars (SAM) of the Mars Science Laboratory mission (Mahaffy et al., 2013), and comparison with abundances on Earth.

Besides CO_2 and H_2O, there is a third component of the Martian atmosphere that shows a significant seasonal variability: the suspended dust. Dust is ubiquitous in the Martian atmosphere and plays a key role in its climate due to its interaction with radiation. The seasonal and interannual variability of dust aerosols, as well as the effect on the radiative environment at the surface, will be shown and discussed in Chapters 5 and 7.

1.2.3. Topographic features

Figure 1.1 shows the topography of Mars, generated from the observations of the Mars Orbiter Laser Altimeter (MOLA), on the Mars Global Surveyor (MGS) mission. The complex topography of Mars exhibits volcanic regions including the highest volcano of the Solar System (Olympus Mons, approximately 25 km high) and large impact basins. There is a clear dichotomy between the two hemispheres: The mean altitude of the Southern Hemisphere is high and the terrain presents a large number of craters, in contrast with the Northern Hemisphere. Topography affects local wind patterns, affecting therefore dust transport or cloud formation.

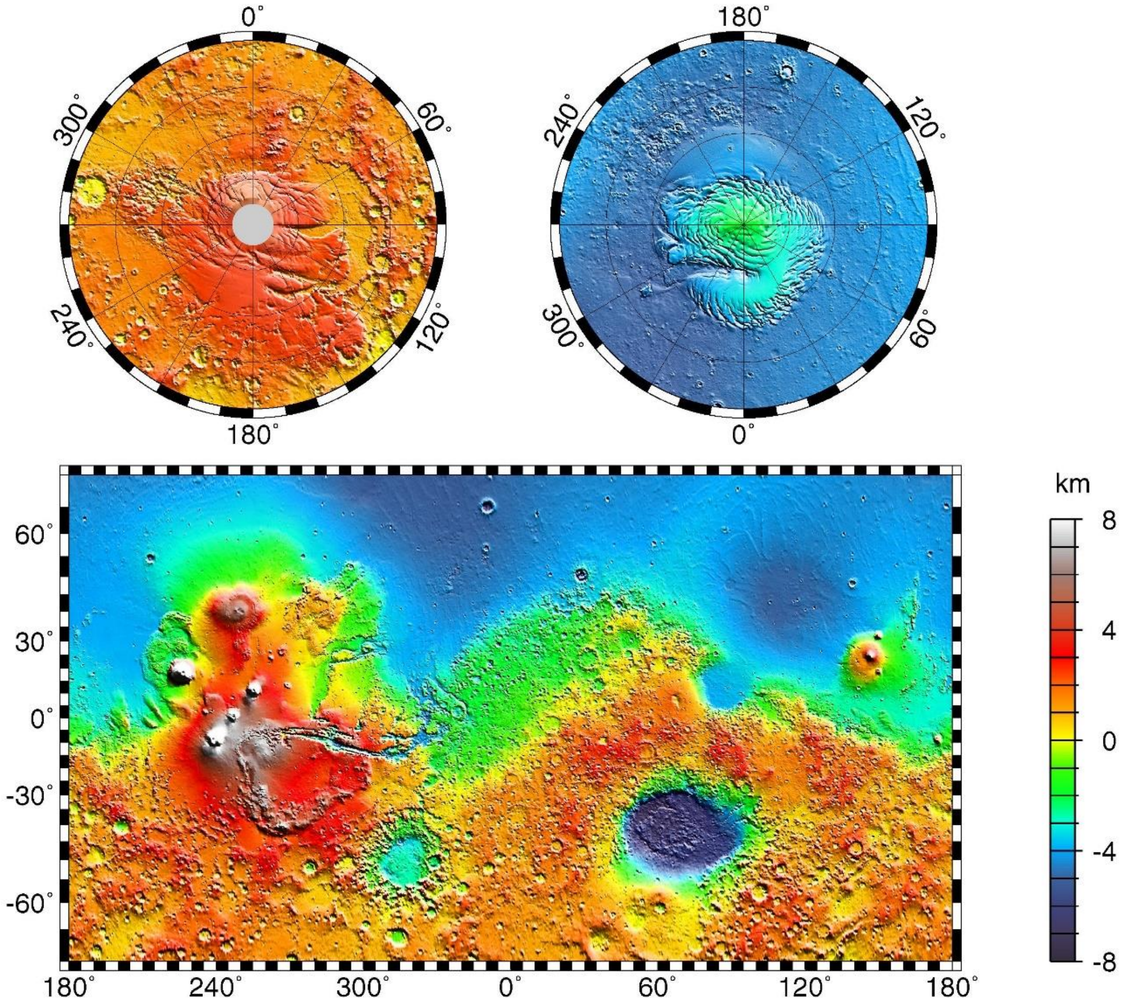

Figure 1.1. Topography of Mars derived from MOLA observations. Image credit: NASA/JPL/GSFC.

Chapter 2. Studies of solar radiation on Mars: Motivation and state of the art

This chapter is divided into four sections. The first section is devoted to the motivation of this work; the second one describes the solar radiation instruments at the Martian surface; the third one is devoted to the state-of-the-art radiative properties of the atmospheric components; finally, the fourth section describes dust opacity and dust aerosol particle size measurements on Mars.

2.1. Motivation of this work

The study of the radiative environment at the surface and in the atmosphere of Mars is paramount to understand and better characterize the physical processes of the atmosphere and the climate of the planet, as well as to determine the biological impact of ultraviolet (UV) radiation. These two objectives are a priority in current and future Mars missions due to their implications in the preparation for the human exploration of the planet.

In particular, solar radiation has implications in several contexts:

1. Solar radiation at the Martian surface is the main term of the energy budget at the Martian surface (Martínez et al., 2014), which drives the ground temperature diurnal evolution (Savijärvi and Kauhanen, 2008; Martínez et al., 2009). Ground temperatures affect, in turn, the thermodynamic processes that occur the Martian planetary boundary layer (Martínez et al., 2009). As an example, there is a correlation between solar insolation at the surface and the dust devil frequency (Petrosyan et al., 2011; Lemmon et al., 2015). There are also correlations between shortwave insolation and other environmental quantities, such as surface temperature and pressure (Martínez et al., 2017). Variations in the amount of radiation absorbed by the atmosphere affect the large scale circulation. Variations in absorbed radiation lead to changes in heating rates (Madeleine et al., 2011), which affect the thermal structure of the atmosphere and, therefore, the dynamical fields (Read and Lewis, 2004).
2. UV radiation has important implications for habitability due to its effects on microorganisms (Cockell and Raven, 2004; Patel et al., 2004). The Biological Action Spectrum for DNA damage is particularly important in the UVC region of the spectrum (λ<280 nm), where its intensity is approximately six orders of magnitude larger than in the UVA region (320 nm < λ < 400 nm) (Córdoba-Jabonero et al., 2003).
3. The interaction between molecules and solar radiation leads to multiple photochemical reactions that affect the composition of the Martian atmosphere (González-Galindo et al., 2005). Moreover, background methane concentrations measured at the MSL location appear to correlate with surface UV insolation at the surface (Webster et al., 2016).

4. Measurements of solar radiation provide information about the atmospheric composition. In particular, these measurements allow the quantification of the atmospheric opacity, which depends mainly on the amount of suspended dust. Moreover, radiation measurements can provide information on aerosol properties, such as particle size.

Considering the importance of solar radiation in several scientific disciplines, it becomes necessary to develop comprehensive and accurate radiative transfer models adapted to the Martian atmosphere. There are a number of reasons that motivate the development of such models:

1. The Martian atmosphere is very different from the atmosphere of the Earth. As shown in Section 1.2.2, the abundances of gas molecules in the Martian atmosphere differ significantly from those on our planet, particularly in the cases of CO_2, N_2 and O_2. The Martian atmosphere is also very thin, with a mean surface pressure that is below 1% of that on Earth. More importantly, dust plays a key role in the scattering and absorption of solar radiation in the Martian atmosphere, whereas its effect in our atmosphere is typically less important. In contrast, clouds, which significantly affect solar radiation on Earth, usually play a minor role (compared to dust) in the Martian atmosphere. For all these reasons, it is important to develop radiative transfer models that contain updated wavelength-dependent radiative properties of the components of the Martian atmosphere.
2. These radiative transfer models allow the quantification of the spectral irradiances, integrated fluxes and daily irradiations at the Martian surface for a wide number of scenarios. These models do not require the validation of additional parametrizations applicable to wide spectral regions, since the irradiance is computed at each desired wavelength.
3. These models are needed to maximize the scientific return of solar radiation measurements on Mars. In order to analyze the acquired data, it is necessary to simulate the spectral irradiances in the spectral region in which the measurements are performed. With radiative transfer models that contain wavelength-dependent radiative properties of the atmosphere it is possible to perform studies of dust aerosol properties from solar radiation measurements.

In this work, we have developed radiative transfer models using two different schemes. The first model, hereinafter COMIMART (COmplutense and MIchigan MArs Radiative Transfer model), uses the delta-Eddington approximation (Joseph et al., 1976) and it is described in Chapter 4. The second model relies on the Monte Carlo method, and we have developed two versions of it: COMIMART-MCF (COmplutense and MIchigan MArs Radiative Transfer model using the Monte Carlo method for Flux calculations) and COMIMART-MCR (COmplutense and MIchigan MArs Radiative Transfer model using the Monte Carlo method for Radiance calculations); it is described in Chapter 6.

Accurate simulations of the solar radiation at the Martian surface require not only comprehensive and validated radiative transfer models, but also an accurate knowledge of the radiative properties of the atmospheric components, suspended dust being especially important. Dust radiative properties are determined by the complex refractive index, size distribution and shape of the suspended dust particles. The radiative quantities that characterize the effect of the atmosphere on the incoming solar radiation and their values for the components of the Martian atmosphere are defined and shown in Section 2.3.

2.2. Solar radiation instruments at the Martian surface

Measuring solar radiation in different bands of the spectrum has become an important objective of various current and future missions to Mars due to its relevance in different aspects of Mars exploration, such as understanding the Martian atmospheric processes and climate, or preparing for human exploration of the planet. In this Section we focus on the two instruments that constitute the context of this work: The UVS of REMS, on board the MSL mission, and MetSIS, of the MetNet mission. The RDS of the Mars 2020 mission is described in Chapter 11.

2.2.1. The UVS of REMS/MSL

The MSL mission was launched on November 26, 2011, and landed on the base of Gale Crater (4.6°S, 137.4°E) on August 5, 2012. The main objective of the MSL mission is to assess whether Mars ever had an environment capable of supporting microbial life. To achieve this objective, the MSL Curiosity rover carries the most capable suite of scientific instruments ever sent to the surface of another planet (Grotzinger et al., 2012). Among these instruments, REMS was designed to investigate environmental conditions relevant to current habitability (Gómez-Elvira et al., 2012).

The REMS instrument includes six sensors that have been measuring atmospheric pressure (Harri et al., 2014a; Haberle et al., 2014), atmospheric relative humidity (Martínez et al., 2016; Harri et al., 2014b), ground and atmospheric temperatures (Martínez et al., 2014; Hamilton et al., 2014), horizontal wind speeds (Newman et al., 2017) and UV radiation fluxes (Smith e al., 2016) for more than two full Martian annual cycles (Gómez-Elvira et al., 2014; Martínez et al., 2017).

The REMS UVS is located on the rover deck (Figure 2.1) and is comprised of six photodiodes to measure UV fluxes in six different bands (Table 2.1). Channel ABC was designed to provide estimates of the total UV irradiance, A and B to compare the UV flux at the surface of Mars with that on Earth, C to provide a first order estimate of the level of biologically damaging irradiance, and D and E channels to match the two UV channels of the Mars Color Imager (MARCI) onboard the Mars Reconnaissance Orbiter (Gómez-Elvira et al., 2012; Wolff et al., 2010).

The REMS UVS nominal strategy for data acquisition consists of 5 minutes of measurements at 1 Hz every Mars hour, with at least an additional hour of 1 Hz measurement during each sol. Given the availability of additional payload energy, the team decided to extend REMS measurements coverage by using the so-called extended blocks, which replace the nominal 5-minute blocks by blocks lasting one or more hours (Gómez-Elvira et al., 2014). This strategy has resulted in UVS measurements covering full diurnal cycles at 1 Hz every few weeks during approximately two full Martian years.

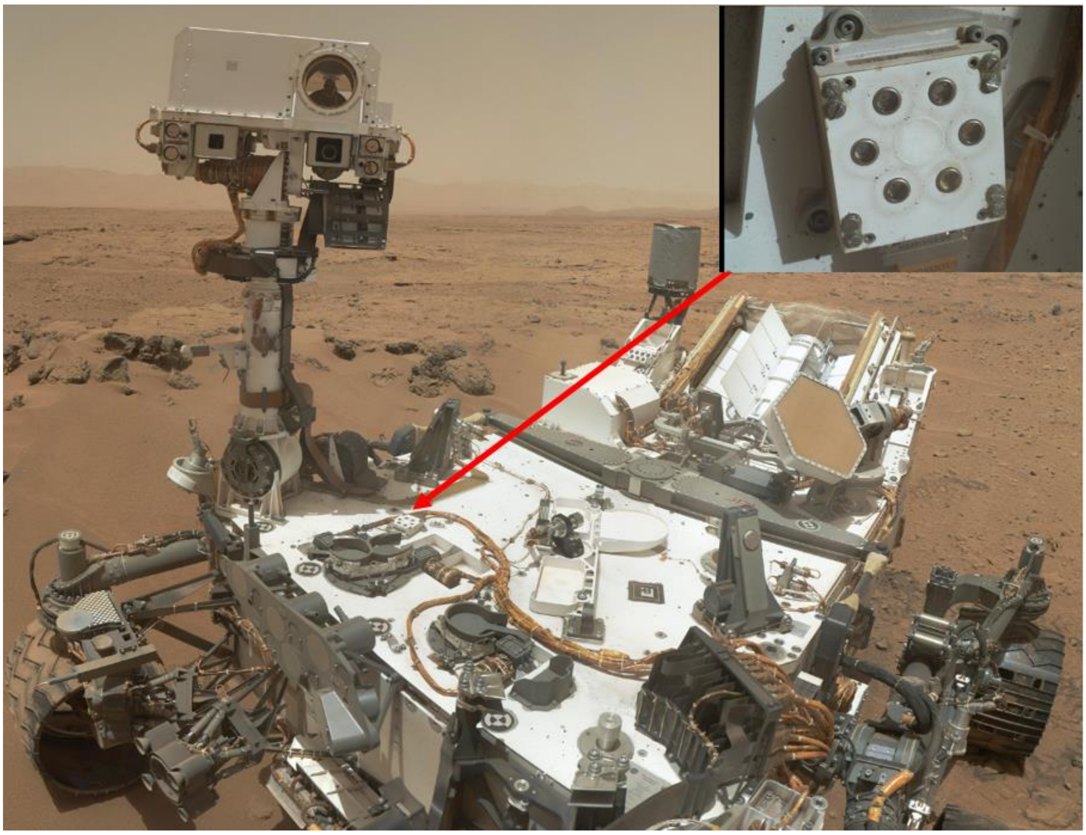

Figure 2.1. Detail of a mosaic of the Curiosity rover from images taken by the Mars Hand Lens Imager (MAHLI) on sol 84 of the mission. The red arrow indicates the REMS UVS. The top-right panel shows a picture taken by MAHLI of the UVS on sol 36 of the mission. Credit of the original images: NASA/JPL-Caltech/MSSS.

Channel	Spectral range (nm)
UVABC	200-380
UVA	320-380
UVB	280-320
UVC	200-280
UVD	230-290
UVE	300-350

Table 2.1. Bandwidths of the six UVS channels (Gómez-Elvira et al., 2012).

The REMS UVS photodiode output currents have been used to retrieve dust aerosol opacity (Smith et al., 2016; Vicente-Retortillo et al., 2015b; Vicente-Retortillo et al., 2016b) and particle size (Vicente-Retortillo et al., 2017) at Gale Crater. The processed REMS UVS data, in units of W/m^2, have not been used due to physical inconsistencies in the calibration function (Vicente-Retortillo et al., 2017; Martínez et al., 2017b). As future research, we plan to correct the processed data sets and to make them available to the scientific community (see Chapter 10).

2.2.2. The MetSIS instrument of MetNet mission

MetNet is a planned mission to Mars, developed by Finland, Russia and Spain. The final objective of the mission is to develop a network of MetNet Landers (MNLs) with atmospheric instruments operating simultaneously for several Martian years (Harri et al., 2017).

Prior to the development of the meteorological network, the first objective is to demonstrate feasibility of the MNL concept with the Mars MetNet Precursor Missions (MMPM). The Solar Irradiance Sensor, MetSIS, will be included in the payload of this precursor mission. MetSIS includes 27 channels covering eleven bands of the spectral range between 200 and 1100 nm (ranging from the ultraviolet to the near infrared) and two sensors of the angular position of the Sun (Romero et al., 2011). Although some channels are located in the lateral faces of the instrument, most of them have a hemispherical FOV and are designed to be pointing to the zenith (Apéstigue et al., 2015). The combined use of the different measurements and modeling results will allow retrievals of atmospheric opacity and dust aerosol particle size (Vicente-Retortillo et al., 2015).

2.3. State-of-the-art radiative properties of the atmospheric components

The components of the Martian atmosphere interact with the incoming solar radiation by means of absorption and scattering processes. Part of the incoming radiation at the top of the atmosphere of the planet (denoted as E) reaches the surface without interacting with the atmosphere or after being scattered in the forward direction; it is called direct (or beam) radiation (B). The fraction of the incoming radiation at the surface that has been scattered in the atmosphere is called diffuse radiation, and it is denoted as D. The total radiation at the surface, T, is the sum of the direct and the diffuse radiation.

The first key radiative parameter needed to perform simulations of solar fluxes at the surface is the opacity τ, which is defined as:

$$\tau = \log\frac{E}{B} \quad (2.1)$$

This atmospheric opacity is calculated from the individual contributions of dust (d), water ice clouds (c) and gas molecules (g):

$$\tau = \tau_d + \tau_c + \tau_g \quad (2.2)$$

Dust is the atmospheric component with the greatest impact on the absorption and scattering of solar radiation. In order to quantify the result of its interaction with solar radiation, three radiative parameters are needed:

1. The extinction efficiency, $Q_{ext,d}$, which is defined as the extinction cross-section (the sum of the scattering and absorption cross-sections) divided by the projected surface area of the dust particles. It is directly proportional to opacity (Madeleine et al., 2011).
2. The single-scattering albedo, $\omega_{0,d}$, which is defined as the ratio between scattering and extinction coefficients. It is the fraction of the radiation interacting with a

particle that is scattered. In the Monte Carlo approach, it represents the surviving fraction of the incoming photons after one interaction with dust particles.

3. The phase function, P_d, which is defined as a function that describes the dependence of scattered radiation as a function of scattering angle; it represents the probability of scattering in any given direction. The first moment of the phase function is the asymmetry factor, which is used in the delta-Eddington approximation (Joseph et al., 1976).

These parameters can be computed from the refractive indices provided by Wolff et al. (2009) and by Wolff et al. (2010). As examples, the computations can be performed assuming that particles are spheres and using Mie theory or assuming that particles are cylinders with a diameter-to-length ratio of 1 and using the T-Matrix code of Mishchenko and Travis (1998).

The three aforementioned parameters depend on the size distribution. Log-normal and power-law size distributions, characterized by the effective radius, r_{eff}, and the effective variance, v_{eff} (Hansen and Travis, 1974), are typically used.

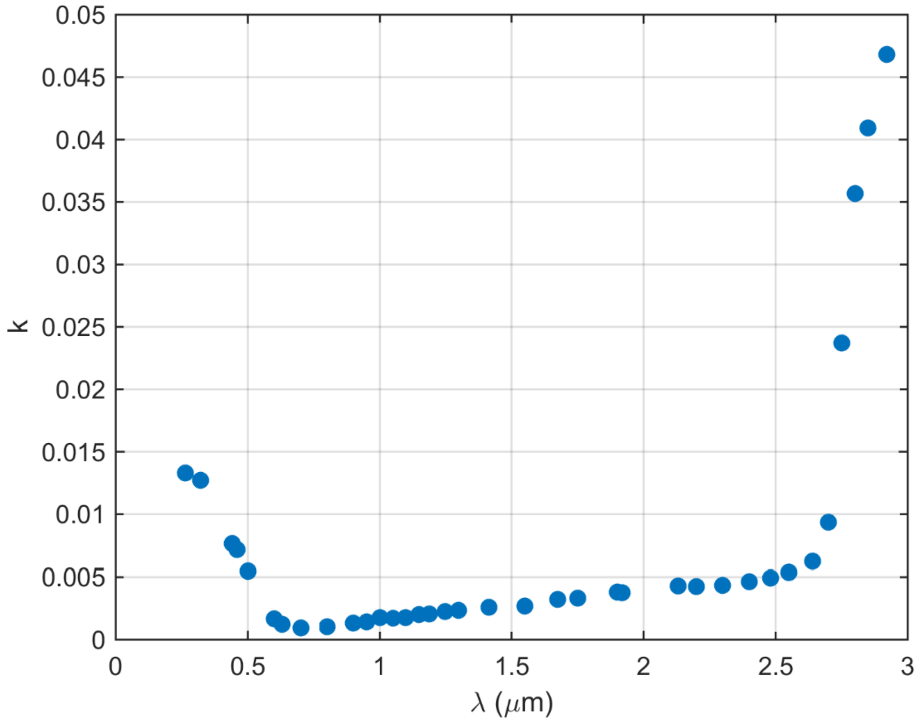

Figure 2.2. Imaginary part of the Martian dust refractive index (*k*) as a function of wavelength, as derived by Wolff et al. (2009) and Wolff et al. (2010).

Figure 2.2 shows the imaginary part (*k*) of the complex refractive index of the Martian suspended dust as a function of wavelength, derived from the observations of the Mars Reconnaissance Orbiter (MRO) performed by the instruments Compact Reconnaissance Imaging Spectrometer for Mars (CRISM) between 440 and 2920 nm (Wolff et al., 2009) and by MARCI in the UV region of the spectrum (Wolff et al., 2010).

The real part is not shown due to its small variation with wavelength: it shows a minimum of 1.45 at 2.75 µm and a maximum of 1.5 at 0.5 µm.

Figure 2.2 shows that Martian dust absorbs radiation at every wavelength of the shortwave spectrum (k = 0 indicates no absorption). Martian dust shows an absorption peak close to λ = 3 µm and a secondary peak in the UV region of the spectrum (λ < 0.4 µm). In contrast, the imaginary part of the refractive index shows a minimum at around λ = 0.7 µm, indicating weak absorption in the visible and near infrared region of the spectrum.

Figure 2.3 shows the extinction efficiency (top), the single-scattering albedo (middle) and the asymmetry factor (bottom) of the Martian dust as a function of wavelength, assuming standard values of r_{eff} = 1.5 µm (Clancy et al., 2003; Wolff and Clancy, 2003; Kahre et al., 2006; Madeleine et al., 2011) and ν_{eff} = 0.3 (Rannou et al., 2006; Madeleine et al., 2011).

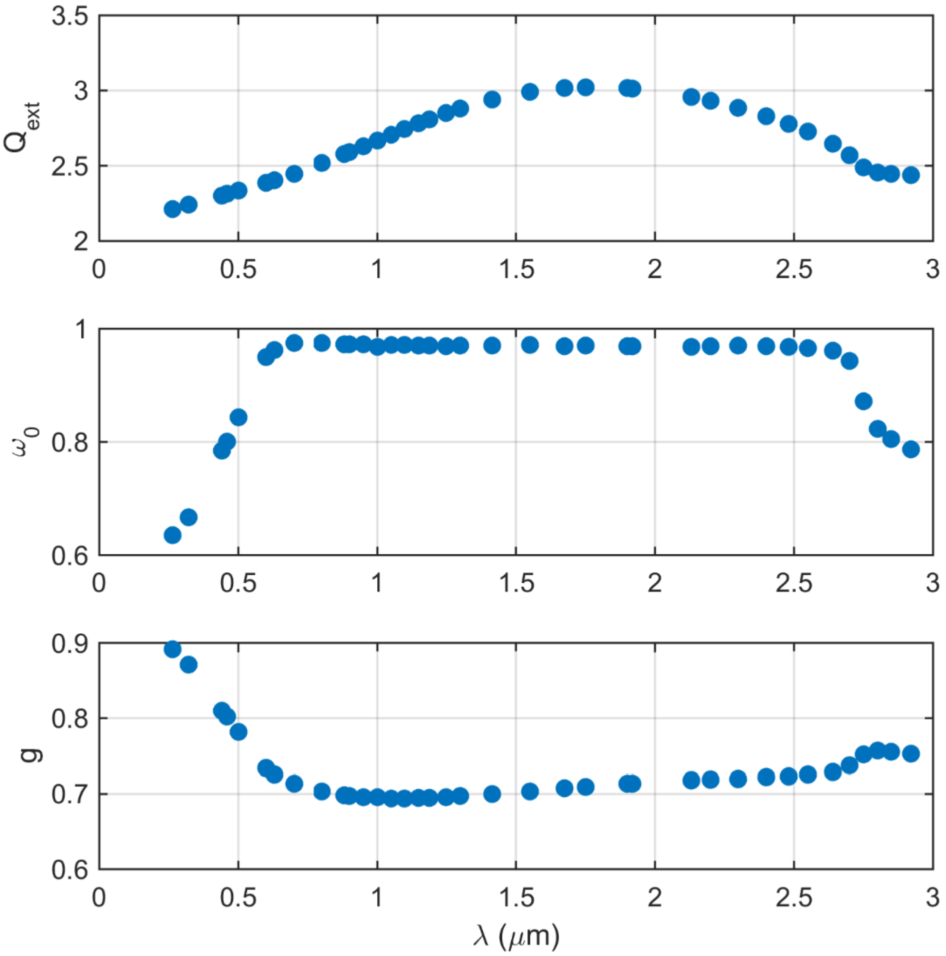

Figure 2.3. Wavelength dependence of extinction efficiency (top), single-scattering albedo (middle) and asymmetry factor (bottom) of the Martian dust, calculated from the refractive indices of Wolff et al. (2009) and Wolff et al. (2010).

As mentioned earlier, extinction efficiency is directly proportional to opacity (Madeleine et al., 2011). Therefore, extinction efficiencies can be used to calculate the spectral behavior of the optical depth by using the opacity at a particular wavelength as a reference, which is typically 880 nm to enable a direct comparison to the measurements taken by the Pancam cameras at the locations of the Mars Exploration Rovers (Lemmon et al., 2015) and by the Mastcam camera at the MSL site (Smith et al., 2016); we denote the dust optical depth at this wavelength by $\tau_{d,880}$. For the canonical size, dust opacity increases with wavelength until a maximum is reached between 1.5 and 2 μm, and UV opacities are expected to be between 10% and 15% smaller than Mastcam opacities at 880 nm. As the ratio between these opacities depends on particle size, temporal variations in the ratio between REMS UV opacities and Mastcam opacities can indicate seasonal changes in dust particle size at Gale Crater.

The single-scattering albedo is above 0.95 in the spectral range between ~0.6 μm and ~2.7 μm, indicating that most of the radiation is scattered in each interaction with dust particles, and only a small percent (below 5%) is absorbed. In contrast, there is a significant decrease towards the ultraviolet region, where more than a 30% of the photon is absorbed in the interaction.

Figure 2.3 also shows that there are two radiative regimes at wavelengths shorter than 1100 nm, which can be used to enhance the scientific return of measurements performed in different bands of this spectral range: in the ultraviolet region the mean scattering angle is very low (high value of the asymmetry factor) and the single-scattering albedo is low, whereas in the near infrared region scattering is less anisotropic and dust absorbs less radiation.

As mentioned before, the radiative properties depend on the effective radius of the dust aerosol size distribution (see Table 2.2). The single-scattering albedo also depends on particle size, and its values increase with decreasing effective radius. In contrast, the asymmetry factor increases with increasing dust particle size.

Figure 2.4 shows the scattering phase functions and the cumulative scattering phase functions at a wavelength of 320 nm assuming four effective radii: 0.5, 1, 1.5 and 2 μm. The panel on the left shows that most of the radiation is scattered in directions that are close to the propagation direction, and this effect increases with increasing particle size. As an example, assuming an effective radius of 1.5 μm, the fraction of the incoming radiation that is scattered with a scattering angle of 1º is more than three orders of magnitude larger than that scattered with a scattering angle of 45º. The right panel shows the cumulative phase functions for scattering angles between 0º and 40º. As another example, this panel shows that the fraction of radiation that is scattered within 10º of the direction before the interaction is 30% for an effective radius of 0.5 μm, whereas it is ~65% for an effective radius of 1.5 μm. The relative differences are even larger for smaller scattering angles. The main conclusion of this figure is that the mean angle of the scattered radiation decreases with increasing particle size. In this idea relies our methodology to retrieve dust aerosol particle size from REMS measurements, as shown in Chapter 7.

r_{eff} (μm)	**ω_0**	**g**
0.5	0.846	0.741
1.0	0.728	0.826
1.5	0.678	0.871
2.0	0.654	0.896

Table 2.2. Single-scattering albedo (ω_0) and asymmetry factor (g) as a function of dust aerosol particle effective radius (r_{eff}) at a wavelength of 320 nm.

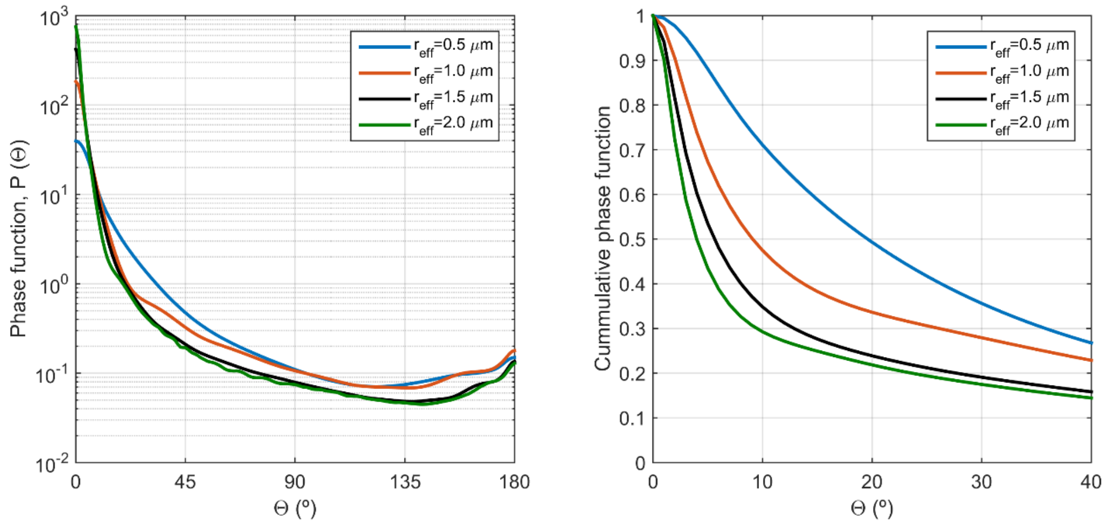

Figure 2.4. Dust aerosol phase function (left) and dust aerosol cumulative phase function (right) as a function of scattering angle (Θ) at a wavelength of 320 nm.

Analogously, water ice radiative properties ($Q_{ext,c}$, $\omega_{0,c}$, P_c and g_c) are calculated from the refractive indices obtained by Warren (1984). In this case, a log-normal size distribution with $r_{eff} = 3$ μm (Wolff and Clancy, 2003) and $\nu_{eff} = 0.1$ (Wolff and Clancy, 2003; Madeleine et al., 2012) is typically selected.

Figure 2.5 shows the extinction efficiency (top), the single-scattering albedo (middle) and the asymmetry factor (bottom) of water ice clouds as a function of wavelength under the assumed effective radius and effective variance.

Similarly to the dust case, extinction efficiency depends on wavelength. In order to obtain water ice opacity at each wavelength, the same procedure as for the dust can be followed, but selecting ~12.1 μm (825 cm^{-1}) as the reference wavelength to simplify the comparison to Thermal Emission Spectrometer (TES) results (Smith 2004).

Water ice is virtually a pure scatterer in the shortwave range, except in the spectral region close to 3 μm, where absorption is significant. As in the dust case, scattering by water ice is far from being isotropic, as the asymmetry factor is high. For the assumed particle sizes, the mean scattering angle is smaller for dust than for water ice in the UV and in part of the visible spectral range, whereas the opposite occurs at longer wavelengths.

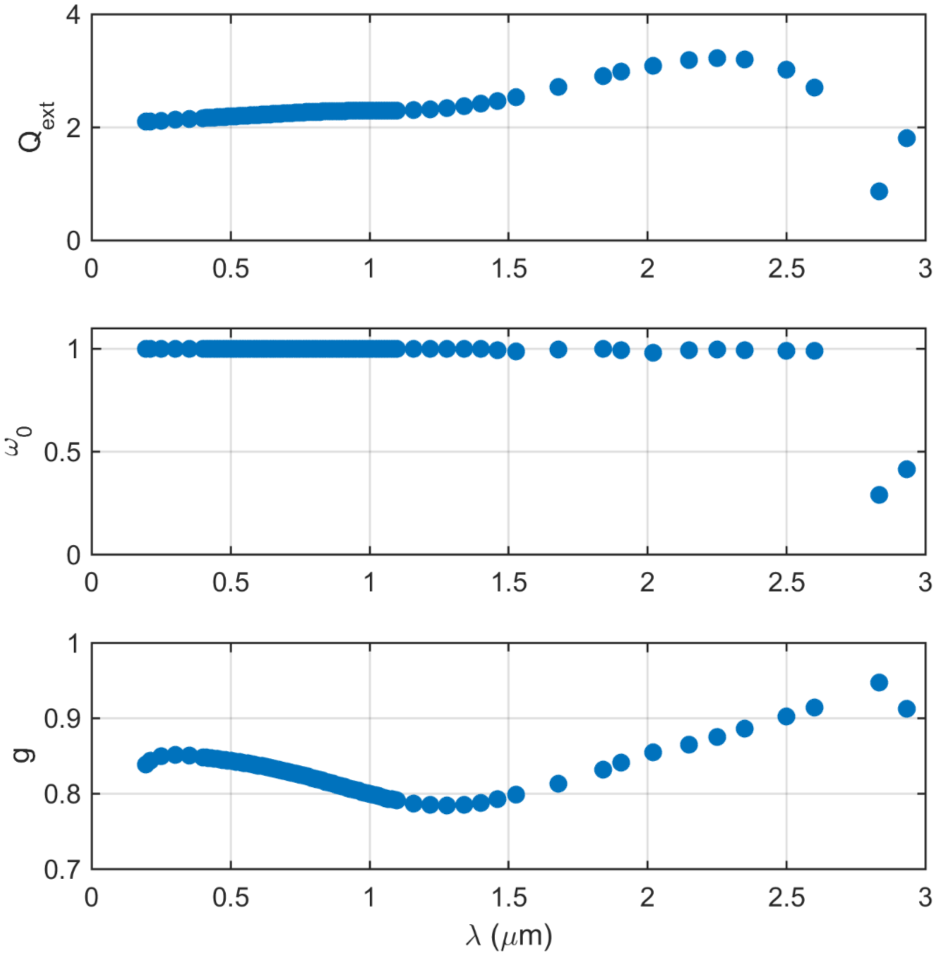

Figure 2.5. Wavelength dependence of extinction efficiency (top), single-scattering albedo (middle) and asymmetry factor (bottom) of water ice, calculated from the refractive indices of Warren (1984).

The interaction of gas molecules with solar radiation is quantified by means of their scattering and absorption cross-sections. The scattering cross-sections are inversely proportional to the fourth power of wavelength; this Rayleigh scattering is less important than on Earth due to the difference in gas density between the two planets.

Absorption by gas molecules is calculated from their absorption cross-sections when an absorption continuum is observed for a particular component. In the solar range, and particularly below 1100 nm (MetSIS range), the main absorbers are CO_2 and O_3. We have included in the model the CO_2 cross-sections of Lewis and Carver (1983) and the O_3 cross-sections of Serdyuchenko et al. (2014).

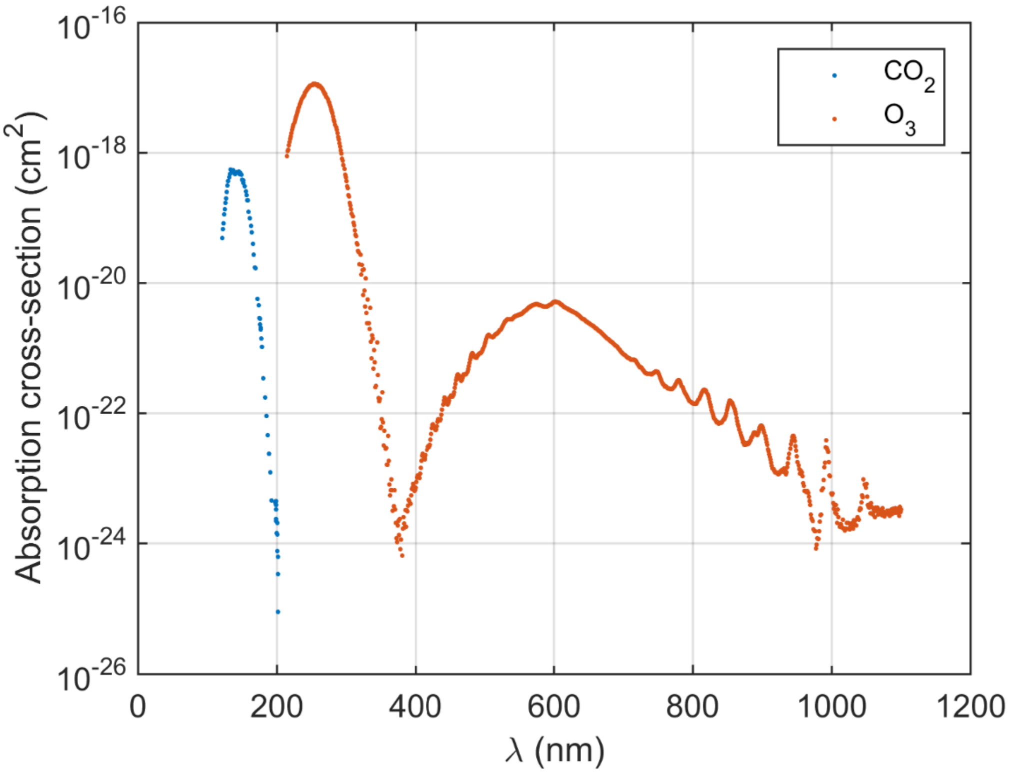

Figure 2.6. Absorption cross sections of CO_2 and O_3 at ~200 K.

Figure 2.6 shows the absorption cross sections of CO_2 and O_3 at a temperature of ~200 K. In the present Martian atmosphere, CO_2 is the gas with the greatest impact on solar radiation. The combination of the high absorption cross-sections and the high abundance of CO_2 in the atmosphere of Mars produces a cut at ~200 nm in the solar spectrum that reaches the Martian surface (abundances are ~10^{23} cm^{-2}). O_3 shows high values of the absorption cross-section in the Hartley band (centered at 255 nm), but its abundance in the Martian atmosphere is typically around 10^{15}-10^{16} cm^{-2} (Perrier et al., 2006). For this reason, O_3 does not have a large impact on the solar flux at the surface (Vicente-Retortillo et al., 2015), but it can leave a signature on the spectral irradiance that can be used to quantify its abundance from measurements at different wavelengths performed by instruments such as the RDS of the Mars 2020 mission (Apéstigue et al., 2015).

2.4. Opacity and dust aerosol particle size measurements on Mars

Dust is ubiquitous in the Martian atmosphere and its interactions with radiation are very strong (Read and Lewis, 2004). Therefore, in order to study the radiative environment at the Martian surface and the atmospheric processes, it is essential to characterize the suspended dust accurately. The spatial distribution and radiative properties of the suspended dust have a strong impact on calculations of heating rates and thus on the atmospheric thermal behavior (Madeleine et al., 2011) and dynamical processes (Read and Lewis, 2004).

Dust opacity controls the amount of radiation that reaches the surface (see Chapters 4 and 5), which is the main term of the energy budget at the surface of Mars (Martínez et al. 2014). This energy budget determines the diurnal cycle of the ground temperature (Savijärvi and Kauhanen, 2008; Martínez et al. 2009), which affects the thermodynamic activity in the planetary boundary layer (Martínez et al. 2011). As an example, dust devils are more frequent on Mars when the insolation is higher and thus the surface is warmer, being therefore more frequent on summer (Petrosyan et al. 2011).

In addition to opacity, dust aerosol particle size is another important quantity in atmospheric studies since it determines the ratio between the atmospheric opacity at solar and infrared wavelengths, affecting heating rates and thermodynamical processes (Kahre et al., 2008; Madeleine et al., 2011; Medvedev et al., 2011). Dust particle size affects opacity if abundances remain constant and also exerts a strong influence on atmospheric transport and gravitational settling rates (Kahre et al., 2008), which are important quantities to correctly represent the dust cycle.

A large number of efforts have been done to characterize the spatial and temporal variability of dust in the last decades. Advances in the characterization of dust have been mainly achieved from orbiter observations, but also from ground measurements. We now describe some of the main achievements in the characterization of dust aerosol opacity and particle size.

2.4.1. Dust opacity measurements

The first measurements were performed at the beginning of the decade of 1970 by the Infrared Interferometer Spectrometer (IRIS) onboard Mariner 9 during the dissipation of the global dust storm in 1971 (Hanel et al., 1972). Between 1976 and 1979, data acquired by the Viking IR Thermal Mapper (IRTM) allowed global dust opacity mapping for more than 1.3 Martian years (Martin and Richardson, 1993); the results showed that there were two planet-encircling dust storms within this temporal range, known as 1977a and 1977b.

Approximately 20 years after Viking observations, the TES onboard the MGS mission began to monitor the atmospheric conditions. Smith (2004) used TES measurements to study the interannual variability of dust opacity between 1999 and 2003. He concluded that during the aphelion season (L_s = 0º - 180º), dust opacity is low and presents low interannual variability; in contrast, during the perihelion season (L_s = 180º - 360º) the atmosphere is dustier and presents higher interannual variability.

More recently, infrared images acquired by the Thermal Emission Imaging System (THEMIS) onboard the Mars Odyssey mission over more than three and a half Martian years (between 2002 and 2008) were used by Smith (2009) to retrieve dust opacities. He showed that the dust activity during Mars Year (MY) 28 was markedly higher than in the previous two Martian years.

Additional retrievals of dust opacity were performed by the Mars Climate Sounder (MCS) onboard the MRO. The combination of TES, THEMIS and MCS measurements has allowed producing a dust climatology covering the temporal range between April 1999 and July 2013 (Montabone et al. 2015), which corresponds to MY 24 to MY 31.

Ground-based observations of opacity, although scarcer than from orbit, are very important because the retrieval process incorporates fewer assumptions than from orbit and thus the uncertainty in the results is lower, providing “ground truth” and complementary information for the analysis of satellite measurements. The opacity measurements performed by the different missions that successfully landed on Mars can be found in Martínez et al. (2017).

Colburn et al. (1989) analyzed Sun images acquired by the cameras at the two Viking landing sites at a wavelength of 670 nm over a span of 1.3 Martian years. These dust opacity measurements covered 328 out of the first 920 sols of Viking Lander 1 (VL1) and 250 out of the 872 sols of Viking Lander 2 (VL2).

Ten years later, Smith and Lemmon (1999) obtained atmospheric opacity values using direct images of the Sun by the Imager for Mars Pathfinder (IMP) during the 83-sol Mars Pathfinder (MPF) mission. They provided hourly opacities between 07:00 and 17:00 LTST (Local True Solar Time) at four wavelengths (450, 670, 883 and 989 nm), with values similar to those at the Viking sites. These measurements were performed in 70 out of the 83 sols of the mission.

The dataset of atmospheric opacity values at the two MER rovers has been obtained from direct solar images of the Sun using the Pancam cameras at the wavelengths of 440 and 880 nm (Lemmon et al. 2015). These time series are the most complete up to date, with opacity values spanning more than 2200 sols for MER-A (Spirit) and more than 4600 sols (approximately seven Martian Years) for MER-B (Opportunity) as of this writing. This optical depth record has been used as “ground truth” results in many studies, such as Wolff et al. (2009), Wolff et al. (2010) or Montabone et al. (2015). The dataset includes values for more than 90% of the sols, providing an excellent temporal coverage to study the seasonal and interannual variability.

Tamppari et al. (2010) showed the opacities at the Phoenix (PHX) landing site, which were derived from direct solar imaging by the Surface Stereo Imager (SSI) at the wavelengths of 451, 671, 887 and 991 nm. Opacities are available for 117 sols out of the 151 sols of the mission.

More recently, images of the Sun by the Mastcam instrument onboard MSL Curiosity rover are providing new aerosol opacity values at the MSL landing site. Measurements are performed at the wavelengths of 440 and 880 nm and the nominal data acquisition strategy consists on measurements performed every three to seven sols (Smith et al., 2016).

All these measurements have provided a detailed picture of the dust cycle. The seasonal and interannual variability of opacity and solar radiation is studied in detail from MER and MSL measurements in Chapter 5. A complementary inclusive discussion of the radiative environment at all the landing sites and of its effect on other meteorological and environmental variables can be found in Chapter 8.

2.4.2. Dust aerosol particle size measurements

The dust aerosol particle size distribution function is usually expressed in terms of the effective radius and the dimensionless effective variance (Hansen and Travis, 1974). Dlugach et al. (2003) provide a detailed description of the values of these two parameters that were available at the beginning of the 2000s, which were retrieved using different methods.

The main methods that have been used to retrieve particle size are:

1. Imaging sky brightness at visible wavelengths from the Martian surface as a function of angular distance from the Sun.
2. Analysis of spectra in the thermal infrared taken as emission-phase functions, where a fixed spot of the surface is viewed at a wide range of emission angles as an orbiter passes over it.
3. Comparison of dust opacities obtained at wavelengths separated by a large spectral range.

Method 1 has been applied to images acquired by the Viking Landers (Pollack et al., 1995), Mars Pathfinder (Tomasko et al., 1999) and the Mars Exploration Rovers (Lemmon et al., 2004). Results from the different missions are in very good agreement, showing values of the mean radii that are very close to the canonical size of 1.5 μm. Values of the effective variance are in the range 0.2 – 0.5.

Method 2 has been applied to spectra obtained by TES on board the MGS mission. Wolff and Clancy (2003) found a representative value of r_{eff} = 1.5 – 1.6 μm, although they observed deviations toward both smaller and larger particle sizes.

Finally, method 3 has been used both from orbiters and from landed missions. Clancy et al. (2003) used TES measurements in the solar band in combination with those in the thermal infrared to estimate dust aerosol particle size. They obtained that the effective radius shows significant seasonal variability, with extreme values that can be below 1 μm and also above 1.7 μm.

Lemmon et al. (2015) compared opacities at the MER landing sites derived from Mini Thermal Emission Spectrometer (Mini-TES) measurements at 9 μm (Smith et al., 2004; Smith et al., 2006) with those derived from Pancam observations at 880 nm. The comparison was made until Mini-TES measurements became useless due to the dust on the sensor. They found that dust aerosol particle size showed seasonal variability, with values typically in the range between 0.7 and 2.1 μm (assuming an effective variance of 0.5), and they also found that larger sizes were associated with periods of high opacity.

In Chapter 7 we present a novel technique to determine dust aerosol particle size at the MSL landing site using measurements of UV radiation acquired by the REMS UVS and Mastcam opacities, and we show and discuss its seasonal and interannual variability.

Chapter 3. Contribution of this Work

The main contribution of this work can be summarized as the achievement of the following objectives:

1. Development of new comprehensive radiative transfer models to calculate the solar radiation that reaches the Martian surface.
2. Development of techniques to retrieve dust aerosol properties from solar radiation data of present and future Mars missions. In particular, these methodologies have been applied to REMS UVS measurements of the MSL mission and have been proposed for MetSIS data of the MetNet Precursor mission.
3. Characterization of the radiative environment at the landing sites of the missions to Mars.
4. Determination of dust aerosol particle size at Gale Crater.

3.1. Development of new comprehensive radiative transfer models for Mars

In the context of the first objective, we have developed two models that use different schemes to solve the radiative transfer equation. The first model uses the delta-Eddington approximation (Joseph et al., 1976) and it is described in Chapter 4, whereas the second model is based on the Monte Carlo method (Iwabuchi, 2006; Melnikova et al., 2012) and it is described in Chapter 6. We have developed these models aiming to answer the following questions:

1. What is the effect of each atmospheric component on the spectral opacity?
2. What are the features of the direct, diffuse and total spectral irradiances under typical and extreme conditions that can be found at the Martian surface?
3. How do the direct, diffuse and total fluxes depend on the amount of dust in the atmosphere (characterized by the opacity)?
4. How does the scattered radiance depend on the dust particle size (characterized by the effective radius of the size distribution)?

3.2. Development of techniques to retrieve dust aerosol properties from solar radiation measurements of Mars missions

We performed a detailed analysis of modeling results, technical specifications of the solar radiation sensors (MetSIS and REMS UVS) and data acquisition strategies in order to address the following question: How can we use the radiative transfer models to optimize the scientific return of the solar radiation measurements?

In particular, we have tried to provide the best answer to the following questions:

1. Which variables are affected by atmospheric opacity?
2. Considering the specifications of the sensors, how can we retrieve the opacity?

3. Which variables are affected by dust aerosol particle size?
4. What are the features of the sensors (angular response, field of view), derived from in situ measurements?
5. From the knowledge of the features of the sensors and measurement strategies, how can we retrieve the effective radius of the dust aerosol size distribution?
6. Is it possible to use different methods that could provide additional information on other quantities (for example, obtain information on article size from combined methods to retrieve opacity)?
7. Which method minimizes the sources of uncertainties?

The proposed methods to retrieve atmospheric opacity and to obtain additional information from MetSIS measurements are described in Chapters 4 and 8. Similarly, the most suitable method that we have developed to determine dust aerosol particle size from REMS measurements is described in Chapter 7. Also, a discussion of a proposed method to retrieve opacity from REMS measurements can be found in Chapter 8.

3.3. Characterization of the radiative environment at the landing sites of the missions

The characterization of the radiative environment at different landing sites of the Mars missions has allowed us to answer the following questions for each site:

1. Which are the typical values of solar radiation at the Martian surface?
2. Which are the features of the seasonal variability? In which locations is it more intense?
3. Which are the features of the interannual variability? When is it larger?
4. How is the contribution to total radiation of the direct and diffuse components? Does it show temporal variability?
5. How is the UV environment at Gale crater?
6. How does solar and UV radiation affect other meteorological and environmental variables?

These questions are addressed in Chapter 5. The UV environment at Gale Crater is shown in Chapter 7, and the effect of solar insolation on other variables is discussed in Chapter 8.

3.4. Determination of dust aerosol particle size at Gale Crater

Focusing on the dust aerosol particle size at Gale Crater, our results are very useful to answer the following questions:

1. What is the typical value of the effective radius?
2. How is its seasonal variability?
3. Does interannual variability exist?
4. Are dust particle size and atmospheric opacity correlated? Is this correlation affected by atmospheric circulations?
5. Which are the implications of dust particle size on the UV environment?

We address these questions in Chapter 7.

Part II

Results

Chapter 4. A model to calculate solar radiation fluxes on the Martian surface

Abstract

We present a new comprehensive radiative transfer model to study the solar irradiance that reaches the surface of Mars in the spectral range covered by MetSIS, a sensor aboard the Mars MetNet mission that will measure solar irradiance in several bands from the ultraviolet (UV) to the near infrared (NIR). The model includes up-to-date wavelength-dependent radiative properties of dust, water ice clouds, and gas molecules. It enables the characterization of the radiative environment in different spectral regions under different scenarios. Comparisons between the model results and MetSIS observations will allow for the characterization of the temporal variability of atmospheric optical depth and dust size distribution, enhancing the scientific return of the mission. The radiative environment at the Martian surface has important implications for the habitability of Mars as well as a strong impact on its atmospheric dynamics and climate.

J. Space Weather Space Clim., **5**, A33 (2015)
DOI: 10.1051/swsc/2015035

RESEARCH ARTICLE

OPEN ACCESS

A model to calculate solar radiation fluxes on the Martian surface

Álvaro Vicente-Retortillo[1,3,*], Francisco Valero[1], Luis Vázquez[2], and Germán M. Martínez[3]

[1] Departamento de Física de la Tierra, Astronomía y Astrofísica II, Facultad de Ciencias Físicas, Universidad Complutense, Madrid, Spain
[*]Corresponding author: `alvarodv@ucm.es`
[2] Departamento de Matemática Aplicada, Facultad de Informática, Instituto de Matemática Interdisciplinar, Universidad Complutense, Madrid, Spain
[3] Department of Atmospheric, Oceanic and Space Sciences, University of Michigan, Ann Arbor, USA

Received 25 March 2015 / Accepted 15 September 2015

ABSTRACT

We present a new comprehensive radiative transfer model to study the solar irradiance that reaches the surface of Mars in the spectral range covered by MetSIS, a sensor aboard the Mars MetNet mission that will measure solar irradiance in several bands from the ultraviolet (UV) to the near infrared (NIR). The model includes up-to-date wavelength-dependent radiative properties of dust, water ice clouds, and gas molecules. It enables the characterization of the radiative environment in different spectral regions under different scenarios. Comparisons between the model results and MetSIS observations will allow for the characterization of the temporal variability of atmospheric optical depth and dust size distribution, enhancing the scientific return of the mission. The radiative environment at the Martian surface has important implications for the habitability of Mars as well as a strong impact on its atmospheric dynamics and climate.

Key words. Spectral irradiance – Modelling – Surface – Planets – Missions

1. Introduction

Advances in space exploration require a deeper knowledge of the environments of the bodies of the solar system. The characterization of the solar radiation reaching planetary environments has become crucial to address aspects related to their habitability and physical processes, resulting in one of the main topics under study in planetary space weather (Lilensten et al. 2014).

Here we focus on the solar radiation reaching the Martian surface. Solar ultraviolet radiation is very important for habitability because it is linked to biological effects and potential survival of organisms at the surface of Mars (Córdoba-Jabonero et al. 2003; Patel et al. 2004). Additionally, surface solar radiation measured at different spectral bands can provide information about the concentration of atmospheric dust and various Martian atmospheric components such as O_3, as well as about their variations from diurnal to annual scales (Perrier et al. 2006; Vázquez et al. 2007; Zorzano et al. 2009; Gómez-Elvira et al. 2012; Lefèvre et al. 2014). Furthermore, the spatial distribution of the absorbed radiation in the atmosphere has an important effect on atmospheric temperatures (Madeleine et al. 2011) and dynamics (Read & Lewis 2004). Also, the solar radiation is the main term of the Martian surface energy budget (Martínez et al. 2014), which in turn controls the diurnal evolution of ground temperature (Savijärvi & Kauhanen 2008; Martínez et al. 2009) and thus the thermodynamic processes in the Martian Planetary Boundary Layer (PBL) (Martínez et al. 2011; Petrosyan et al. 2011).

The Rover Environmental Monitoring Station (REMS) UV sensor on board the Mars Science Laboratory (MSL) mission measures the solar radiation at the surface of Gale crater (4.6° S) in six bands between 200 and 380 nm. In support of the REMS UV sensor, and to extend its measuring range, the Mars MetNet Mission (http://metnet.fmi.fi) includes a Solar Irradiance Sensor (MetSIS) as part of its payload, which has been designed to measure solar radiation at the Martian surface in several bands up to 1100 nm. Most of the MetSIS channels have a hemispherical field of view and are designed to be pointing to the zenith, measuring therefore the solar irradiance at the surface.

Here we present a new comprehensive radiative transfer model that calculates the spectral solar irradiance from wavelength-dependent radiative parameters, enabling calculations of solar radiation fluxes in different spectral regions covered by MetSIS and REMS. The various results of the model provide information about the radiative environment at the Martian surface under typical and extreme scenarios, and allow comparisons between model results and in situ measurements, improving the scientific return of present and future missions to Mars.

In Section 2, we describe the radiative transfer model, hereinafter COMIMART (COmplutense and MIchigan MArs Radiative Transfer model). In Section 3, we validate COMIMART using as a reference solar fluxes calculated by the DISORT radiative transfer algorithm (Stamnes et al. 1988). In Section 4, we show important results derived from the model to characterize the radiative environment at the Martian surface: first, we present an analysis of the contributions of the individual atmospheric components to the total optical depth and perform sensitivity studies for scenarios that cover most of the possible atmospheric compositions at low and mid-latitudes; then, we analyze the diurnal evolution of integrated solar fluxes in the

MetSIS band 200–1100 nm under different scenarios and compare them with fluxes calculated in the full shortwave spectral range; finally, we study spectral irradiances in the range 200–1100 nm also under different scenarios, and describe a method to estimate the optical depth and particle size distribution from the model and in situ measurements in different bands. In Section 5, we summarize our results and discuss their importance.

2. Description of the model

The solar radiation at the top of the atmosphere (TOA) and the radiative properties of the atmosphere govern the solar flux that reaches the surface of Mars. The calculation of the solar radiation at the TOA and the determination of the radiative properties of the Martian atmosphere based on updated wavelength-dependent radiative properties of its components are described below.

2.1. Solar spectrum at the top of the atmosphere

The spectral irradiance that reaches a horizontal surface at the TOA as a function of the latitude and time of the year can be determined using the expression

$$E = E_m \left[\sin\varepsilon \sin L_s \sin\phi + \left(1 - \sin^2\varepsilon \sin^2 L_s\right)^{1/2} \times \cos\phi \cos\frac{2\pi t}{P}\right]\left[\frac{1 + e\cos\left(L_s - L_{s,p}\right)}{1 - e^2}\right]^2, \quad (1)$$

where E_m represents the spectral irradiance at the mean distance between the Sun and Mars (1.52 AU), $e = 0.0934$ is the eccentricity of the orbit of Mars, $L_{s,p} = 251°$ is the solar longitude at the perihelion, $\varepsilon = 25.2°$ is the Martian obliquity, $P = 88{,}775$ s is the length of a sol (a Martian day), ϕ is the latitude, and t is the time measured in seconds from local noon (Haberle et al. 1993; Patel et al. 2002). In COMIMART, E_m is determined from the 2000 American Society for Testing and Materials (ASTM) Standard Extraterrestrial Solar Spectrum Reference E-490-00 (http://rredc.nrel.gov/solar/spectra/am0).

The first bracket on the right-hand side of Eq. (1) represents the cosine of the solar zenith angle, while the second one shows the ratio of the mean distance between the Sun and Mars to the distance at a given orbital position. By using Eq. (1) we are assuming that the Sun is a point source, a standard approximation for radiative transfer studies on the Earth due to the small errors involved except during sunrise or sunset (Stamnes et al. 2000), which become even smaller for Mars due to the larger distance to the Sun.

2.2. Radiative properties of the Martian atmosphere

The different components of the Martian atmosphere interact with the solar radiation by means of absorption and scattering processes. The components considered in this model are dust, water ice clouds, and gas molecules (CO_2, N_2, Ar, O_2, O_3, and H_2O). These components are denoted with the subscripts d, c, and g.

In order to obtain the amount of radiation that reaches the surface, the total atmospheric optical depth τ is calculated from the individual contributions of each atmospheric component as

$$\tau(\lambda) = \tau_g(\lambda) + \tau_d(\lambda) + \tau_c(\lambda). \quad (2)$$

The optical depth of each component can be separated into two terms: one accounting for scattering (indicated with the subscript s) and the other for absorption (denoted with the subscript a). Following this notation, Eq. (2) can be rewritten as

$$\tau(\lambda) = \tau_{gs}(\lambda) + \tau_{ds}(\lambda) + \tau_{cs}(\lambda) + \tau_{ga}(\lambda) + \tau_{da}(\lambda) + \tau_{ca}(\lambda). \quad (3)$$

A description of the calculation of the terms of Eq. (3) is provided below, beginning with dust, continuing with clouds, and ending with the terms related to the gas molecules.

Among the various Martian atmospheric constituents, dust has the greatest impact on the absorption and scattering of solar radiation. In order to quantify the result of its interaction with solar radiation, three radiative parameters are needed: the extinction efficiency, $Q_{\mathrm{ext},d}(\lambda)$, defined as the extinction cross-section (the sum of the scattering and absorption cross-sections) divided by the projected surface area of the spherical particle; the single scattering albedo, $\omega_{0,d}(\lambda)$, defined as the ratio between scattering and extinction coefficients; and the asymmetry factor, $g_d(\lambda)$, defined as the first moment of the phase function, which represents the probability of scattering in any given direction.

In COMIMART, we calculate updated wavelength-dependent values of these three parameters by using the Mie theory and the refractive indices presented by Wolff et al. (2009) and Wolff et al. (2010). These three parameters also depend on the size distribution of the particles. Here we assume a log-normal size distribution, characterized by the effective radius, r_{eff}, and the effective variance, v_{eff} (Hansen & Travis 1974), and select standard values of $r_{\mathrm{eff}} = 1.5$ μm (Clancy et al. 2003; Wolff & Clancy, 2003; Kahre et al. 2006; Madeleine et al. 2011) and $v_{\mathrm{eff}} = 0.3$ (Rannou et al. 2006; Madeleine et al. 2011). The reader is referred to Section 4.3 for a discussion of the impact of choosing different size distributions on the calculation of the spectral irradiance.

Madeleine et al. (2011) show that the opacity of the atmosphere is directly proportional to the extinction efficiency. Thus, by using the value of the optical depth at any particular wavelength as a reference, we calculate the dust opacity $\tau_d(\lambda)$ at any other wavelength from the corresponding value of $Q_{\mathrm{ext},d}(\lambda)$. We have chosen 880 nm as a reference in COMIMART to enable a direct comparison to the measurements taken by the Pancam cameras at the locations of the Mars Exploration Rovers (Lemmon et al. 2015) and by the Mastcam cameras at the MSL site; we denote the dust optical depth at this wavelength by $\tau_{d,880}$. The model enables the calculation of the two contributions (scattering and absorption) to τ_d. The scattering optical depth due to dust particles in Eq. (3) is obtained by multiplying $\tau_d(\lambda)$ by $\omega_{0,d}(\lambda)$.

Solar radiation also interacts with water ice clouds. In order to quantify their effect, we calculate the water ice radiative properties ($Q_{\mathrm{ext},c}(\lambda)$, $\omega_{0,c}(\lambda)$, and $g_c(\lambda)$) from the refractive indices given by Warren (1984). In this case, we select a log-normal size distribution with $r_{\mathrm{eff}} = 3$ μm (Wolff & Clancy 2003) and $v_{\mathrm{eff}} = 0.1$ (Wolff & Clancy 2003; Madeleine et al. 2012). In order to obtain $\tau_c(\lambda)$, we follow the same procedure as for the dust, but selecting 825 cm^{-1} (roughly 12.1 μm) as the reference wavelength to simplify the comparison to Thermal Emission Spectrometer (TES) results (Smith 2004). Thus, we obtain $\tau_c(\lambda)$ as

$$\tau_c(\lambda) = \frac{Q_{\mathrm{ext},c}(\lambda)}{Q_{\mathrm{ext},c,12.1}(1 - \omega_{0,c12.1})}\tau_{ca,12.1}, \tag{4}$$

where $\tau_{ca,12.1}$ stands for the TES absorption optical depth. We have followed the same scheme as in the dust case to calculate the absorption and scattering cloud optical depths at each wavelength.

The interaction of gas molecules with solar radiation is quantified by means of their scattering and absorption cross-sections. The total optical depth due to scattering by gas molecules is given by the sum of the scattering optical depths of CO_2, N_2, Ar, and O_2, which are calculated multiplying their column abundance N by their Rayleigh scattering cross-section σ_s as follows

$$\tau_{gs} = \sigma_{s,\mathrm{CO_2}}N_{\mathrm{CO_2}} + \sigma_{s,\mathrm{N_2}}N_{\mathrm{N_2}} + \sigma_{s,\mathrm{Ar}}N_{\mathrm{Ar}} + \sigma_{s,\mathrm{O_2}}N_{\mathrm{O_2}}. \tag{5}$$

Note that scattering by O_3 and H_2O is not considered because these molecules are variable trace species in the Martian atmosphere, and thus we can consider their effect on Rayleigh scattering negligible. The column abundance is obtained using the expression

$$N = \frac{p \times \mathrm{Av}}{M \times g^*}n_{\mathrm{rel}}, \tag{6}$$

where p represents the pressure at the surface, Av is the Avogadro's number, M is the molecular mass of the gas, g^* is the gravity, and n_{rel} is the relative abundance of the gas in the atmosphere. The scattering cross-section is obtained as

$$\sigma_s(\lambda) = \frac{24\pi^3}{\lambda^2 N_s^2}\left(\frac{n^2(\lambda) - 1}{n^2(\lambda) + 2}\right)^2 F_k(\lambda), \tag{7}$$

where N_s represents the number of molecules per unit of volume, n is the refractive index, and F_k is the King correction factor (Sneep & Ubachs 2005). Refractive indices for CO_2 and O_2 are taken from Sneep & Ubachs (2005), while for N_2 and Ar they are taken from Weber (2003) and references herein. King correction factors for CO_2, O_2, N_2, and Ar are taken from Sneep & Ubachs (2005).

Absorption by gas molecules is calculated from their absorption cross-sections when an absorption continuum is observed for a particular component. In addition to the absorption continua, some gas molecules of the Martian atmosphere, especially CO_2 and H_2O, show absorption lines that can be characterized individually in the shortwave range (Rothman et al. 2013). We have not included these lines in the model because they have a negligible effect in the 200–1100 nm range, and still a very small effect in the remaining range of the shortwave range (the reader is referred to Sect. 3.1.1 for further details on this assumption). Taking this into account, the total optical depth due to absorption by gas molecules is calculated from

$$\tau_{ga} = \sigma_{a,\mathrm{CO_2}}N_{\mathrm{CO_2}} + \sigma_{a,\mathrm{O_2}}N_{\mathrm{O_2}} + \sigma_{a,\mathrm{O_3}}N_{\mathrm{O_3}} + \sigma_{a,\mathrm{H_2O}}N_{\mathrm{H_2O}}, \tag{8}$$

where σ_a represents the absorption cross-section of each gas. Since the mixing ratios of O_3 and H_2O are not vertically uniform, their column abundances are not obtained from Eq. (6), but introduced as model inputs.

In the present Martian atmosphere, CO_2 is the gas with the greatest impact on solar radiation. CO_2 absorption cross-sections have been included for the spectral range between 122 and 202 nm (Lewis & Carver 1983; Ityaksov et al. 2008), this last value representing the wavelength at which CO_2 absorption approximately begins to be negligible (Ityaksov et al. 2008). The high values of the absorption cross-section, together with the CO_2 abundance in the Martian atmosphere, produce a cut at roughly 200 nm in the solar spectrum that reaches the Martian surface. The temperature dependence of the cross-sections measured in the range from 200 K to 370 K by Lewis & Carver (1983) has been included in COMIMART, but due to the low spectral irradiance at these wavelengths and the aforementioned cut in the spectrum, its impact on the solar flux at the surface is small.

Besides CO_2, there are other radiatively active gas molecules, although they are present in small amounts in the Martian atmosphere. We have included O_3 cross-sections in the ranges 214–1100 nm and 203–293 K (Serdyuchenko et al. 2014) and O_2 cross-sections in the ranges 176–242.5 nm and 200–300 K (Frederick & Mentall 1982). Despite the cut in the spectrum produced by CO_2, we have included H_2O cross-sections in the range 182–197 nm (Parkinson & Yoshino 2003) to allow studies in scenarios with very different relative molecular abundances. H_2O_2 molecule presents absorption in the UV region with relatively high absorption cross-sections (Lin et al. 1978), but its effect has not been considered here because its mixing ratio shows typical values as low as 10^{-8} (Encrenaz et al. 2012).

Once the total optical depth attributable to all the atmospheric components is obtained, effective values for the single scattering albedo and for the asymmetry factor are determined. The former is given by the ratio between the total scattering optical depth (the sum of the first three terms of the right-hand side of Eq. (3)) and the total optical depth (Eq. (2)); the latter is obtained from the equation

$$g = \frac{\tau_{ds}g_d + \tau_{cs}g_c}{\tau_{gs} + \tau_{ds} + \tau_{cs}}, \tag{9}$$

where the assumption of isotropic molecular scattering has been taken.

2.3. Calculating solar fluxes

We calculate solar fluxes in any given band by using the delta-Eddington approximation, which is based on the two-stream Eddington approximation for multiple scattering plane-parallel atmospheres, except that it includes a delta adjustment in the phase function to improve the accuracy when the asymmetry factor is high (Joseph et al. 1976). This is the case of the Martian aerosols, particularly in the UV spectral region. In the delta-Eddington approximation, the asymmetry factor, the single scattering albedo and the optical depth are transformed according to Joseph et al. (1976) as

$$g' = \frac{g}{1+g}, \tag{10}$$

$$\omega' = \omega_0\frac{1 - g^2}{1 - \omega_0 g^2}, \tag{11}$$

$$\tau' = \tau\left(1 - \omega_0 g^2\right). \tag{12}$$

After the calculation of the aforementioned radiative parameters, and assuming a single layer atmosphere (see Sect. 3.1.2

for further details on this assumption), solar fluxes at the surface are estimated using the following set of equations (Haberle et al. 1993; Patel et al. 2002)

$$T = E[C_1 \exp(-k\tau)(1+P') + C_2 \exp(k\tau)(1-P') - (\alpha+\beta-1)\exp(-\tau/\mu_0)], \tag{13}$$

$$k = [3(1-\omega_0)(1-g\omega_0)]^{1/2}, \tag{14}$$

$$P' = \frac{2}{3}\left[\frac{3(1-\omega_0)}{1-g\omega_0}\right]^{1/2}, \tag{15}$$

$$\alpha = \frac{3}{4}\mu_0\omega_0\frac{1+g(1-\omega_0)}{1-\mu_0^2k^2}, \tag{16}$$

$$\beta = \frac{1}{2}\mu_0\omega_0\frac{1/\mu_0+3\mu_0 g(1-\omega_0)}{1-\mu_0^2k^2}, \tag{17}$$

$$C_1 = -\frac{(1-P')C_3\exp(-\tau/\mu_0)-(\alpha+\beta)C_4\exp(k\tau)}{(1+P')C_4\exp(k\tau)-(1-P')C_5\exp(-k\tau)}, \tag{18}$$

$$C_2 = \frac{(1+P')C_3\exp(-\tau/\mu_0)-(\alpha+\beta)C_5\exp(-k\tau)}{(1+P')C_4\exp(k\tau)-(1-P')C_5\exp(-k\tau)}, \tag{19}$$

$$C_3 = A + (1-A)\alpha - (1+A)\beta, \tag{20}$$

$$C_4 = 1 - A + P'(1+A), \tag{21}$$

$$C_5 = 1 - A - P'(1+A). \tag{22}$$

In these expressions, T is the total (direct + diffuse) flux at the surface in the selected spectral region, μ_0 is the cosine of the solar zenith angle at the TOA, and A is the surface albedo. Note that the dependence of τ, ω_0, g, and A on wavelength is not explicitly shown.

The direct (beam) flux, B, is calculated using the Beer-Lambert law:

$$B = E \times \exp(-\tau/\mu_0), \tag{23}$$

where τ is the value of the atmospheric optical depth before using Eq. (12). Finally, the diffuse flux, D, is obtained by subtracting the direct component from the total flux at the surface.

3. Model testing and validation

In this section we discuss various assumptions considered in the model and then validate their results by comparing the calculated surface fluxes to those obtained using the DISORT algorithm (Stamnes et al. 1988).

3.1. Discussion on model assumptions

3.1.1. Effect of individual absorption lines

We discuss the impact of the individual CO_2 and H_2O lines on surface fluxes and show that it can be neglected in the spectral region between 200 and 1100 nm, and that it is still very small in the remaining range of the shortwave range.

We quantify the impact of these individual lines by using the atmospheric radiative transfer model MODTRAN (MODerate resolution atmospheric TRANsmission; Berk et al. 1998) as follows. We introduce an aerosol-free atmospheric vertical profile based on the reference profile shown by Savijärvi et al. (2005). We obtain that when $\mu_0 = 1$, CO_2 and H_2O absorb together only about 1% of the incoming solar radiation at the top of the atmosphere. Moreover, the absorption due to these individual lines is much smaller between 200 and 1100 nm, representing only a 0.0091% of E when the Sun is at the zenith. When $\mu_0 = 0.5$, the fraction of E absorbed by these lines increases because of the longer optical path, but its value remains very small (0.016%). These results confirm that the effect of these lines on the solar flux measured at wide spectral bands in the MetSIS range is negligible. In addition, considering the effect of each individual line at the corresponding wavelength would require a very high spectral resolution, significantly slowing down the computing process.

3.1.2. Single layer approximation

We test the validity of the single layer approximation by using DISORT to calculate and compare fluxes at the surface under five different scenarios and for two different scattering regimes. For each scenario and regime, we first consider two layers (with dust at the bottom and ice clouds on top), and then only a single layer. As shown below, the differences are negligible from 200 to 1100 nm (MetSIS range).

The five scenarios are defined as follows. The first represents typical clear conditions, with $\tau_d = 0.3$ and $\tau_c = 0.02$, and with the Sun at the zenith ($\mu_0 = 1$). The second scenario considers the same τ_d and μ_0, but a higher cloud optical depth ($\tau_c = 0.15$). Scenarios 3 and 4 are like 1 and 2, respectively, but with $\mu_0 = 0.5$. Finally, scenario 5 considers the same τ_c and μ_0 as 2, but under typical dusty conditions ($\tau_d = 1$).

For each scenario, we select two different scattering regimes. This is because the dust single scattering albedo, the dust and water ice clouds asymmetry factor, and the surface albedo show significantly different properties in the UV (200–400 nm) and NIR (700–1100 nm) regions. In particular, the dust single scattering albedo and asymmetry factor show small spectral variability between 700 and 1100 nm, with calculated values around 0.97 and 0.70, respectively. Toward the UV region, the dust single scattering albedo decreases and the asymmetry factor increases. Moreover, the surface albedo also depends on the wavelength, with lower values in the UV region (Perrier et al. 2006) than in the NIR (Mustard & Bell 1994).

In the two-layer case and for the bottom dust layer, we set representative values of $\omega_{0,d} = 0.67$ and $g_d = 0.87$ in the UV, and $\omega_{0,d} = 0.97$ and $g_d = 0.70$ in the NIR. For the top cloud layer, we set representative values of $\omega_{0,c} = 1$ and $g_c = 0.85$ in the UV, and $\omega_{0,c} = 1$ and $g_c = 0.81$ in the NIR. In the one

Table 1. Comparison between *T/E* for a single effective atmospheric layer (denoted by the subscript 1) and *T/E* for a vertically inhomogeneous atmosphere, for the conditions described in the text.

	UV conditions			NIR conditions		
Scenario	$(T/E)_1$	$(T/E)_2$	Rel. error (%)	$(T/E)_1$	$(T/E)_2$	Rel. error (%)
1	0.89787	0.89757	0.033	0.98431	0.98420	0.011
2	0.89211	0.89084	0.143	0.98153	0.98114	0.040
3	0.78715	0.78660	0.070	0.90046	0.90046	$<10^{-4}$
4	0.76555	0.76388	0.219	0.87848	0.87864	−0.018
5	0.68327	0.68106	0.324	0.91125	0.91059	0.072

Table 2. *T/E* calculated using DISORT (top) and COMIMART (middle), and relative departures (bottom), for $\omega_0 = 0.67$, $g = 0.87$, and $A = 0.03$.

		$\omega_0 = 0.67$, $g = 0.87$, $A = 0.03$				
				μ_0		
		0.3	**0.5**	**0.7**	**0.85**	**1**
			T/E (DISORT)			
	0.3	0.6540	0.7904	0.8525	0.8798	0.8986
	0.6	0.4366	0.6201	0.7221	0.7701	0.8044
τ	**1**	0.2711	0.4491	0.5755	0.6415	0.6909
	1.5	0.1644	0.3035	0.4314	0.5074	0.5680
	2.5	0.0744	0.1465	0.2419	0.3132	0.3781
	5	0.0162	0.0311	0.0595	0.0908	0.1284
			T/E (COMIMART)			
	0.3	0.6808	0.7955	0.8519	0.8783	0.8974
	0.6	0.4735	0.6343	0.7245	0.7694	0.8028
τ	**1**	0.3021	0.4706	0.5825	0.6425	0.6890
	1.5	0.1819	0.3258	0.4420	0.5103	0.5658
	2.5	0.0766	0.1587	0.2521	0.3172	0.3755
	5	0.0133	0.0283	0.0594	0.0910	0.1263
			Relative departure (%)			
	0.3	4.10	0.65	−0.07	−0.17	−0.14
	0.6	8.46	2.29	0.34	−0.09	−0.20
τ	**1**	11.43	4.79	1.22	0.16	−0.28
	1.5	10.63	7.35	2.46	0.58	−0.38
	2.5	2.96	8.35	4.23	1.27	−0.67
	5	−17.71	−9.03	−0.20	0.27	−1.62

layer case, we calculate the effective radiative parameters as described in Section 2 by considering the optical depths of each scenario and the single scattering albedo and asymmetry factor values defined above. Finally, we set values of $A = 0.03$ in the UV and $A = 0.25$ in the NIR.

Table 1 shows the values of *T/E* for the single layer and two-layer cases under the five scenarios described above and for the two scattering regimes. It also shows the relative error in considering a single layer. For any possible combination of the selected scenarios and scattering regimes, the relative error is below 0.4%. In particular, due to the different values of the radiative parameters of the dust and water ice clouds layers in the two scattering regimes, the departure between the single and two-layer approximation in the UV is higher than in the NIR (where it is about 10^{-2}%), but it is still very small (approximately 10^{-1}%). Therefore, the single layer approximation is valid to calculate the solar fluxes that reach the Martian surface in the MetSIS range.

3.2. Validation of the model

We validate COMIMART by comparing the calculated surface fluxes to those obtained using the DISORT algorithm. Values of solar fluxes at the surface depend on the optical depth, single scattering albedo, asymmetry factor, surface albedo, and zenith angle. As in Section 3.1.2, we analyze both fluxes in the UV and NIR scattering regimes for several optical depths and zenith angles, and select two sets of radiative parameters for each region, with $\omega = 0.67$, $g = 0.87$, and $A = 0.03$ in the UV regime, and $\omega = 0.97$, $g = 0.70$, and $A = 0.25$ in the NIR regime. The selected combination of scenarios and scattering regimes encompasses a comprehensive representation of the Mars' atmospheric radiative properties and solar geometries, ensuring a thorough validation of COMIMART.

In the DISORT model, we select a Henyey-Greenstein phase function (Henyey & Greenstein 1941) to be consistent with the transformation of the radiative parameters in the delta-Eddington approximation shown by Eqs. (10)–(12). Also, we set the number of streams to 32 to obtain highly accurate flux values.

We show in Table 2 (UV) and Table 3 (NIR) the ratio of the flux at the surface to the flux at the top of the atmosphere (*T/E*) calculated with DISORT (top) and with COMIMART (middle) for representative values of μ_0 and τ. We also show the relative departure, in percentage, between COMIMART and DISORT (bottom). For high values of μ_0 and for typical optical depths

Table 3. As in Table 2, but for $\omega_0 = 0.97$, $g = 0.70$, and $A = 0.25$.

$\omega_0 = 0.97$, $g = 0.70$, $A = 0.25$						
				μ_0		
		0.3	**0.5**	**0.7**	**0.85**	**1**
			T/E (DISORT)			
τ	**0.3**	0.7948	0.9038	0.9524	0.9721	0.9846
	0.6	0.6701	0.8168	0.8979	0.9345	0.9590
	1	0.5693	0.7221	0.8265	0.8796	0.9178
	1.5	0.4907	0.6308	0.7447	0.8101	0.8608
	2.5	0.3910	0.5027	0.6092	0.6810	0.7436
	5	0.2457	0.3146	0.3851	0.4397	0.4950
			T/E (COMIMART)			
τ	**0.3**	0.8266	0.9055	0.9445	0.9628	0.9761
	0.6	0.7129	0.8278	0.8923	0.9244	0.9483
	1	0.6129	0.7429	0.8276	0.8727	0.9076
	1.5	0.5308	0.6578	0.7538	0.8089	0.8533
	2.5	0.4253	0.5305	0.6270	0.6893	0.7432
	5	0.2675	0.3317	0.4006	0.4529	0.5039
			Relative departure (%)			
τ	**0.3**	4.00	0.18	−0.83	−0.96	−0.86
	0.6	6.39	1.34	−0.63	−1.08	−1.12
	1	7.65	2.88	0.14	−0.79	−1.11
	1.5	8.18	4.27	1.23	−0.15	−0.87
	2.5	8.77	5.52	2.92	1.22	−0.06
	5	8.89	5.43	4.02	3.00	1.80

between 0.3 and 1.5 (Lemmon et al. 2015), the results obtained with both models are in excellent agreement, with absolute values of the relative departure ~1% in the NIR region and even lower in the UV. For low values of μ_0, relative departures between both models are slightly higher, with values typically between 4% and 10% regardless of the value of τ. Still, the absolute departure stays comparable to that at higher solar elevations because for lower μ_0 values, the calculated fluxes are smaller. Therefore, except at high solar zenith angles, corresponding to the times of the day close to sunrise and sunset (when the plane-parallel atmosphere assumption loses validity), the results obtained with COMIMART are accurate in the two scattering regimes.

4. Results

4.1. Effect of individual atmospheric components and sensitivity studies

Here we study the relative contribution of each atmospheric component to the total atmospheric optical depth under a typical scenario, and then we perform sensitivity studies to check the robustness of the results to changes in atmospheric conditions. These sensitivity studies show a method to estimate the optical depth from MetSIS measurements and model results.

The total optical depth is given by the sum of the individual terms in Eq. (3). We analyze the relative contribution of each of these terms under typical clear Martian atmospheric conditions at low and mid-latitudes, corresponding to the initially selected landing sites for the MetNet mission. We characterize these conditions by choosing values of dust optical depth $\tau_{d,880} = 0.3$ (Lemmon et al. 2015), water ice clouds absorption optical depth $\tau_{ca,12.1} = 0.02$ (typical value outside the aphelion cloud belt; Smith 2004; Madeleine et al. 2012), and ozone column abundance of $N_{O_3} = 1$ µm-atm (Perrier et al. 2006).

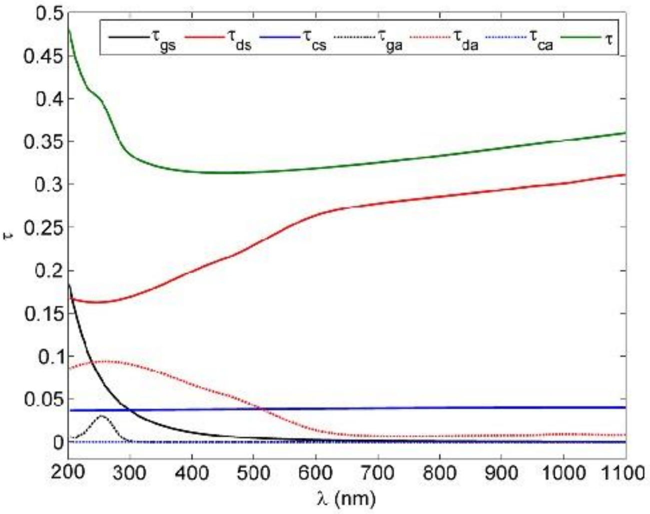

Fig. 1. Spectral behavior of the scattering and absorption optical depths (denoted by subscripts *s* and *a*) of dust, water ice clouds, and gas molecules (denoted by subscripts *d*, *c*, and *g*) for $\tau_{d,880} = 0.3$, $\tau_{ca,12.1} = 0.02$, and $N_{O_3} = 1$ µm-atm.

Figure 1 shows the spectral behavior of the six terms involved in Eq. (3). Even for a clear ($\tau_{d,880} = 0.3$) atmosphere, dust has the greatest impact among the atmospheric constituents on the absorption and scattering of solar radiation. The values of τ_{ds} are larger than those of τ_{da}, particularly in the NIR, where values of τ_{da} represent only about 3% of the total dust optical depth.

The effect of gas molecules on the total optical depth is significant at short wavelengths in the UV region. There, the scattering is mostly caused by CO_2 (97.62%), followed by contributions from N_2 (1.72%), Ar (0.62%), and O_2 (0.04%). The absorption optical depth of the gas molecules is noticeable in the range 200–300 nm and it shows a maximum at 255 nm, caused by the O_3 Hartley band. At wavelengths shorter than 202 nm, τ_{ga} markedly increases (not shown in Fig. 1 for clarity purposes), causing the cut in the spectrum due to CO_2 absorption (the absorption optical depth of CO_2 is around 10 at 186 nm and four orders of magnitude higher at 150 nm).

There is virtually no radiation absorbed by the water ice clouds in the 200–1100 nm region, with a maximum ratio τ_{ca}/τ_{cs} lower than 10^{-4} ($\omega_{0,c} \sim 1$ in this spectral range). In general, the effect of water ice clouds on the total optical depth is stronger than that of gas molecules, except in the UV region, where the scattering by gas molecules exceeds that by ice clouds.

We note that the effect of variations in the ozone column abundance and of the temperature dependence of the cross-sections on the calculated solar fluxes is insignificant. For instance, the surface solar flux between 200 and 310 nm at the equator, at noon, and at $L_s = 270°$ is approximately 8.18 W/m^2 when $N_{O_3} = 1$ μm-atm. If we triple this value, the flux at the surface would be 8.04 W/m^2, and thus the decrease is lower than 1.8%. The effect of temperature is even weaker: the difference between 203 K and 218 K (which is the temperature considered by Patel et al. 2002) is only of 0.0014%, even for a high value of $N_{O_3} = 3$ μm-atm. These effects are even weaker if we consider the band between 200 and 1100 nm, where the described changes in concentration and temperature represent, respectively, 0.033% and less than a 10^{-4}% of the total flux.

After having weighted the contribution of the individual atmospheric components to the total spectral optical depth for a particular scenario, we perform sensitivity studies to analyze the solar flux at the surface in the range 200–1100 nm (which is covered by one of the MetSIS channels) for a wider variety of scenarios. In particular, we define 1000 atmospheric scenarios covering typical and extreme scenarios found at low and mid-latitudes, in which $\tau_{d,880}$ ranges between 0 and 1.5, $\tau_{ca,12.1}$ between 0 and 0.15, and N_{O_3} between 1 and 3 μm-atm.

Figure 2 shows the ratio *T/E* for each scenario when $\mu_0 = 0.85$. A similar behavior has been found for different values of μ_0. This ratio is mainly affected by dust optical depth, showing a decrease of about a 20% between low (~0.3) and high (~1.5) values of τ_d. The effect of water ice clouds is very small because both the values and variability of τ_c are much lower than those for τ_d, with changes in *T/E* below 2% between the extreme scenarios ($\tau_c = 0$ and $\tau_c = 0.15$). Finally, variations of O_3 abundance in the range 1–3 μm-atm (represented in Fig. 2 by different marker sizes) have a negligible effect on *T/E*, with changes lower than 0.04%.

The described behavior of *T/E* suggests a method to estimate dust optical depth from MetSIS measurements in a specific band. From a given measurement of *T*, we first calculate the ratio *T/E*, with *E* given by Eq. (1), and then we use a look-up table generated from model results for different optical depths to find the one that best matches the observations. We complement this method to retrieve dust optical depths with an alternative approach described in Section 4.3.

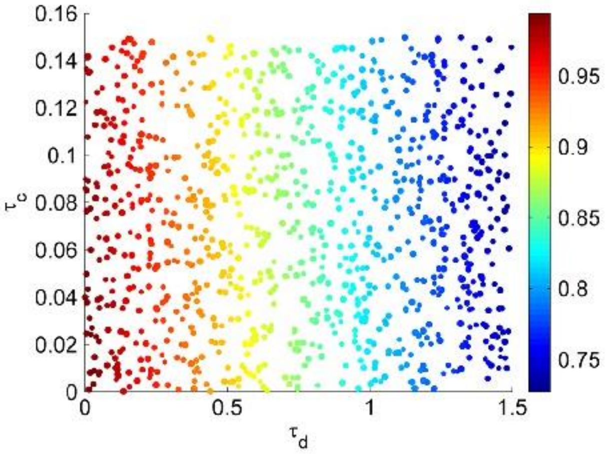

Fig. 2. *T/E* for 1000 atmospheric scenarios characterized by dust optical depth (horizontal axis), water ice clouds optical depth (vertical axis), and ozone abundance (marker size, which increases with ozone abundance, with values between 1 μm-atm and 3 μm-atm).

4.2. Diurnal evolution of solar fluxes under different scenarios

Here we characterize the radiative environment at the latitude range of the initially selected MetNet landing sites (30° N–30° S) in the MetSIS spectral range 200–1100 nm. We first analyze the diurnal evolution of the solar flux and the total amount of energy received during one sol (the daily irradiation) as a function of latitude and τ. Then, we compare solar fluxes in the range 200–1100 nm with the total shortwave radiation. This comparison is important because it allows to estimate the total shortwave flux, which is a key term to calculate the surface energy budget and thus the thermal inertia (Martínez et al. 2014), from in situ measured fluxes between 200 and 1100 nm.

Figure 3 shows the diurnal evolution of the surface solar flux in the 200–1100 nm band at four different latitudes of 30° N, 10° N, 10° S, and 30° S at the Northern Hemisphere winter solstice ($L_s = 270°$). Around this time of the year and at these latitudes, dust optical depths are expected to be high (Lemmon et al. 2015), significantly exceeding the optical depth of water ice clouds (Smith 2004). Thus, we set typical values for these dusty conditions of $\tau_{d,880} = 1$, $\tau_{ca,12.1} = 0.02$ and surface albedo at 750 nm $A_{750} = 0.25$ (mean value between bright and dark regions of Mars; Mustard & Bell 1994).

The diffuse radiation (*D*) is higher than the direct component (*B*) at the four considered locations, with the ratio direct to diffuse irradiation (*B/D*) increasing toward the South from 0.23 at 30° N to 0.55 at 30° S. This is expected because the mean photon path between the TOA and the surface increases northward. Further valuable information can be obtained when analyzing the ratio between the diffuse irradiation at the surface and the irradiation at the TOA (*D/E*). This ratio shows small latitudinal variability, taking values between 0.504 and 0.525, and thus allowing for a very simple estimation of the diffuse daily irradiation just from the model results at the TOA. We note that for clearer atmospheres, the ratio *D/E* presents a larger latitudinal variability (between 0.288 and 0.379 for $\tau_{d,880} = 0.3$), and thus the diurnal evolution of the diffuse flux at the surface provided by the model is necessary to compute the diffuse daily irradiation at each latitude.

We complement the previous analysis with the study of variations of the surface solar flux between 200 and 1100 nm at a given latitude due to changes in τ. Figure 4 shows the diurnal evolution of the surface solar flux at an equatorial location ($\phi = 0°$) at $L_s = 270°$ for a range of dust optical depths at 880 nm between 0 and 4.6, which is the maximum

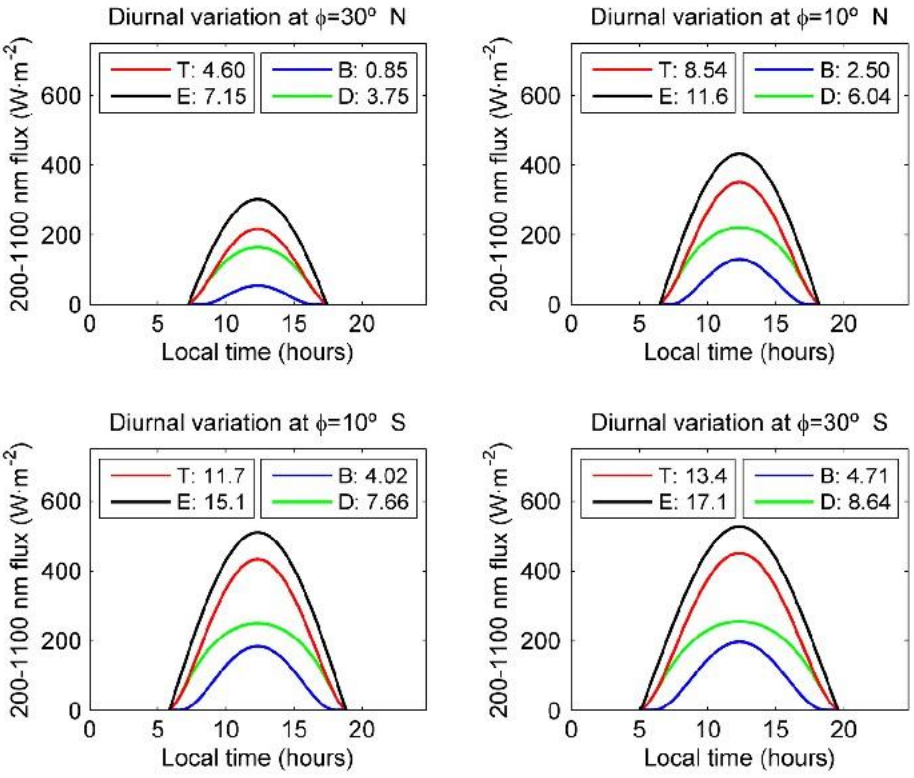

Fig. 3. Diurnal evolution of the direct (*B*, blue line), diffuse (*D*, green line), and total (*T*, red line) surface solar flux between 200 and 1100 nm at four different latitudes during the Northern Hemisphere winter solstice, for $\tau_{d,880} = 1$ and $\tau_{ca,12.1} = 0.02$. The flux at the TOA (*E*) is represented by the black line. The values of the legend represent daily irradiation between 200 and 1100 nm in MJ m^{-2}.

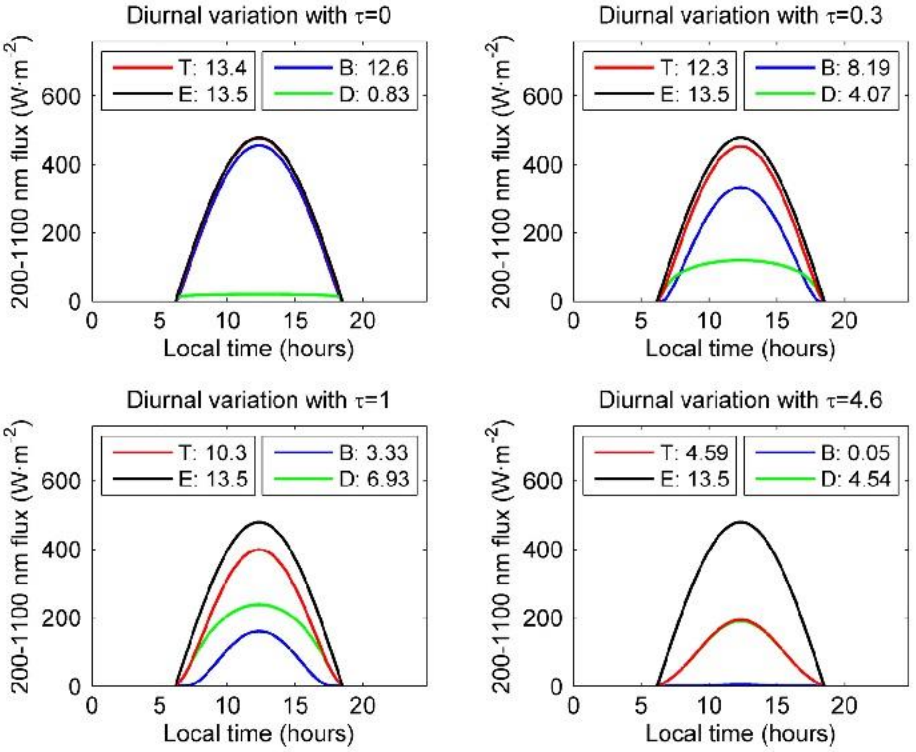

Fig. 4. As in Figure 3, but for different values of $\tau_{d,880}$ in the range 0–4.6 at a fixed latitude $\phi = 0°$.

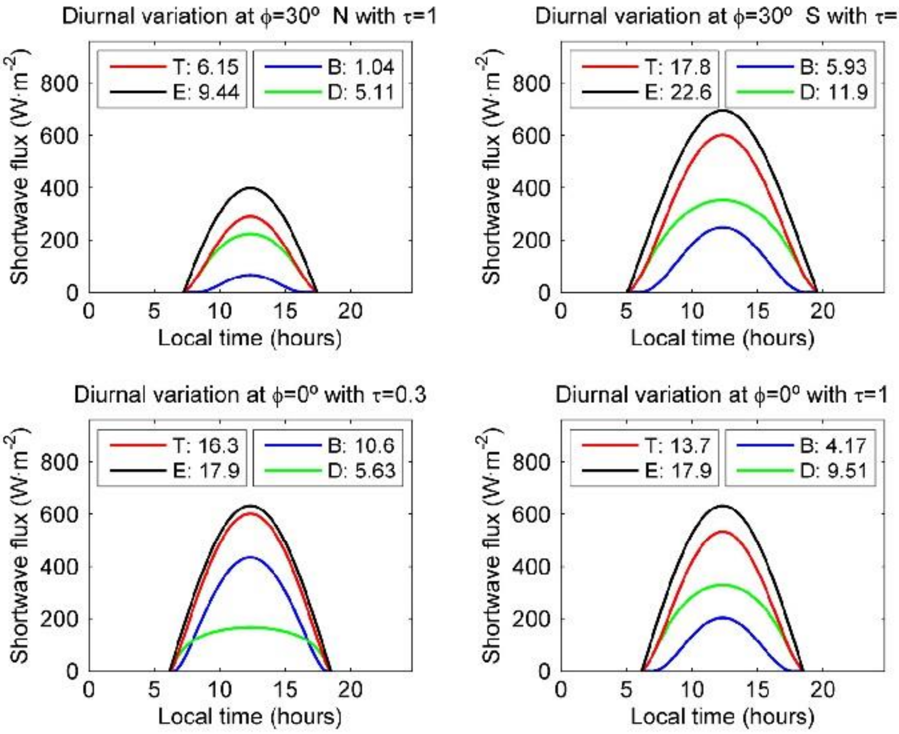

Fig. 5. As in Figure 3, but for the total shortwave flux, and for the combinations of ϕ and $\tau_{d,880}$ specified in the titles.

optical depth observed at the opportunity landing site during the first five Mars years of measurements (Lemmon et al. 2015).

The diurnal evolution of solar radiation at the surface is mainly affected by the amount of dust in the atmosphere, as expected from the sensitivity studies shown in the previous section. In the dust-free scenario, the total irradiation at the surface accounts for about 99% of its value at the TOA (T/E = 0.99), the remaining 1% being backscattered to space by water ice clouds and molecular gases or being absorbed by gas molecules (the absorption by water ice clouds is negligible in the MetSIS range, as discussed in the previous section). Most of the surface flux is composed by direct radiation (B/T = 0.94) due to the small optical depths of water ice clouds and gas molecules, which have a small and a virtually negligible impact between 200 and 1100 nm, respectively, with more than 90% of the diffuse irradiation caused by the water ice clouds.

When the dust optical depth is 0.3, which is a typical value under clear conditions at the Spirit landing site (Lemmon et al. 2015), the total irradiation at the surface accounts for about 91% of its value at the TOA (T/E = 0.91). In this case, the ratio between direct and total irradiation (B/T) becomes 0.68, and the amount of direct radiation is larger than the diffuse one except at and near sunrise and sunset Sun's positions, which is consistent with a longer solar ray path at those times.

Under dusty conditions (τ = 1), the ratio between the irradiation at the surface and that at the TOA is T/E = 0.76. In this case, the diffuse flux is always larger than the direct one, with the B/T ratio showing values of 0.32, which highlights the important role played by the diffuse radiation in the daily irradiation.

Under very dusty conditions (τ = 4.6), there is virtually no direct radiation at the surface and $B/T \sim 0.01$. However, since the dust single scattering albedo and the asymmetry factor are relatively high, even under these conditions a significant amount of radiation reaches the surface (T/E = 0.34).

We compare now solar fluxes in the range 200–1100 nm with fluxes in the entire shortwave range. Figure 5 shows the diurnal evolutions of the total shortwave flux and the daily irradiations at L_s = 270° for four of the scenarios shown in Figures 3 and 4: ϕ = 30° N and $\tau_{d,880}$ = 1; ϕ = 30° S and $\tau_{d,880}$ = 1; ϕ = 0° and $\tau_{d,880}$ = 0.3; and ϕ = 0° and $\tau_{d,880}$ = 1. In each scenario, the ratio of the direct irradiation in the MetSIS range to the total shortwave direct irradiation (B/B_{SW}) is higher than E/E_{SW}. This is because the weighted mean extinction efficiency is lower between 200 and 1100 nm than in the total shortwave range. Therefore, for a given location, B/B_{SW} increases with optical depth. In particular, B/B_{SW} increases at the equator from 0.77 when τ = 0.3 to 0.89 when τ = 4.6. For the same reason, the ratio B/B_{SW} increases for a given optical depth when the mean solar elevation decreases: For τ = 1, its value is 0.818 for ϕ = 30° N and 0.795 for ϕ = 30° S.

In contrast, D/D_{SW} shows a weak dependence on the scenario, taking values between 0.724 and 0.734. The values of T/T_{SW} at $\phi = 0°$ decrease as the optical depth increases (T/T_{SW} = 0.755 when τ = 0.3 and T/T_{SW} = 0.732 when τ = 4.6) because the relative contribution of the diffuse component to the total radiation increases with the optical depth. For the three scenarios of Figure 5 with τ = 1, the ratio T/T_{SW} shows a very small variability, taking values between 0.748 at ϕ = 30° N and 0.750 at ϕ = 30° S due to changes in the mean solar zenith angle. We have also calculated the ratio T/T_{SW} for the 1000 scenarios defined in the previous section. As it happened for T/E (Fig. 2), the ratio is controlled

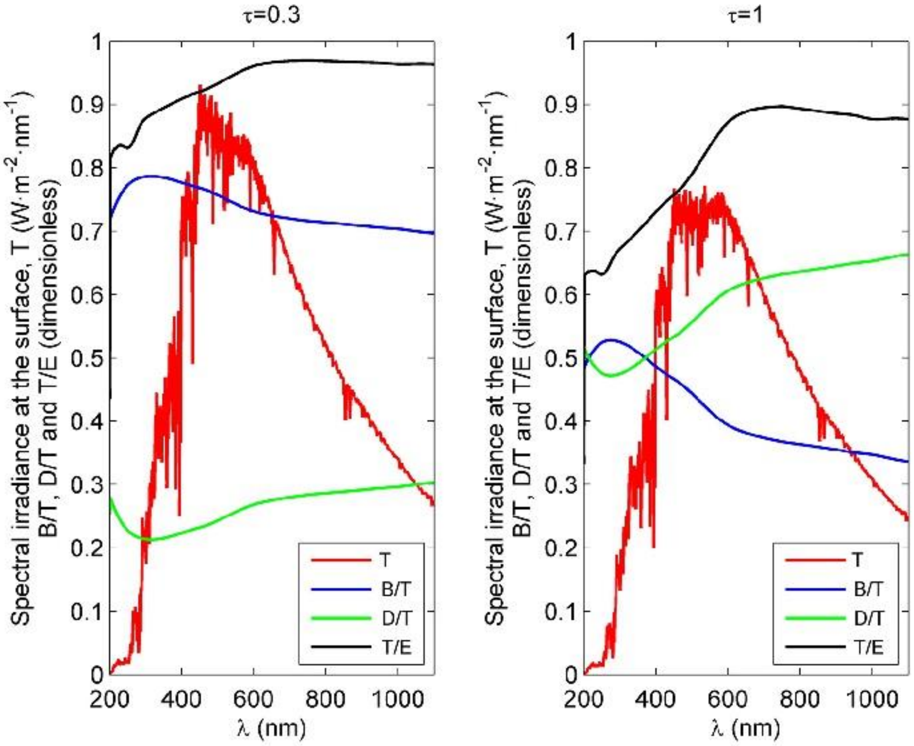

Fig. 6. Total surface spectral irradiance (*T*, red line), ratios of direct and diffuse irradiances to *T*, *B/T* (blue line) and *D/T* (green line), and ratio of *T* to the irradiance at the TOA, *T/E* (black line), between 200 and 1100 nm for clear (left) and dusty (right) conditions. Simulations run for $\phi = 0°$, $L_s = 270°$, $\tau_{ca,12.1} = 0.02$, $N_{O_3} = 1$ µm-atm, at local noon.

by the dust optical depth. These results show that the shortwave flux can be estimated from the flux between 200 and 1100 nm and from the model-derived ratios.

4.3. Spectral irradiance under different scenarios

In this subsection we complement the study of broadband solar fluxes by analyzing their spectral features between 200 and 1100 nm. Figure 6 shows a comparison between the total spectral irradiance at the surface (*T*) and the ratios *B/T*, *D/T*, and *T/E* for two different values of dust optical depths at 880 nm ($\tau_{d,880} = 0.3$ and $\tau_{d,880} = 1$). In both cases, $\phi = 0°$, $A_{750} = 0.25$, $L_s = 270°$, $\tau_{ca,12.1} = 0.02$, $N_{O_3} = 1$ µm-atm, and $t = 0$ (which corresponds to noon).

For every wavelength in the range 200–1100 nm, the direct radiation at the surface is larger than the diffuse component when $\tau_{d,880} = 0.3$. However, similar values of diffuse and direct spectral irradiance are found in the UV range when $\tau_{d,880} = 1$, while at longer wavelengths the diffuse component becomes larger than the direct component.

The *D/T* (*B/T*) ratio increases (decreases) for every wavelength with dust opacity. However, the qualitative behavior of *D/T* and *B/T* is similar for both optical depths. At the shortest wavelengths, *D/T* decreases toward longer wavelengths mainly due to the decreasing effect of Rayleigh scattering. Then, up to 600 nm, *D/T* increases markedly mainly due to the increase in dust single scattering albedo. Between 600 and 1100 nm, *D/T* keeps increasing with wavelength due to the increase in the spectral optical depth, but at a smaller rate.

The ratio *T/E* decreases with increasing values of dust optical depth, and its qualitative behavior is similar for both optical depths. As the dust optical depth increases, the difference between the UV and NIR scattering regimes becomes more apparent, and this causes a more pronounced increase in *T/E* across visible wavelengths. Therefore, as the dust optical depth increases, the shape of the total spectral irradiance changes, with its peak shifting toward longer wavelengths.

Taking advantage of the spectral behavior of *T/E* described above, we show an alternative method to retrieve dust optical depth from MetSIS measurements in different spectral bands. While the method shown in Section 4.1 is based on the effect of optical depth on the ratio *T/E* in a given spectral region, the alternative method described here relies on the effect of optical depth on the differences between the values of *T* measured in bands with different radiative properties.

Figure 7 shows the ratio between the spectral irradiance at the surface at 440 nm and at 600 nm, which correspond to the centers of two MetSIS channels, for values of $\tau_{d,880}$ in the range 0–1.5, $\tau_{ca,12.1}$ in the range 0–0.15, and N_{O_3} in the range 1–3 µm-atm. As in Figure 2, the ratio T_{440}/T_{600} is mainly controlled by dust optical depth because in this spectral range the radiative properties of water ice clouds show a small dependence on wavelength and the variability of τ_c is smaller than that of τ_d. The differences in the typical range of optical depths can reach a 20%, with the lowest ratios occurring at high optical depths, being consistent with the behavior of *T/E* described above. As in the case where only one band is used, a look-up table showing values of the ratio of *T* at different bands (i.e. 440 and 600 nm) is generated from model results for different optical depths to find the one that best matches the observations.

By using both methods to estimate optical depths, we can obtain further information on the particle size distribution because the spectral radiative properties (used to retrieve the

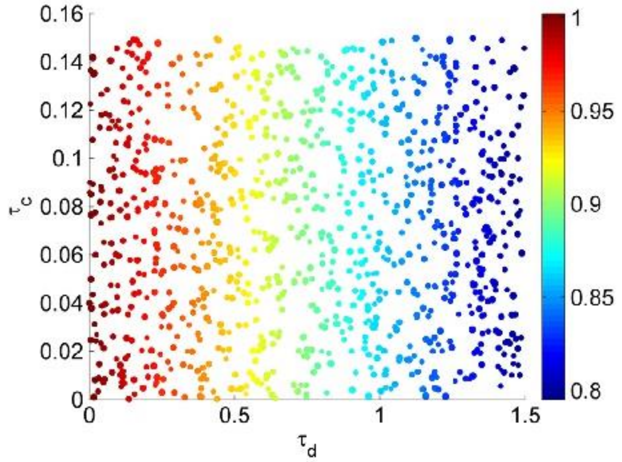

Fig. 7. As in Figure 2, but for the ratio of the spectral irradiance at 440 nm to that at 600 nm, T_{440}/T_{600}.

optical depth) depend on such distributions. As an example, there is a difference of 4% between T_{440}/T_{600} using a log-normal dust size distribution with $r_{\mathrm{eff}} = 1.5$ μm and $v_{\mathrm{eff}} = 0.3$, and using the same distribution but with $r_{\mathrm{eff}} = 1$ μm and the same v_{eff} value. Therefore, we can estimate the optical depth by comparing the measurements in different bands with generated look-up tables of T/E for the wider MetSIS band (first method) and T_{440}/T_{600} (second method) for different size distributions, and then identify the size distribution for which the difference between the two optical depths at the reference wavelength is minimum.

Using the model and with some additional information, we can obtain an optical depth from the measurements at other MetSIS channels. As an example, we could use the wider channels in the UVA (315–400 nm) and NIR (700–1100 nm) regions. By knowing the surface pressure, the effect of Rayleigh scattering is considered for the calculation of the UVA flux, and then a value of the optical depth can be obtained from the ratio $T_{\mathrm{UVA}}/T_{\mathrm{NIR}}$. Subsequently, it is possible to compare the results to check the consistency of the retrieved optical depths.

From the results shown in this section we can conclude that useful scientific information, such as temporal variations from diurnal to seasonal time scales of the atmospheric optical depth and particle size distribution, can be obtained from a comparison between measurements and COMIMART results.

5. Summary and conclusions

We have developed a comprehensive radiative transfer model to study the solar irradiance that reaches the Martian surface. It includes updated wavelength-dependent radiative parameters for dust, water ice clouds, and gas molecules. The model enables the characterization of the radiative environment under different scenarios in the spectral regions covered by MetSIS and REMS UV sensors.

The model is very versatile as it contains a number of input parameters that can be modified: dust optical depth at 880 nm, water ice clouds opacity at 825 cm^{-1}, abundance of different atmospheric gases, local time, solar longitude, latitude, surface albedo, spectral band and the wavelength-dependent values of extinction efficiency, single scattering albedo, and asymmetry factor. By combining different values of these parameters a wide number of scenarios can be defined, covering the range of conditions that can be found in the Martian atmosphere.

We have validated the model by comparing the calculated surface fluxes to those obtained using the DISORT algorithm, showing an excellent agreement for a wide range of conditions. In addition, we have tested some important assumptions considered in the model, showing their validity in the range between 200 and 1100 nm.

We have shown results of different nature: diurnal evolution of the solar fluxes at the surface (both the direct and diffuse components), spectral irradiance features, and daily irradiation values. We have discussed the effect of the different atmospheric components on the total spectral atmospheric optical depth, and have described two alternative methods to retrieve atmospheric optical depths from in situ measurements. The first considers measured and calculated fluxes in a single band, while the second considers measured and calculated fluxes in different bands with different radiative properties; by combining both methods, additional information about particle size distribution can be obtained. Therefore, the use of the COMIMART model in combination with measurements by the MetSIS sensor aboard the MetNet mission can greatly enhance its scientific return.

Acknowledgements. This work has been partially supported by the research projects AYA2011-29967-C05-02, CGL2011-25327 and EU ERA-NET Plus (PCIN-2014-013-C07-04), and by the Instituto de Matemática Interdisciplinar (IMI) of the Universidad Complutense. The author A. Vicente-Retortillo wishes to acknowledge the Spanish Ministry of Economy and Competitiveness (MINECO) for the granted FPI fellowship (BES-2012-059241). We want to thank M.J. Wolff and an anonymous reviewer for their excellent suggestions to improve the paper. The editor thanks M.J. Wolff and an anonymous referee for their assistance in evaluating this paper.

References

Berk, A., L.S. Bernstein, G.P. Anderson, P.K. Acharya, D.C. Robertson, J.H. Chetwynd, and S.M. Adler-Golden. MODTRAN cloud and multiple scattering upgrades with application to AVIRIS. *Remote Sens. Environ.*, **65**, 367–375, 1998, DOI: 10.1016/S0034-4257(98)00045-5.

Clancy, R.T., M.J. Wolff, and P.R. Christensen. Mars aerosol studies with the MGS TES emission phase function observations: optical depths, particle sizes, and ice cloud types versus latitude and solar longitude. *J. Geophys. Res.*, **108**, 5098, 2003, DOI: 10.1029/2003JE002058.

Córdoba-Jabonero, C., L.M. Lara, A.M. Mancho, A. Márquez, and R. Rodrigo. Solar ultraviolet transfer in the Martian atmosphere: biological and geological implications. *Planet. Space Sci.*, **51 (6)**, 399–410, 2003, DOI: 10.1016/S0032-0633(03)00023-0.

Encrenaz, T., T.K. Greathouse, F. Lefèvre, and S.K. Atreya. Hydrogen peroxide on Mars: observations, interpretation and future plans. *Planet. Space Sci.*, **68 (1)**, 3–17, 2012, DOI: 10.1016/j.pss.2011.03.019.

Frederick, J.E., and J.E. Mentall. Solar irradiance in the stratosphere: implications for the Herzberg continuum absorption of O_2. *Geophys. Res. Lett.*, **9 (4)**, 461–464, 1982, DOI: 10.1029/GL009i004p00461.

Gómez-Elvira, J., C. Armiens, L. Castañer, M. Domínguez, M. Genzer, et al. REMS: the environmental sensor suite for the Mars Science Laboratory rover. *Space Sci. Rev.*, **170 (1–4)**, 583–640, 2012, DOI: 10.1007/s11214-012-9921-1.

Haberle, R.M., C.P. McKay, J.B. Pollack, O.E. Gwynne, D.H. Atkinson, J. Appelbaum, G.A. Landis, R.W. Zurek, and D.J. Flood. Atmospheric effects on the utility of solar power on Mars. In: J.S. Lewis, M.S. Matthews, and M.L. Guerrieri, Editors. *Resources of Near-Earth Space*, The University of Arizona Press, Tuscon, 845–885, 1993.

Hansen, J.E., and L.D. Travis. Light scattering in planetary atmospheres. *Space Sci. Rev.*, **16**, 527–610, 1974.

Henyey, L.G., and J.L. Greenstein. Diffuse radiation in the galaxy. *Astrophys. J.*, **93**, 70–83, 1941.

Ityaksov, D., H. Linnartz, and W. Ubachs. Deep-UV absorption and Rayleigh scattering of carbon dioxide. *Chem. Phys. Lett.*, **462 (1)**, 31–34, 2008, DOI: 10.1016/j.cplett.2008.07.049.

Joseph, J.H., W.J. Wiscombe, and J.A. Weinman. The delta-Eddington approximation for radiative flux transfer. *J. Atmos. Sci.*, **33 (12)**, 2452–2459, 1976,
DOI: 10.1175/1520-0469(1976)033<2452:TDEAFR>2.0.CO;2.

Kahre, M.A., J.R. Murphy, and R.M. Haberle. Modeling the Martian dust cycle and surface dust reservoirs with the NASA Ames general circulation model. *J. Geophys. Res.*, **111**, E06008, 2006, DOI: 10.1029/2005JE002588.

Lefèvre, F., F. Montmessin, A. Määttänen, and J.L. Bertaux. The Martian ozone layer as seen by SPICAM: 2004-2011. In: F. Forget, and M. Millour, Editors. *The Fifth International Workshop on the Mars Atmosphere: Modelling and Observation*, Oxford, UK, 2014, id.3403.

Lemmon, M.T., M.J. Wolff, J.F. Bell III, M.D. Smith, B.A. Cantor, and P.H. Smith. Dust aerosol, clouds, and the atmospheric optical depth record over 5 Mars years of the Mars Exploration Rover mission. *Icarus*, **251**, 96–111, 2015,
DOI: 10.1016/j.icarus.2014.03.029.

Lewis, B.R., and J.H. Carver. Temperature dependence of the carbon dioxide photoabsorption cross section between 1200 and 1970 Å. *J. Quant. Spectrosc. Radiat. Transfer*, **30 (4)**, 297–309, 1983, DOI: 10.1016/0022-4073(83)90027-4.

Lilensten, J., A.J. Coates, V. Dehant, T.D. De Wit, R.B. Horne, F. Leblanc, J. Luhmann, E. Woodfield, and M. Barthélemy. What characterizes planetary space weather? *Astron. Astrophys. Rev.*, **22 (1)**, 1–39, 2014,
DOI: 10.1007/s00159-014-0079-6.

Lin, C.L., N.K. Rohatgi, and W.B. DeMore. Ultraviolet absorption cross sections of hydrogen peroxide. *Geophys. Res. Lett.*, **5 (2)**, 113–115, 1978, DOI: 10.1029/GL005i002p00113.

Madeleine, J.-B., F. Forget, E. Millour, L. Montabone, and M.J. Wolff. Revisiting the radiative impact of dust on Mars using the LMD Global Climate Model. *J. Geophys. Res.*, **116**, E11010, 2011, DOI: 10.1029/2011JE003855.

Madeleine, J.-B., F. Forget, E. Millour, T. Navarro, and A. Spiga. The influence of radiatively active water ice clouds on the Martian climate. *Geophys. Res. Lett.*, **39**, L23202, 2012,
DOI: 10.1029/2012GL053564.

Martínez, G.M., F. Valero, and L. Vázquez. Characterization of the Martian surface layer. *J. Atmos. Sci.*, **66 (1)**, 187–198, 2009,
DOI: 10.1175/2008JAS2765.1.

Martínez, G.M., F. Valero, and L. Vázquez. The TKE budget in the convective Martian planetary boundary layer. *Q. J. R. Meteorol. Soc.*, **137 (661)**, 2194–2208, 2011, DOI: 10.1002/qj.883.

Martínez, G.M., N. Rennó, E. Fischer, C.S. Borlina, B. Hallet, et al. Surface energy budget and thermal inertia at Gale Crater: calculations from ground-based measurements. *J. Geophys. Res. [Planets]*, **119 (8)**, 1822–1838, 2014,
DOI: 10.1002/2014JE004618.

Mustard, J.F., and J.F. Bell III. New composite reflectance spectra of Mars from 0.4 to 3.14 μm. *Geophys. Res. Lett.*, **21 (5)**, 353–356, 1994, DOI: 10.1029/94GL00198.

Parkinson, W.H., and K. Yoshino. Absorption cross-section measurements of water in the wavelength region 181–199 nm. *Chem. Phys.*, **294 (1)**, 31–35, 2003, DOI: 10.1016/S0301-0104(03)00361-6.

Patel, M.R., J.C. Zarnecki, and D.C. Catling. Ultraviolet radiation on the surface of Mars and the Beagle 2 UV sensor. *Planet. Space Sci.*, **50 (9)**, 915–927, 2002,
DOI: 10.1016/S0032-0633(02)00067-3.

Patel, M.R., A. Bérces, T. Kerékgyárto, G. Rontó, H. Lammer, and J.C. Zarnecki. Annual solar UV exposure and biological effective dose rates on the Martian surface. *Adv. Space Res.*, **33 (8)**, 1247–1252, 2004, DOI: 10.1016/j.asr.2003.08.036.

Perrier, S., J.L. Bertaux, F. Lefèvre, S. Lebonnois, O. Korablev, A. Fedorova, and F. Montmessin. Global distribution of total ozone on Mars from SPICAM/MEX UV measurements. *J. Geophys. Res.*, **111**, E09S06, 2006,
DOI: 10.1029/2006JE002681.

Petrosyan, A., B. Galperin, S.E. Larsen, S.R. Lewis, A. Määttänen, et al. The Martian atmospheric boundary layer. *Rev. Geophys.*, **49 (3)**, RG3005, 2011, DOI: 10.1029/2010RG000351.

Rannou, P., S. Perrier, J.L. Bertaux, F. Montmessin, O. Korablev, and A. Rébérac. Dust and cloud detection at the Mars limb with UV scattered sunlight with SPICAM. *J. Geophys. Res.*, **111**, E09S10, 2006, DOI: 10.1029/2006JE002693.

Read, P.L., and S.R. Lewis. *The Martian climate revisited: atmosphere and environment of a desert planet*, Springer-Verlag, Berlin, ISBN: 978-3-540-40743-0, 2004.

Rothman, L.S., I.E. Gordon, Y. Babikov, A. Barbe, D.C. Benner, et al. The HITRAN2012 molecular spectroscopic database. *J. Quant. Spectrosc. Radiat. Transfer*, **130**, 4–50, 2013,
DOI: 10.1016/j.jqsrt.2013.07.002.

Savijärvi, H., and J. Kauhanen. Surface and boundary-layer modelling for the Mars Exploration Rover sites. *Q. J. R. Meteorol. Soc.*, **134 (632)**, 635–641, 2008,
DOI: 10.1002/qj.232.

Savijärvi, H., D. Crisp, and A.-M. Harri. Effects of CO_2 and dust on present-day solar radiation and climate on Mars. *Q. J. R. Meteorol. Soc.*, **131**, 2907–2922, 2005,
DOI: 10.1256/qj.04.09.

Serdyuchenko, A., V. Gorshelev, M. Weber, W. Chehade, and J.P. Burrows. High spectral resolution ozone absorption cross-sections – Part 2: temperature dependence. *Atmos. Meas. Tech.*, **7**, 625–636, 2014, DOI: 10.5194/amt-7-625-2014.

Smith, M.D. Interannual variability in TES atmospheric observations of Mars during 1999–2003. *Icarus*, **167 (1)**, 148–165, 2004,
DOI: 10.1016/j.icarus.2003.09.010.

Sneep, M., and W. Ubachs. Direct measurement of the Rayleigh scattering cross section in various gases. *J. Quant. Spectrosc. Radiat. Transfer*, **92 (3)**, 293–310, 2005,
DOI: 10.1016/j.jqsrt.2004.07.025.

Stamnes, K., S.C. Tsay, W. Wiscombe, and K. Jayaweera. Numerically stable algorithm for discrete-ordinate-method radiative transfer in multiple scattering and emitting layered media. *Appl. Opt.*, **27**, 2502–2509, 1988,
DOI: 10.1364/AO.27.002502.

Stamnes, K., S.C. Tsay, W. Wiscombe, and I. Laszlo. *DISORT, a general-purpose FORTRAN program for Discrete-Ordinate-Method radiative transfer in scattering and emitting layered media: documentation of methodology, version 1.1.* ftp://climate1.gsfc.nasa.gov/wiscombe/Multiple_Scatt/DISORTReport1.1.pdf, 2000

Vázquez, L., M.P. Zorzano, and S. Jiménez. Spectral information retrieval from integrated broadband photodiode Martian ultraviolet measurements. *Opt. Lett.*, **32 (17)**, 2596–2598, 2007,
DOI: 10.1364/OL.32.002596.

Warren, S.G. Optical constants of ice from the ultraviolet to the microwave. *Appl. Opt.*, **23 (8)**, 1206–1225, 1984,
DOI: 10.1364/AO.23.001206.

Weber, M.J. *Handbook of optical materials*, CRC Press, Boca Raton, Florida, ISBN: 0-8493-3512-4, 2003.

Wolff, M.J., and R.T. Clancy. Constraints on the size of Martian aerosols from Thermal Emission Spectrometer observations. *J. Geophys. Res.*, **108**, 5097, 2003, DOI: 10.1029/2003JE002057.

Wolff, M.J., M.D. Smith, R.T. Clancy, R. Arvidson, M. Kahre, F. Seelos IV, S. Murchie, and H. Savijärvi. Wavelength dependence of dust aerosol single scattering albedo as observed by the Compact Reconnaissance Imaging Spectrometer. *J. Geophys. Res.*, **114**, E00D04, 2009, DOI: 10.1029/2009JE003350.

Wolff, M.J., R.T. Clancy, J.D. Goguen, M.C. Malin, and B.A. Cantor. Ultraviolet dust aerosol properties as observed by MARCI. *Icarus*, **208 (1)**, 143–155, 2010, DOI: 10.1016/j.icarus.2010.01.010.

Zorzano, M.P., L. Vázquez, and S. Jiménez. Retrieval of ultraviolet spectral irradiance from filtered photodiode measurements. *Inverse Prob.*, **25 (11)**, 115023, 2009, DOI: 10.1088/0266-5611/25/11/115023.

Cite this article as: Vicente-Retortillo Á, Valero F, Vázquez L & Martínez GM. A model to calculate solar radiation fluxes on the Martian surface. *J. Space Weather Space Clim.*, **5**, A33, 2015, DOI: 10.1051/swsc/2015035.

Chapter 5. Seasonal and interannual variability of solar radiation at Spirit, Opportunity and Curiosity landing sites

Abstract

In this article we characterize the radiative environment at the landing sites of NASA's Mars Exploration Rover (MER) and Mars Science Laboratory (MSL) missions. We use opacity values obtained at the surface from direct imaging of the Sun and our radiative transfer model COMIMART to analyze the seasonal and interannual variability of the daily irradiation at the MER and MSL landing sites. In addition, we analyze the behavior of the direct and diffuse components of the solar radiation at these landing sites.

Seasonal and interannual variability of solar radiation at Spirit, Opportunity and Curiosity landing sites

Álvaro VICENTE-RETORTILLO[1], Mark T. LEMMON[2], Germán M. MARTÍNEZ[3], Francisco VALERO[4], Luis VÁZQUEZ[5], Mª Luisa MARTÍN[6]

[1]Departamento de Física de la Tierra, Astronomía y Astrofísica II, Universidad Complutense de Madrid, Madrid, Spain, alvarodv@ucm.es. [2]Department of Atmospheric Sciences, Texas A&M University, College Station, TX, USA, lemmon@tamu.edu. [3]Department of Climate and Space Sciences and Engineering, University of Michigan, Ann Arbor, MI, USA, gemartin@umich.edu. [4]Departamento de Física de la Tierra, Astronomía y Astrofísica II, Universidad Complutense de Madrid, Madrid, Spain, valero@ucm.es. [5]Departamento de Matemática Aplicada, Universidad Complutense de Madrid, Madrid, Spain, lvazquez@fdi.ucm.es. [6]Departamento de Matemática Aplicada, Universidad de Valladolid, Segovia, Spain, mlmartin@eii.uva.es.

Received: 14/04/2016
Accepted: 22/09/2016

Abstract
In this article we characterize the radiative environment at the landing sites of NASA's Mars Exploration Rover (MER) and Mars Science Laboratory (MSL) missions. We use opacity values obtained at the surface from direct imaging of the Sun and our radiative transfer model COMIMART to analyze the seasonal and interannual variability of the daily irradiation at the MER and MSL landing sites. In addition, we analyze the behavior of the direct and diffuse components of the solar radiation at these landing sites.

Key words: Solar radiation; Mars Exploration Rovers; Mars Science Laboratory; opacity, dust; radiative transfer model; Mars exploration.

Variabilidad estacional e interanual de la radiación solar en las coordenadas de aterrizaje de Spirit, Opportunity y Curiosity

Resumen
El presente artículo está dedicado a la caracterización del entorno radiativo en los lugares de aterrizaje de las misiones de la NASA de *Mars Exploration Rover* (MER) y de *Mars Science Laboratory* (MSL). Se hace uso de las opacidades obtenidas a partir de imágenes directas del Sol y de nuestro modelo de transferencia radiativa COMIMART con el fin de analizar la variabilidad estacional e interanual de la irradiación diaria en las coordenadas de aterrizaje de los MER y de MSL. Asimismo, se analiza el comportamiento de las componentes directa y difusa de la radiación solar en estos lugares de aterrizaje.

Palabras clave: Radiación solar; Mars Exploration Rovers; Mars Science Laboratory; opacidad; polvo; modelo de transferencia radiativa; exploración de Marte.

Summary: Introduction. 1. Dust opacity measurements on Mars 2. COMIMART Radiative Transfer model: Description and sensitivity studies 3. Temporal and spatial variability of daily irradiation at the

http://dx.doi.org/10.5209/rev_FITE.2016.v28.53900

top of the atmosphere 4. Results: radiative environment at the MER and MSL landing sites 5. Conclusions. Acknowledgements. References.

Normalized reference
Vicente-Retortillo, A., Lemmon, M. T., Martínez, G. M., Valero, F., Vázquez, L., Martín, M. L. (2016). Seasonal and interannual variability of solar radiation at Spirit, Opportunity and Curiosity landing sites. *Física de la Tierra,* Vol., 28, 111-127.

Introduction

The study of the radiation environment at the Martian surface is important because of the role that solar radiation plays in constraining the habitability of Mars and in driving its atmospheric dynamics. Ultraviolet radiation has the potential to damage the DNA (Córdoba-Jabonero et al.,, 2003) while solar radiation feeds atmospheric thermodynamic processes occurring in the first meters of the Martian atmosphere, the so-called planetary boundary layer.

In this article we study the variability of the daily irradiation at the surface (also called insolation and defined as the total amount of solar energy received during one sol) at the landing sites of MER Spirit (14.57°S, 175.48°E) and Opportunity (1.95°S, 354.47°E) and MSL Curiosity (4.59°S, 137.44°E) rovers on seasonal and interannual time scales. We also discuss the variability of the diffuse and direct components of the insolation at these three locations.

In section 1 we review several efforts to retrieve dust opacity both from satellites and ground measurements, and we show the opacities at the Spirit, Opportunity and Curiosity landing sites. In section 2 we describe our COmplutense and MIchigan MArs Radiative Transfer model (COMIMART) and perform sensitivity studies to validate the assumption of using atmospheric optical depths as dust opacities. In section 3 we analyze the behavior of the total radiation at the top of the atmosphere. In section 4 we characterize the radiative environment at the three selected landing sites. Finally, we highlight our main conclusions in section 5.

1. Dust opacity measurements on Mars

An accurate characterization of suspended dust is essential for studies of the Martian atmosphere. The spatial distribution and radiative properties of dust have a strong impact on calculations of heating rates and thus on the atmospheric thermal behavior (Madeleine et al., 2011) and dynamical processes (Read and Lewis, 2004). Dust controls the amount of radiation that reaches the surface, which is the principal term of the energy budget at the surface of Mars (Martínez et al., 2014). This energy budget determines the diurnal cycle of the temperature of the ground (Savijärvi and Kauhanen, 2008; Martínez et al., 2009), which in turn affects the thermodynamic activity in the planetary boundary layer (Martínez et al., 2011). As an example, dust devils are more frequent on Mars when the insolation is higher and therefore the surface is warmer, being therefore more frequent on Summer than at other times of the year (Petrosyan et al., 2011).

A wide number of efforts have been done to characterize the spatial and temporal variability of dust in the last decades. Advances in the characterization of dust have been mainly achieved from orbiter observations, but also from ground measurements. We now describe some of the main efforts regarding this matter.

In the early 70s, measurements by the Infrared Interferometer Spectrometer (IRIS) onboard Mariner 9 enabled the observation of the dissipation of the global dust storm in 1971 (Hanel et al., 1972). Between 1976 and 1979, data acquired by the Viking IR Thermal Mapper (IRTM) allowed global dust opacity mapping for more than 1.3 Martian years (Martin and Richardson, 1993); the results showed that there were two planet-encircling dust storms within this temporal range, known as 1977a and 1977b.

In 1999, the Thermal Emission Spectrometer (TES) onboard the Mars Global Surveyor (MGS) mission began to monitor the atmospheric conditions. Using TES measurements, Smith (2004) studied the interannual variability of dust opacity between 1999 and 2003. He concluded that during the aphelion season (solar longitude L_s between 0° and 180°), dust opacity is low and presents low interannual variability; in contrast, during the perihelion season (solar longitude L_s between 180° and 360°) the atmosphere is dustier and presents higher interannual variability.

More recently, infrared images acquired by the Thermal Emission Imaging System (THEMIS) onboard the Mars Odyssey mission over more than 3.5 years (between 2002 and 2008) were used by Smith (2009) to retrieve dust opacities. He showed that the dust activity during Mars Year 28 was markedly higher than in the previous two Mars Years (MY).

In 2006, the Mars Climate Sounder (MCS) onboard the Mars Reconnaissance Orbiter allowed additional retrievals of dust opacity. The combination of TES, THEMIS and MCS measurements has allowed producing a dust climatology from MY 24 to MY 31, covering the temporal range between April 1999 and July 2013 (Montabone et al., 2015).

Ground-based observations of opacity, although scarcer than from orbit, are very important because the retrieval process incorporates fewer assumptions than from orbit and thus the uncertainty in the results is lower, providing “ground truth” and complementary information for the analysis of satellite measurements.

Colburn et al. (1989) analyzed approximately 1.3 Martian years of Sun images acquired in the second half of the 70s at the two Viking landing sites, obtaining numerous values of the atmospheric opacity which showed a number of seasonal peaks.

Ten years later, Smith and Lemmon (1999) obtained atmospheric opacity values using direct images of the Sun by the Imager for Mars Pathfinder (IMP) during the 83-sol Mars Pathfinder mission. They provided hourly opacities between 07:00 and 17:00 LTST at four wavelengths: 450, 670, 883 and 989 nm, with values similar to those at the Viking sites.

Up to date, the most complete dataset of atmospheric opacity values obtained from ground measurements has been provided by the Pancam camera onboard the two

MER rovers. Using direct solar images of Sun, opacity values spanning more than 2200 sols for Spirit and more than 4300 sols (more than six Mars Years) for Opportunity have been retrieved (Lemmon et al., 2015). This optical depth record has been used as "ground truth" results in many studies, such as Wolff et al. (2009), Wolff et al. (2010) or Montabone et al. (2015). More recently, images of the Sun by the Mastcam instrument onboard MSL Curiosity rover are providing new aerosol opacity values at the MSL landing site.

From top to bottom, we show in Figure 1 atmospheric opacity values at the Spirit, Opportunity and Curiosity landing sites. At the three landing sites on each year, the perihelion season is dustier than the aphelion season. This seasonal behavior is in agreement with that derived from TES measurements (Smith, 2004). In particular, the lowest annual opacity values occur at L_s = 120° - 140°, while the highest annual values occur at L_s = 220° - 240° at the three landing sites. Opacities higher than 4 observed at the Spirit and Opportunity landing sites between L_s = 265° and L_s = 295° of MY 28 correspond to a global dust storm.

2. COMIMART Radiative Transfer model: Description and sensitivity studies

COMIMART is a new Martian radiative transfer model that we developed in 2015 and that we presented in Vicente-Retortillo et al. (2015). Our model enables the characterization of the radiative environment in different spectral regions in the solar range under different scenarios. In particular, it enables the calculation of spectral irradiances at the surface as well as the diurnal evolution of surface fluxes and daily irradiations. It also allows calculating the direct and diffuse components of solar radiation at the surface. COMIMART includes updated spectral radiative properties of atmospheric dust, water ice clouds and gas molecules. The input parameters of our model include dust opacity at 880 nm, water ice clouds opacity, abundance of the atmospheric gases, surface albedo, values at each wavelength of the radiative parameters (extinction efficiency, single scattering albedo and asymmetry factor), time of the day and of the year, latitude and spectral range.

The dust radiative parameters can be computed for any particle size distribution using Mie theory from spectral refractive indices. We have selected the refractive indices calculated by Wolff et al. (2009) and Wolff et al. (2010). The model assumes a log-normal particle size distribution, which is characterized by the effective radius and the dimensionless effective variance (Hansen and Travis, 1974). We have selected the canonical values for these parameters: an effective radius of 1.5 μm (Clancy et al., 2003; Wolff and Clancy, 2003; Kahre et al., 2006; Madeleine et al., 2011) and an effective variance of 0.3 (Rannou et al., 2006; Madeleine et al., 2011).

Similarly, water ice radiative properties are computed from the refractive indices provided by Warren (1984). In this case, we have selected a log-normal size distribution with an effective radius of 3 μm (Wolff and Clancy, 2003) and effective variance of 0.1 (Wolff and Clancy, 2003; Madeleine et al., 2012). We have assumed a water ice absorption opacity of 0.02 at 12.1 μm, which is a typical value outside the aphelion cloud belt (Smith 2004, Madeleine et al., 2012).

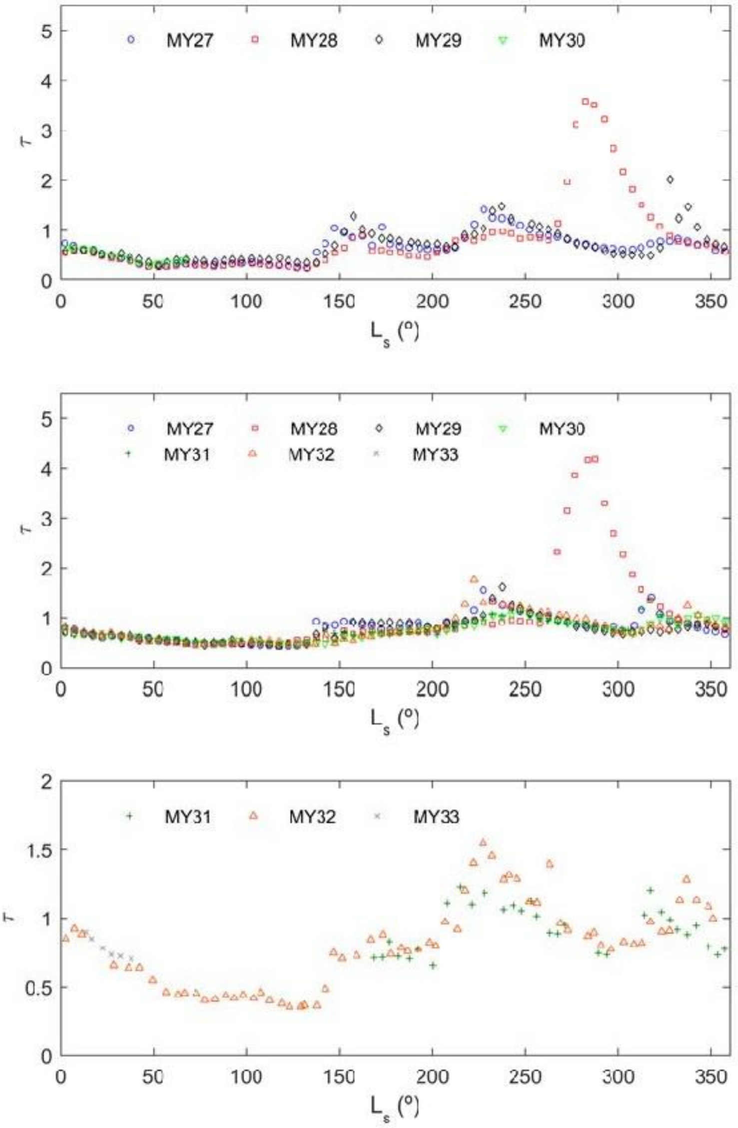

Figure 1. Temporal evolution of the atmospheric opacity at 880 nm at the Spirit (top), Opportunity (middle) and Curiosity (bottom) landing sites, as a function of solar longitude. Note that the vertical axis of the third panel is different from the previous two.

In this article, we have assumed that the retrieved atmospheric opacity at each of the three analyzed landing sites is entirely caused by dust particles. Lemmon et al. (2015) concluded that ice clouds did not show a significant contribution to the atmospheric opacity at the Spirit landing site but that they contributed to the total opacity at the Opportunity site. However, we show that the validity of our assumption is very good to calculate the daily irradiation at the surface.

Table 1. Direct (B), diffuse (D) and total (T) daily irradiations at the Opportunity landing site at $L_s = 90°$ for different relative contributions of water ice clouds to total opacity. Differences with respect to the scenario with only dust are also shown.

% of ice aerosols	Dust opacity	WIC opacity	B (MJ/m^2)	D (MJ/m^2)	T (MJ/m^2)	B/B_0	D/D_0	T/T_0
0	0.440	0.000	6.26	4.47	10.73	1.000	1.000	1.000
10	0.396	0.044	6.25	4.55	10.80	0.998	1.018	1.007
20	0.352	0.088	6.25	4.63	10.88	0.998	1.036	1.014
30	0.308	0.132	6.24	4.72	10.96	0.997	1.056	1.021
40	0.264	0.176	6.23	4.80	11.03	0.995	1.074	1.028
50	0.220	0.220	6.23	4.89	11.12	0.995	1.094	1.036
60	0.176	0.264	6.22	4.97	11.19	0.994	1.112	1.043
100	0.000	0.440	6.19	5.32	11.51	0.989	1.190	1.073

Table 1 shows the direct (B, column 4), diffuse (D, column 5) and total (T, column 6) daily irradiations at a solar longitude $L_s = 90°$ at the Opportunity landing site for a typical clear atmospheric opacity of 0.44 and for different relative contributions of ice aerosols. The last three columns represent the ratio between the direct, diffuse and total daily irradiations for each scenario and their counterparts in the scenario with absence of water ice clouds (denoted as WIC).

These results show that, even for the highest realistic fraction of ice aerosols (60%), differences with the cloud-free scenario are below 1%, 12% and 5% in the direct, diffuse and total irradiations at the surface, respectively. Differences are smaller for the conditions found during most of the year (Smith, 2004). Therefore, we can assume that the retrieved atmospheric opacity is caused by dust particles to calculate the daily irradiation.

3. Temporal and spatial variability of daily irradiation at the top of the atmosphere

In this section we show the daily irradiation at the top of the atmosphere as a function of the time of the year and latitude. The daily irradiation can be calculated using the expression

$$E = \frac{88775}{\pi} E_0 \left[\frac{1 + e\cos(L_s - L_{s,p})}{1 - e^2} \right]^2 \left[(1 - \sin^2 \varepsilon \sin^2 L_s)^{1/2} \cos\phi \sin H + H \sin\varepsilon \sin L_s \sin\phi \right] \qquad (1)$$

where $E_0 = 590\ W/m^2$ is the solar irradiance at the mean distance between Mars and the Sun (1.52 AU), $e = 0.0934$ is the eccentricity of the Martian orbit, $\epsilon = 25.2°$ is the obliquity of Mars, $L_{s,p} = 251°$ is the solar longitude at the perihelion, ϕ is the latitude and H is the half of the length of the day expressed in radians calculated as

$$\cos(H) = -\tan\phi \frac{\sin\varepsilon \sin L_s}{(1 - \sin^2 \varepsilon \sin^2 L_s)^{1/2}} \qquad (2)$$

where if cos (H) is greater than +1 (smaller than -1), then H is 0 (π).

Figure 2 shows the daily irradiation at the top of the atmosphere as a function of latitude and solar longitude. As on Earth, there are polar nights in the winter Hemisphere, annual maximum values are found in polar latitudes in both hemispheres at around their respective summer solstices, and the seasonal variability at low latitudes is lower than at higher latitudes. However, there are some noticeable differences between Mars and our planet. The most striking difference is the stronger asymmetry between the aphelion and the perihelion season on Mars. This is explained by the eccentricity of the Martian orbit, which is higher than on Earth. On a planetary average, the aphelion season is colder than the perihelion season. Moreover, a higher daily insolation causes warmer ground temperatures, which stimulate the lifting of dust from the surface into the atmosphere. Therefore, the most favorable conditions for the formation of dust storms can be found during summer in the Southern Hemisphere. In conclusion, the dichotomy between the relatively cold and clear aphelion season and the relatively warm and dusty perihelion season is mainly caused by the seasonal asymmetries in solar insolation.

It is also interesting to notice that the variability of the insolation at each latitude along the year is clearly higher in the Southern Hemisphere than in the Northern Hemisphere, causing a stronger thermal contrast between summer and winter in the Southern Hemisphere than in the Northern Hemisphere.

4. Results: radiative environment at the MER and MSL landing sites

In this section we show results for the seasonal and interannual daily irradiation at the MERs and MSL landing sites, as well as an analysis of the direct, diffuse and total daily irradiations at the locations of the three rovers. We use atmospheric opacities at 880 nm derived from ground-based measurements of the Pancam instrument onboard the Mars Exploration Rovers (Lemmon et al., 2015) and Mastcam instrument onboard MSL Curiosity rover along with our radiative transfer model to obtain the results mentioned above.

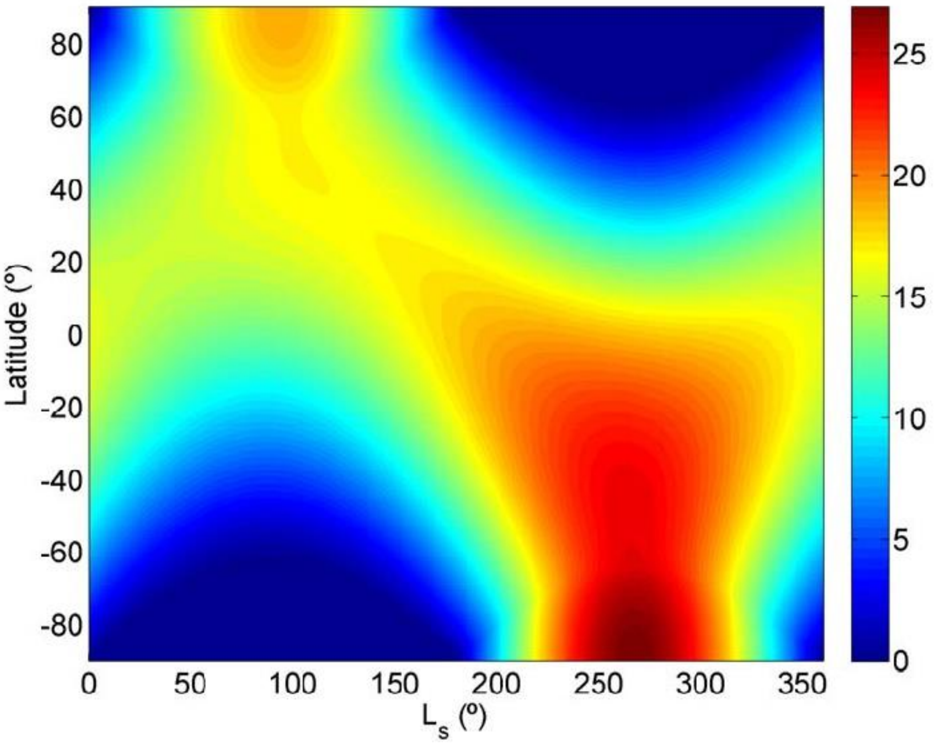

Figure 2. Temporal and spatial variability of daily irradiation (MJ/m^2) at the top of the atmosphere.

We first compare the behavior of total insolation at the Spirit, Opportunity and Curiosity landing sites, and then we analyze further details about the total, direct and diffuse components at each location. Figure 3 shows the daily irradiation at the Spirit (top), Opportunity (middle) and Curiosity (bottom) landing sites. At each site, the lowest annual values occur around the aphelion. At this time, the total insolation is slightly above 8 MJ/m^2 at the Spirit location and above 10 MJ/m^2 at the Opportunity and Curiosity landing sites. On the contrary, the highest daily irradiations occur around the perihelion, with values higher than 17 MJ/m^2 at the Spirit landing site and around 16 MJ/m^2 at the Opportunity and Curiosity locations. Since the radiation at the surface is modulated by the radiation at the top of the atmosphere, the annual amplitude in the daily irradiation is higher at the southernmost location, i.e., at the Spirit landing site. There, the total insolation around the perihelion is more than twice its value around the aphelion; in contrast, at the Opportunity and Curiosity landing sites, the highest annual values are about 60% higher than the lowest annual values.

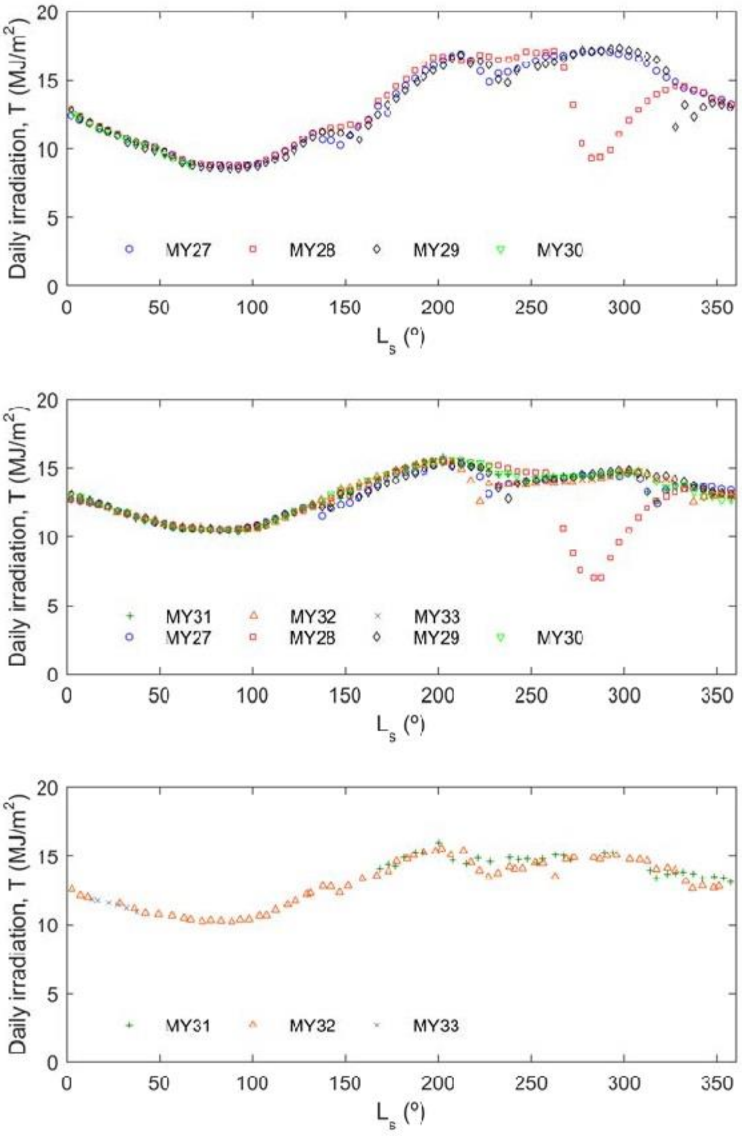

Figure 3. Total daily irradiation at the Spirit (top), Opportunity (middle) and Curiosity (bottom) landing sites.

The most striking feature is the abrupt decrease in the insolation occurred during the second Mars Year of the mission at the Spirit and Opportunity landing sites due to the major dust storm. It is possible to identify other local to regional dust storms that were observed only at one of the MER landing sites, such as the ones that caused a decrease at the Spirit location around $L_s = 155°$ and $L_s = 330°$ during MY 29.

4.1 Spirit landing site

The first panel of Figure 4 shows the ratio between the total irradiation at the surface (T) and the total irradiation at the top of the atmosphere (E) at the Spirit landing site. Except for the perihelion season on MY 28 when a major dust storm occurred, this ratio shows a low seasonal variability, with the surface receiving approximately 80% of the daily irradiation at the top of the atmosphere throughout the year.

The second panel of Figure 4 shows the diffuse daily irradiation (D) at the surface. It presents a strong seasonal variability with annual maximum values occurring during the perihelion season on each year. During the aphelion season, the diffuse irradiation is weaker because the atmosphere is relatively clear (Figure 1, top). The remarkable increase around $L_s = 150°$ is attributed to an increase in atmospheric opacity and to a decrease in the distance between Mars and the Sun. The interannual variability depends on the season, being high close to the perihelion and low close to the aphelion.

The third panel of Figure 4 shows the ratio between the direct irradiation (B) and the diffuse irradiation D. There is a clear dichotomy between the aphelion season, when the atmosphere is relatively clear and the direct component dominates, and the perihelion season, when the atmosphere is dustier and the diffuse component becomes more important than the direct irradiation. The pattern of the aphelion season is repeated every year with small variations.

4.2. Opportunity landing site

The top panel of Figure 5 shows the ratio T/E from MY 27 to MY33. As at the Spirit landing site, approximately 80% of the solar daily irradiation at the top of the atmosphere reaches the surface throughout the year. The small differences between both landing sites are explained by spatial variations in the opacity and by slightly different mean solar zenith angles due to the difference in latitude.

This typical ratio of T/E = 0.8 decreased dramatically during the dust storm occurred during the perihelion season on MY 28 (squares). During this event, the fraction of incoming solar radiation that interacted with the atmospheric aerosols increased markedly, with less than 40% of the total energy at the top of the atmosphere reaching the ground.

The values of the diffuse daily irradiation are shown in the second panel of Figure 5. The seasonal behavior is similar to that at the Spirit landing site, with the lowest annual values occurring in the aphelion season and the highest around the perihelion. However, the annual amplitude is smaller at the Opportunity landing site because it is

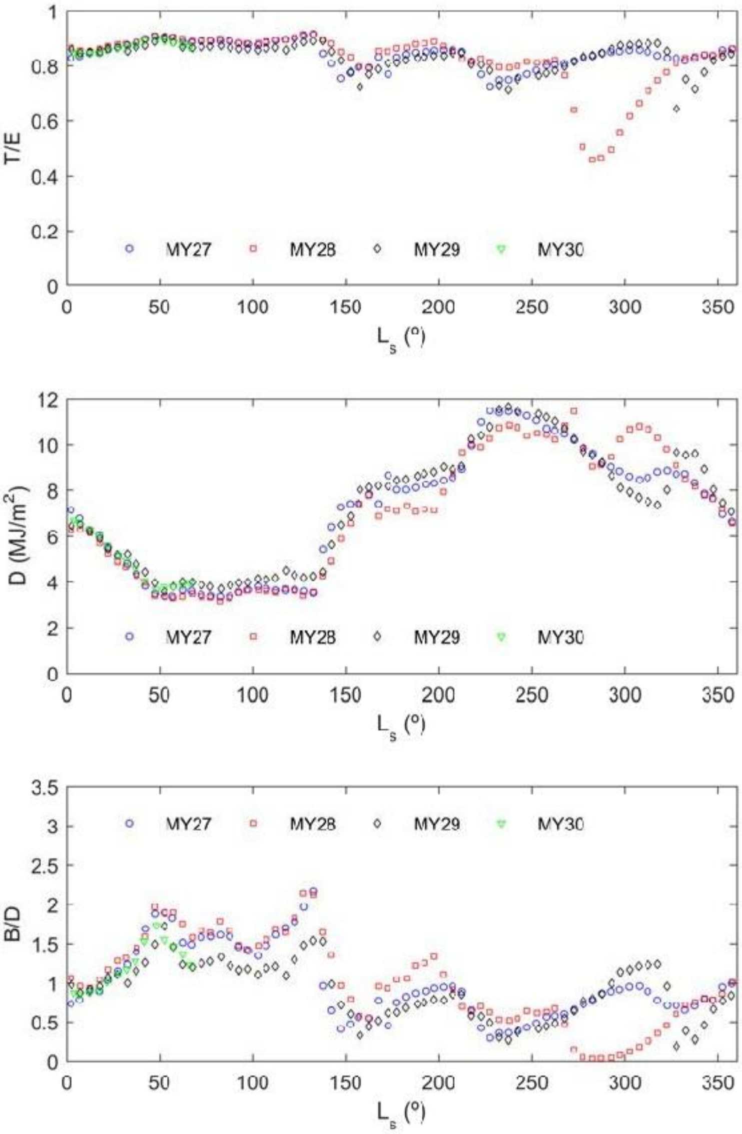

Figure 4. Ratio of total insolation at the surface (T) to that at the top of the atmosphere (E) (upper panel), diffuse daily irradiation D (middle panel), and ratio of direct (B) to diffuse (D) insolation (lower panel) at the Spirit landing site.

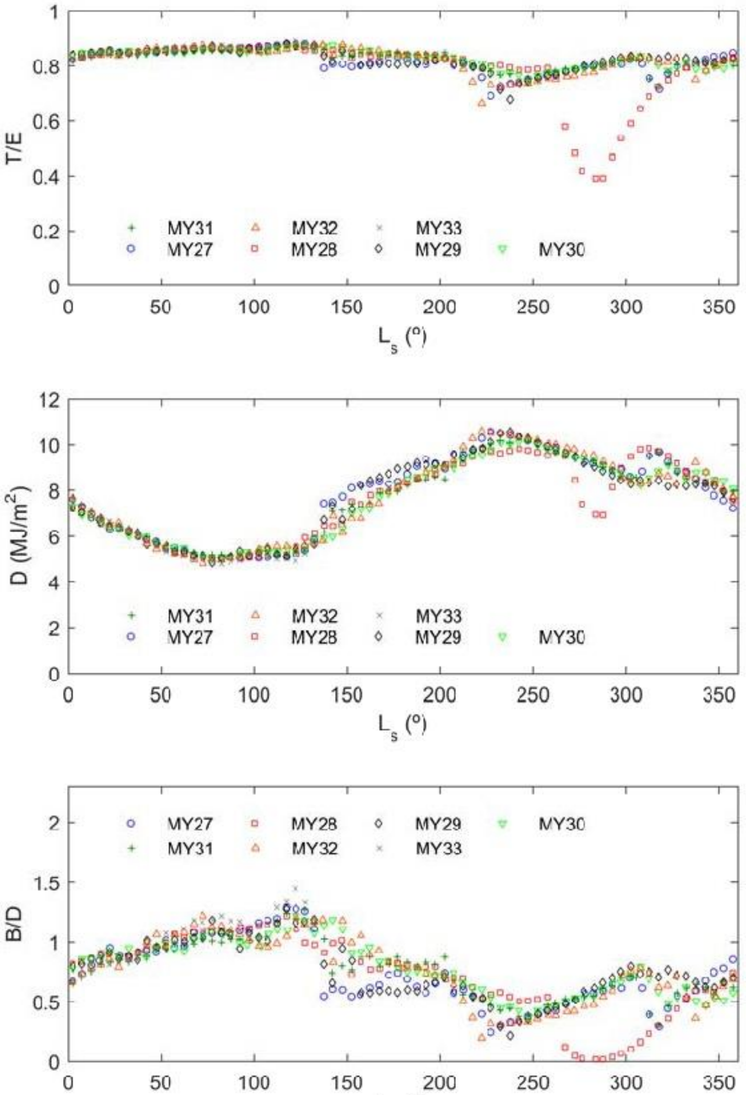

Figure 5. As in Figure 4, but for the Opportunity landing site.

closer to the equator and, therefore, the annual variability at the top of the atmosphere is lower.

Outside major dust storms, the diffuse irradiation at the surface increases with the opacity. However, the opposite behavior is observed during the major dust storm on MY 28, when a local minimum in the amount of diffuse radiation occurred because virtually all the incoming radiation interacted with atmospheric dust, and therefore the fraction of absorbed and reflected radiation by the particles increased significantly.

The ratio B/D is represented in the third panel of Figure 5. Although the qualitative behavior is similar to that at the Spirit location, there is one important difference. At the Opportunity site, this ratio is above one only during a short period of the aphelion season. This is mainly caused by higher opacities at this site (Figure 1, top and middle), which are partly affected by the aphelion cloud belt.

This panel also shows that the interannual variability is very low during the clear season, but that it increases in the perihelion season. It is interesting to notice that during the major dust storm on MY 28, there was virtually no direct radiation reaching the surface at the Mars Exploration Rovers landing sites.

4.3 Curiosity landing site

In the first panel of Figure 6 we show the seasonal evolution of the ratio T/E. This ratio varies between 0.7 during the perihelion season and 0.9 in the clear season. Since the total insolation is also smaller in the aphelion season, we conclude that there is more atmospheric heating due to suspended dust during the perihelion season. This panel also shows that MSL has not been affected by intense dust storms during MY 31 and MY 32.

The seasonal evolution of the diffuse daily irradiation is represented in the second panel of Figure 6. It shows a similar behavior to that at the Opportunity landing site. This was expected, since both latitudes are similar. In fact, the correlation coefficient between the diffuse daily irradiations at both landing sites is $R^2 = 0.94$.

The third panel of Figure 6 shows the variability of the ratio B/D. During the perihelion season, the diffuse component is always larger than the direct component, and a low interannual variability is observed. At the MSL landing site, in contrast to Opportunity, the direct irradiation is higher than the diffuse one during a large fraction of the aphelion season. This is a consequence of a smaller atmospheric opacity, which could be partially explained by a smaller influence of water ice clouds.

5. Conclusions

In this article we have used our radiative transfer model COMIMART and in-situ measurements of atmospheric opacity to characterize the radiative environment at the landing sites of the Mars Exploration Rovers (Spirit and Opportunity) and Mars Science Laboratory (Curiosity) missions.

The interannual variability of the daily irradiation at the surface of each of the three landing sites is relatively low. The exception occurred on MY 28, when a major dust storm evolved. At seasonal time scales, the variability of the daily irradiation is

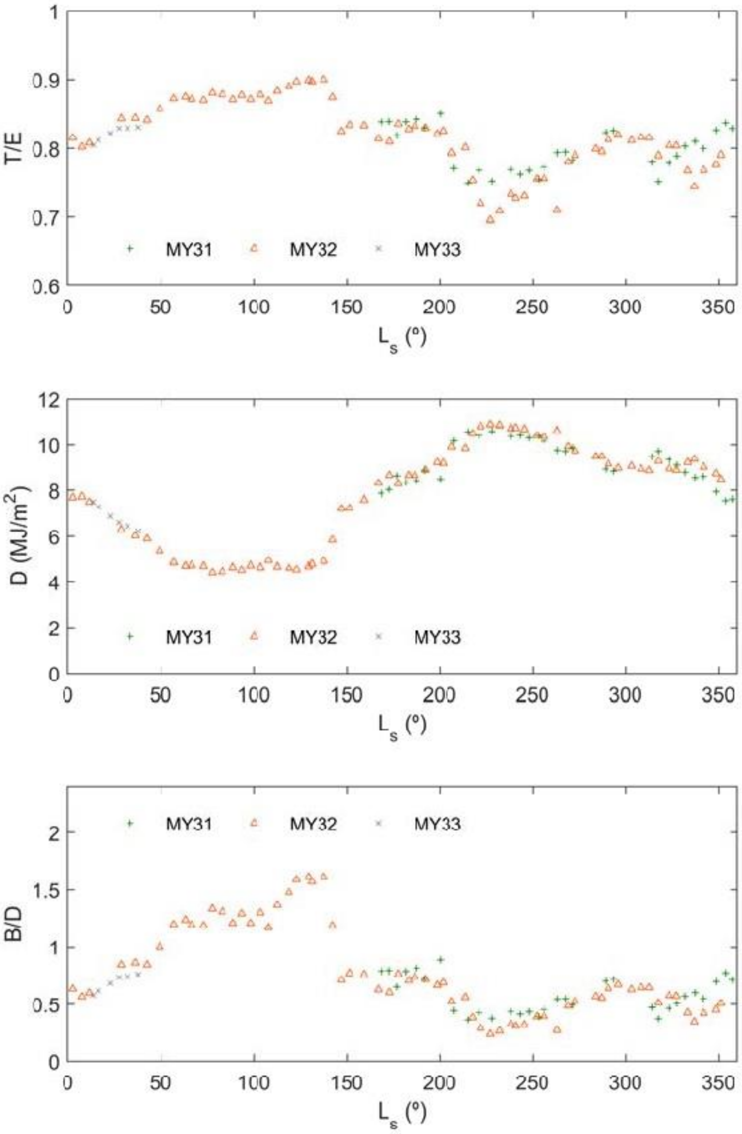

Figure 6. As in Figure 4, but for the Curiosity landing site. The reader is referred to Martínez et al. (2016; this issue) for an analysis of the ultraviolet insolation at the MSL landing site.

higher during the perihelion season, when the amount of suspended dust is usually relatively high. In contrast, the radiative environment during the aphelion season shows a very similar behavior every Martian year.

A dichotomy in the relative importance of the direct and diffuse components is observed at the three landing sites. During the aphelion season, the atmosphere is relatively clear and direct radiation prevails. In contrast, the higher amount of dust in the atmosphere during the perihelion season leads to a higher fraction of the incoming radiation being scattered, and hence the direct radiation diminishes, becoming the diffuse component more important.

Characterization of the seasonal and interannual variability of the daily irradiation at the surface is very important to prepare for future human exploration of Mars. It allows quantifying the daily doses of ultraviolet radiation and their potential effects on astronauts, which is necessary prior sending manned missions to Mars, and it also contributes to understand the thermodynamic processes of the atmosphere as well as, in longer time scales, the climate of Mars. To these ends, the solar radiation at the surface will be measured in several bands of the shortwave spectrum by the ExoMars 2020 (http://exploration.esa.int/jump.cfm?oid=56933) and Mars 2020 (Apéstigue et al. 2015) missions, complementing and expanding the solar radiation dataset derived from MER and MSL measurements.

Acknowledgements

This work has been partially supported by the research projects AYA2011-29967-C05-02 and CGL2011-25327. The author A. Vicente-Retortillo wishes to acknowledge the Spanish Ministry of Economy and Competitiveness (MINECO) for the granted FPI fellowship (BES-2012-059241).

References

APÉSTIGUE, V., ARRUEGO, I., MARTÍNEZ, J., JIMÉNEZ, J. J., RIVAS, J. et al. (2015). Radiation and Dust Sensor for MARS2020: technical design and development status overview. European Planetary Science Congress 2015, 27 September - 2 October, 2015, Nantes, France. Vol. 10, EPSC2015-813.

CLANCY, R.T., WOLFF, M. J., CHRISTENSEN, P. R. (2003). Mars aerosol studies with the MGS TES emission phase function observations: optical depths, particle sizes, and ice cloud types versus latitude and solar longitude. *J. Geophys. Res.*, 108, 5098, doi: 10.1029/2003JE002058.

COLBURN, D. S., POLLACK, J. B., HABERLE, R. M. (1989). Diurnal variations in optical depth at Mars. *Icarus*, 79 (1), 159-189, doi: 10.1016/0019-1035(89)90114-0.

CÓRDOBA-JABONERO, C., LARA, L. M., MANCHO, A. M., MÁRQUEZ, A., RODRIGO, R. (2003). Solar ultraviolet transfer in the Martian atmosphere: biological and geological implications. *Planet. Space Sci.*, 51 (6), 399–410, doi: 10.1016/S0032-0633(03)00023-0.

HANEL, R., CONRATH, B., HOVIS, W., KUNDE, V., LOWMAN, P. et al. (1972). Investigation of the Martian environment by infrared spectroscopy on Mariner 9. *Icarus,* 17, 423–42, doi: 10.1016/0019-1035(72)90009-7.

HANSEN, J.E., TRAVIS, L. D. (1974). Light scattering in planetary atmospheres. *Space Sci. Rev*., 16, 527–610.

KAHRE, M. A., MURPHY, J. R., HABERLE, R. M. (2006). Modeling the Martian dust cycle and surface dust reservoirs with the NASA Ames general circulation model. *J. Geophys. Res*.,111, E06008, doi: 10.1029/2005JE002588.

LEMMON, M. T., WOLFF, M. J., BELL III, J. F., SMITH, M. D., CANTOR, B. A., SMITH, P. H. (2015). Dust aerosol, clouds, and the atmospheric optical depth record over 5 Mars years of the Mars Exploration Rover mission. *Icarus*, 251, 96–111, doi: 10.1016/j.icarus.2014.03.029.

MADELEINE, J.-B., FORGET, F., MILLOUR, E., MONTABONE, L., WOLFF, M. J. (2011). Revisiting the radiative impact of dust on Mars using the LMD Global Climate Model. *J. Geophys. Res*., 116, E11010, doi: 10.1029/2011JE003855.

MADELEINE, J.-B., FORGET, F., MILLOUR, E., NAVARRO, T., SPIGA, A. (2012). The influence of radiatively active water ice clouds on the Martian climate. *Geophys. Res. Lett*., 39, L23202, doi: 10.1029/2012GL053564.

MARTIN, T. Z., RICHARDSON, M. I. (1993). New dust opacity mapping from Viking infrared thermal mapper data. *J. Geophys. Res*. 98:10941–49, doi: 10.1029/93JE01044.

MARTÍNEZ, G. M., VALERO, F., VÁZQUEZ, L. (2009). Characterization of the Martian surface layer. *J. Atmos. Sci*., 66 (1), 187–198, doi: 10.1175/2008JAS2765.1.

MARTÍNEZ, G. M., VALERO, F., L. VÁZQUEZ, L. (2011). The TKE budget in the convective Martian planetary boundary layer. *Q. J. R. Meteorol. Soc*., 137 (661), 2194–2208, doi: 10.1002/qj.883.

MARTÍNEZ, G. M., RENNÓ, N., FISCHER, E., BORLINA, C. S., HALLET, B. et al. (2014). Surface energy budget and thermal inertia at Gale Crater: calculations from ground-based measurements. *J. Geophys. Res. [Planets]*, 119 (8), 1822–1838, doi: 10.1002/2014JE004618.

MARTÍNEZ, G. M., DE LA TORRE, M., VICENTE-RETORTILLO, A., KEMPPINEN, O., RENNO, N., LEMMON, M. (2016). An overview of the environmental conditions at Gale Crater from MSL/REMS measurements. *Física de la Tierra*, this issue.

MONTABONE, L., FORGET, F., MILLOUR, E., WILSON, R. J., LEWIS, S. R. et al. (2015). Eight-year climatology of dust optical depth on Mars. *Icarus*, 251, 65-95, doi: 10.1016/j.icarus.2014.12.034.

PETROSYAN, A., GALPERIN, B., LARSEN, S. E., LEWIS, S. R., MÄÄTTÄNEN, A. et al. (2011). The Martian atmospheric boundary layer. *Rev. Geophys.,* 49 (3), RG3005, doi: 10.1029/2010RG000351.

RANNOU, P., PERRIER, S., BERTAUX, J. L., MONTMESSIN, F., KORABLEV, O., RÉBÉRAC, A. (2006). Dust and cloud detection at the Mars limb with UV scattered sunlight with SPICAM. *J. Geophys. Res.*, 111, E09S10, doi: 10.1029/2006JE002693.

READ, P. L., LEWIS, S. R. (2004). The Martian climate revisited: atmosphere and environment of a desert planet, Springer-Verlag, Berlin, ISBN: 978-3-540-40743-0.

SAVIJÄRVI, H., KAUHANEN, J. (2008). Surface and boundary layer modelling for the Mars Exploration Rover sites. *Q. J. R. Meteorol. Soc.*, 134 (632), 635–641, doi: 10.1002/qj.232.

SMITH, M. D. (2004). Interannual variability in TES atmospheric observations of Mars during 1999–2003. *Icarus*, 167 (1), 148–165, doi: 10.1016/j.icarus.2003.09.010.

SMITH, M. D. (2009). THEMIS observations of Mars aerosol optical depth from 2002–2008. *Icarus*, 202(2), 444-452, doi: 10.1016/j.icarus.2009.03.027.

SMITH, P. H., LEMMON, M. T. (1999). Opacity of the Martian atmosphere measured by the imager for Mars Pathfinder. *J. Geophys. Res.* 104, 8975–8985, doi: 10.1029/1998JE900017.

VICENTE-RETORTILLO, Á., VALERO, F., VÁZQUEZ, L., MARTÍNEZ, G. M. (2015). A model to calculate solar radiation fluxes on the Martian surface. *J. Space Weather Space Clim.*, 5, A33, doi: 10.1051/swsc/2015035.

WARREN, S. G. (1984). Optical constants of ice from the ultraviolet to the microwave. *Appl. Opt.*, 23 (8), 1206–1225, doi: 10.1364/AO.23.001206.

WOLFF, M. J., CLANCY, R. T. (2003). Constraints on the size of Martian aerosols from Thermal Emission Spectrometer observations. *J. Geophys. Res.*, 108, 5097, doi: 10.1029/2003JE002057.

WOLFF, M. J., SMITH, M. D., CLANCY, R. T., ARVIDSON, R., KAHRE, M., SEELOS IV, F., MURCHIE, S., SAVIJÄRVI, H. (2009). Wavelength dependence of dust aerosol single scattering albedo as observed by the Compact Reconnaissance Imaging Spectrometer. *J. Geophys. Res.*, 114, E00D04, doi: 10.1029/2009JE003350.

WOLFF, M. J., CLANCY, R. T., GOGUEN, J. D., MALIN, M. C., CANTOR, B. A. (2010). Ultraviolet dust aerosol properties as observed by MARCI. *Icarus*, 208 (1), 143–155, doi: 10.1016/j.icarus.2010.01.010.

Chapter 6. A new Monte Carlo radiative transfer model to determine dust aerosol particle size at Gale Crater

The radiative transfer model COMIMART (Chapter 4) is suitable for characterizing the radiative environment at the Martian surface because it calculates the solar radiation fluxes under a wide variety of conditions (resulting from combinations of Sun positions and atmospheric radiative properties) with high accuracy and with a small computing effort. However, as it will be shown in Chapter 7, when dealing with REMS UVS measurements, it is important to consider that:

1. The photodiodes are not necessarily facing the zenith (due to rover tilt)
2. Some regions of its field of view are blocked by the masthead and the mast of the rover (see also Figure 2.1)
3. The response of the photodiode shows a strong dependence on the solar zenith angle relative to the rover frame.

For these three reasons, the radiance becomes the important radiative quantity for the retrievals using REMS data. Radiances cannot be computed using the delta-Eddington approximation, since this approach directly integrates over the entire hemisphere. Therefore, we have developed a radiative transfer model based on the Monte Carlo method.

We have developed, in turn, different versions of the model using the Monte Carlo method. Here we describe the two main approaches, the first one being mainly oriented to flux calculations (COMIMART-MCF) and the second one being optimized for radiance calculations (COMIMART-MCR). The last section is devoted to the presentation of results obtained with the two versions of the model.

6.1. The Monte Carlo method for flux calculations (COMIMART-MCF)

Also known as statistical modeling, the Monte Carlo method allows solving a wide range of radiative transfer problems with different levels of complexity. We have developed a model adapted to the Martian atmosphere. Since we focus on REMS UV data, we do not include thermal emission, and since we analyze measurements when solar zenith angles are small, we assume a plane-parallel atmosphere.

The Monte Carlo method relies on the generation of random numbers between 0 and 1, that we will denote as ρ. Let P be the probability of a discrete random process. If the generated random number is smaller or equal to P, then we can assume that the process occurs. Due to the statistical nature of this method, the reliability of the results increases with the amount of generated numbers.

Three different processes are simulated in our radiative transfer model: The trajectories of the photons, and their interaction with the surface and with the atmosphere.

We now describe how these processes are simulated, based on the expressions provided by Melnikova et al. (2012).

The trajectory of the photon in the atmosphere is simulated in terms of the optical depth, τ^*. Let the photon be in the level τ_1^* following a direction determined by the cosine of the zenith angle μ. The photon's free path is analogous to the transfer of the direct radiation in the atmosphere and, therefore, the probability of reaching a level τ_2^* is given by Beer's law. Using the probability distribution associated to this law, the free path of the photon is simulated following the expression:

$$\tau_2^* = \tau_1^* - \mu \cdot log(1-\rho) \quad (6.1)$$

The trajectory of the photon ends when the photon escapes back to space, or when it is absorbed either by the surface or by the atmosphere.

When the photon reaches the surface, it may be absorbed or it may continue its trajectory upward. If ρ is larger than the surface albedo, the photon is absorbed. Otherwise, the optical depth, the cosine of the zenith angle and the azimuth angle after the interaction with the surface are calculated as follows:

$$\tau_2^* = \tau \quad (6.2)$$

$$\mu_2 = -\rho^{1/2} \quad (6.3)$$

$$\phi_2 = 2\pi\rho \quad (6.4)$$

where τ is the opacity of the atmosphere.

In order to simulate the interactions with the atmosphere, the single-scattering albedo of the atmosphere, ω_0, is considered. The single-scattering albedo is here interpreted as the probability of undergoing a scattering process in that interaction. If ρ is larger than ω_0, the photon is absorbed and its trajectory finishes. Otherwise, the photon is scattered, and the new direction is simulated.

The new direction is provided by the simulated values of the cosine of the scattering angle (Θ) and the scattering azimuth angle (Φ). The scattering angle is determined by the scattering phase function. For radiance calculations the phase function becomes a key parameter; however, for flux calculations the exact behavior of the phase function is not necessary and it is often represented by the Henyey-Greenstein phase function (Henyey and Greenstein, 1941), which depends on the asymmetry factor (*g*) as follows:

$$P(\Theta) = \frac{1-g^2}{2\cdot(1+g^2-2g\mu)^{\frac{3}{2}}} \quad (6.5)$$

Hence, the cosine of the scattering angle is simulated as:

$$\cos\Theta = \frac{1+g^2-\left[\frac{1-g^2}{1-g+2g\rho}\right]^2}{2g} \quad g \neq 0 \quad (6.6)$$

$$\cos\Theta = 2\rho - 1 \quad g = 0 \quad (6.7)$$

Since the considered phase functions do not show azimuthal dependence, the value of Φ is given by:

$$\Phi = 2\pi\rho \qquad (6.8)$$

Once the two scattering angles have been simulated, the new direction of the photon, characterized by the zenith and azimuth angles μ_2 and ϕ_2, can be calculated as:

$$\mu_2 = \mu_1 \cos\Theta \; - \sqrt{(1-\mu_1^2)(1-(\cos\Theta\,)^2)}\cos\Phi \qquad (6.9)$$

$$\cos(\phi_2 - \phi_1) = \frac{\cos\Theta - \mu_1\mu_2}{\sqrt{(1-\mu_1^2)(1-\mu_2^2)}} \qquad (6.10)$$

where μ_1 and ϕ_1 are the zenith and azimuth angles before the interaction.

The simulations are performed for a number of photons, N_0, that guarantees the accuracy of the results. Experiments under different conditions have been performed to find the best choice for N_0 (Vicente-Retortillo, 2015c). Here we show the results of a test experiment performed to study the accuracy and computing time of the simulations.

Figure 6.1 shows the downward (green lines) and upward (red lines) fluxes as a function of optical depth for a scenario defined by a purely absorbing atmosphere ($\omega_0 = 0$) with $\tau_0 = 0.5$ and the Sun being at the zenith ($\mu_0 = 1$). The surface below is completely reflective (A = 1), the reflectance being isotropic. Both panels show the results from ten simulations, and N_0 is 10^3 (left) and 10^5 (right).

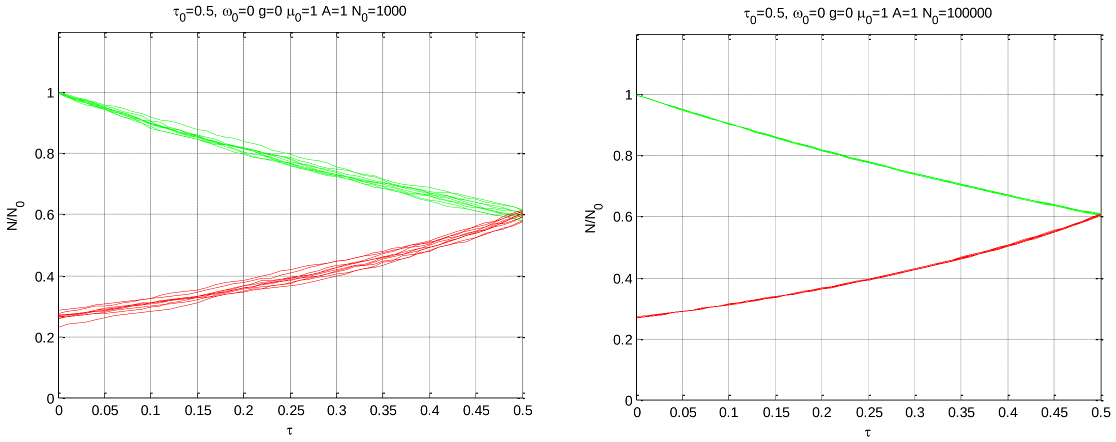

Figure 6.1. Downward (green) and upward (red) fluxes for the test case specified in the titles, with 10^3 (left) and 10^5 (right) photons.

The downward flux shows an exponential decay, in agreement with Beer's law (since scattering is absent, only the direct beam reaches the surface). The upward flux presents, as expected, a similar behavior. However, this flux undergoes a larger attenuation, i.e., the fraction of the reflected flux that reaches the TOA is smaller than the fraction of the incoming flux that reaches the surface. This is because we have assumed that the reflections are not specular but isotropic and, therefore, the mean path between the surface and the top of the atmosphere of the photons moving upward is larger than that between the top of the atmosphere and the surface of the incoming photons.

Figure 6.1 also shows that, when performing the simulations with 10^3 photons, the spread of the results is moderately large; in contrast, the spread when the simulations are performed with 10^5 photons is very small, becoming visually almost unnoticeable.

Table 6.1 shows the computing time (t) and the standard deviation (σ) of the ten simulated fluxes at the surface as a function of the number of photons for the test scenario defined above. The standard deviation is proportional to the square root of N_0, whereas the computing time is proportional to N_0 (in order to reduce the spread by one order of magnitude, it is necessary to increase the computing time by two orders of magnitude). From this table we conclude that the selection of 10^5 photons is suitable for flux calculations.

N_0	t (s)	σ (%)
10^3	0.42	2.5
10^4	4	0.79
10^5	39	0.26

Table 6.1. Computing time (t) and relative standard deviation (σ) of the 10 simulated fluxes at the surface as a function of the selected number of incoming photons (N_0) assuming the test scenario defined above.

The model COMIMART-MCF can also be used to calculate the angular distribution of the incoming photons, which is associated with the radiance. This can be performed by dividing the hemispherical surface crossed by the downwelling photons into a number of regions, and storing each photon that reaches the Martian surface in its appropriate region.

However, when a division of the sky into a large number of regions becomes necessary, such as in our calculations for the REMS UVS, a large number of photons is needed in order to acquire accurate results. As an example, let us use a 360-by-360 grid to represent the sky (which is the actual size that we have selected for our calculations). Let us assume that, as in the previous example, a 60% of the incoming photons at the top of the atmosphere reach the surface. By performing the simulations with 10^5 photons, $6 \cdot 10^4$ will reach the surface and stored in the grid. Since the grid has $360^2 \sim 1.3 \cdot 10^5$ cells, the number of photons in each cell will be generally not representative due to the high uncertainty associated with the combination of the statistical nature of the Monte Carlo method and a small sample.

To illustrate this, Figure 6.2 shows the simulated angular distribution of 10^5 incoming photons from the Sun situated at the zenith in a Rayleigh-scattering atmosphere with $\tau = 0.5$. Although visually it can provide information about the scattering properties of the atmosphere, several grids remain empty due to the small size of the sample and the results cannot satisfy the requirement of accurate calculations.

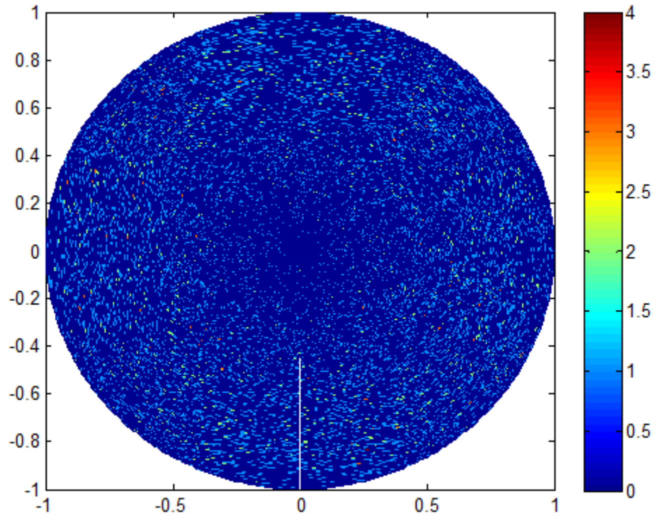

Figure 6.2. Angular distribution of incoming photons at the surface assuming an atmosphere with molecular (Rayleigh) scattering and opacity $\tau = 0.5$. The simulation is performed considering 10^5 photons, which is an insufficient amount for these simulations, since the maximum number of photons in a cell is 4 and a significant fraction of the grid is empty (color code).

Accurate radiance calculations with this Monte Carlo model require a significantly larger number of photons than flux calculations. As shown in Table 6.2, this would increase the computing cost of the simulations. For this reason, we have developed a second Monte Carlo radiative transfer model for radiance calculations, COMIMART-MCR.

N_0	t (s)
10^5	6.5
10^6	62
10^7	638

Table 6.2. Computing time (t) for simulations performed varying the number of photons (N_0).

6.2. The Monte Carlo method for radiance calculations (COMIMART-MCR)

As shown in the previous section, the developed radiative transfer model using the Monte Carlo method is suitable for flux simulations, but radiance calculations would demand significantly high computation times. We have developed a second radiative transfer model based on the Monte Carlo method, but using a different approach, which optimizes radiance calculations.

Before describing this second approach, we focus on the aerosol radiative properties that have been included in this model. The radiative properties (and especially the phase function) for different dust effective radii are required for our studies. As discussed in Chapter 2, extinction efficiencies, single-scattering albedos and scattering phase functions can be computed for different particle sizes and shapes from refractive indices. Here we have assumed that particles are cylinders characterized by having their diameter equal to their height. These parameters were chosen to retrieve the refractive indices in Wolff et al. (2009) and Wolff et al. (2010), and therefore the consistency in our calculations is optimized.

The wavelength-dependent radiative properties have been computed using the T-matrix code developed by Mischchenko and Travis (1998). In all the calculations we have assumed a power-law size distribution (Hansen and Travis, 1974; Mishchenko and Travis, 1994) with effective variance of 0.3 (Madeleine et al., 2011).

In this second approach, radiances are computed following the local estimation method (Marchuk et al., 1980; Iwabuchi, 2006). Besides simulating the new direction of each photon after each scattering event, the scattered radiation in each direction is also computed for each scattering event, optimizing the quality of the results (as an example, assuming an atmosphere that scatters in all directions, the radiance at each cell would be larger than 0 even if only one photon was considered in the simulation). We now describe the algorithm for the developed COMIMART-MCR model:

First, the dust aerosol effective radius and the relative contribution to atmospheric opacity of dust and water ice are selected. Then, the effective radiative properties of the atmosphere (opacity, single-scattering albedo and scattering phase function) are computed as:

$$\tau = \tau_d + \tau_c \qquad (6.11)$$

$$\omega_0 = \frac{\tau_d}{\tau}\omega_{0,d} + \frac{\tau_c}{\tau}\omega_{0,c} \qquad (6.12)$$

$$P = \frac{\frac{\tau_d}{\tau}\omega_{0,d}\cdot P_d + \frac{\tau_c}{\tau}\omega_{0,c}\cdot P_c}{\frac{\tau_d}{\tau}\omega_{0,d} + \frac{\tau_c}{\tau}\omega_{0,c}} \qquad (6.13)$$

where the subscripts *d* and *c* denote dust and water ice clouds, respectively.

After computing the atmospheric radiative properties, the simulation can be initialized. In order to further optimize the computing time, the photon is forced to remain in the atmosphere, that is, it cannot reach the surface and it cannot escape to space (this way no time is spent in computing the direct radiation at the surface, which can be easily computed following Beer's law). This purpose is achieved by modifying the expression of the photon's free path as follows:

$$\tau_2 = \tau_1 - \mu \cdot log\left(1 - \rho\left(1 - e^{-\left|\frac{(\tau_1 - \tau_0)}{\mu}\right|}\right)\right) \qquad \mu \geq 0 \qquad (6.14)$$

$$\tau_2 = \tau_1 - \mu \cdot log\left(1 - \rho\left(1 - e^{-\left|\frac{\tau_1}{\mu}\right|}\right)\right) \qquad \mu < 0 \qquad (6.15)$$

When simulating the interaction with the atmosphere, the weight of the photon (which is 1 at the beginning of the simulation) is multiplied by the single-scattering albedo in order to suppress the fraction of the photon absorbed in the interaction:

$$w' = w \cdot \omega_0 \qquad (6.16)$$

The surviving part of the photon is scattered in all directions, contributing to the radiance received from each cell of the defined 360-by-360 grid at the surface and its counterpart at the top of the atmosphere. The radiance at the n-th cell at the surface is computed as follows:

$$L_n = \frac{w}{2\pi} \cdot \frac{P(\Theta_n) \cdot e^{-(\tau_0 - \tau_1)/\mu_n}}{\mu_n} \quad (6.17),$$

where Θ_n is the scattering angle of the scattered radiation that reaches the n-th cell, P is the scattering phase function, τ_1 is the optical depth at which the scattering process occurs and μ_n is the zenith angle of the n-th cell.

Similarly, the radiance at the n-th cell at the TOA is calculated as:

$$L_{n,TOA} = \frac{w}{2\pi} \cdot \frac{P(\Theta_{n,TOA}) \cdot e^{-|\tau_1/\mu_{n,TOA}|}}{|\mu_{n,TOA}|} \quad (6.18)$$

The radiances at both grids are integrated to calculate the fraction of the photon that has reached the surface (w_S) or escaped back to space (w_{TOA}), and the new weight of the photon is computed as:

$$w' = w - w_s - w_{TOA} \quad (6.19),$$

where the fractions of the photons are:

$$w_s = \sum_{n=1}^{N} L_n \cdot \mu_n \cdot \Omega_n \quad (6.20)$$

$$w_{TOA} = \sum_{n=1}^{N} L_{n,TOA} \cdot \mu_{n,TOA} \cdot \Omega_{n,TOA} \quad (6.21)$$

In these expressions, Ω_n is the solid angle of the n-th cell and N is the total number of cells of each grid (360^2).

The next step is to compute the cumulative phase function to simulate the direction in which the remaining fraction of the photon is scattered. The cosine of the scattering angle is simulated by finding a generated random number between 0 and 1 (ρ, which is interpreted as the value of the cumulative phase function) in a look-up table containing the cumulative phase function as a function of the cosine of the scattering angle. The exact value of the cosine of the scattering angle is obtained by interpolation. Finally, the new direction of the surviving part of the photon is calculated following Equations (6.6) to (6.10).

The described process is repeated until the weight of the photon is below a given threshold (10^{-3} in our calculations).

This radiative transfer model has been validated by comparing the results with those using the radiative transfer model DISORT (Stamnes et al., 1988) as a reference. This validation is shown in the supporting information of Chapter 7.

6.3. Flux and radiance calculations using the Monte Carlo radiative transfer models

In this section we show examples of the simulated quantities using our two Monte Carlo schemes. We use COMIMART-MCF to compute the evolution of the downwelling and upwelling fluxes as a function of optical depth for different scenarios, and COMIMART-MCR to simulate radiances for different dust aerosol effective radii.

Figure 6.3 shows the downward and upward fluxes as a function of optical depth for two scenarios with an atmospheric opacity of 0.5. The panels represent the fluxes at 320 nm (left) and 880 nm (right). There are remarkable differences between these two scattering regimes, which are summarized in Table 6.3. The fraction of the incoming radiation absorbed in the atmosphere is roughly 7 times higher at 320 nm due to the high value of the single-scattering albedo at 880 nm, which leads to the absorption of only 2.4% of the incoming radiation at that wavelength. The fraction of incoming radiation that reaches the surface is smaller at 320 nm due to the differences in absorbed and scattered radiation. The fraction of radiation that is reflected back to space is approximately 10 times larger at 880 nm because the surface albedo is significantly larger at 880 nm than in the UV region of the spectrum. Although radiation at the surface is smaller in the UV, the fraction absorbed by the surface is larger at 320 nm due to the significantly lower value of the surface albedo.

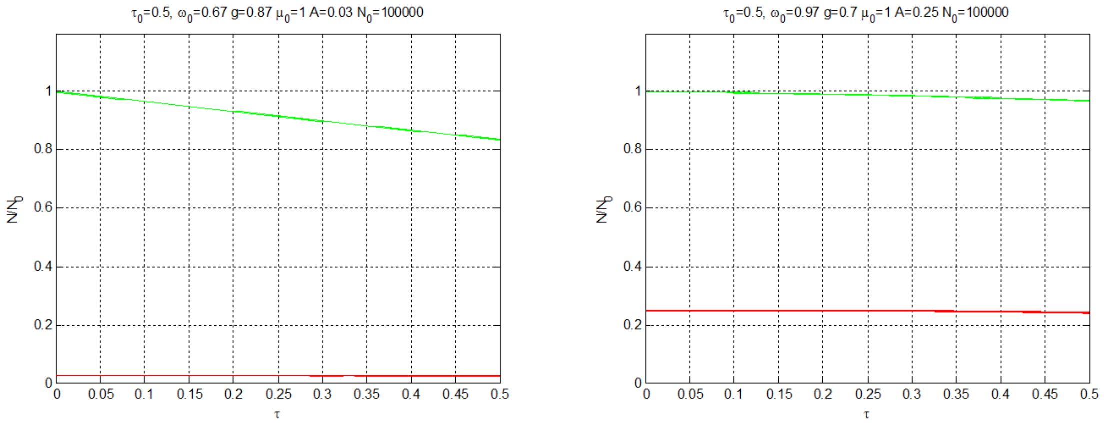

Figure 6.3. Downward (green) and upward (red) fluxes as a function of optical depth for the conditions indicated in the titles. Single-scattering albedos and asymmetry factors correspond to 320 nm (left) and 880 nm (right) assuming an effective radius of 1.5 µm.

% of incoming flux:	**320 nm**	**880 nm**
Reaching the surface	83.6	96.8
Absorbed by surface	81.1	72.7
Absorbed in the atmosphere	16.4	2.4
Reflected to space	2.5	24.9

Table 6.3. Differences between fluxes at 320 nm and 880 nm for an atmospheric opacity of 0.5 and with the Sun at the zenith.

We analyze now the main results derived from COMIMART-MCR, focusing on their applications to retrieve dust aerosol particle size at Gale Crater. Figure 6.4 shows the computed scattered radiances for four dust aerosol effective radii of the particles, assuming a typical atmospheric opacity of 0.7 and that the Sun is at the zenith. In order to make the comparison easier, only the values that are above 1% of the maximum scattered radiance are shown.

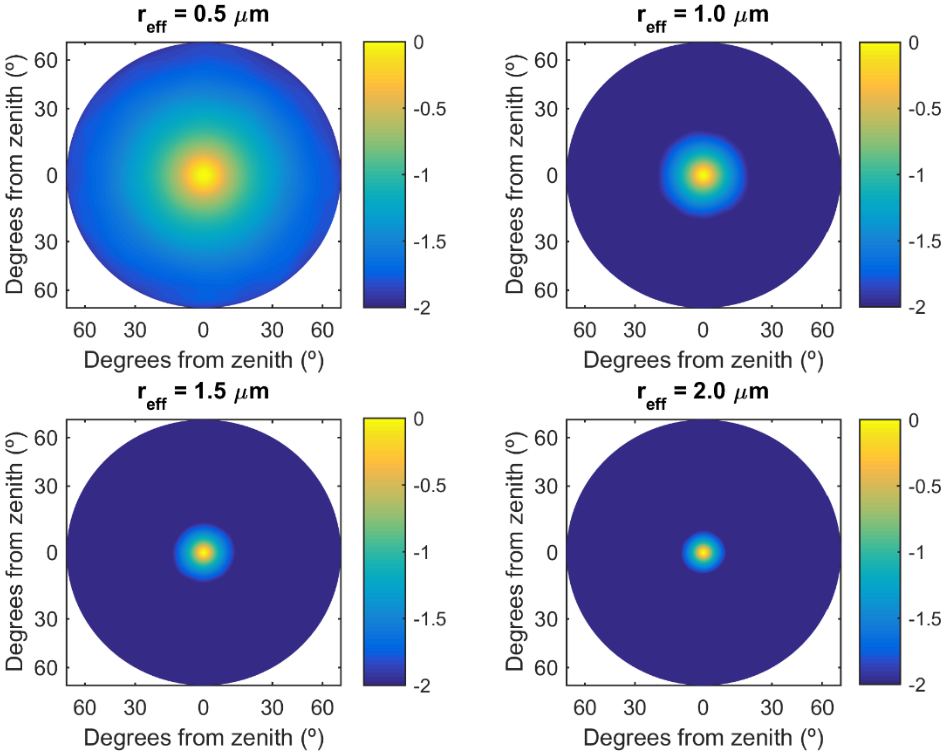

Figure 6.4. Radiances simulated with COMIMART-MCR for four different values of dust aerosol effective radius, as indicated in the titles. The radiance values are shown in logarithmic scale using color code, and are normalized by the maximum value of the scattered radiance field (for example, a value of -1 indicates that the radiance at that cell is 10^{-1} times the radiance at the cell containing the peak value). For comparison purposes, only radiances above 1% (value of -2) of the peak value are plotted, and regions where radiances are below this threshold are shown in dark blue.

The top left panel of Figure 6.4 shows that spatial variations in the scattered radiance are smooth, with reliable values at each cell at an affordable computing time of ~150 s for each scenario. By comparing it with Figure 6.2 and Table 6.2, the improvement in radiance calculations achieved with COMIMART-MCR becomes apparent: COMIMART-MCR provides radiances faster and with higher quality than COMIMART-MCF.

Figure 6.4 shows that the region in which radiances are above 1% of the maximum value decreases with increasing effective radius: for an effective radius of 0.5 µm (top left), this region covers virtually the entire hemisphere, whereas for an effective radius of 2 µm (bottom right) this region is confined within a small region very close to the solar disk. Therefore, the effective radius of the dust particles significantly affects the change in the scattered radiance as the Sun moves behind an opaque object. This effect constitutes the basis of our methodology to retrieve dust aerosol particle size at Gale Crater using REMS UVS measurements, as it will be shown in Chapter 7.

Chapter 7. Determination of dust aerosol particle size at Gale Crater using REMS UVS and Mastcam measurements

Abstract

We calculate the seasonal and interannual variation in dust aerosol particle size above Gale Crater during the first 1413 Martian solar days (sols = 24.6 h) of the Mars Science Laboratory mission. Measurements of UV radiation made by the Rover Environmental Monitoring Station in combination with atmospheric opacities retrieved from the Mastcam instrument are used for the calculations. Our results indicate that the dust effective radius varies significantly with season, ranging from ~0.6 μm during the low opacity season (Ls = 60°–140°) to ~2 μm during the high opacity season (L_s = 180°–360°). Our results suggest that Gale Crater is affected by dust events of high aerosol content originated at various distances from it. Our results improve the accuracy of estimations of ultraviolet radiation fluxes at the Martian surface. Moreover, our results have important implications because the lifetime of suspended dust and its ability to nucleate clouds are affected by particle size.

AGU PUBLICATIONS

Geophysical Research Letters

RESEARCH LETTER

10.1002/2017GL072589

Key Points:

- We have developed a novel methodology to retrieve dust aerosol particle size at Gale Crater using Mars Science Laboratory data
- The retrieved dust effective radii range from 0.6 μm during the clear aphelion season to 2 μm during the dusty perihelion season
- Our results improve the estimation of ultraviolet radiation fluxes at the Martian surface

Supporting Information:

- Supporting Information S1

Correspondence to:
Á. Vicente-Retortillo,
alvarodv@ucm.es

Citation:
Vicente-Retortillo, Á., G. M. Martínez, N. O. Renno, M. T. Lemmon, and M. de la Torre-Juárez (2017), Determination of dust aerosol particle size at Gale Crater using REMS UVS and Mastcam measurements, *Geophys. Res. Lett.*, *44*, doi:10.1002/2017GL072589.

Received 11 JAN 2017
Accepted 6 APR 2017
Accepted article online 17 APR 2017

Determination of dust aerosol particle size at Gale Crater using REMS UVS and Mastcam measurements

Álvaro Vicente-Retortillo[1,2], Germán M. Martínez[2], Nilton O. Renno[2], Mark T. Lemmon[3], and Manuel de la Torre-Juárez[4]

[1]Departamento de Física de la Tierra, Astronomía y Astrofísica II, Universidad Complutense de Madrid, Madrid, Spain, [2]Department of Climate and Space Sciences and Engineering, University of Michigan, Ann Arbor, Michigan, USA, [3]Department of Atmospheric Sciences, Texas A&M University, College Station, Texas, USA, [4]Jet Propulsion Laboratory, California Institute of Technology, Pasadena, California, USA

Abstract We calculate the seasonal and interannual variation in dust aerosol particle size above Gale Crater during the first 1413 Martian solar days (sols = 24.6 h) of the Mars Science Laboratory mission. Measurements of UV radiation made by the Rover Environmental Monitoring Station in combination with atmospheric opacities retrieved from the Mastcam instrument are used for the calculations. Our results indicate that the dust effective radius varies significantly with season, ranging from ~0.6 μm during the low opacity season ($L_s = 60°–140°$) to ~2 μm during the high opacity season ($L_s = 180°–360°$). Our results suggest that Gale Crater is affected by dust events of high aerosol content originated at various distances from it. Our results improve the accuracy of estimations of ultraviolet radiation fluxes at the Martian surface. Moreover, our results have important implications because the lifetime of suspended dust and its ability to nucleate clouds are affected by particle size.

Plain Language Summary The Martian atmosphere transports large amounts of dust, which interacts strongly with solar and infrared radiation. The large spatial and temporal variability in atmospheric dust load creates complex feedbacks connecting dust lifting with the evolving atmospheric circulations. The size of suspended aerosols affects the surface and atmospheric heating rates, influencing the Martian climate. In this work, we have calculated the dust aerosol particle size above Gale Crater during the first 1413 sols of the Mars Science Laboratory (MSL) mission using measurements of UV radiation made for the first time from the surface of Mars. Our results indicate that the dust effective radius varies significantly with season, ranging from ~0.6 μm during the clear season to ~2 μm during the dusty season. Our results suggest that Gale Crater is affected by dust events of high aerosol content originated at various distances from it. Our results are important because the lifetime of suspended dust and its ability to nucleate clouds are affected by the particle size.

1. Introduction

Dust is ubiquitous in the Martian atmosphere and interacts strongly with solar and thermal radiation [*Read and Lewis*, 2004]. In particular, dust particle size determines the ratio between the atmospheric opacity at short and long wavelengths, affecting heating rates and influencing the thermal and dynamical structure of the Martian atmosphere [*Kahre et al.*, 2008; *Madeleine et al.*, 2011; *Medvedev et al.*, 2011]. Moreover, dust particle size strongly influences atmospheric transport and gravitational settling rates [*Kahre et al.*, 2008].

The Mars Science Laboratory (MSL) Curiosity rover landed at 4.6°S and has been operating for more than two Martian years. Curiosity is equipped with environmental and remote sensing science instruments [*Grotzinger et al.*, 2012] capable of providing insight into the size of atmospheric aerosols. In particular, the Rover Environmental Monitoring Station (REMS) contains a UV sensor (UVS) that has been measuring solar radiation at the surface of Mars for the first time in six bands between 200 and 380 nm [*Gómez-Elvira et al.*, 2012], while observations from the Mast Camera (Mastcam) instrument have been used to retrieve atmospheric dust opacity from direct images of the Sun at the wavelengths of 440 and 880 nm [*Smith et al.*, 2016].

In section 2, we present a novel methodology to determine dust particle sizes using REMS/UVS measurements in combination with Mastcam retrievals of atmospheric opacity. In section 3, we show the retrieved values of the dust particle size and analyze its seasonal and interannual variability during the first 1413 sols (Martian solar days; sols = 24.6 h) of the MSL mission. In section 4, we discuss the impact of atmospheric

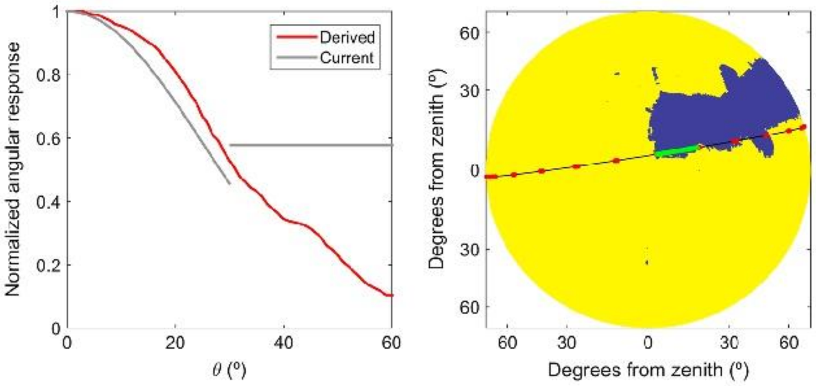

Figure 1. (left) Empirically derived angular response of the UVE channel (red line) and current angular response (gray line) used to obtain processed UV fluxes (in units of W m^{-2}) available in the NASA PDS as ENVRDR data. Our empirically derived calibration function has been obtained by iteratively calculating the ratio as a function of zenith angle between measured and simulated output currents, both normalized. The angular response that we derive is consistent with that obtained by *Smith et al.* [2016]. (right) Empirically derived field of view (FOV) of the REMS UVE channel. The region blocked by the masthead and by the mast of the rover is shown in dark blue.

circulations at Gale Crater on the relationship between atmospheric opacity and dust particle sizes. We also discuss the seasonal evolution of the UV radiation at Gale Crater and the impact of particle size on it. Finally, in section 5 we summarize the main results of our study.

2. Methodology

2.1. Data Selection

The REMS/UVS nominal strategy for data acquisition consists of 5 minutes of measurements at 1 Hz every hour, with at least an additional hour of measurements at 1 Hz during each sol [*Gómez-Elvira et al.*, 2014], while the Mastcam nominal strategy for atmospheric opacity retrievals consists of measurements made every three to seven sols [*Smith et al.*, 2016].

This study uses the photodiode output currents (stored as TELRDR products in the NASA Planetary Data System (PDS)) of the REMS/UVS UVE channel (300–350 nm), the ancillary data records (ADR) containing the geometry of the rover and the Sun, and the values of the atmospheric opacity at the reference wavelength of 880 nm retrieved from the Mastcam measurements. The UVE channel is selected for this study because it matches the 320 nm UV channel of the Mars Color Imager on board the Mars Reconnaissance Orbiter, from which the refractive indices that we use in the calculations of the radiative properties of the dust particles are obtained [*Wolff et al.*, 2010].

We use UVS TELRDR measurements conducted when the Sun is temporarily blocked by the masthead or the mast of the rover because values of the photodiode output currents depend on the dust aerosol particle size during these shadow events. As the Sun moves toward the edge of the blocked region of the field of view (FOV), the relative change in the irradiance measured by the UVS decreases with decreasing aerosol particle size. This effect is illustrated in Figure S1 (see supporting information). In order to accurately calculate the fraction of the incoming radiation that is blocked, we use only UVS TELRDR measurements made when the masthead is in its most typical position (azimuth ~ −179° and elevation ~43°).

2.2. Calculation of Radiative Properties and Radiances

Dust radiative properties, in particular single scattering albedo and scattering phase function, are key to determine radiation at the surface accurately. These two parameters depend on the refractive indices, the shape, and the size distribution of the dust particles. We calculate the single-scattering albedo and scattering phase function using a T-Matrix code [*Mishchenko and Travis*, 1998], assuming that particles are cylinders with diameter-to-length ratio $D/L = 1$ [*Wolff et al.*, 2009] that follow a power law distribution [*Hansen and Travis*, 1974; *Mishchenko and Travis*, 1994] with a typical effective variance of 0.3 [*Rannou et al.*, 2006; *Madeleine et al.*, 2011]. Next, we simulate the hemispherical UV radiance at the surface during shadow events using a Monte Carlo radiative transfer scheme. UV fluxes and radiances simulated using this scheme are in

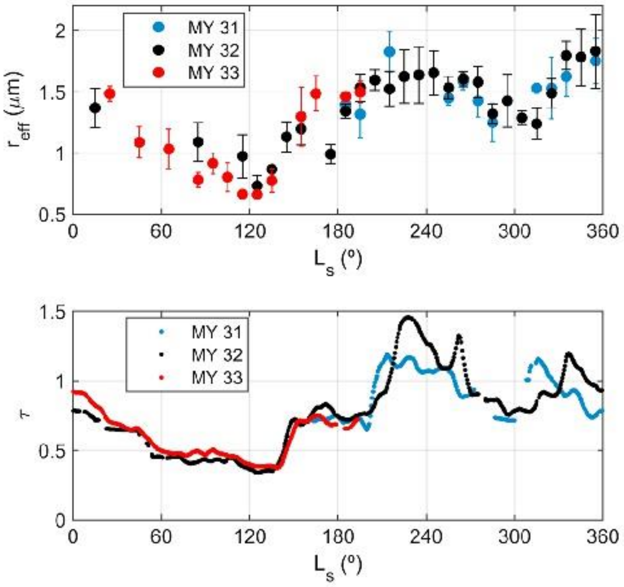

Figure 2. (top) Seasonal variability of dust aerosol particle effective radii for MY 31 (blue), 32 (black), and 33 (red). (bottom) Seasonal variability of averaged Mastcam atmospheric opacity for MY 31 (blue), 32 (black), and 33 (red).

excellent agreement with those estimated using the COMIMART and DISORT models [*Vicente-Retortillo et al.*, 2015; *Stamnes et al.*, 1988]. Details on our Monte Carlo model and its validation are provided in the supporting information (Texts S1 and S2, and Figure S2).

2.3. Simulation of the Photodiode Output Current

We calculate the photodiode output current using the simulated UV radiance and an empirical model that considers the tilt and orientation of the rover, the angular response of the photodiode as a function of the zenith angle (θ), and the region of the FOV blocked by the masthead and the mast.

The empirical angular response of the UVE channel obtained using TELRDR and ADR products is shown in Figure 1 (left). The angular response used to obtain processed UV fluxes (in units of W m^{-2}, stored as ENVRDR products in the NASA PDS) from the TELRDR products is shown for comparison. Our empirically derived calibration function differs from the one used to produce the ENVRDR products. Thus, for physical consistency, we use the photodiode output currents (TELRDR products) and the empirical angular response in our calculations instead of the processed UV fluxes (ENVRDR products).

The empirically derived blocked region of the FOV is shown in Figure 1 (right). The black line represents the trajectory of the Sun across the FOV on sol 1362, the red dots represent REMS measurement sessions, and the green dots represent the selected shadow event.

2.4. Particle Size Retrieval

We use UVS TELRDR measurements covering the full duration of each shadow event. For each of these measurements, we simulate the output currents (S) as a function of the effective radius as

$$S = \sum_{i=1}^{N} L_i \cdot \mu_i \cdot R_i \cdot F_i \cdot \Omega_i,$$

where L is the simulated radiance, μ is the cosine of the zenith angle, R is the value of the normalized angular response, F indicates whether the incoming radiance is blocked ($F = 0$) or not ($F = 1$), Ω is the solid angle, and i denotes each of the $N = 360^2$ grid cells separated by 0.25° in zenith angle and by 1° in azimuth. The computed radiances are stored in a 5-D lookup table as a function of opacity, solar zenith angle, and dust aerosol effective radius.

Then, the ratios between the output currents as the Sun moves toward the edge of the blocked region of the FOV, simulated as a function of the dust aerosol effective radius, are calculated. From these simulated ratios, we determine the radii that best match the measured ratios. Finally, for each solar longitude (L_s) and Martian year, we calculate the mean and the standard deviation of the corresponding retrieved radii. Error bars in Figures 2 and 3 represent these standard deviations.

Our estimations of the dust aerosol effective radii are robust to changes in dust opacity. To illustrate this, we select sol 1362 (when the atmospheric opacity (τ) was ~0.7 and the dust particle size that we retrieve is slightly above 1.5 μm). Table 1 shows that when $r_{eff} = 1.5$ μm, underestimated and overestimated opacities of 0.5 and 1.0 lead to departures of only -0.4% and 4% in the simulated ratio with respect to the

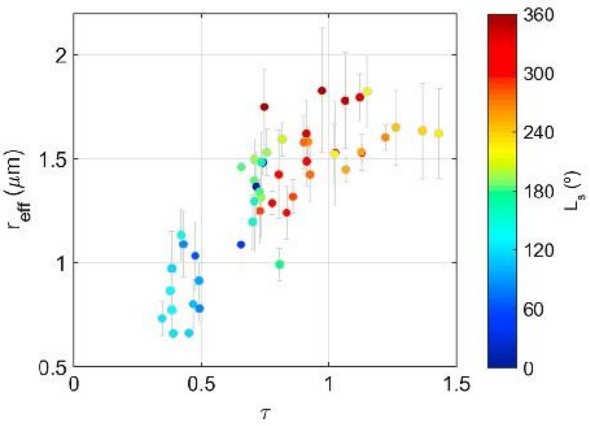

Figure 3. Dust aerosol particle size at the MSL landing site as a function of atmospheric opacity (τ) and solar longitude (L_s).

observed ratio, which in turn result in changes of the retrieved effective radii of only −4% and 6%, respectively (not shown in the table). Discrepancies between observed and simulated ratios are significantly larger for the other considered radii, showing that the ratio between output currents during a shadow event is a suitable parameter to retrieve dust particle sizes (section 2.1). Further evidence of the strong dependence of observed ratios on the dust particle size is given in the supporting information (Figure S3).

In this study, we have not considered the contribution of water ice clouds to atmospheric opacity. However, the impact of clouds on the retrieved value of dust particle sizes is generally small. As an example, we select a shadow event on sol 1280, when the total atmospheric opacity is around the annual minimum (L_s = 122°) and the water ice contribution to opacity is expected to be maximum [*Smith*, 2004]. Assuming that the fraction of opacity contributed by ice is 10%, 20%, 30%, and 40%, we obtain increases in the retrieved effective radius below 3%, 9%, 18%, and 28%, respectively. In Gale Crater, this fraction is typically below 20% except during the low opacity season (especially around $L_s \sim$ 120°), when it can be in the range 30–40% [*McConnochie et al.*, 2015]. The water ice radiative properties were determined using the refractive indices given by *Warren* [1984], assuming spherical particles with a size distribution characterized by an effective radius of 3 μm [*Wolff and Clancy*, 2003] and an effective variance of 0.1 [*Wolff and Clancy*, 2003; *Madeleine et al.*, 2012].

Other sources of uncertainties include simulated radiances (which are mainly affected by the scattering phase function) and the empirically derived angular response. These and other sources of uncertainty are explained in detail in the supporting information (Text S3).

3. Results

The seasonal and interannual variability of the dust particle effective radius is shown in Figure 2 (top) as a function of L_s for MY 31 (blue), MY 32 (black), and MY 33 (red). Mastcam dust opacity values obtained using a running mean of 10 sols are shown in Figure 2 (bottom) for comparison.

Dust particle size shows a significant seasonal variability, with values of the effective radius ranging from ~0.6 to ~2 μm. During the aphelion season (L_s = 0°–180°), the dust particle size is relatively small, with an annual minimum of ~0.6 μm at $L_s \sim$ 125°, coinciding with the lowest annual values of atmospheric opacity. During the perihelion season (L_s = 180°–360°), the dust particle size is significantly larger with two relative maxima associated with periods of enhanced dust activity between L_s = 210°–270° and L_s = 310°–350°, and one relative minimum coinciding with a local minimum in the atmospheric opacity at $L_s \sim$ 300°.

Table 1. Discrepancy (%) Between Simulated and Observed UVS TELRDR Ratios During a Shadow Event on Sol 1362 as a Function of Atmospheric Opacity (τ) and Dust Effective Radius (r_{eff})[a]

		r_{eff} (μm)			
		0.5	1.0	1.5	2.0
τ	0.1	28.5	11.8	*−3.8*	−19.8
	0.5	28.2	14.2	*−0.4*	−15.8
	1.0	27.7	15.6	*4.0*	−11.4
	1.5	26.0	17.0	*6.8*	−7.6

[a] On this sol, the opacity is ~0.7 and the retrieved dust particle effective radius is slightly above 1.5 μm.

From an interannual perspective, the seasonal cycle of the dust aerosol particle size is similar from MY

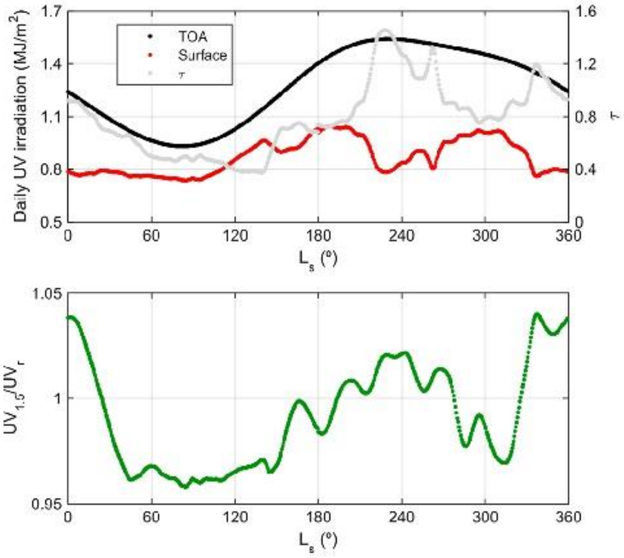

Figure 4. (top) Daily UV irradiation at the TOA (black) and at the surface (red) of Gale Crater calculated using Mastcam opacities (gray) and the retrieved effective radii during the perihelion season of MY 32 and the aphelion season of MY 33 shown in Figure 2. (bottom) Ratio between the daily UV irradiation assuming $r_{\mathrm{eff}} = 1.5$ μm and the one using the retrieved radii.

31 to MY 33, although some differences exist. On one hand, dust effective radii during the low opacity season (L_s = 60°–140°) in MY 33 are lower than in MY 32 (Figure 2, top). These differences could result from the combination of smaller dust particles and a larger contribution of water ice clouds to the total atmospheric opacity during the aphelion season of MY 33, as the increase in water ice cloud fraction leads to an underestimation of the retrieved radii due to the changes in the aerosol radiative properties that are not being considered (section 2.4). On the other hand, observed differences between MY 31 and 32 during the perihelion season are associated with interannual variability in the events of enhanced opacity (Figure 2, bottom).

Our results are consistent with those obtained for the Mars Exploration Rovers (MER) Spirit and Opportunity landing sites. At both MER locations, particle sizes were found to range from 0.7 to 2.1 μm, with the lowest values occurring during the low atmospheric opacity season, and the largest values generally occurring when the opacity peaks [*Lemmon et al.*, 2015].

4. Discussion

4.1. Implications of Atmospheric Circulations on the Correlation Between Opacity and Dust Particle Size

Figure 3 shows the retrieved effective radii as a function of atmospheric opacity measured by Mastcam, with color code indicating L_s. The correlation between the two variables is apparent (R^2 = 0.67), especially during the aphelion season, when $\tau < 1$. This behavior is physically consistent because dust particles are expected to be smaller during the low atmospheric opacity season because larger particles lifted during dust events settle more rapidly than the smallest particles.

The lack of a clear correlation between atmospheric opacity and dust particle size during the perihelion season (when $\tau > 1$) suggests that Gale Crater is affected by dust events originated at various distances from the observation site (likely outside Gale Crater). The larger particle radii and smaller opacity of the events represented by the brown points suggest that they are associated with dust events originated closer to Gale Crater than the higher opacity and lower radii events represented by yellow-orange points because larger particles are expected to be deposited more rapidly during transport (smaller particles remain suspended for longer periods of time). This is further supported by strong and persistent northerly and northwesterly winds at Gale Crater during the perihelion season centered around L_s = 270° [*Rafkin et al.*, 2016]. The lack of correlation between atmospheric opacity and dust particle size at high opacity values has also been observed at the MER sites [*Lemmon et al.*, 2015].

4.2. Implications of Dust Particle Size on the UV Environment

Quantification of the UV radiation at the Martian surface is important for assessing the habitability of the planet [*Córdoba-Jabonero et al.*, 2003]. The daily UV irradiation (defined as the total amount of solar energy received during 1 sol from the ultraviolet region of the spectrum) is of particular interest because of its effects on microorganisms [*Cockell and Raven*, 2004] and the correlation that appears to exist with variations in background methane concentrations measured at the MSL landing site [*Webster et al.*, 2016]. The daily UV irradiation is controlled by the seasonal evolution of the solar radiation at the top of the atmosphere (TOA) and by the radiative properties of the atmosphere, in which dust particle size plays an important role.

Figure 4 (top) shows the seasonal evolution of the daily UV irradiation at the TOA and at the surface of Gale Crater, along with opacity values retrieved from Mastcam. To calculate the daily UV irradiation at the surface, we use the COMIMART radiative transfer model [*Vicente-Retortillo et al.*, 2015] with retrieved Mastcam opacities at 880 nm and calculated dust particle effective radii shown in Figure 2 as inputs. In this model, these opacities are scaled to UV wavelengths using the ratio of the computed extinction efficiencies, calculated using the refractive indices obtained by *Wolff et al.* [2009] and *Wolff et al.* [2010], and which in turn depend on the retrieved effective radii. We consider the perihelion season of MY 32 and the aphelion season of MY 33 to cover one full Martian year. The highest values of the UV irradiation at the surface are found at $L_s \sim 185°–200°$ and $L_s \sim 295°–310°$, when the UV irradiation at the TOA is relatively high and the atmospheric opacities are the lowest of the dusty season. The lowest annual values occur between $L_s = 0°$ and 100°, when the radiation at the TOA is relatively low and its decrease toward the annual minimum is partially compensated by the decrease in opacity. Minimum values also occur at $L_s \sim 230°$, when the irradiation at the TOA is close to the maximum but the atmospheric opacity shows the highest annual values, and at $L_s \sim 335°$, when the second maximum in atmospheric opacity occurs.

In order to illustrate the impact of considering a variable particle size on the calculations of the ultraviolet radiation at the Martian surface, we show in Figure 4 (bottom) the ratio between the daily UV irradiation at the surface assuming a constant effective radius of 1.5 μm and that assuming a time-dependent size as shown in Figure 2. When the fixed effective radius of 1.5 μm is assumed, daily UV irradiations are underestimated during the low opacity season ($L_s = 60° – 140°$) and around the local minimum in opacity and effective radius at $L_s \sim 300°$, while they are overestimated during the periods of enhanced opacity ($L_s = 210°–270°$ and $L_s \sim 335°$), when particles are larger.

5. Conclusions

We have developed a novel methodology to calculate dust aerosol particle size at Gale Crater and analyzed its temporal variability during the first 1413 sols of the MSL mission. We have used measurements of UV radiation acquired at the Martian surface for the first time by the REMS UVS and atmospheric opacity values retrieved from the Mastcam instrument.

Dust aerosol particle size shows a significant seasonal variability, with effective radii ranging from ~0.6 to ~2 μm. The lowest values are found during the low opacity season, whereas the highest ones are typically associated with events of enhanced dust content. From an interannual perspective, the general behavior of the particle size evolution in MY 31–32 is similar to that in MY 32–33. During the low opacity season ($L_s = 60°–140°$) in MY 33, the retrieved dust effective radii are significantly lower than in MY 32. A larger contribution of water ice clouds to the total atmospheric opacity during the aphelion season of MY 33, which we have not considered in our calculations of the effective radii, can partially explain such a departure.

The correlation between atmospheric opacity and dust aerosol particle size is apparent during the aphelion season, when the atmospheric opacity is low. The lack of a clear correlation between both quantities during the perihelion dusty season suggests that Gale Crater is affected by dust events originating at various distances from the rover site.

The determination of dust aerosol particle size is important because it leads to improvements in the accuracy of calculations of the UV environment at the surface and aerosol atmospheric transport, including gravitational settling rates. In addition, it leads to improvements in predictions of atmospheric heating rates, which affect the atmospheric thermal and dynamical fields.

Acknowledgments
This study has been partially supported by the research projects AYA2011-29967-C05-02 and CGL2011-25327, funded by the Spanish Ministry of Economy and Competitiveness, and by JPL grant number 1449038. Also, the author A. Vicente-Retortillo wishes to acknowledge the Ministry FPI Scholarship (BES-2012-059241) for the financial support and training. N.O. Renno acknowledges the support from the National Science Foundation via Award AGS 1526444. REMS TELRDR and ADR products can be found in the NASA PDS (http://atmos.nmsu.edu/PDS/data/mslrem_1001/DATA/).

References

Cockell, C. S., and J. A. Raven (2004), Zones of photosynthetic potential on Mars and the early Earth, *Icarus*, *169*, 300–310, doi:10.1016/j.icarus.2003.12.024.

Córdoba-Jabonero, C., L. M. Lara, A. M. Mancho, A. Márquez, and R. Rodrigo (2003), Solar ultraviolet transfer in the Martian atmosphere: Biological and geological implications, *Planet. Space Sci.*, *51*, 399–410, doi:10.1016/S0032-0633(03)00023-0.

Gómez-Elvira, J., et al. (2012), REMS: The environmental sensor suite for the Mars Science Laboratory rover, *Space Sci. Rev.*, *170*, 583–640, doi:10.1007/s11214-012-9921-1.

Gómez-Elvira, J., et al. (2014), Curiosity's rover environmental monitoring station: Overview of the first 100 sols, *J. Geophys. Res. Planets*, *119*, 1680–1688, doi:10.1002/2013JE004576.

Grotzinger, J. P., et al. (2012), Mars Science Laboratory mission and science investigation, *Space Sci. Rev.*, *170*, 5–56, doi:10.1007/s11214-012-9892-2.

Hansen, J. E., and L. D. Travis (1974), Light scattering in planetary atmospheres, *Space Sci. Rev.*, *16*, 527–610.

Kahre, M. A., J. L. Hollinsworth, R. M. Haberle, and J. R. Murphy (2008), Investigations of the variability of dust particle sizes in the Martian atmosphere using the NASA Ames general circulation model, *Icarus*, *195*, 576–597, doi:10.1016/j.icarus.2008.01.023.

Lemmon, M. T., M. J. Wolff, J. F. Bell III, M. D. Smith, B. A. Cantor, and P. H. Smith (2015), Dust aerosol, clouds, and the atmospheric optical depth record over 5 Mars years of the Mars exploration rover mission, *Icarus*, *251*, 96–111, doi:10.1016/j.icarus.2014.03.029.

Madeleine, J.-B., F. Forget, E. Millour, L. Montabone, and M. J. Wolff (2011), Revisiting the radiative impact of dust on Mars using the LMD global climate model. *J. Geophys. Res.*, *116*, E11010, doi:10.1029/2011JE003855.

Madeleine, J.-B., F. Forget, E. Millour, T. Navarro, and A. Spiga (2012), The influence of radiatively active water ice clouds on the Martian climate, *Geophys. Res. Lett.*, *39*, L23202, doi:10.1029/2012GL053564.

McConnochie, T. H., et al. (2015), ChemCam passive sky spectroscopy at Gale Crater: Diurnal and seasonal cycles of O_2, H_2O, and aerosols, presented at 2015 AGU Fall Meeting, San Francisco, Calif.

Medvedev, A. S., T. Kuroda, and P. Hartogh (2011), Influence of dust on the dynamics of the Martian atmosphere above the first scale height, *Aeolian Res.*, *3*(2), 145–156, doi:10.1016/j.aeolia.2011.05.001.

Mishchenko, M. I., and L. D. Travis (1994), Light scattering by polydispersions of randomly oriented spheroids with sizes comparable to wavelengths of observation, *Appl. Opt.*, *33*, 7206–7225, doi:10.1364/AO.33.007206.

Mishchenko, M. I., and L. D. Travis (1998), Capabilities and limitations of a current FORTRAN implementation of the T-matrix method for randomly oriented, rotationally symmetric scatterers, *J. Quant. Spectrosc. Radiat. Transfer*, *60*, 309–324.

Rafkin, S. C. R., J. Pla-Garcia, M. Kahre, J. Gomez-Elvira, V. E. Hamilton, M. Marín, S. Navarro, J. Torres, and A. Vasavada (2016), The meteorology of Gale Crater as determined from rover environmental monitoring station observations and numerical modeling. Part II: Interpretation, *Icarus*, *280*, 114–138, doi:10.1016/j.icarus.2016.01.031.

Rannou, P., S. Perrier, J. L. Bertaux, F. Montmessin, O. Korablev, and A. Rébérac (2006), Dust and cloud detection at the Mars limb with UV scattered sunlight with SPICAM, *J. Geophys. Res.*, *111*, E09S10, doi:10.1029/2006JE002693.

Read, P. L., and S. R. Lewis (2004), *The Martian Climate Revisited: Atmosphere and Environment of a Desert Planet*, 326 pp., Springer-Verlag, Berlin.

Smith, M. D. (2004), Interannual variability in TES atmospheric observations of Mars during 1999–2003, *Icarus*, *167*, 148–165, doi:10.1016/j.icarus.2003.09.010.

Smith, M. D., M.-P. Zorzano, M. Lemmon, J. Martín-Torres, and T. Mendaza de Cal (2016), Aerosol optical depth as observed by the Mars Science Laboratory REMS UV photodiodes, *Icarus*, *280*, 234–248, doi:10.1016/j.icarus.2016.07.012.

Stamnes, K., S. C. Tsay, W. Wiscombe, and K. Jayaweera (1988), Numerically stable algorithm for discrete-ordinate-method radiative transfer in multiple scattering and emitting layered media, *Appl. Opt.*, *27*, 2502–2509, doi:10.1364/AO.27.002502.

Vicente-Retortillo, A., F. Valero, L. Vázquez and G. M. Martínez (2015), A model to calculate solar radiation fluxes on the Martian surface, *J. Space Weather Space Clim.*, *5*, A33, doi:10.1051/swsc/2015035.

Warren, S. G. (1984), Optical constants of ice from the ultraviolet to the microwave, *Appl. Opt.*, *23*, 1206–1225, doi:10.1364/AO.23.001206.

Webster, C. R., P. R. Mahaffy, S. K. Atreya, and the SAM Science Team (2016), Low background levels of Mars methane at gale crater indicate seasonal cycle: Updated results from TLS-SAM on Curiosity, presented at 2016 AGU Fall Meeting, San Francisco, Calif.

Wolff, M. J., and R. T. Clancy (2003), Constraints on the size of Martian aerosols from thermal emission spectrometer observations, *J. Geophys. Res.*, *108*(E9), 5097, doi:10.1029/2003JE002057.

Wolff, M. J., M. D. Smith, R. T. Clancy, R. Arvidson, M. Kahre, F. Seelos IV, S. Murchie, and H. Savijärvi (2009), Wavelength dependence of dust aerosol single scattering albedo as observed by the compact reconnaissance imaging spectrometer, *J. Geophys. Res.*, *114*, E00D04, doi:10.1029/2009JE003350.

Wolff, M. J., R. T. Clancy, J. D. Goguen, M. C. Malin, and B. A. Cantor (2010), Ultraviolet dust aerosol properties as observed by MARCI, *Icarus*, *208*, 143–155, doi:10.1016/j.icarus.2010.01.010.

Geophysical Research Letters

Supporting Information for

Determination of dust aerosol particle size at Gale Crater using REMS UVS and Mastcam measurements

Álvaro Vicente-Retortillo[1,2], Germán M. Martínez[2], Nilton O. Renno[2], Mark T. Lemmon[3] and Manuel de la Torre-Juárez[4]

[1]Departamento de Física de la Tierra, Astronomía y Astrofísica II, Universidad Complutense de Madrid, Madrid, Spain

[2]Department of Climate and Space Sciences and Engineering, University of Michigan, Ann Arbor, Michigan, USA.

[3]Department of Atmospheric Sciences, Texas A&M University, College Station, Texas, USA

[4]Jet Propulsion Laboratory, California Institute of Technology, Pasadena, California, USA.

Contents of this file

Figures S1 to S3

Texts S1 to S3

Introduction

This supporting information consists of three text segments and three figures to illustrate our methodology to retrieve dust aerosol particle size (Figure S1), to describe our Monte-Carlo radiative transfer model (Text S1), to validate our Monte-Carlo radiative transfer model (Text S2 and Figure S2), to show further evidence of the seasonal variability of dust aerosol particle size (Figure S3) and to list the sources of uncertainties in our results (Text S3).

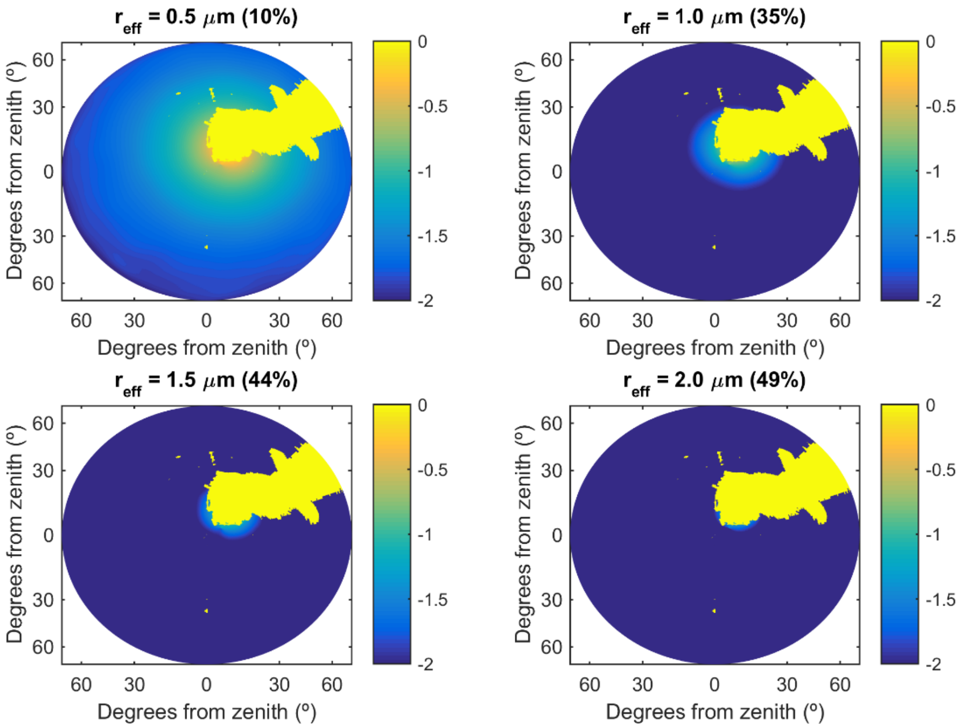

Figure S1. Simulated radiances at 11:29:06 LMST (central point of a shadow event) on sol 775 of the MSL mission considering the empirically derived field of view of the REMS UVE channel for four different values of dust aerosol effective radius. The radiance values are shown in logarithmic scale using color code, and are normalized by the maximum value of the scattered radiance field (for example, a value of -1 indicates that the radiance at that cell is 10^{-1} times the radiance at the cell containing the peak value). For comparison purposes, only radiances above 1% (value of -2) of the peak value are plotted, and regions where radiances are below this threshold are shown in dark blue. The blocked region of the FOV is shown in yellow. The region in which radiances are above 1% of the maximum value decreases with increasing effective radius: for an effective radius of 0.5 µm (top left), this region covers virtually the entire hemisphere, whereas for an effective radius of 2 µm (bottom right) this region is virtually confined within the blocked region of the FOV. Thus, the relative increase in the blocked fraction of scattered radiation with respect to the situation at the limit of the shadow event (when the Sun is very close to the edge of the blocked region of the FOV) increases significantly with effective radius, as quantified in parenthesis in the title of each panel (from 10% with r_{eff} = 0.5 µm to 49% with r_{eff} = 2 µm).

Text S1. The Monte Carlo radiative transfer model: Description

Solar fluxes on the Martian surface can be directly simulated with modest computational effort using radiative transfer models which, despite their relative simplicity, can provide accurate results [*Vicente-Retortillo et al.*, 2015]. However, since the incoming radiation that is blocked by the masthead and the mast of the rover as a function of particle size is the key quantity in our study, a model capable of calculating radiances is needed. This is why we use our Monte-Carlo radiative transfer model, which calculates radiances by simulating photons' trajectories as a function of optical depth. Since these trajectories are not simulated as a function of height, knowledge of the dust vertical profile is not necessary. Aerosols are assumed to be well mixed, with no variations in single-scattering albedo and phase function as a function of optical depth. At each scattering event, a fraction of the photons (which depends on the single-scattering albedo) is absorbed, and then photons are fractionated and scattered in all directions, and these fractions are calculated according to the selected phase function. After performing the simulations, radiances at the surface are stored in lookup tables as a function of opacity, dust effective radius and solar zenith angle (see Section 2).

Text S2. The Monte Carlo radiative transfer model: Validation

We have calculated radiances under six scenarios using our Monte Carlo model and DISORT [*Stamnes et al.*, 1988]. Each scenario is defined by selecting a value of dust opacity (0.5, 1 or 1.5), along with a single-scattering albedo and a phase function with asymmetry factor corresponding to dust effective particle radii of 1.5 or 1 µm. We have compared the radiances obtained with the two models for each scenario as a function of zenith angle, concluding that they are in excellent agreement. Among the three selected opacities, the largest mean relative departures were found for $\tau = 1$. For the two scenarios with $\tau = 1$, mean relative departures of 1.4% when $r_{eff} = 1.5$ µm and of 0.95% when $r_{eff} = 1$ µm are obtained after averaging the absolute values of the relative departures of the radiances within 20º of the solar disk as a function of zenith angle.

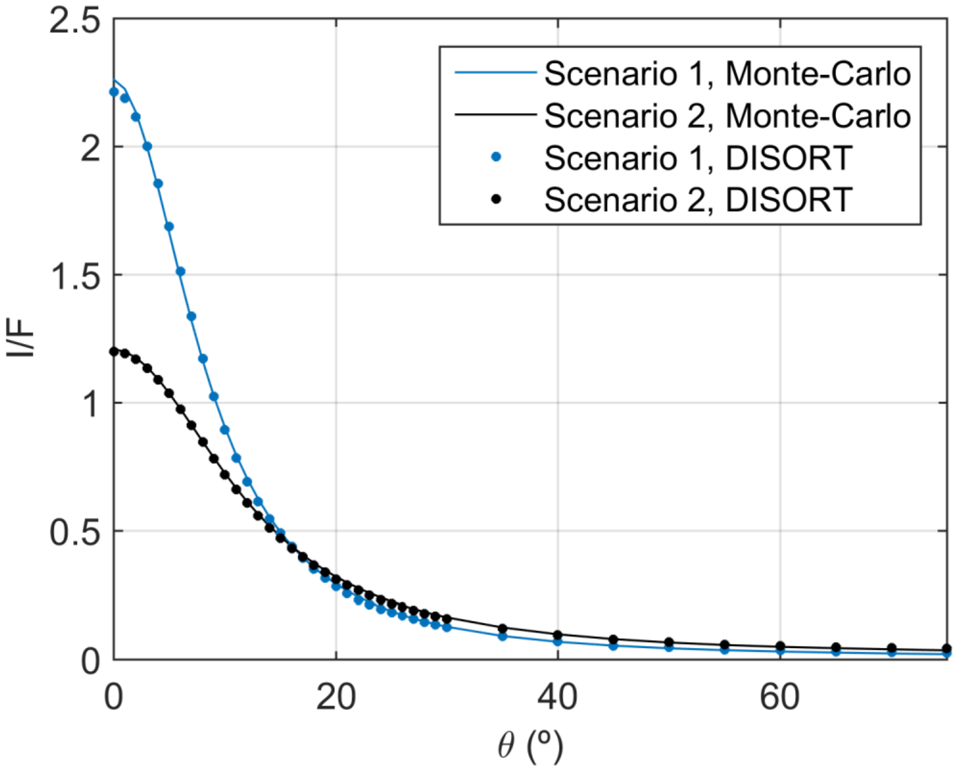

Figure S2. Intensities normalized by the total flux as a function of zenith angle when $\tau = 1$ and $r_{eff} = 1.5$ µm (scenario 1, blue) and when $\tau = 1$ and $r_{eff} = 1$ µm (scenario 2, black), using our Monte Carlo model (solid lines) and DISORT (circles). The agreement between the two models is excellent.

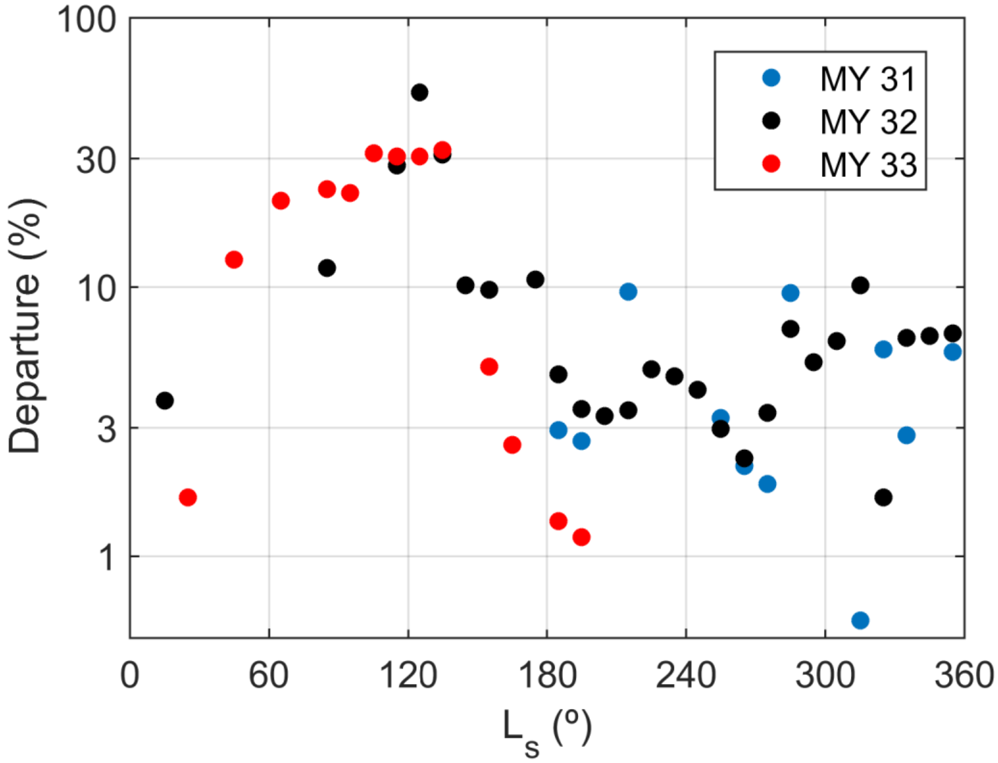

Figure S3. Departures of observed ratios between output currents during shadow events from ratios simulated assuming a constant effective radius of 1.5 μm. Colors as in Figure 2. Departures below 3% are found at solar longitudes when the effective radius is close to 1.5 μm (see Figure 2, top). In contrast, departures around 30% are found during the low opacity season at L_s ~ 120º, when retrieved effective radii are the smallest (~0.6 μm).

Text S3. Uncertainties

In addition to the quantitative analyses of the uncertainties associated to dust and water ice contents performed in Section 2.4, in this section we list and comment additional sources of uncertainties in our results. Quantifications of the effect of each of these additional sources are subject to a large number of free parameters that cannot be straightforwardly constrained. Moreover, the combined effect depends on each particular measurement of each shadow event. To be conservative, we have discarded shadow events in which the uncertainty in the retrieved radius was estimated to be above 0.2 μm. These sources of uncertainties are:

a) Observations: The original requirements of REMS photodiodes were to provide UV fluxes (ENVRDR products) with an accuracy better than 10% with respect to maximum expected values [*Gómez-Elvira et al.*, 2014]. The uncertainties in the fluxes are mainly caused by inaccuracies in the angular response calibration function and by the effects of dust deposited on the sensor, and the noise in the output currents is virtually negligible. As mentioned in Section 2, uncertainties associated to inaccuracies in the angular response are mitigated by using the output currents (TELRDR products) and our empirical angular response function. Similarly, uncertainties associated to dust deposition are mitigated by calculating the ratios of measurements performed during shadow events. Since the duration of these events typically ranges from a few minutes to 1 or 2 hours, the impact of dust attenuation on each single measurement is assumed to be constant and thus cancel out when taking the ratio of such measurements.

b) Radiative transfer model: Biases in simulated radiances using our Monte-Carlo model are small (see Figure S2). Simulated radiances are also affected by the aerosol vertical distribution. We have assumed that aerosols are well mixed, which is a valid assumption in the absence of water ice clouds.

c) Empirical model of the angular response: Uncertainties in the angular response can be associated with modeling results and with the features of the sensor. Uncertainties in modeling results are caused by uncertainties in the radiances simulated with the Monte-Carlo model. This implies that the empirically derived angular response may differ slightly from the actual response, but it allows a consistent conversion from simulated radiances to output currents, which is very important in order to obtain reliable results. There is also an uncertainty associated to azimuthal variations in the spatial response. These variations are typically small for small solar zenith angles, but increase for zenith angles larger than 30º-40º. This uncertainty is mitigated by selecting measurements that were performed in a short period of time (with small variations in Sun position). Thus, any inaccuracy in the angular response will be compensated when calculating the ratios of the output currents. For this reason, we have only selected shadow events with solar zenith angles smaller than 30º or with solar zenith angles typically between 30º and 40º but with a relative change in the angular response smaller than a 15%.

d) Radiative parameters: Phase functions and single-scattering albedos present uncertainties associated with the refractive indices (which could be subject to temporal variations caused by changes in dust composition) and with the assumed particle shape (cylinders) and size distribution (monomodal). Since the actual properties of the Martian dust are not well known, our selection is performed to optimize consistency with the selected refractive indices. There is a well-known discrepancy between the simulated and the observed phase functions in the backscatter direction, but our retrievals are mainly affected by the behavior of the phase function for small scattering angles, where the agreement between simulated and experimental phase functions is very good [*Wolff et al.*, 2010]. Uncertainties in opacity (mainly because Mastcam observations do not coincide in time with REMS shadow events) can also slightly affect the results, as shown in Table 1. Finally, a significant presence of water ice clouds can also affect the results, as quantified in Section 2.4.

Part III

Discussion

Chapter 8. Discussion

The papers presented in Chapters 4 – 7 contain a comprehensive discussion of the main results. In this chapter, we present a complementary and inclusive discussion of the results presented in this work.

We first discuss different methods of obtaining aerosol properties from solar radiation measurements at the Martian surface. Second, we discuss the effect of the radiative environment at the Martian surface on other meteorological and environmental variables using the measurements acquired by the missions that have landed on Mars. Third, we discuss some important findings derived from the analysis of REMS UV data, such as the importance of developing an empirical model of the FOV and angular response of the photodiodes for studies of the aerosol properties. Finally, we include a discussion of the contribution of this work from a global perspective.

8.1. Methods to obtain aerosol properties from solar radiation measurements

From our studies on the effect of the individual contributions of the different atmospheric constituents to the total atmospheric opacity we have shown that, even under relatively clear conditions that can be found at the Martian surface, dust has the greatest impact on the scattering and absorption of shortwave radiation. Other components can also be important, but only at specific wavelengths: CO_2 below 300 nm (due to absorption below 200 nm and due to scattering in the remaining range) and O_3 at ~255 nm. These results imply that special attention has to be devoted to dust radiative properties when developing a radiative transfer model. Small variations in dust radiative properties have a larger impact on the shortwave fluxes than large variations in the abundance of some trace gases, such as ozone. For this reason, the importance of including in the radiative transfer model state-of-the-art wavelength-dependent dust radiative properties cannot be overemphasized.

Due to the impact of suspended dust particles on solar radiation, measurements of total radiation at the surface provide an estimate of the atmospheric opacity. The ratio between the radiation at the surface (*T*) and that at the TOA (*E*) can be directly used to estimate dust opacity: by calculating the ratios T/E for different amounts of dust using COMIMART, the atmospheric opacity can be retrieved by finding the simulated value of T/E that best matches the observations. As an example, using the MetSIS channel with the widest spectral range (200 – 1100 nm), T/E is expected to change between virtually one for $\tau \sim 0$ and ~0.75 for $\tau \sim 1.5$.

The relative contribution of the direct and diffuse components to total radiation strongly depends on opacity. Figure 8.1 shows the behavior of the direct and diffuse components of the solar radiation at the surface as a function of dust opacity for the conditions described in the caption. The direct (beam) radiation shows an exponential decay with opacity. In contrast, diffuse radiation increases with opacity until a maximum is reached when τ = 1.41. The figure shows that the importance of the diffuse component increases with opacity: for this scenario, direct radiation is larger than the diffuse radiation for opacities approximately below 1, whereas diffuse radiation becomes more important that the direct component for opacities above 1. The relative importance of the diffuse radiation varies significantly with opacity, ranging from values below 20% for low opacities (τ = 0.3) to values above 60% for high opacities (τ = 1.5). The ratio D/T is a very suitable method to retrieve dust opacity, since it has numerous advantages over other methods, as it will be discussed below.

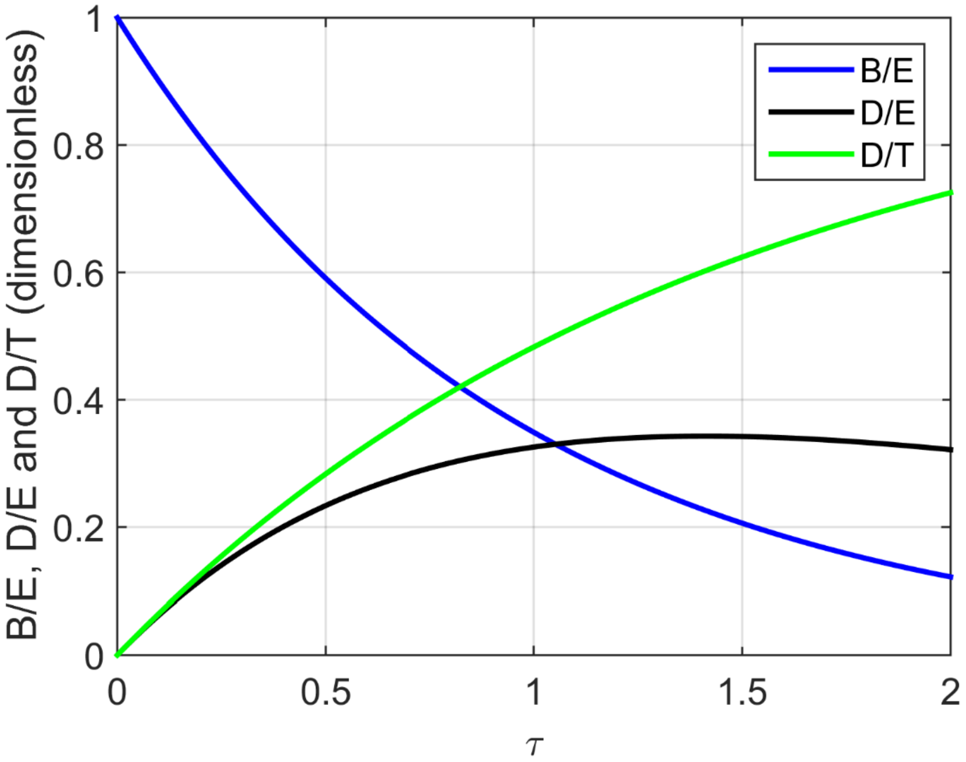

Figure 8.1. Ratio between the direct radiation at the surface and the radiation at the TOA (B/E, blue line), ratio between diffuse radiation at the surface and the radiation at the TOA (D/E, black line) and ratio between diffuse and total radiation at the surface (D/T, green line) as a function of dust opacity at a wavelength of 320 nm, assuming an effective radius of 1.5 μm and that the cosine of the solar zenith angle is 0.95.

The values shown in Figure 8.1 depend on the dust radiative parameters (single-scattering albedo and phase function), which depend on wavelength. Figure 8.2 shows the behavior of the direct and diffuse components as a function of opacity, but at 600 nm, where the single-scattering albedo is higher and the asymmetry factor is lower than in the ultraviolet region. Figure 8.2 also shows the ratio between the normalized total irradiance at the surface at 320 nm and that at 600 nm. By definition, the behavior of direct radiation at both wavelengths is identical. However, the values and the behavior of the diffuse radiation are clearly different: at 600 nm, values are higher and the maximum occurs at opacities above 2. For this reason, total radiation decreases slower at 600 nm than at 320 nm. Hence, total radiation measured in spectral bands with significantly different dust radiative properties can be used to retrieve opacity. We have also proposed this method to obtain opacities from MetSIS measurements.

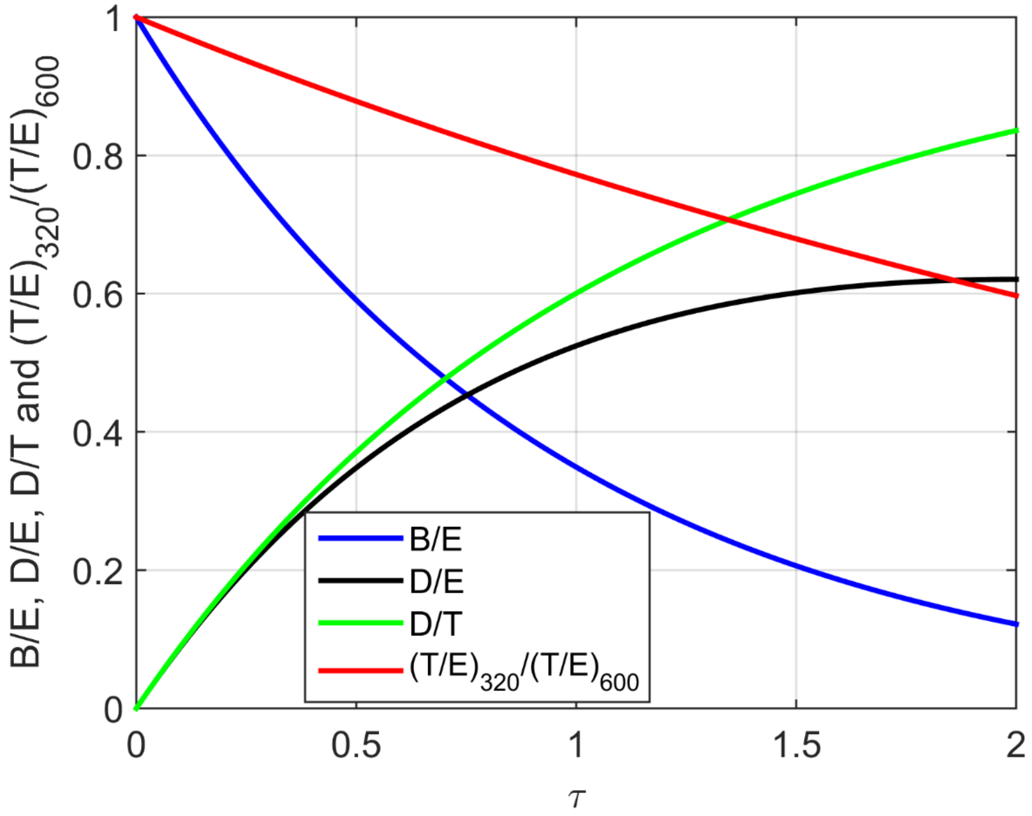

Figure 8.2. As in Figure 8.1, but for the wavelength of 600 nm. The ratio between the normalized irradiance at the surface at 320 nm and that at 600 nm is represented by the red line.

The combination of the two proposed methods to determine atmospheric opacity can provide additional information about dust aerosol particle size. Since dust radiative properties depend also on the effective radius of the particle size distribution, the opacities retrieved with the two methods are expected to match only if the assumed effective radius is correct. If the results do not match, calculations can be performed for other effective radii, and the value for which the difference between the opacities obtained with the two methods is minimized can be used as a good estimation of the dust particle size.

In summary, we have presented two different methods of obtaining dust opacity from solar radiation measurements at the Martian surface. In particular, we have shown how the combination of COMIMART results and MetSIS measurements can greatly enhance the scientific return of the MetSIS mission.

8.2. Effect of the radiative environment at the Martian surface on meteorological and environmental variables

We have used COMIMART to characterize the radiative environment at the Martian surface. The seasonal and interannual variability of solar radiation at the MER and MSL landing sites has been shown and discussed in Chapter 5. However, the discussion can be enriched by analyzing the radiative environment at the locations of all the landed missions, including this way a larger latitudinal range. Moreover, we discuss the implications of daily insolations (defined as the solar irradiance integrated over one sol) on other meteorological and environmental variables.

The temporal evolution of opacity and solar insolation at the locations of the landed missions (VL1, VL2, MPF, MER-A, MER-B, PHX and MSL) is shown in Figure 8.3. During the aphelion season, the opacity values (left panels of Figure 8.3) are low (typically below 1) and the interannual variability is also small (mean standard deviation around 0.05 at the Spirit landing site and around 0.03 at the Opportunity location). In contrast, during the perihelion season, both the opacity values and their interannual variability are significantly larger. This behavior can be explained in terms of the differences in solar insolations (right panels of Figure 8.3) between the perihelion and the aphelion seasons, which produce on average higher temperatures during the former, and these higher temperatures enhance the injection of dust particles into the atmosphere by means of wind stress and dust devils (Haberle et al., 1982; Newman et al., 2002a; Newman et al., 2002b; Kahre et al., 2006; Greeley et al., 2010; Martínez et al., 2017). Opacity values retrieved from satellite measurements show that this seasonal variability is also observed on a planetary scale (Smith, 2004; Montabone et al., 2015).

Another remarkable feature shown in Figure 8.3 is the presence of global dust storms on some Martian years, which show extraordinarily high opacity values ($\tau > 3$). These dust storms have a strong impact on atmospheric circulations and on the surface radiation budget, and therefore on other quantities that are relevant from a meteorological perspective, such as surface pressure, air temperature and ground temperature (Martínez et al., 2017). Two global dust storms have been measured from the surface: the Viking Landers observed the one on MY 12, and The Mars Exploration Rovers performed measurements during the dust storm on MY 28. These two dust storms occurred shortly after the perihelion (at $L_s \sim 300^o$ in MY 12 and around $L_s \sim 280^o$ in MY 28). It is interesting to note that, at those solar longitudes, there is typically a minimum in dust opacity in the remaining Martian years.

Although there is a significant interannual variability in atmospheric opacity during the perihelion season, there are some common features in its behavior at the different landing sites. There are two periods of enhanced dust content at each location: the first one occurs at $L_s = 210 – 240^o$, and the second one at $L_s = 320 – 340^o$. The exception is found at the MER-A location, where there is a third peak in dust opacity at $L_s = 150 – 170^o$.

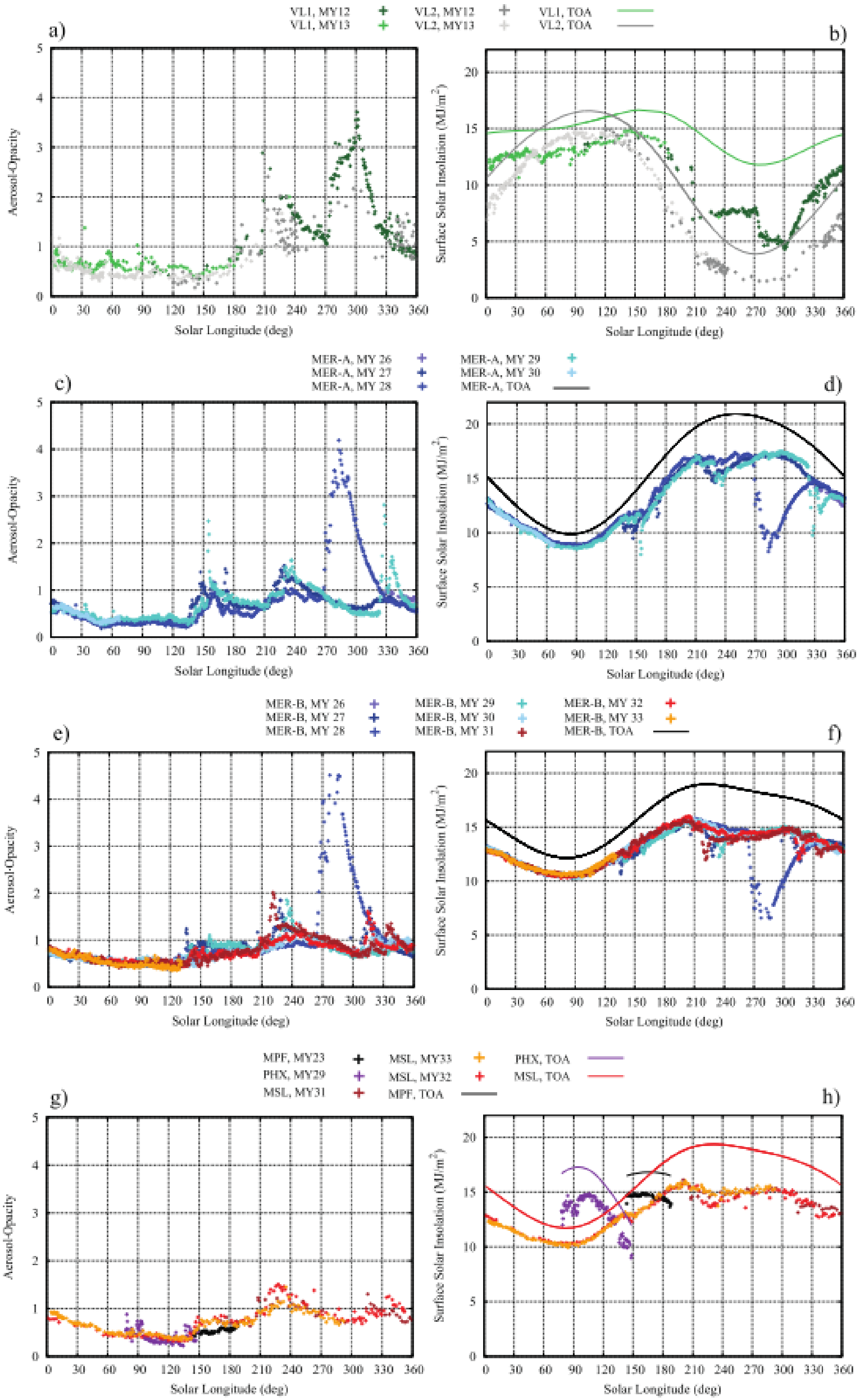

Figure 8.3. Temporal evolution of opacity and solar insolation at the VL1 and VL2 (a-b), MER-A (c-d), MER-B (e-f), MPF, PHX and MSL (g-h) landing sites (Martínez et al., 2017).

The solar insolations shown in the right panels of Figure 8.3 have been simulated using COMIMART. For these calculations, we have assumed that only the suspended dust contributes to the atmospheric opacity. There are situations in which water ice clouds contribute significantly to opacity, such as during the aphelion cloud belt or at the edges of the polar caps (Toigo and Richardson, 2000; Smith, 2004; Madeleine et al., 2012; Lemmon et al., 2015). However, compared to dust, its effect on the radiation that reaches the surface is typically minor: assuming that dust and water ice clouds contribute equally to the total atmospheric opacity, the difference in the solar insolation at L_s = 90º ranges from 3% to 5% (depending on the landing site) with respect to the values calculated assuming that water ice clouds are absent.

The highest values of the daily insolation at the VL1 and VL2 landing sites occur at L_s ~150º and L_s ~120º, respectively. Around those solar longitudes, insolations at the TOA show the maximum values, whereas atmospheric opacities show the minimum values. At these locations of the Northern Hemisphere, the seasonal variability in surface insolation is enhanced because the maximum (minimum) insolation at the TOA occurs during the clear aphelion (dusty perihelion) season.

The opposite occurs at the locations in the Southern Hemisphere: at the MER and MSL landing sites, the seasonal variability in surface insolation is smaller because the increase in opacity towards the perihelion season counteracts the increase in daily insolation at the TOA. The highest values at these landing sites (except during MY 28 at the MER locations) occur at L_s ~200º and at L_s ~300º, when the insolation at the TOA is close to the annual maximum and the values of the atmospheric opacity are the lowest of the perihelion season.

After completing the discussion on the radiative environment at each landed mission on Mars, we discuss the effects of opacity and solar insolation on other meteorological and environmental quantities.

The top panel of Figure 8.4 shows the daily mean atmospheric pressure measured at the VL1, VL2, MPF, PHX and MSL missions. There is a significant seasonal variability in the daily mean surface pressure at each location, which is caused by the sublimation and condensation of the CO_2 polar caps. During the southern spring, part of the southern polar cap sublimates, and the released CO_2 leads to an increase in surface pressure until L_s ~ 260º. During the cold season of the Southern Hemisphere, the deposition of CO_2 into the southern polar cap leads to a decrease in surface pressure until L_s ~ 150º. The relative minima and maxima at L_s ~ 345º and L_s ~ 55º are caused by these processes associated wuth the northern polar cap.

As it happened with atmospheric opacity, interannual variability of surface pressure is small during the aphelion season, but it increases during the perihelion season. In particular, there is a significant difference between the measurements of MY 12 and MY 13 at the VL2 location around L_s = 280º. The increase in surface pressure observed during MY 12 was caused by the descending branch of the tropical overturning circulation, which was intensified by the global dust storm (Figure 8.3, panel a) (Haberle et al., 1982; Wilson, 1997).

The bottom panel of Figure 8.4 shows the amplitude of the diurnal variation in surface pressure at the aforementioned landing sites. The amplitude of the diurnal variation is small during the aphelion season and increases during the perihelion season. In fact, the largest amplitudes are found at the VL1 and VL2 locations around $L_s = 280^o$ during MY 28, which is when the global dust storm occurred. From this figure, it is straightforward to conclude that there is a clear correlation between atmospheric opacity and the diurnal amplitude of the surface pressure, which has been extensively studied (Zurek and Leovy, 1981; Bridger and Murphy, 1998; Wilson and Hamilton, 1996; Guzewich et al., 2016).

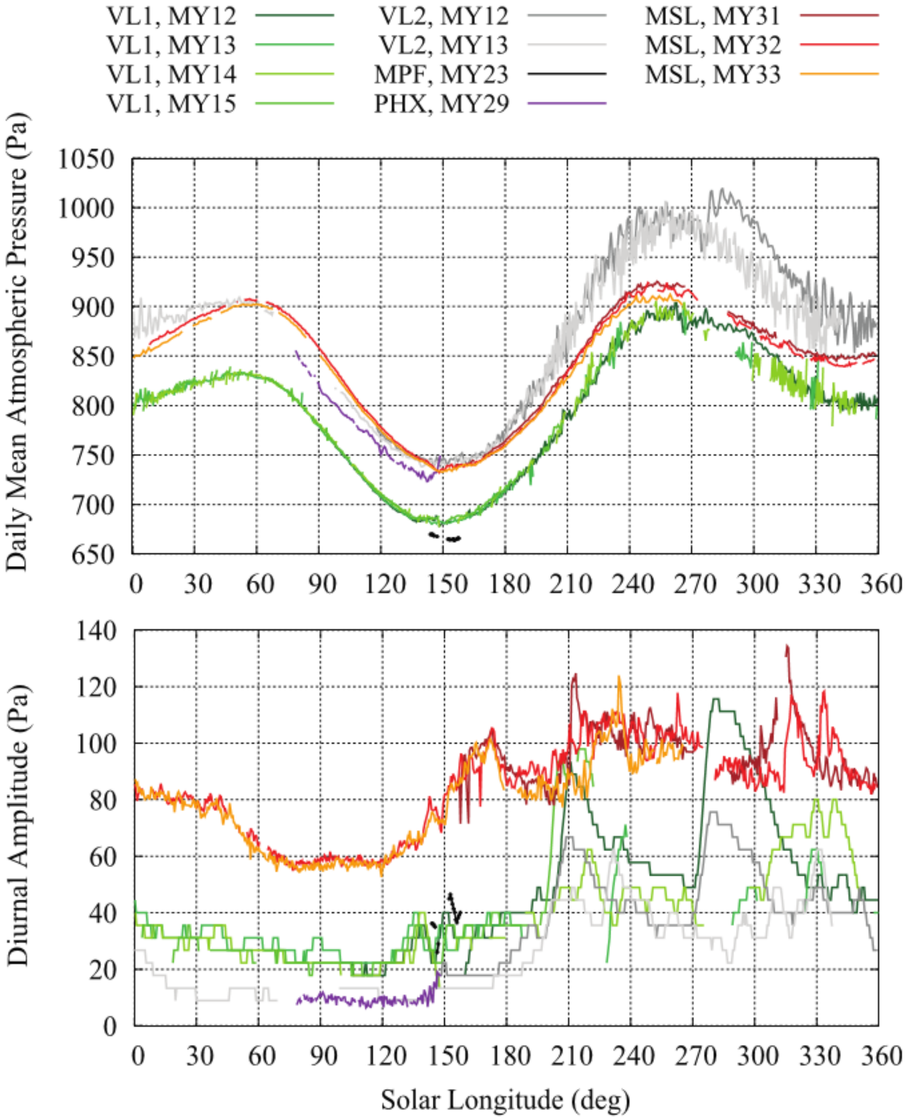

Figure 8.4. Temporal evolution of daily mean atmospheric pressure (top) and diurnal amplitude (bottom) at the VL1 (green), VL2 (gray), MPF (black), PHX (purple) and MSL (orange, red and brown) locations (Martínez et al., 2017).

The top panel of Figure 8.5 shows the daily mean near-surface air temperature measured at the considered landing sites. The annual amplitude of the daily mean air temperature decreases from ~60 K at the VL2 location to ~20 K at the MSL landing site. This behavior is consistent with the increase in the annual amplitude of daily insolation at the surface with latitude, as shown in Figure 8.3. The extreme mean temperatures at the different landing sites coincide with their respective extremes in daily insolation at the surface.

Similarly, the bottom panel of Figure 8.5 shows the diurnal amplitude of near-surface air temperature at the various locations. The most striking feature is the abrupt decrease at the VL1 location around Ls ~275º during MY 12- The reason for this decrease is the global dust storm, which causes a significant attenuation of the incoming radiation, as shown in Figure 8.3, panel b. The effect of the dust storm is less remarkable at the VL2 location due to the small solar insolation at that time of the year.

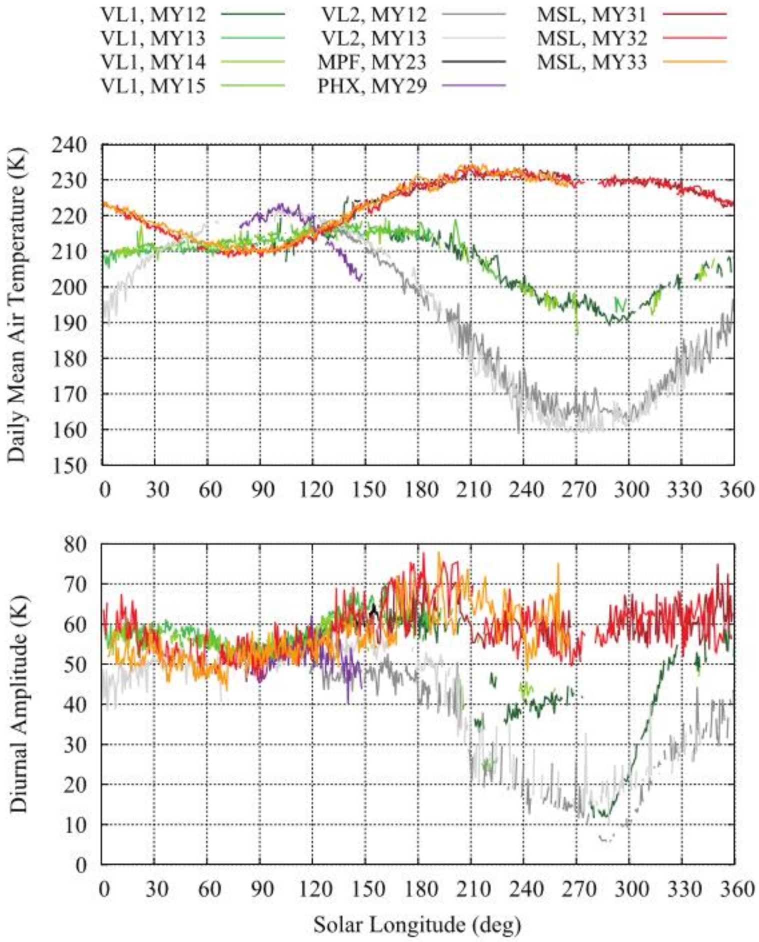

Figure 8.5. As in Figure 8.4, but for the near-surface air temperature (Martínez et al., 2017).

Ground and near-surface air temperatures are affected by solar insolation in a very similar way. Ground temperatures at the MSL landing site show the lowest values at L_S ~85º, when the daily insolation is around the minimum, whereas the highest values occur at L_S ~210º, when the daily insolation is around the annual maximum (Martínez et al., 2017). In this case it should be noted that variations in the diurnal amplitude of ground temperature are mainly affected by changes in the thermal inertia of the terrain traversed by the rover (Vasavada et al., 2017). However, for a given terrain, changes in atmospheric opacity also cause variations in the daily amplitude of ground temperature (Määttänen and Savijärvi, 2004). Notwithstanding, these variations are smaller than those caused by changes in the thermal inertia (Martínez et al., 2014).

Finally, the UV fluxes at Gale Crater simulated using COMIMART have been provided to analyze the seasonal variations in methane concentrations measured with the Tunable Laser Spectrometer (TLS) of the MSL mission. The background methane levels (below 1 ppbv) show a seasonal cycle that appears to correlate with UV fluxes at the surface: values around 0.2 ppbv are found when the daily UV irradiation is close to the annual minimum, whereas concentrations around 0.9 ppbv are found under high daily UV irradiations (Webster et al., 2016).

8.3. Important findings derived from the analysis of REMS UV data

We now discuss some important findings derived from the analysis of REMS UV data. Originally, the objective was not to determine dust aerosol particle size, but dust opacity.

Ideally, we could retrieve dust opacity by calculating the ratio between the irradiance at the surface and that at the TOA. However, this simple approach cannot be applied to REMS measurements due to several reasons:

1. The REMS UV fluxes (in W/m^2) are affected by dust deposition and inaccuracies in the angular response calibration function that has been used to produce these processed data (see Chapter 10 for further details).
2. The field of view of the sensor is not hemispheric and the spatial response of the photodiodes at high values of the zenith angle is very low, as shown in Chapter 7.
3. Part of the FOV is blocked by the mast and the masthead of the rover (Vicente-Retortillo et al., 2017).
4. The rover is usually tilted, and therefore the sensor is not facing the zenith.
5. This approach requires a very accurate knowledge of the spectral range of the photodiode, which is affected by temperature and aging.

Physical inconsistencies in the angular response calibration function would irremediably lead to incorrect retrievals of the opacity (for example, two measurements performed within seconds, but at both sides of $\theta = 30^{\circ}$, would lead to completely different values of the opacity due to the discontinuity in the processed data at $\theta = 30^{\circ}$).

Dust deposited on the sensor is another impediment to the application of this approach. As dust deposits on the sensor, attenuation increases, and therefore the overestimation in the retrieved opacity becomes larger.

Reasons 2 – 4 imply that not all the scattered radiation is detected by the photodiodes. Therefore, the diffuse component calculated using COMIMART would not provide accurate results.

In order to apply this method, the radiation at the TOA has to be computed assuming a spectral range. Since the spectral irradiance shows abrupt changes in the UV (Vicente-Retortillo et al., 2015), small inaccuracies in the assumed range would lead to large errors in the retrieved opacities.

The uncertainty caused by the inaccuracies in the angular response calibration function can be minimized by using the photodiode output currents in combination with an empirical angular response function that converts output currents to irradiances. This empirical angular response has been shown in Vicente-Retortillo et al., (2017).

The uncertainty introduced by the attenuation caused by the dust deposited on the sensor can be virtually cancelled by using measurements that are separated by a very short period of time (typically minutes or 1 – 2 hours).

In order to obtain reliable results, an accurate characterization of the FOV is needed. This empirically derived FOV is presented in Vicente-Retortillo et al., (2017). Also, radiance calculations are needed in order to accurately account for the fraction of the incoming radiation that is blocked by the masthead and the mast of the rover. Moreover, the empirical model considers also rover tilt and orientation, and this improves the quality of the retrievals.

Finally, the lack of knowledge of the exact spectral range of the photodiode loses importance when analyzing the ratios between pairs of measurements, since this way the spectral range (and even the exact irradiance) becomes irrelevant.

For all these reasons, we propose a novel technique to calculate the atmospheric opacity from the photodiode output currents of the REMS UVS that does not require the knowledge of the UV irradiance in units of W/m^2 (and, therefore, it is not sensitive to dust deposition or to inaccuracies in the angular response calibration function).

This technique is based on the idea discussed at the beginning of this chapter. When the opacity increases, the ratio between diffuse and total (direct + diffuse) radiation increases. By analyzing the measurements, values for the diffuse (D) and total (T) signals can be estimated, and the ratio D/T allows to retrieve the opacity. Figure 8.6 shows the measurements for two sols: under dusty conditions (sol 801), D/T is larger than under relatively clear conditions (sol 647). Additional details of the methodology can be found in Vicente-Retortillo et al., (2015b) and Vicente-Retortillo et al., (2016b).

The left panel of Figure 8.7 shows the retrieved atmospheric opacities using the proposed technique. For comparison, the right panel shows Mastcam opacities at 880 nm. The behavior of the UV opacity is consistent with Mastcam measurements: the lowest values are found at L_s ~120º and the highest values occur at L_s ~ 220º. However, the annual amplitude of the UV opacities is significantly lower than that of Mastcam opacities: these variations in the ratio τ_{UV}/τ_{880} suggests variations in dust aerosol particle size.

After this finding, we started a new analysis of REMS UV data, but now from a different perspective: How could we retrieve dust aerosol particle size from these measurements? The objective was very ambitious; in fact, these retrievals were not listed as the expected results from REMS UVS measurements (Gómez-Elvira et al., 2012).

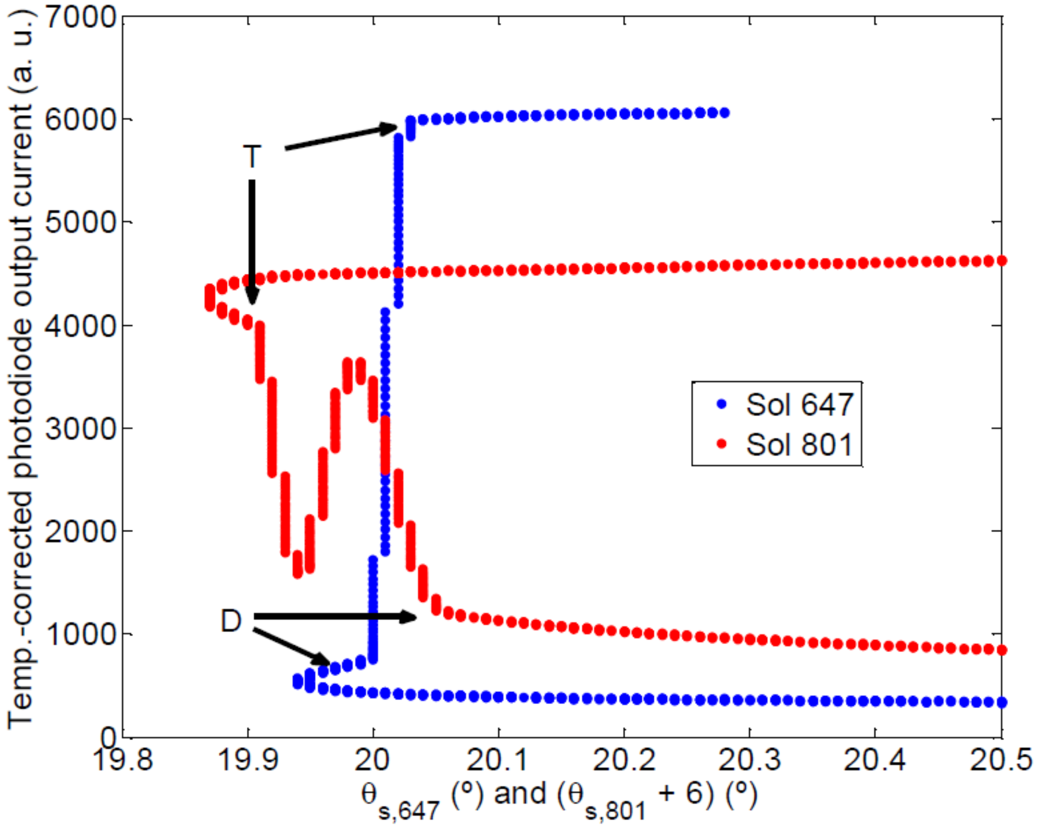

Figure 8.6. Measurements in the UVA channel during the shadow events on sols 647 and 801 as a function of the solar zenith angle relative to REMS rover frame. The higher value of D/T on sol 801 indicates a higher opacity.

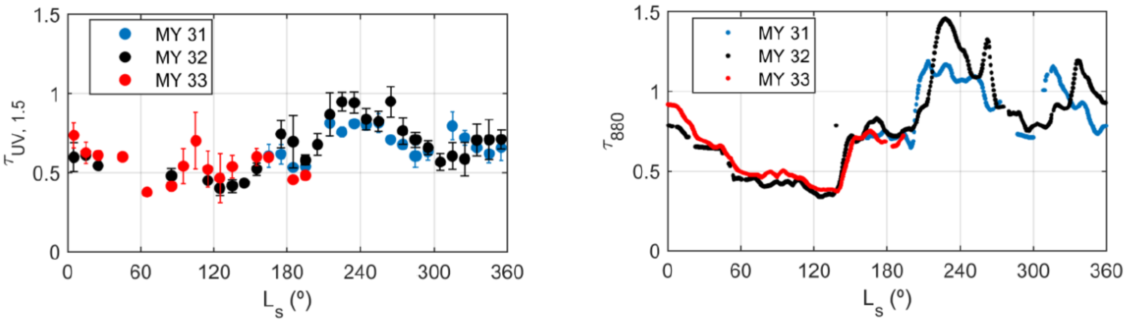

Figure 8.7. (Left) Atmospheric opacity derived from REMS UV measurements, assuming an effective radius of 1.5 µm. (Right) Atmospheric opacity derived from Mastcam observations at 880 nm.

After analyzing several options, we developed the methodology presented in Vicente-Retortillo et al., (2017), which relies on the fact that the radiance is significantly affected by the dust aerosol scattering phase function, which in turn depends on dust aerosol particle size.

Our results have provided not only estimations of the mean value of the effective radii of the particles, but also the seasonal and interannual variability of dust aerosol particle size at the MSL location.

The values and the seasonal evolution of dust aerosol particle size at Gale Crater are consistent with those derived from MER observations: at those locations, effective radii were typically in the range 0.7 – 2.1 μm, with the lowest values occurring during the aphelion season, and the largest values being associated with events of enhanced dust content.

Our results are also consistent with those derived completely independently from passive sky observations performed by ChemCam, a spectrometer on board the MSL mission (McConnochie et al., 2017).

8.4. Contribution of this work from a global perspective

Throughout this thesis we have obtained results that contribute to extend our knowledge of the radiative environment at the Martian surface and of the properties of the suspended dust. These results have important implications in several contexts:

1. From a meteorological and climatological perspective, a correct characterization of dust aerosol particles is needed. Dust aerosol particle size has a strong effect on atmospheric heating rates, and therefore on the thermal and dynamical field of the atmosphere. Moreover, it has strong implications on aerosol atmospheric transport, including gravitational settling rates. It has also important implications in cloud microphysics, since the ability of dust to nucleate clouds depends on the particle size.
2. The accurate characterization of the radiative environment at the Martian surface is also important from the aforementioned perspective. We have discussed the important effect of solar insolation at the surface on surface pressure and on ground and near-surface air temperatures.
3. The developed radiative transfer models have been extremely useful because the detailed analysis of the results has enabled the development of techniques that can greatly enhance the scientific return of solar radiation measurements performed by current and future missions to Mars. As an example, dust aerosol particle size has been retrieved from REMS UVS measurements using one of these techniques. We have also proposed techniques to retrieve opacity and dust aerosol particle size from MetSIS measurements.
4. From the perspective of the habitability and future human exploration of the planet, UV radiation has important implications due to its effects on microorganisms. Moreover, methane is a potential signature of ongoing or past biological activity (although it can also be produced abiologically) on Mars. In this context, we have characterized the UV environment at the MSL location, and the simulated UV insolations have been used to study their correlation with background methane concentrations.

Part IV

Conclusions

Chapter 9. Conclusions

The main conclusions of this work are presented in this chapter. The conclusions are divided into four sections, according to the four general objectives described in Chapter 3.

9.1. Development of new radiative transfer models adapted to the Martian atmosphere

We have developed radiative transfer models following two approaches: the delta-Eddington approximation and the Monte Carlo method. We first list the main conclusions obtained using the first model (COMIMART) and then those obtained using the second one (COMIMART-MCF and COMIMART-MCR).

9.1.1. Conclusions obtained with the COMIMART model

1. We have developed a new comprehensive radiative transfer model (COMIMART) to study the solar irradiance at the surface of Mars.
2. COMIMART includes state-of-the-art radiative properties for dust, water ice clouds and gas molecules. The dependence on wavelength of these properties is also included in the model.
3. The model can be used to characterize the radiative environment under different conditions in any spectral region of the shortwave range. Fluxes can be computed in bands with important implications, such as those covered by the REMS UVS, by MetSIS or the entire shortwave range.
4. An important feature of the model is its versatility. COMIMART contains several input parameters that can be easily modified: dust opacity at the reference wavelength of 880 nm, effective radius of the dust aerosol particles, opacity of water ice clouds at 12.1 μm, abundance of the different gas molecules, solar longitude, local time, latitude, surface albedo and spectral band. Moreover, radiative parameters can be altered to allow calculations under any possible combination of extinction efficiency, single-scattering albedo and asymmetry factor. Due to this versatility, the range of scenarios that can be found in the Martian atmosphere is covered due to the wide range of conditions that can be defined by combining the different input parameters.
5. Fluxes obtained with COMIMART are in excellent agreement with those computed using the DISORT algorithm as a reference under a wide range of scenarios.
6. COMIMART provides results of different nature: diurnal evolution of the direct and diffuse components of the incoming radiation at the surface, spectral irradiance features and values of the daily irradiation. These results have enabled the characterization of the radiative environment at the Martian surface.
7. Solar fluxes are controlled by the amount of dust in the atmosphere at the majority of wavelengths. Gas molecules can also play a role in the UV region, and CO_2

produces a cut in the spectrum at wavelengths shorter than ~200 nm. Water ice clouds are virtually pure scatterers over a wide range of the shortwave spectral region.

8. Considering the aforementioned conclusions, COMIMART does not only enable the characterization of the radiative environment at the Martian surface, but can also greatly enhance the scientific return of measurements of the solar flux on the surface of Mars.

9.1.2. Conclusions from COMIMART-MCF and COMIMART-MCR

1. We have developed two versions of a radiative transfer model that relies on the Monte Carlo method. As COMIMART, the two versions of the model include state-of-the-art radiative properties of the components of the Martian atmosphere. These versions of the model enable the simulation of the radiances at the Martian surface.
2. In the first version of the model, COMIMART-MCF, photons are scattered in one single direction after each interaction with the atmospheric components. For this reason, a very large number of photons is needed in order to obtain a detailed map of the angular distribution of the incoming photons. Therefore, high computational cost is required to achieve accuracy in the simulated radiances. However, simulated fluxes (the result of integrating the incoming photons from each direction) are reliable with a modest computation effort.
3. In the second version, COMIMART-MCR, the photon is scattered in all directions after each interaction, and the fraction of the photon scattered in each direction is determined by the scattering phase function. This approach allows obtaining accurate results at each cell of the grid where radiances are stored with a reasonable computing effort. Hence, this second method is optimized for radiance simulations.
4. Due to the stochastic nature of the Monte Carlo method, there is an intrinsic uncertainty in the results. This uncertainty can be reduced by increasing the number of photons in each simulation. However, it should be noted that in order to reduce the spread of the results in approximately one order of magnitude, an increase of two orders of magnitude in the number of photons is required, and the number of photons is proportional to the computing time.
5. The model is very versatile, with several inputs that can be modified: dust opacity, water ice contribution to total opacity, dust scattering phase function, water ice scattering phase function, single-scattering albedo of dust and water ice, Sun position, number of photons, model version and desired outputs and angular resolution.
6. Radiances (and fluxes) obtained with this model are in excellent agreement with those computed using the DISORT algorithm as a reference under different scenarios.
7. The model provides results of different nature: fluxes at the Martian surface, downwelling and upwelling fluxes at any atmospheric level, radiances at the Martian surface with any angular resolution and downwelling and upwelling radiances at any atmospheric level and with any angular resolution.
8. Simulated radiances are very sensitive to dust aerosol scattering phase function, which in turn depends on the effective radius of dust particles. This is the basis of our methodology to retrieve dust particle size at the MSL landing site.

9.2. Development of techniques to retrieve dust aerosol properties from solar radiation data of present and future Mars missions.

We have developed techniques to retrieve dust aerosol properties (opacity and dust particle size) from solar radiation measurements of present (Mars Science Laboratory) and future (MetNet) missions to Mars. The conclusions enumerated below have been useful to provide an answer on how can we use the developed radiative transfer models to enhance the scientific return of solar radiation measurements from the Martian surface:

1. There are several variables affected by atmospheric opacity. The first one is the total radiation at the surface: the ratio between the radiation at the surface and that at the TOA increases with decreasing opacity. Second, by definition, the direct radiation at the surface, which decreases with opacity. And third, the diffuse radiation at the surface; the behavior of this quantity depends on the radiative properties of the atmosphere, but in most cases it increases with opacity until a given optical path is reached, and then decreases with increasing opacity.
2. In order to retrieve opacity from *in situ* measurements using one channel, the quantity that minimizes the uncertainties in the retrieved values is the ratio between direct and total radiation (assuming that both measurements are separated in time only a few minutes). The advantage of this method is that any uncertainty in individual measurements (caused, for example, by dust deposition) is virtually cancelled.
3. In the case of MetSIS, requirements needed to apply the method described in the previous conclusion are not expected to be available. However, we have presented two additional methods to retrieve opacity from MetSIS measurements. The first one relies on the fluxes measured in a single band and the second requires measurements performed simultaneously in two bands with different radiative properties.
4. In the case of REMS UVS, the aforementioned requirements are met when the solar disk moves from the blocked to the unblocked region of the FOV, or vice versa.
5. There are several variables affected by dust aerosol particle size. First, since radiative properties depend on the effective radius, both diffuse and total radiation are affected. The second quantity is the ratio between total radiation measured in spectral bands with different radiative properties. And third, the scattered radiance, since the phase function depends on particle size.
6. In order to retrieve dust aerosol particle size from *in situ* measurements using one channel, the quantity that minimizes the uncertainties in the retrieved values is the behavior of the scattered radiance because the effect of particle size on the phase function is typically remarkable (see Figure 2.4).
7. In the case of MetSIS, we have shown that the combination of the two methods that we have proposed to retrieve the opacity can provide additional information on dust aerosol particle size.
8. In the case of REMS UVS, the method described in conclusion 6 of this section can be applied following a new approach that we have developed: the behavior of the measurements during shadow events depends on aerosol phase function, and therefore on dust particle size.

9. Finally, in order to apply these techniques, it is necessary to accurately characterize the sensors. We have used REMS measurements and the radiative transfer models to develop an empirical model of the FOV and of the angular responses of the sensors. We will also show in Chapter 10 our estimates on another important quantity for the characterization of the sensor: the attenuation of the incoming radiation caused by dust deposited on it.

9.3. Characterization of the radiative environment at the landing sites of the missions

We have used our radiative transfer model COMIMART and values of atmospheric opacity derived from observations performed by landed missions on Mars to characterize the radiative environment at the locations of those missions. Especial attention has been devoted to the radiative environment at the locations of the Mars Exploration Rovers and Mars Science Laboratory. The radiative environment has also been simulated at the locations of the Viking Landers, Mars Pathfinder and Phoenix landing sites.

1. The daily irradiation at the TOA shows a significant temporal and spatial variability. As on Earth, maximum values are found at the poles around the summer solstices, and the minimum values are found during the polar nights around the winter solstices. There is a strong asymmetry in insolation between the aphelion and the perihelion season due to the eccentricity of the Martian orbit, significantly higher than on Earth. This asymmetry causes the dichotomy between the cold and clear aphelion season and the warm and dusty perihelion season.
2. The seasonal variability of the daily irradiation at the surface shows a strong latitudinal dependence. Considering the landed missions, the smallest amplitudes are found at low latitudes, with values typically between 10 and 15 MJ/m^2 at MER-B (Opportunity) and MSL landing sites. The largest amplitude is expected to occur at the Phoenix landing site, with values between 0 and 15 MJ/m^2. The highest values are found at the MER-A (Spirit) location, with values around 17 MJ/m^2. In the Northern Hemosphere, maximum values occur during the aphelion season, when the insolation at the TOA shows high values and opacities are low; in contrast, maximum values in the Southern Hemisphere occur during the perihelion season, when opacities are high, but the insolation at the TOA reaches maximum values.
3. The radiative environment at the surface shows interannual variability. This variability is small during the clear aphelion season, becoming significantly larger during the dusty perihelion season. The most clear example of interannual variability can be found in the measurements of the Mars Exploration Rovers at L_s = 270 – 300º. The global dust storm of MY 28 caused a remarkable drop in the daily insolations to values that were below the annual minimum during a time of the year in which, in absence of the storm, values should be around the annual maximum.
4. The behavior of the direct and diffuse components of the incoming radiation has been studied at the MER and MSL landing sites. During the clear aphelion season, the direct component prevails; in contrast, during the dusty perihelion season the

direct radiation diminishes due to the increase in opacity; therefore, diffuse radiation becomes more important than the direct component.

5. The daily UV environment at the MSL location is very interesting because of its implications in numerous studies. The maximum values of daily UV irradiation at Gale Crater are found at L_s ~185 – 200º and L_s ~295 – 310º, when opacities are the lowest of the dusty season and insolations at the TOA are high. The lowest values occur between L_s = 0 – 100º, when radiation at the TOA is low, and during the peaks in opacity around L_s ~230º and L_s ~335º.

6. Changes in solar radiation and opacity affect other meteorological variables. Dust storms lead to a significant increase in the daily amplitude of surface pressure. The seasonal variability of the daily mean air temperature is larger at locations that are far from the equatorial region mainly due to the increase in the annual amplitude of the daily irradiation at the surface with latitude. The daily amplitude of air temperature decreases during dust storms. Ground temperature is also mainly controlled by the radiation budget at the surface.

7. Simulated UV daily irradiations have been provided to analyze methane measurements at Gale Crater. Background methane concentrations appear to show a seasonal cycle that correlates with these UV irradiations.

9.4. Determination of dust aerosol particle size at Gale Crater

We have developed a new methodology to calculate the seasonal and interannual variability of dust aerosol particle size at Gale Crater during the first 1413 sols (more than two Martian years) of the MSL mission. REMS UVS and Mastcam measurements have been used in this study. Our main conclusions are presented below:

1. Dust aerosol particle size varies significantly with season. Effective radii of the size distribution range from ~0.6 to ~2 μm.

2. The largest particle sizes are typically associated with events of enhanced opacity, whereas the smallest ones are found during the low opacity season (L_s = 60 – 140º).

3. The general behavior of the seasonal cycle during the first year of the mission (MY 31-32) is similar to that during the second year (MY 32-33). However, effective radii during the aphelion season are significantly lower in MY 33 than in the previous year. This can be partially explained by a larger contribution of water ice clouds to the total atmospheric opacity during the aphelion season of MY 33.

4. There is a clear correlation between opacity and dust particle size during the aphelion season, when opacities are low; this is physically consistent, since larger particles settle first. The lack of correlation during the dusty season suggests that dust events affecting the crater are originated at various distances from the MSL location.

5. These results have led to an improvement in the accuracy of the seasonal variability of UV daily irradiations at Gale Crater. Results are also important because dust aerosol particle size affects aerosol atmospheric transport (including gravitational settling rates) and atmospheric heating rates, which in turn affect the thermal and dynamical fields of the atmosphere.

Part V

Future Research

Chapter 10. Generation of UV radiation data products at Gale Crater by correcting REMS UV data from dust deposition and sensor's angular response

10.1. Introduction

The UVS of REMS, onboard the MSL mission, has completed more than two Martian years of measurements at Gale Crater (4.6°S, 137.4°E). Due to its location on the rover deck, the UVS has been exposed to dust deposition. Nominal UVS operations lasted until sol 154, when for the first time degradation of the UVS due to dust deposition led to deviations from nominal values above 10%, with increasing deviations in time. In addition, inaccuracies in the calibration function of the angular response of the UVS have led to discrepancies between measured and physically-consistent UV fluxes when the solar zenith angle (θ) relative to the rover frame is between 20º and 55º. In particular, derived UVS fluxes present a non-physical discontinuity at θ = 30º caused by a discontinuity in the calibration function (Vicente-Retortillo et al., 2017; Martínez et al., 2017b).

The highest-level UVS data archived in the NASA Planetary Data System (PDS) are the ENVRDR and MODRDR products. The ENVRDR products contain UV fluxes in units of W/m^2 for each of the six UVS channels (UVA, UVB, UVC, UVABC, UVD and UVE), while the MODRDR products contain identical data but with values of UV fluxes removed when θ is between 20º and 55º and when the rover or its arm are moving.

We aim to correct the highest-level UVS data from the effects of dust deposition and inaccuracies in the angular response. In particular, our goals are:

1. To correct the ENVRDR data set from the effects of dust degradation and inaccuracies in the angular response for each of the six UVS channels and archive the corrected data set in the NASA PDS.

2. To calculate the MODRDR values when 20º < θ < 55º for each of the six UVS channels using corrected ENVRDR products and archive the complete data set in the NASA PDS.

In Sections 10.2 and 10.3 we show that the values of UV fluxes are strongly affected by inaccuracies in the angular response functions and by the degradation of the UVS due to dust deposition. Sections 10.4 and 10.5 are devoted to the methodology and preliminary results for the UVA channel. In particular, in Section 10.4 we describe our methodology to correct the data from inaccuracies in the angular response function. Analogously, in Section 10.5 we describe our methodology to correct the data from the effects of dust deposition on the sensor. In Section 10.6 we evaluate the expected uncertainties in the corrected data products. Finally, in Section 10.7 we describe the expected impact of this work.

10.2. Inaccuracies in the angular response calibration function

Inaccuracies in the angular response calibration function of each UVS channel lead to physically-inconsistent variations in UV fluxes values stored as ENVRDR data when the solar zenith angle relative to the rover frame is between 20º and 55º. In particular, UV fluxes in ENVRDR products show a non-physical discontinuity at θ = 30º caused by the use of two different calibration functions that do not converge to the same value at 30º.

As an example, the current angular response calibration function for the UVA channel is shown in Figure 10.1 (a). The UVA fluxes obtained when this angular response calibration function is applied to the output currents measured by the UVA photodiode on sol 91 are shown in Figure 10.1 (b). The discontinuity in the UVA fluxes at θ = 30º is caused by the discontinuity in the angular response calibration function. In contrast, values of the photodiode output current show a consistent behavior when θ = 30º (Figure 10.1 (b), blue curve).

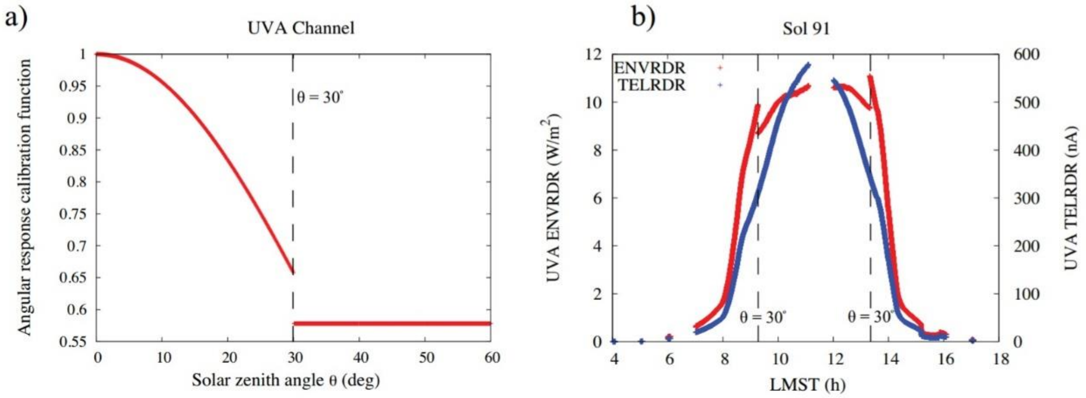

Figure 10.1. (a) Current UVA angular response calibration function as a function of the solar zenith angle relative to the rover frame (θ). A similar qualitative behavior is found for the other UVS channels (for UVE channel, see Vicente-Retortillo et al., 2017), with a discontinuity at θ = 30º and a constant value beyond. (b) The UVA output currents measured on sol 91 (blue curve; TELRDR data) vary smoothly with solar zenith angle, but the UVA fluxes (red curve; ENVRDR data) contain a discontinuity when θ = 30º. This discontinuity is caused by the discontinuity in the instrument angular response calibration function shown on the left. As explained in the text, our goal is to fix this problem for each UVS channel by replacing the current angular response calibration function by a physically-consistent function derived empirically using a method that we already developed and demonstrated (see Section 10.4).

We plan to use physically-consistent empirical angular responses that do not show discontinuities at θ = 30º, such as the one that has been used to simulate the photodiode output currents in our retrievals of dust aerosol particle size, to correct UV fluxes. To generate such responses, we plan to use TELRDR (which do not show a discontinuity at θ = 30º) and ADR products (see Section 10.4 for details). In addition, we plan to complete the MODRDR products, currently missing when 20º < θ < 55º. During the first 1159 sols of the MSL mission, measurements acquired when 20º < θ < 55º represent 45% of the whole set of UVS data with θ < 90º. This is shown in Figure 10.2, where the current ENVRDR data set is shown in red as a function of the sol number and Local Mean Solar Time (LMST), with missing MODRDR data when 20º < θ < 55º overlaid in gray. Throughout the mission and in particular around the solstices (L_s around 90º and 270º), measurements acquired when 20º < θ < 55º include a significant fraction of the diurnal cycle.

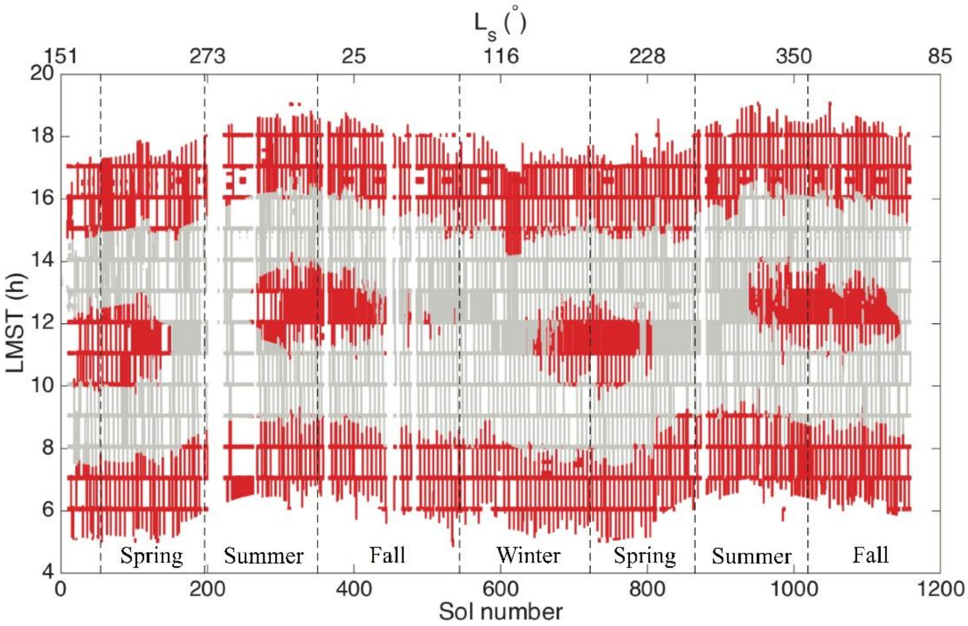

Figure 10.2. Temporal coverage of REMS UVS ENVRDR data shown in red, with missing MODRDR data (20º < θ < 55º) overlaid in gray. We plan to correct the entire ENVRDR data set from the effects of dust degradation and inaccuracies in the angular response and to complete the MODRDR data set by adding data when 20º < θ < 55º for each of the six UVS channels.

10.3. Degradation of the UVS due to Dust Deposition

The REMS UVS has been exposed to dust deposition due to its location on the rover deck. Figure 10.3 shows the UVS at the beginning of the mission (sol 36, left panel) and approximately two Martian years later (sol 1314, right panel).

Design constraints ruled out any active protection system, although each photodiode was embedded in a samarium cobalt magnetic ring to deflect the trajectories of falling dust and thus mitigate the dust degradation effect (Gómez-Elvira et al., 2014). Nominal UVS operations lasted until sol 154, when for the first time degradation of the UVS due to dust deposition led to deviations from nominal values in the ENVRDR products above 10%, with increasing deviations in time.

Dust deposited on the UVS causes underestimation in measured UV fluxes and complicates the analyses of the seasonal and interannual evolution of UV radiation at the surface of Gale Crater. As an example, we show UVA fluxes measured on sols 76 and 745 in Figure 10.4. Since Mastcam dust opacity values and Sun-Mars distance were roughly the same on both sols ($\tau = 0.78$ and $L_s \sim 193^o$), similar UVA levels are expected. However, UVA fluxes measured during the second Martian year of the mission (blue curve) are significantly lower than during the first year (red curve).

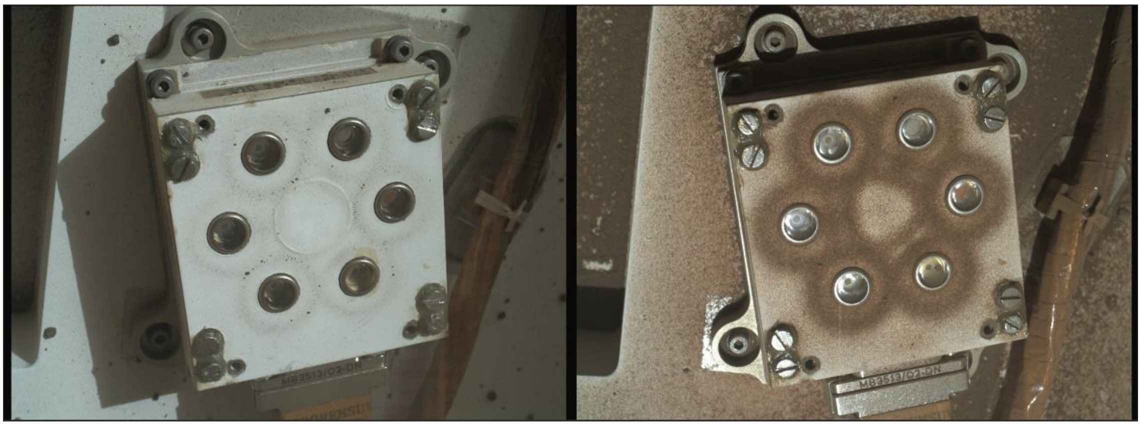

Figure 10.3. MAHLI images of the REMS UVS on sols 36 (left) and 1314 (right). A significant amount of dust has been deposited on the sensor, especially around the circular magnets that surround each photodiode.

10.4. Correction of UVA data from the effects of the angular response

As shown in Section 10.2, the use of an angular response calibration function that has a discontinuity at a solar zenith angle of $\theta = 30^o$ (Figure 10.1 (a)) causes an artificial discontinuity in UV fluxes (Figure 10.1 (b), red curve). We have developed a methodology to obtain physically consistent empirical calibration functions for each UVS channel that do not show discontinuities at $\theta = 30^o$. In addition to their dependence on the solar zenith angle (as in Figure 10.1 (a)), our calibration functions also consider a dependence on the azimuth angle with respect to the rover frame (ϕ), which, according to our preliminary results for the UVA channel, exists. This is necessary for producing physically consistent data products. The sequential steps followed to derive corrected angular responses as a function of θ and ϕ are:

1. From the analysis of the position of the Sun relative to the rover frame (ADR products), we select measurements of photodiode output currents (TELRDR products) on each sol taken when ϕ is outside the range from -100º to 10º. This way, we avoid shadows cast over the UVS by the presence of the masthead and the mast of the rover, which would lead to the generation of inaccurate angular response calibration functions.
2. Among the measurements selected in step 1, we select those corresponding to sols when measurements at $\theta = 20^o$ were taken because the output current signal is very accurate at this angle (signal is stronger when the Sun is close to the zenith) and because UVS measurements at $\theta = 20^o$ show the best coverage throughout the mission.
3. On each sol with measurements at $\theta = 20^o$ and ϕ outside the range from -100º to 10º, we normalize measurements of output currents to the measurement taken at

θ = 20º. By doing this, the effects in the output current due to dust opacity, distance to the Sun and dust deposition are taken into account.

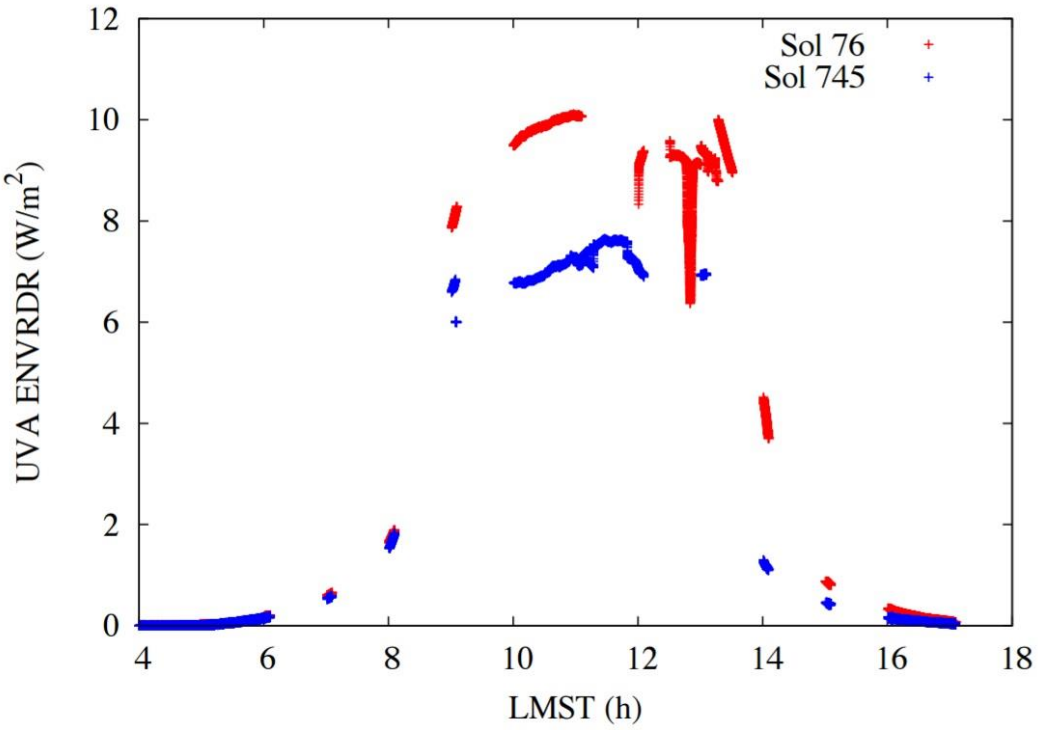

Figure 10.4. Diurnal evolution of UVA ENVRDR data on sols 76 and 745, separated by one Martian year and with roughly the same opacity, as indicated by independent opacity measurements by Mastcam. The sudden decrease in UVA flux at about 13 LMST on sol 76 is due to a partial shadow cast over the UVA channel. Despite the fact that similar values of UV fluxes are expected, UVA fluxes on sol 745 are significantly lower because of the effects of dust deposited on the sensor.

4. We bin the normalized measurements as a function of sol number, ϕ and θ. Each bin has a width of 10º in ϕ and 1º in θ.
5. For each bin in ϕ, we obtain a curve as a function of θ calculated by averaging normalized measurements using available sols for each θ.
6. We simulate the UV flux at the surface as a function of θ using a Monte Carlo radiative transfer model (Vicente-Retortillo et al., 2017) and we normalize the values to that at θ = 20º.
7. We obtain the angular response for each bin in ϕ by calculating the ratio between the curves obtained in steps 5 and 6, and then we further normalize this ratio to the value at θ = 0º. Curves for the initially missing values of ϕ are obtained by interpolation.

The top panel of Figure 10.5 shows the corrected angular response calibration function obtained for the UVA channel following the steps described above, as well as the current UVA angular response. The corrected angular response calibration function does not show discontinuities at θ = 30º nor a constant value beyond. Additionally, for a

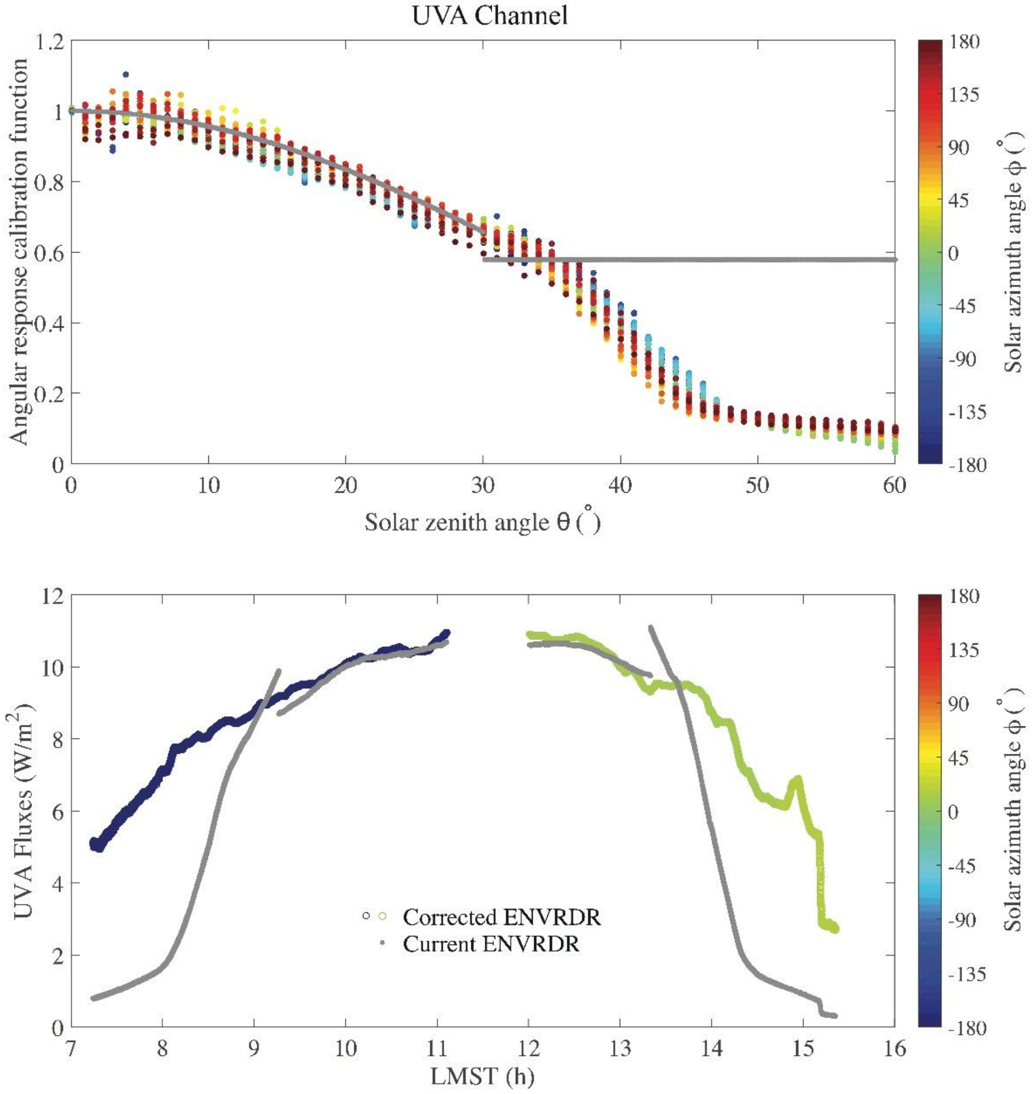

Figure 10.5. (Top) Current (gray) and corrected (colored as a function of ϕ) UVA angular response calibration functions. The corrected angular response calibration function produces a significant improvement in the data because: (1) it does not present a discontinuity at θ = 30º, (2) it does not show a constant value beyond 30º, and (3) it considers the significant variations with respect to ϕ for a given value of θ. (Bottom) Current (gray) and corrected (colored as a function of ϕ) UVA ENVRDR products on sol 91. Corrected UVA fluxes are very similar to the values stored at the PDS when θ < 20º, but they differ significantly beyond 20º due to differences in the angular responses.

given value of θ it shows significant variations with respect to ϕ. By applying this angular response to UVA photodiode output currents measured on sol 91 (L_s ~ 203º), we obtain corrected UVA fluxes shown in the bottom panel of Figure 10.6 (blue and green curves, the color indicating the solar azimuth angle relative to the rover frame). Current ENVRDR UVA fluxes (gray curve) are shown for comparison. The agreement between current and corrected UVA fluxes is very good when θ < 20º, while for θ > 20º differences between current and corrected UVA fluxes are significant due to differences in angular responses.

10.5. Correction of UVA data from the effects of dust deposition

We have developed a methodology to correct UV fluxes from the effect of dust deposition by calculating a parameter (hereinafter called dust attenuation factor) that depends only on the amount of dust deposited on the UVS and thus can be used to quantify this effect. The dust attenuation factor is obtained from photodiode outputs currents (TELRDR products), ancillary data records containing the geometry of the rover and the position of the Sun with respect to it (ADR products) and Mastcam dust opacities as explained below:

1. We select the daily maximum value of the photodiode output current on those sols when Mastcam performed measurements of dust opacity.
2. We correct each daily maximum value from the effect of the Sun-Mars distance by normalizing the measured values by the variations in Sun-Mars distance.
3. We correct the values obtained in the previous step from the effect of the angular response. This is done using corrected angular response calibration functions (top panel of Figure 10.5).
4. We correct the values obtained in the previous step from the effect of the solar zenith angle by dividing them by the cosine of the solar zenith angle at the TOA.
5. We use Mastcam opacity values and our model COMIMART (Vicente-Retortillo et al., 2015) to remove the effect of dust opacity from results obtained in the previous step.
6. We normalize the values obtained in step 5 to those of the first sol on which Mastcam measured the opacity on Mars (sol 33) to set the value of the dust attenuation factor equal to one at the beginning of the mission.

If dust had not been deposited on the UVS, there would be no attenuation in the UVS signal and therefore the values obtained in step 5 would be constant throughout the mission. Since this is not the case (see Figures 10.3 and 10.4), the dust attenuation factor obtained following the 6 steps described above varies with sol number. As an example, we show the dust attenuation factor calculated for the UVA channel in the top panel of Figure 10.6. A dust attenuation factor value equal to 1 indicates that there is no additional attenuation caused by deposited dust compared to the beginning of the mission, while a value equal to 0.5 indicates that 50% of the incoming radiation is attenuated by dust deposited on the sensor. The quantitative and qualitative behavior of the dust attenuation factor shown in Figure 10.6 is consistent with that obtained following a different approach by Smith et al. (2016), including the increase observed between sols 840 and 920.

By applying the UVA dust attenuation factor to output currents measured on sols 76 and 745, we obtain corrected UVA fluxes shown in the bottom panel of Figure 10.6. Corrected values of UVA fluxes on both sols are now similar (compared to those shown in Figure 10.4), as expected on sols separated by one Martian year and with a similar opacity retrieved from Mastcam measurements. Differences between both sols are mostly explained by differences in rover orientation and tilt, changes in the orientation of the masthead of the rover and by uncertainties in the derived dust attenuation factor (see Section 10.6).

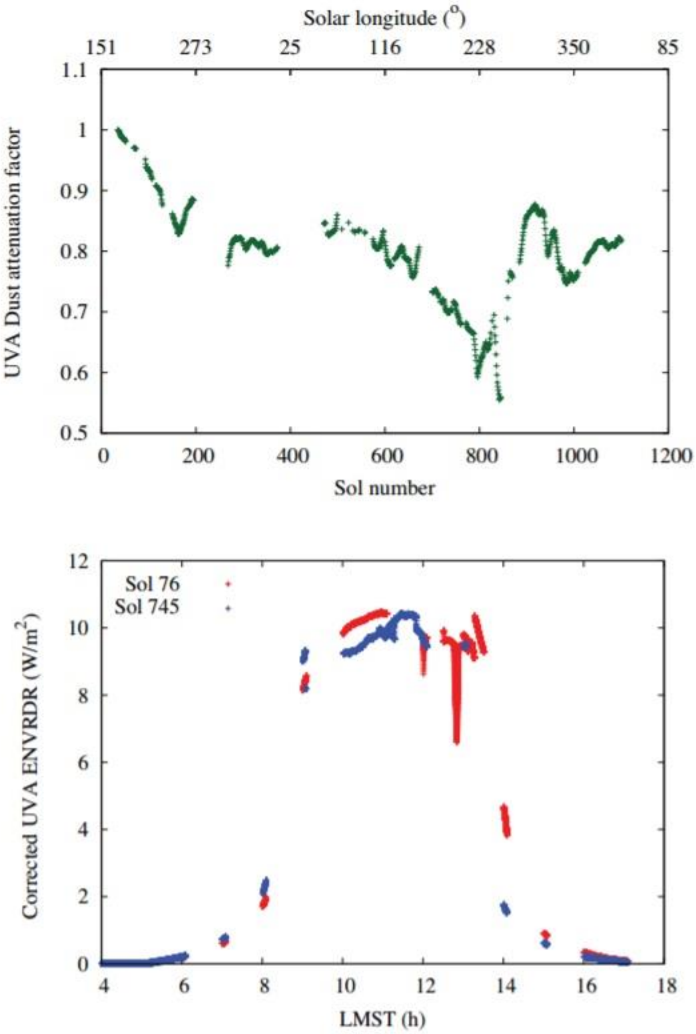

Figure 10.6. (Top) Temporal evolution of the dust attenuation factor obtained for the UVA channel. (Bottom) Corrected UVA fluxes on sols 76 and 745 using the dust attenuation factor shown in the top panel. In contrast to the UVA fluxes shown in Figure 10.4 (current values), corrected UVA fluxes show similar values on both sols, as expected on sols separated by one Martian year and with a similar opacity retrieved from Mastcam measurements.

10.6. Evaluation of Expected Uncertainties in Corrected Products

The original functional requirements of REMS photodiodes were to deliver UV fluxes with an accuracy better than 10% with respect to maximum expected values (Gómez-Elvira et al., 2012). UV fluxes in ENVRDR and MODRDR products currently available in the PDS include an estimated uncertainty of 10% during the first 154 sols. After sol 154, the uncertainty is considered to be above 10% because of dust deposition on the sensor.

Most of the uncertainty in the current UV fluxes derived from measurements during the first 154 sols is caused by the application of an angular response calibration function that does not include a dependence on the solar azimuth angle with respect to rover frame, and that has a discontinuity at $\theta = 30^{o}$ and a constant value when $\theta > 30^{o}$ (Figure 10.1 (a)). We have calculated the spread of the corrected UVA angular response calibration function that we have derived with respect to ϕ for a fixed value of θ and have observed that the relative standard deviation is below 5% for $\theta < 37^{o}$, peaks at 20% for $\theta = 45^{o}$, and decreases to values below 10% when $48^{o} < \theta < 59^{o}$ (top panel of Figure 10.5). In addition, there are large discrepancies between the corrected and the current UVA angular response when $\theta > 30^{o}$ (top panel of Figure 10.5). For these two reasons, the overall accuracy of the corrected data products is expected to be better than the current one, especially when $30^{o} < \theta < 60^{o}$.

The main uncertainties in the corrected ENVRDR products are caused by inaccuracies in the corrected angular response calibration function and the obtained dust attenuation factor. Next, we show a preliminary evaluation of expected uncertainties due to the correction from both effects.

The uncertainties in the corrected UVA angular response calibration function (top panel of Figure 10.5) can be quantified by calculating the standard deviation between values corresponding to a fixed pair of θ and ϕ values on different sols. Our preliminary analysis indicates that the standard deviations averaged over ϕ are below 7% with a mean value of 4% for $\theta < 60^{o}$. In order to quantify the uncertainties due to the application of the dust attenuation factor (top panel of Figure 10.6), we plan to generate an ensemble of dust attenuation factors for each UVS channel calculated following the methodology explained in Section 10.5 but using a quantity different from the daily maximum in the TELRDR products (see step 1 in Section 10.5). As an example, we have performed preliminary estimations of UVA dust attenuation factors using four additional quantities: the photodiode output current value at 10 am, 11 am, 12 pm and at the time when θ is the lowest (when the photodiode output current is expected to be close to but not necessarily coincide with the daily maximum). The dust attenuation factors obtained using these four quantities follow a similar trend to that shown in the top panel of Figure 10.6 obtained using the daily maximum in the TELRDR products. The relative standard deviation shows a moderate sol-to-sol variability, but it is below 10% for 98% of the sols and its mean value remains below 5%. In any case this dust attenuation factor will improve the accuracy of the UV measurements because dust deposition has occasionally caused errors of more than 30%, as shown in Figure 10.6.

We expect the uncertainties in corrected UV fluxes to be lower than the current value, which is 10% in the first 154 sols of the MSL mission. By performing an exhaustive analysis of the measurements and of the corrected values we will provide a more accurate estimation of the uncertainties. As a final example of the performance of our methodology after correcting from the effects of dust deposition and inaccuracies in the angular response, Figure 10.7 shows current and corrected ENVRDR UVA fluxes on sol 730. The corrected values do not present discontinuities at $\theta = 30^{o}$. In addition, the accuracy of the fluxes for lower zenith angles is improved and the effect of dust deposition on the sensor is quantified.

Our final objective is to calculate the corrected values for every measurement on every sol for the six channels of the UVS sensor and to estimate their uncertainties.

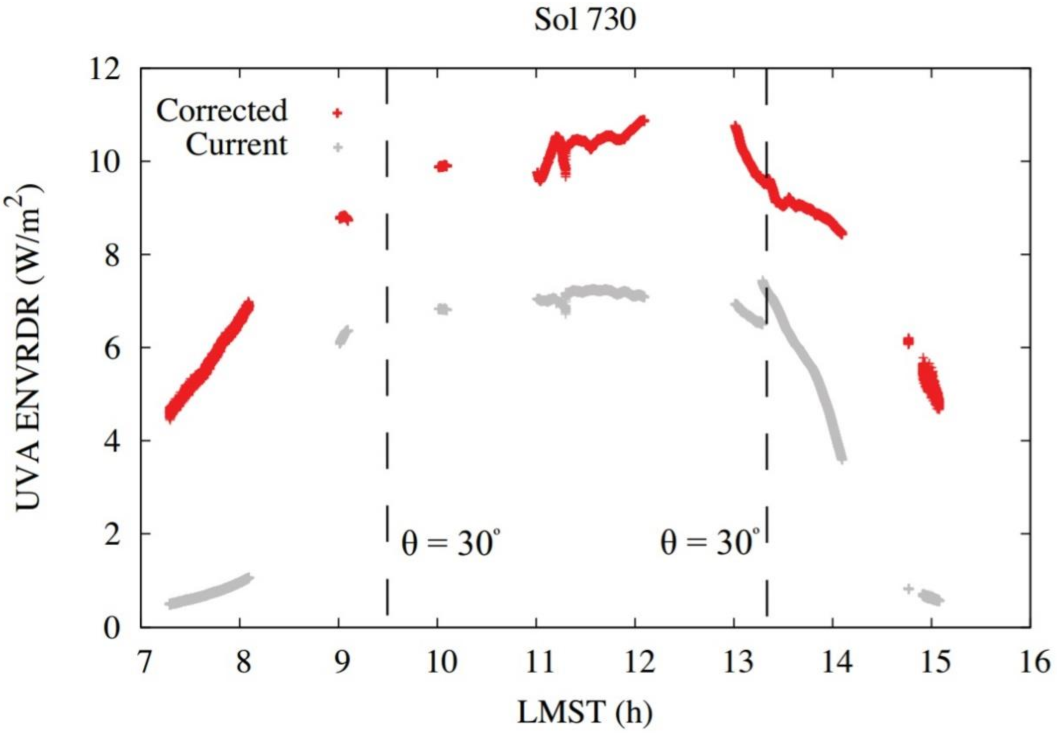

Figure 10.7. Current (gray) and corrected (red) UVA fluxes on sol 730. The red curve is obtained by correcting the gray curve from the effects of dust deposition and inaccuracies in the angular response. Our corrected values at around noon result in UVA fluxes 60 % greater than current values.

10.7. Applications of the corrected data

The generated corrected data products (ENVRDR and MODRDR) will allow:

1. To assess risks of UV radiation and dust to the health of human explorers (MEPAG’s Goal IV: B6).
2. To analyze the relation between seasonal changes in UV radiation at Gale Crater and seasonal patterns found in the background methane concentration to test for the presence of biogenic gases that could migrate from habitable deep subsurface environments to surface environments (MEPAG’s Goal III: A1.3).
3. To compare the UV radiation environment at different locations, as two Mars missions carrying UV sensors in their payloads are scheduled within the next years (ExoMars Surface Science Platform in 2020, and NASA's Mars 2020).

The results of this work are important for habitability studies because UV radiation is linked to biological effects and potential survival of organisms at the surface of Mars (Cockell et al., 2000; Patel et al., 2004). Values of UV fluxes at the surface in combination with results from radiative transfer modeling are needed to calculate biologically weighted irradiances for DNA damage (Córdoba-Jabonero et al., 2003; Patel et al. 2004), particularly values of UVB, UVC and UVD. Corrected UV fluxes are also useful to analyze temporal variations in dust aerosol properties (Vicente-Retortillo et al., 2016b; Vicente-Retortillo et al., 2017), which has a strong impact on the atmospheric dynamics and climate of Mars (Read and Lewis, 2004; Madeleine et al., 2011). Finally, corrected UVD and UVE fluxes can provide ground-truth to measurements by the MARCI instrument on board the Mars Reconnaissance Orbiter satellite (Gómez-Elvira et al., 2012; Wolff et al., 2010).

Chapter 11. Studies associated with Mars 2020 MEDA instrument

11.1. The Mars 2020 mission

The Mars 2020 rover mission is part of NASA's long-term Mars Exploration Program. The mission is scheduled to be launched in July or August 2020. After the third Mars 2020 Landing Site Workshop, the number of locations proposed as potential landing sites was reduced from eight to three. The two preferred landing sites after this workshop are Jezero Crater (18.85ºN, 77.52ºE) and NE Syrtis (18ºN, 77ºE); a third location, Columbia Hills (14.55ºS, 175.63ºE), remains as candidate because its current unfavorable evaluation compared to the other two landing sites might substantially change after revision, as indicated by the Project Scientist and the Deputy Project Scientist of the mission.

Mars 2020 will contribute to the four main science goals of the aforementioned Mars Exploration Program:

1. Determine whether life ever existed on Mars.
2. Characterize the climate of Mars.
3. Characterize the geology of Mars.
4. Prepare for human exploration of the planet.

The Mars 2020 rover is based on the MSL rover, but it includes upgraded instruments that will allow a better understanding of Mars, particularly regarding the four scientific objectives of the Mars Exploration Program.

Among the proposed scientific instruments, NASA has announced the selection of the following payload:

1. Mastcam-Z, a camera system with zoom capability which will mainly allow studies of the mineralogy of the surface, but will also allow opacity retrievals.
2. The Mars Oxygen ISRU Experiment (MOXIE), an instrument to investigate exploration technologies, which will produce oxygen from the abundant carbon dioxide of the atmosphere.
3. Planetary Instrument for X-ray Lithochemistry (PIXL), which will allow a detailed analysis of the chemical elements of the Martian surface.
4. The Radar Imager for Mars' Subsurface Exploration (RIMFAX), which will provide a very high resolution of the geologic structure of the subsurface.
5. Scanning Habitable Environments with Raman & Luminescence for Organics and Chemicals (SHERLOC), the first UV Raman spectrometer to fly to the Martian surface, and which can also detect organic compounds.

6. SuperCam, an instrument that can provide imaging, chemical composition analysis and mineralogy of the Martian surface, and which can also detect organic compounds from a distance.

7. Mars Environmental Dynamics Analyzer (MEDA), which is described in detail below.

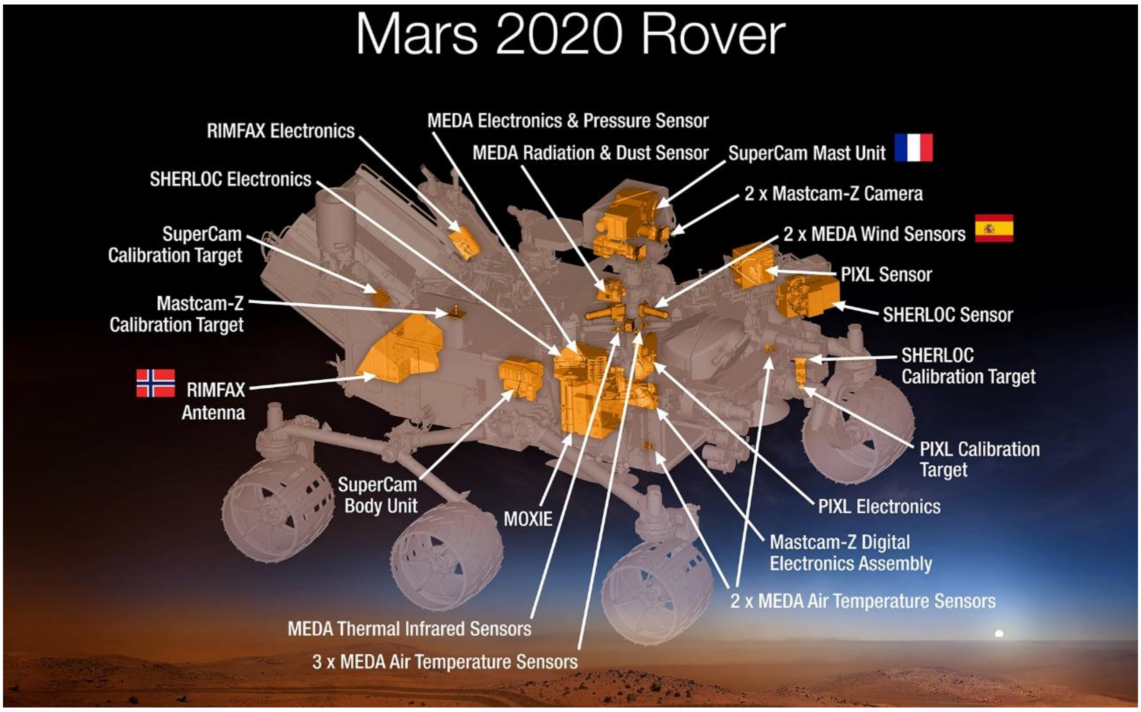

Figure 11.1. Scientific payload of the Mars 2020 mission. Image credit: NASA.

11.2. The Mars Environmental Dynamics Analyzer (MEDA)

The Mars Environmental Dynamics Analyzer is a suite of environmental instruments that address investigation goals related with points 2 and 4 of the Mars Exploration Program: perform measurements of atmospheric parameters at the Martian surface, and characterize size and shape of the Martian dust. In particular, MEDA contains a wind sensor (WS), a pressure sensor (PS), a relative humidity sensor (HS), five air temperature sensors (ATS), a thermal infrared sensor (TIRS) and the radiation and dust sensor (RDS) which includes a camera (SkyCam) (Rodriguez-Manfredi et al., 2016).

The MEDA baseline strategy for data acquisition consists of measurements performed at a frequency of 1 Hz during 30 minutes per hour, although this operational plan might change based on power and data volume availability (Rodriguez-Manfredi et al., 2017). The selected payload and operational strategy will ensure investigations on:

1. The radiative (and physical) properties of the local atmospheric suspended particles, such as opacity (and, therefore, particle abundance) and scattering phase function (and, thus, size distribution and shape).

2. The relationship between these properties and the meteorological cycles in diurnal, seasonal and interannual timescales.

3. The diurnal, seasonal and interannual cycles of the solar UV, visible and NIR radiation at the Martian surface.
4. The local fluxes of energy and H_2O between the surface and the atmosphere.
5. The agreement between modeling results and MEDA observations.
6. The conditions leading to dust lifting and the effects of the local wind regimes on the dust cycle and variability.
7. The environmental context for weathering and preservation potential of a possible cache sample.
8. The differences and similarities between the environmental variables at the Mars 2020 location and those at Viking, Phoenix, Pathfinder, and Mars Science Labortory landing sites.
9. The relationship between the surface environment and the large-scale dynamics observed from orbiters.
10. The effect of environmental parameters on the MOXIE efficiency.

In Sections 11.3 and 11.4 we describe the two sensors to which we expect to devote most of our research efforts in the context of the Mars 2020 mission: TIRS and RDS.

11.3. The Thermal InfraRed Sensor (TIRS)

The Thermal InfraRed Sensor (TIRS) is one of the six instruments included in MEDA (Pérez Izquierdo et al., 2016). It has been designed to measure:

1. The net thermal infrared radiation at the surface
2. The near-surface air temperature
3. The surface reflectance of solar visible and near infrared radiation
4. The skin brightness temperature of the surface.

Moreover, in combination with measurements of other MEDA measurements, it will allow the quantification of:

1. The total surface energy budget
2. The local surface albedo
3. The thermal inertia of the local terrain

The TIRS instrument contains five channels. The spectral bands, pointing angles and measured quantities of these channels are summarized in Table 11.1. TIRS measurements will provide information on three of the four quantities needed to quantify the radiation budget at the surface: upward and downward longwave radiation and upward shortwave radiation; the fourth quantity (downward shortwave radiation) will be provided by the panchromatic channel of the RDS (CH 7, TOP, see Section 11.4). TIRS includes one channel measuring in the CO_2 absorption band at 15 μm that will provide retrievals of the near surface atmospheric temperature, and a fifth channel, which has already been used to retrieve ground temperature and surface thermal inertia at the MSL location (Gómez-Elvira et al., 2012; Hamilton et al., 2014; Martínez et al., 2014).

Figure 11.2. TIRS bread board model. Figure from Pérez Izquierdo et al., 2016.

Channel	Pointing angle	Filter band (µm)	Purpose
IR1	+35º (upward)	6.5-30	Downward LW
IR2	+35º (upward)	14.5-15.5	Air temperature
IR3	-35º (downward)	0.3-3	Upward SW
IR4	-35º (downward)	6.5-30	Upward LW
IR5	-35º (downward)	8-14	Ground temperature

Table 13.1. Description of the channels of the TIRS instrument (Pérez Izquierdo et al., 2016).

The TIRS will be accommodated on the Remote Sensing Mast of the rover at a height of 1.5 m, and each channel will have an external FOV of ±20º in the horizontal direction and of ±10º in the vertical direction. The pointing angles and FOV of the sensor ensure a homogeneous composition of the observed terrain and minimize the effect of the rover.

11.4. The Radiation and Dust Sensor (RDS)

MEDA includes as part of its payload a Radiation and Dust Sensor (RDS), which also contains the SkyCam camera (Apéstigue et al., 2015). The main objectives of the instrument are to characterize in different timescales:

1. Dust opacity
2. Dust particle size distribution
3. Dust morphology
4. UV fluxes at the surface
5. Shortwave fluxes at the surface
6. Ozone abundance

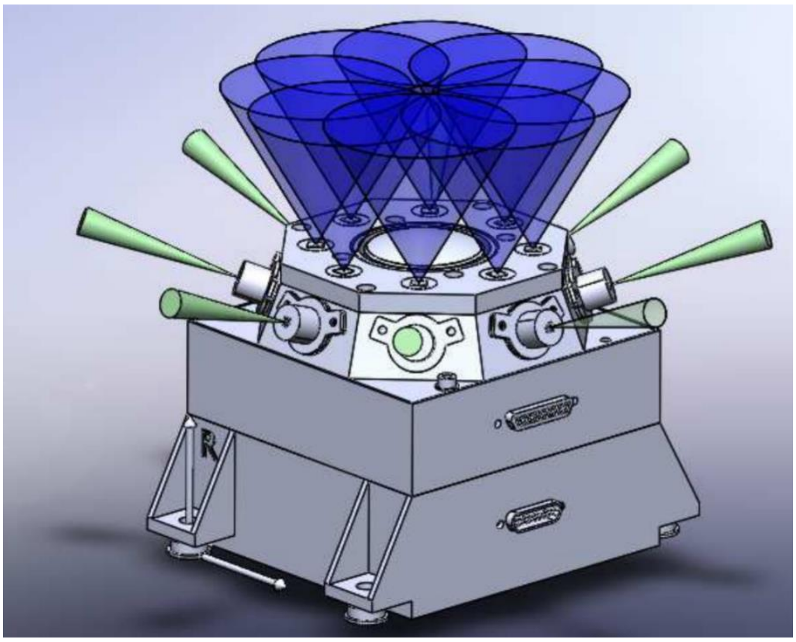

Figure 11.3. Schematic model of the Radiation and Dust Sensor, showing the FOV of the photodiodes. CH7 of the upward looking photodiodes will finally have a FOV of ±90º (not shown). Figure from Apéstigue et al., 2015.

Channel	Pointing angle (º)	Spectral band (nm)	Purpose
CH1, TOP	0	255±5	O_3 column abundance
CH2, TOP	0	295±5	O_3 column abundance
CH3, TOP	0	250-400	UV radiation at the surface
CH4, TOP	0	450±40	Dust opacity and particle size. Dust deposition.
CH5, TOP	0	650±25	Dust opacity and particle size. Dust deposition.
CH6, TOP	0	750±5	Dust opacity and particle size. Dust deposition.
CH7, TOP	0	190-1100	Shortwave flux at the surface
CH8, TOP	0	950±50	Dust opacity and particle size.
CH1, SIDE	N.A.	750±5	Dark current estimation
CH 2-7, SIDE	70	750±5	Sky brightness mapping.
CH 8, SIDE	55	750±5	Sky brightness mapping.

Table 11.2. Description of the RDS photodiodes.

The RDS contains eight photodiodes looking upward, a second set of side-looking photodiodes and the dedicated camera. It will be located on the rover deck. The looking upward photodiodes will have a FOV of ±15º, except Channel 7, which will have a FOV of ±90º. The side looking photodiodes will have a narrower FOV (±5º, except Channel 1, which will be blind) and will be separated by approximately 45º in azimuth. The spectral bands, pointing angles and measured quantities of the photodiodes are summarized in Table 11.2.

Channels 1 and 2 of the upward looking set of photodiodes will provide information on the ozone column abundance. Channel 1 measures in the center of the Hartley absorption band and channel 2 measures in the edge of the band; since the ozone absorption cross-section is different in the two channels, the ratio between the absorbed radiation in the two spectral regions depends on the amount of ozone in the atmosphere. Channel 3 will provide information on the UV radiation levels, as well as on their diurnal, seasonal and interannual variability. Channels 4, 5, 6 and 8 will provide dust opacity values; by analyzing the wavelength dependence of the retrieved opacities, additional information on dust particle size will be obtained. Channels 4 and 6 will also allow a cross-calibration with MastCam-Z (see Section 11.1): the differences between the opacities retrieved with these channels and with their counterparts of MastCam-Z will provide an estimation of the amount of dust deposited on the RDS. Similarly, channel 5 could also provide an estimation of the dust deposited both on the sensor. Channel 7 will provide a measurement that will be used as a proxy to estimate the total shortwave flux at the surface, which is very useful in order to quantify the surface energy budget (see Section 11.3).

The side looking set of photodiodes will provide maps of the sky brightness. As shown in Vicente-Retortillo et al. (2017), the sky brightness is affected by the dust scattering phase function. Therefore, these measurements will provide information on dust particle size and shape.

11.5. Future research

In the context of the TIRS instrument, we plan to develop a radiative transfer model for thermal infrared radiation in preparation for future data analysis. The first step will be to determine the spectral radiative properties of the Martian atmosphere in the TIRS spectral range (6-30 μm). In the second step, we will develop a scheme to calculate the longwave radiation spectral irradiances and total fluxes at the Martian surface. In the third step, we will adapt the radiative transfer model to the viewing geometry of the TIRS channels. The combination of modeling results and observations will allow the retrievals of infrared opacities, which in turn could provide information on the effective radius of the size distribution, since the ratio between opacities at different wavelengths depends on the particle size (Medvedev et al., 2011).

Focusing on the RDS instrument, we plan to adapt our methodology to retrieve dust aerosol particle size from REMS and Mastcam measurements (Vicente-Retortillo et al., 2017) to the specifications of these photodiodes. In particular, we will perform simulations using our Monte Carlo radiative transfer model for the different spectral bands. Opacities could also be retrieved from the comparison between measurements during shadow events and measurements in which the direct beam is not blocked by the rover (Vicente-Retortillo et al., 2015b). A comparison between these results and those obtained with other methods can be performed, assessing this way the confidence in the retrieved quantities.

Bibliography

Apéstigue, V., Arruego, I., Martínez, J., Jiménez, J. J., Rivas, J. et al. (2015). Radiation and Dust Sensor for MARS2020: technical design and development status overview. European Planetary Science Congress 2015, 27 September - 2 October, 2015, Nantes, France. Vol. 10, EPSC2015-813.

Berk, A., Bernstein, L. S., Anderson, G. P., Acharya, P. K., Robertson, D. C., Chetwynd, J. H., and Adler-Golden, S. M. (1998). MODTRAN cloud and multiple scattering upgrades with application to AVIRIS. *Remote Sens. Environ.*, 65, 367-375, doi:10.1016/S0034-4257(98)00045-5.

Bridger, A. F., J.R. Murphy (1998). Mars' surface pressure tides and their behavior during global dust storms. *J. Geophys. Res*. 103(E4), 8587–8601.

Clancy, R. T., Wolff, M. J., and Christensen, P. R. (2003). Mars aerosol studies with the MGS TES emission phase function observations: Optical depths, particle sizes, and ice cloud types versus latitude and solar longitude, *J. Geophys. Res.*, 108, 5098, doi:10.1029/2003JE002058.

Cockell, C. S., Catling, D. C., Davis, W. L., Snook, K., Kepner, R. L., Lee, P., and McKay, C. P. (2000). The ultraviolet environment of Mars: biological implications past, present, and future. *Icarus*, 146(2), 343-359.

Cockell, C.S. and J. A. Raven (2004), Zones of photosynthetic potential on Mars and the early Earth, *Icarus*, 169, 300-310, doi:10.1016/j.icarus.2003.12.024.

Colburn, D. S., Pollack, J. B., Haberle, R. M. (1989). Diurnal variations in optical depth at Mars. Icarus, 79 (1), 159-189, doi: 10.1016/0019-1035(89)90114-0.

Córdoba-Jabonero, C., L.M. Lara, A.M. Mancho, A. Márquez, and R. Rodrigo (2003), Solar ultraviolet transfer in the Martian atmosphere: biological and geological implications, *Planet. Space Sci.*, 51, 399–410, doi: 10.1016/S0032-0633(03)00023-0.

Dlugach, Z. M., Korablev, O. I., Morozhenko, A. V., Moroz, V. I., Petrova, E. V., and Rodin, A. V. (2003). Physical properties of dust in the Martian atmosphere: Analysis of contradictions and possible ways of their resolution. *Sol. Syst. Res.*, 37(1), 1-19.

Encrenaz, T., Greathouse, T. K., Lefèvre, F., and Atreya, S. K. (2012). Hydrogen peroxide on Mars: Observations, interpretation and future plans. Planet. Space Sci., 68 (1), 3-17, doi:10.1016/j.pss.2011.03.019.

Frederick, J. E., and Mentall, J. E. (1982). Solar irradiance in the stratosphere: Implications for the Herzberg continuum absorption of O_2. *Geophys. Res. Lett.*, 9 (4), 461-464, doi: 10.1029/GL009i004p00461.

Gómez-Elvira, J., et al. (2012), REMS: The Environmental Sensor Suite for the Mars Science Laboratory Rover, *Space Sci. Rev.*, 170, 583-640, doi:10.1007/s11214-012-9921-1.

Gómez-Elvira, J., et al. (2014), Curiosity's rover environmental monitoring station: Overview of the first 100 sols, *J. Geophys. Res. Planets*, 119, 1680–1688, doi:10.1002/2013JE004576.

González-Galindo, F., López-Valverde, M. A., Angelats i Coll, M., and Forget, F. (2005). Extension of a Martian general circulation model to thermospheric altitudes: UV heating and photochemical models. *J. Geophys. Res. Planets*, 110(E9).

Greeley, R., D. Waller, N. Cabrol, G. Landis, M.T. Lemmon, L. Neakrase, M.P. Hoffer, S. Thompson, P. Whelley (2010). Gusev crater, Mars: observations of three dust devil seasons. *J. Geophys. Res*. 115, E00F02, doi:10.1029/2010JE003608

Grotzinger, J.P., et al. (2012). Mars Science Laboratory Mission and Science Investigation, *Space Sci. Rev.*, 170, 5-56, doi:10.1007/s11214-012-9892-2.

Guzewich, S.D., C.E. Newman, M. de la Torre Juárez, R.J. Wilson, M. Lemmon, M.D. Smith, H. Kahanpää, A.M. Harri (2016). Atmospheric tides in Gale Crater, Mars. *Icarus* 268, 37–49.

Haberle, R. M., B.L. Conway, J.B. Pollack. (1982). Some effects of global dust storms on the atmospheric circulation of Mars, Icarus, 50(2–3), 322–367.

Haberle, R. M., McKay, C. P., Pollack, J. B., Gwynne, O. E., Atkinson, D. H., Appelbaum, J., Landis, G. A., Zurek, R. W. and Flood, D. J. (1993). Atmospheric effects on the utility of solar power on Mars. In: Lewis, J. S., Matthews, M. S., Guerrieri, M. L. (Eds.), Resources of Near-Earth Space. The University of Arizona Press, Tuscon, 845–885.

Haberle, R. M., et al. (2014). Preliminary interpretation of the REMS pressure data from the first 100 sols of the MSL mission, J. Geophys. Res. Planets, 119, 440–453, doi:10.1002/2013JE004488.

Hamilton, V. E., A.R. Vasavada, E. Sebastián, M. Torre-Juárez, M. Ramos, C. Armiens, R.E. Arvidson, I. Carrasco, P.R. Christensen, M.A. De Pablo, W. Goetz (2014). Observations and preliminary science results from the first 100 sols of MSL Rover Environmental Monitoring Station ground temperature sensor measurements at Gale Crater. *J. Geophys. Res., Planets* 119(4), 745–770.

Hanel, R., Conrath, B., Hovis, W., Kunde, V., Lowman, P. et al. (1972). Investigation of the Martian environment by infrared spectroscopy on Mariner 9. *Icarus*, 17, 423–42, doi:10.1016/0019-1035(72)90009-7.

Hansen, J.E., and L.D. Travis (1974), Light scattering in planetary atmospheres. *Space Sci. Rev.*, 16, 527–610.

Harri, A. M., et al. (2014a). Pressure observations by the Curiosity rover: Initial results. *J. Geophys. Res. Planets*, 119(1), 82-92.

Harri, A. M., M. Genzer, O. Kemppinen, J. Gomez-Elvira, R.M. Haberle, J. Polkko, H. Savijärvi, N. Rennó, J.A. Rodriguez-Manfredi, W. Schmidt, M. Richardson (2014b). Mars Science Laboratory relative humidity observations: initial results. *J. Geophys. Res. Planets* 119(9), 2132–2147.

Harri, A. M., et al. (2017). The MetNet vehicle: a lander to deploy environmental stations for local and global investigations of Mars. *Geoscientific Instrumentation, Methods and Data Systems*, 6(1), 103.

Henyey, L. G., and Greenstein, J. L. (1941). Diffuse radiation in the galaxy. *Astrophys. J.*, 93, 70-83.

Ityaksov, D., Linnartz, H., and Ubachs, W. (2008). Deep-UV absorption and Rayleigh scattering of carbon dioxide. *Chem. Phys. Lett.*, 462 (1), 31-34, doi: 10.1016/j.cplett.2008.07.049.

Iwabuchi, H. (2006). Efficient Monte Carlo methods for radiative transfer modeling. *J. Atmos. Sci*., 63, 2324-2339.

Joseph, J. H., Wiscombe, W. J., and Weinman, J. A. (1976). The delta-Eddington approximation for radiative flux transfer. *J. Atmos. Sci*., 33 (12), 2452-2459, doi: 10.1175/1520-0469(1976)033<2452:TDEAFR>2.0.CO;2.

Kahre, M. A., Murphy, J. R. and Haberle, R. M. (2006). Modeling the Martian dust cycle and surface dust reservoirs with the NASA Ames general circulation model, *J. Geophys. Res.*, 111, E06008, doi:10.1029/2005JE002588.

Kahre, M.A., J.L. Hollinsworth, R.M. Haberle and J.R. Murphy (2008), Investigations of the variability of dust particle sizes in the martian atmosphere using the NASA Ames General Circulation Model, *Icarus*, 195, 576-597, doi: 10.1016/j.icarus.2008.01.023.

Lefèvre, F., Montmessin, F., Määttänen, A., and Bertaux, J. L. The Martian Ozone Layer as Seen by SPICAM: 2004-2011. In: The Fifth International Workshop on the Mars Atmosphere: Modelling and Observation (Oxford, U.K., January 2014). Edited by F. Forget and M. Millour, id.3403.

Lemmon, M. T., Wolff, M. J., Smith, M. D., Clancy, R. T., Banfield, D., et al. (2004). Atmospheric imaging results from the Mars exploration rovers: Spirit and Opportunity. *Science*, 306(5702), 1753-1756.

Lemmon, M.T., M.J. Wolff, J.F. Bell III, M.D. Smith, B.A. Cantor, and P.H. Smith (2015), Dust aerosol, clouds, and the atmospheric optical depth record over 5

Mars years of the Mars Exploration Rover mission, *Icarus*, 251, 96–111, doi: 10.1016/j.icarus.2014.03.029.

Lewis, B. R., and Carver, J. H. (1983). Temperature dependence of the carbon dioxide photoabsorption cross section between 1200 and 1970 Å. *J. Quant. Spectrosc. Ra.*, 30 (4), 297-309, doi: 10.1016/0022-4073(83)90027-4.

Lilensten, J., Coates, A. J., Dehant, V., De Wit, T. D., Horne, R. B., Leblanc, F., Luhmann, J., Woodfield, E. and Barthélemy, M. (2014). What characterizes planetary space weather? *Astron. Astrophys. Rev.*, 22 (1), 1-39, doi: 10.1007/s00159-014-0079-6.

Lin, C. L., Rohatgi, N. K., and DeMore, W. B. (1978). Ultraviolet absorption cross sections of hydrogen peroxide. *Geophys. Res. Lett.*, 5 (2), 113-115, doi: 10.1029/GL005i002p00113.

Määttänen, A. and H. Savijärvi (2004). Sensitivity tests with a one-dimensional boundary-layer Mars model. *Bound.-Layer Meteorol*. 113(3), 305–320.

Mahaffy, P. R., Webster, C. R., Atreya, S. K., Franz, H., Wong, M., et al. (2013). Abundance and isotopic composition of gases in the martian atmosphere from the Curiosity rover. *Science*, 341(6143), 263-266.

Madeleine, J.-B., F. Forget, E. Millour, L. Montabone, and M.J. Wolff (2011), Revisiting the radiative impact of dust on Mars using the LMD Global Climate Model. *J. Geophys. Res.*, 116, E11010, doi: 10.1029/2011JE003855.

Madeleine, J.-B., F. Forget, E. Millour, T. Navarro, and A. Spiga (2012), The influence of radiatively active water ice clouds on the Martian climate, *Geophys. Res. Lett.*, 39, L23202, doi: 10.1029/2012GL053564.

Marchuk, G., G. Mikhailov, M. Nazaraliev, R. Darbinjan, B. Kargin, and B. Elepov (1980). *The Monte Carlo Methods in Atmospheric Optics*. Springer-Verlag.

Martin, T. Z., Richardson, M. I. (1993). New dust opacity mapping from Viking infrared thermal mapper data. *J. Geophys. Res*. 98:10941–49, doi: 10.1029/93JE01044.

Martínez, G. M., Valero, F., and Vázquez, L. (2009). Characterization of the Martian surface layer. *J. Atmos. Sci.*, 66 (1), 187-198, doi: 10.1175/2008JAS2765.1.

Martínez, G. M., Valero, F., and Vázquez, L. (2011). The TKE budget in the convective Martian planetary boundary layer. *Q. J. Roy. Meteor. Soc.*, 137 (661), 2194-2208, doi: 10.1002/qj.883.

Martínez, G. M., Rennó, N., Fischer, E., Borlina, C. S., Hallet, B. et al. (2014). Surface energy budget and thermal inertia at Gale Crater: Calculations from ground-based measurements. *J. Geophys. Res. Planets*, 119 (8), 1822–1838, doi: 10.1002/2014JE004618.

Martínez, G. M., Fischer, E., Renno, N.O., Sebastián, E., Kemppinen, O., Bridges, N., Borlina, C., Meslin, P.-Y., Genzer, M., Harri, A.-M., Vicente-Retortillo, A., Ramos, M., de la Torre-Juárez, M., Gómez, F., Gómez-Elvira, J., and the REMS team (2016). Likely Frost Events at Gale Crater: Analysis from MSL/REMS measurements. *Icarus*, 280, 93-102, doi: 10.1016/j.icarus.2015.12.004.

Martinez, G.M., Newman, C., Vicente-Retortillo, A., Fischer, E., Renno, N.O., Richardson, M., Gómez-Fairén, A., Guzewich, S.D., Haberle, R.M., Kemppinen, O., Lemmon, M.T., Smith, M.D., de la Torre-Juárez, M. and Vasavada, A. (2017). Characterization of the modern Martian climate near the surface: A review of in-situ data from Viking to Curiosity, *Space Science Reviews*, doi:10.1007/s11214-017-0360-x.

Martínez, G., M., A. Vicente-Retortillo, N. O. Renno and J. Gómez-Elvira (2017b). Generation of UV radiation data at Gale crater by correcting REMS UV measurements from dust deposition and sensor's angular response. 48th Lunar and Planetary Science Conference, March 20-24 2017, The Woodlands, Texas, USA.

McConnochie, T.H., et al. (2015), ChemCam Passive Sky Spectroscopy at Gale Crater: Diurnal and Seasonal cycles of O2, H2O, and aerosols. 2015 AGU Fall Meeting, San Francisco, California, USA.

McConnochie, T. H., et al. (2017). Water Vapor and Aerosols from Chemcam Passive Sky Observations. The Sixth International Workshop on the Mars Atmosphere: Modelling and Observations, January 17-20, Granada, Spain.

Medvedev, A. S., T. Kuroda and P. Hartogh (2011), Influence of dust on the dynamics of the martian atmosphere above the first scale height, *Aeolian Res.*, 3(2), 145-156, doi: 10.1016/j.aeolia.2011.05.001.

Melnikova, I., Kuznetsov, A., Pozdnyakov, D., Seroukhova, O., Vasiley, A. (2012). *Remote Sensing of the Environment and Radiation Transfer: An Introductory Survey*, Springer.

Mishchenko, M. I., and L. D. Travis (1994), Light scattering by polydispersions of randomly oriented spheroids with sizes comparable to wavelengths of observation. *Appl. Opt.*, 33, 7206-7225, doi:10.1364/AO.33.007206.

Mishchenko, M. I., and L. D. Travis (1998), Capabilities and limitations of a current FORTRAN implementation of the T-matrix method for randomly oriented, rotationally symmetric scatterers. *J. Quant. Spectrosc. Radiat. Transfer*, 60, 309-324.

Montabone, L., Forget, F., Millour, E., Wilson, R. J., Lewis, S. R. et al. (2015). Eight-year climatology of dust optical depth on Mars. *Icarus*, 251, 65-95, doi: 10.1016/j.icarus.2014.12.034.

Mustard, J. F., and Bell III, J. F. (1994). New composite reflectance spectra of Mars from 0.4 to 3.14 µm. *Geophys. Res. Lett.*, 21 (5), 353-356, doi: 10.1029/94GL00198.

Newman, C. E., S.R. Lewis, P.L. Read, F. Forget (2002a). Modeling the Martian dust cycle. 1. Representations of dust transport processes. *J. Geophys. Res*. 107(E12), 5123, doi:10.1029/2002JE001910.

Newman, C. E., S.R. Lewis, P.L. Read, F. Forget (2002b). Modeling the Martian dust cycle. 2. Multiannual radiatively active dust transport simulations. *J. Geophys. Res*. 107(E12), 5124, doi:10.1029/2002JE001920.

Newman, C. E., J. Gómez-Elvira, M. Marín, S. Navarro, J. Torres, M.I. Richardson, J.M. Battalio, S.D., Guzewich, R. Sullivan, M. de la Torre-Juárez, A.R. Vasavada, N.T. Bridges (2017). Winds measured by the Rover Environmental Monitoring Station (REMS) during the Mars Science Laboratory (MSL) rover's Bagnold Dunes Campaign and comparison with numerical modeling using MarsWRF. *Icarus*, 291, 203-231, doi:10.1016/j.icarus.2016.12.016.

Parkinson, W. H., and Yoshino, K. (2003). Absorption cross-section measurements of water in the wavelength region 181-199 nm. *Chem. Phys*., 294 (1), 31-35, doi: 10.1016/S0301-0104(03)00361-6.

Patel, M. R., Zarnecki, J. C., and Catling, D. C. (2002). Ultraviolet radiation on the surface of Mars and the Beagle 2 UV sensor. *Planet. Space Sci*., 50 (9), 915-927, doi: 10.1016/S0032-0633(02)00067-3.

Patel, M. R., Bérces, A., Kerékgyárto, T., Rontó, G., Lammer, H., and Zarnecki, J. C. (2004). Annual solar UV exposure and biological effective dose rates on the Martian surface. *Adv. Space Res*., 33 (8), 1247-1252, doi: 10.1016/j.asr.2003.08.036.

Pérez-Izquierdo, J., Sebastián Martínez, E., Bravo, A., Ferrándiz, R., Ramos, M., Martínez, G., and Rodríguez Manfredi, J. A. (2016). The MEDA's Radiometer TIRS for the MARS2020 Mission. In AAS/Division for Planetary Sciences Meeting Abstracts (Vol. 48).

Perrier, S., Bertaux, J. L., Lefèvre, F., Lebonnois, S., Korablev, O., Fedorova, A., and Montmessin, F. (2006). Global distribution of total ozone on Mars from SPICAM/MEX UV measurements. *J. Geophys. Res.,* 111, E09S06, doi:10.1029/2006JE002681.

Petrosyan, A., Galperin, B., Larsen, S. E., Lewis, S. R., Määttänen, A., et al. (2011). The Martian atmospheric boundary layer. *Rev. Geophys*., 49 (3), RG3005, doi: 10.1029/2010RG000351.

Pollack, J.B., Ockert-Bell, M.E., and Shepard, M.K. (1995). Viking Lander Image Analysis of Martian Atmospheric Dust, *J. Geophys. Res*., 100(3), 5235-5250.

Rafkin, S.C.R., J. Pla-Garcia, M. Kahre, J. Gomez-Elvira, V. E. Hamilton, M. Marín, S. Navarro, J. Torres, A. Vasavada (2016), The meteorology of Gale Crater as determined from Rover Environmental Monitoring Station observations and numerical modeling. Part II: Interpretation, *Icarus*, 280, 114-138, doi:10.1016/j.icarus.2016.01.031.

Rannou, P., S. Perrier, J.L. Bertaux, F. Montmessin, O. Korablev, and A. Rébérac (2006), Dust and cloud detection at the Mars limb with UV scattered sunlight with SPICAM. *J. Geophys. Res.*, 111, E09S10, doi: 10.1029/2006JE002693.

Read, P.L., and S.R. Lewis (2004), *The Martian climate revisited: atmosphere and environment of a desert planet*, Springer-Verlag, Berlin, ISBN: 978-3-540-40743-0.

Rodriguez-Manfredi, J. A., et al. (2016). MEDA: The Mars Environmental Dynamics Analyzer for Mars 2020. LPI Contributions, 1980.

Rodríguez-Manfredi, J. A., et al. (2017). Atmospheric Science with whe Mars 2020 Rover - The MEDA Instrument. The Sixth International Workshop on the Mars Atmosphere: Modelling and Observations, January 17-20, Granada, Spain.

Romero, P., Barderas, G., Vazquez-Poletti, J. L., and Llorente, I. M. (2011). Spatial chronogram to detect Phobos eclipses on Mars with the MetNet Precursor Lander. *Planet. Space Sci.*, 59(13), 1542-1550.

Rothman, L. S., Gordon, I. E., Babikov, Y., Barbe, A., Benner, D. C. et al. (2013). The HITRAN2012 molecular spectroscopic database. *J. Quant. Spectrosc. Ra.*, 130, 4-50, doi: 10.1016/j.jqsrt.2013.07.002.

Savijärvi, H., Crisp, D. and Harri, A.-M. (2005). Effects of CO_2 and dust on present-day solar radiation and climate on Mars. *Q. J. Roy. Meteorol. Soc.*, 131, 2907–2922, doi: 10.1256/qj.04.09

Savijärvi, H., and Kauhanen, J. (2008). Surface and boundary-layer modelling for the Mars Exploration Rover sites. *Q. J. Roy. Meteor. Soc.*, 134 (632), 635-641, doi: 10.1002/qj.232.

Serdyuchenko, A., Gorshelev, V., Weber, M., Chehade, W. and Burrows, J. P. (2014). High spectral resolution ozone absorption cross-sections – Part 2: Temperature dependence. *Atmos. Meas. Tech.*, 7, 625-636, doi:10.5194/amt-7-625-2014.

Sheehan, W. (1996). The planet Mars: a history of observation and discovery.

Smith, M.D. (2004), Interannual variability in TES atmospheric observations of Mars during 1999–2003, *Icarus*, 167, 148–165, doi: 10.1016/j.icarus.2003.09.010.

Smith, M.D., M.J. Wolff, N. Spanovich, A. Ghosh, D. Banfield, P.R. Christensen, G.A. Landis, S.W. Squyres (2006). One Martian year of atmospheric observations using MER Mini-TES. *J. Geophys.Res*. 111, E12S13, doi:10.1029/2006JE002770

Smith, M. D. (2009). THEMIS observations of Mars aerosol optical depth from 2002–2008. *Icarus*, 202(2), 444-452, doi: 10.1016/j.icarus.2009.03.027.

Smith, M. D., M.-P. Zorzano, M. Lemmon, J. Martín-Torres, T. Mendaza de Cal (2016), Aerosol optical depth as observed by the Mars Science Laboratory REMS UV photodiodes, *Icarus*, 280, 234-248, doi:10.1016/j.icarus.2016.07.012.

Smith, P. H., Lemmon, M. T. (1999). Opacity of the Martian atmosphere measured by the imager for Mars Pathfinder. *J. Geophys. Res*. 104, 8975–8985, doi: 10.1029/1998JE900017.

Sneep, M., and Ubachs, W. (2005). Direct measurement of the Rayleigh scattering cross section in various gases. *J. Quant. Spectrosc. Ra*., 92 (3), 293-310, doi:10.1016/j.jqsrt.2004.07.025.

Stamnes, K., S.C. Tsay, W. Wiscombe, and K. Jayaweera (1988), Numerically stable algorithm for discrete-ordinate-method radiative transfer in multiple scattering and emitting layered media, *Appl. Opt.*, 27, 2502–2509, doi: 10.1364/AO.27.002502.

Stamnes, K., Tsay, S. C., Wiscombe, W. and Laszlo, I. DISORT, a general-purpose FORTRAN program for Discrete-Ordinate-Method radiative transfer in scattering and emitting layered media: documentation of methodology, version 1.1, ftp://climate1.gsfc.nasa.gov/wiscombe/Multiple_Scatt/DISORTReport1.1.pdf, march 2000.

Tamppari, L. K., D. Bass, B. Cantor, I. Daubar, C. Dickinson et al. (2010). Phoenix and MRO coordinated atmospheric measurements. *J. Geophys. Res*. 115, E00E17, doi:10.1029/2009JE003415.

Toigo, A. D. and M.I. Richardson (2000). Seasonal variation of aerosols in the Martian atmosphere. *J. Geophys. Res*. 105(E2), 4109–4121, doi:10.1029/1999JE001132

Tomasko, M.G., Doose, L.R., Lemmon, M., et al. (1999). Properties of Dust in the Martian Atmosphere from the Imager on Mars Pathfinder, J. Geophys. Res., 104, 8987–9007.

Vasavada, A. R., S. Piqueux, K.W. Lewis, M.T. Lemmon, M.D. Smith (2017). Thermophysical properties along Curiosity's traverse in Gale crater, Mars. *Icarus* 284, 372–386.

Vázquez, L., Zorzano, M. P., and Jiménez, S. (2007). Spectral information retrieval from integrated broadband photodiode Martian ultraviolet measurements. *Opt. Lett.*, 32 (17), 2596-2598, doi: 10.1364/OL.32.002596.

Vicente-Retortillo, A., F. Valero, L. Vázquez and G. M. Martínez (2015), A model to calculate solar radiation fluxes on the Martian surface. *J. Space Weather Space Clim.*, 5, A33, doi:10.1051/swsc/2015035.

Vicente-Retortillo, A., G. M. Martínez, N. O. Renno, M. T. Lemmon, E. L. Mason, M. de la Torre-Juárez (2015b). UV Opacity at Gale Crater from MSL/REMS Measurements. 2015 AGU Fall Meeting, December 14-18 2015, San Francisco, California, USA.

Vicente-Retortillo, A. (2015c). Characterization of solar radiation on Mars with the Monte-Carlo method. IX Workshop of Young Researchers in Mathematics, 21-23 September 2015, Madrid, Spain.

Vicente-Retortillo, A., Lemmon, M.T., Martínez, G. M., Valero, F., Vázquez, L. and Martín, M. L. (2016). Seasonal and interannual variability of solar radiation at Spirit, Opportunity and Curiosity landing sites. *Física de la Tierra* (invited), 28, 111-117.

Vicente-Retortillo, A., G. M. Martínez, N. O. Renno, M. T. Lemmon, E. L. Mason, M. de la Torre-Juárez (2016b). A Novel Technique to Calculate UV Opacity at Gale Crater from MSL/REMS Measurements. EGU General Assembly 2016, April 17-22 2016, Vienna, Austria.

Vicente-Retortillo, A., Martínez, G.M., Renno, N.O., Lemmon, M.T., and de la Torre-Juárez, M. (2017). Determination of dust aerosol particle size at Gale Crater using REMS/UVS and Mastcam measurements, *Geophys. Res. Lett.*, 44, doi:10.1002/2017GL072589.

Warren, S.G. (1984), Optical constants of ice from the ultraviolet to the microwave. *Appl. Opt.*, 23, 1206–1225, doi: 10.1364/AO.23.001206.

Weber, M. J. (2003). Handbook of optical materials, CRC Press, ISBN 0-8493-3512-4.

Webster, C.R., P.R. Mahaffy, S.K. Atreya and the SAM Science Team (2016), Low Background Levels of Mars Methane at Gale Crater Indicate Seasonal Cycle: Updated Results from TLS-SAM on Curiosity, presented at 2016 AGU Fall Meeting, San Francisco, California, USA.

Wilson, R.J. and K. Hamilton (1996). Comprehensive model simulation of thermal tides in the Martian atmosphere. *J. Atmos. Sci.* 53(9), 1290–1326.

Wilson, R. J. (1997). A general circulation model simulation of the Martian polar warming. *Geophys. Res. Lett*. 24(2), 123–126.

Wolff, M.J., and R.T. Clancy (2003), Constraints on the size of Martian aerosols from Thermal Emission Spectrometer observations. *J. Geophys. Res.*, 108, 5097, doi: 10.1029/2003JE002057.

Wolff, M.J., M.D. Smith, R.T. Clancy, R. Arvidson, M. Kahre, F. Seelos IV, S. Murchie, and H. Savijärvi (2009), Wavelength dependence of dust aerosol single-scattering albedo as observed by the Compact Reconnaissance Imaging Spectrometer. *J. Geophys. Res.*, 114, E00D04, doi: 10.1029/2009JE003350.

Wolff, M.J., R.T. Clancy, J.D. Goguen, M.C. Malin, and B.A. Cantor (2010), Ultraviolet dust aerosol properties as observed by MARCI, *Icarus*, 208, 143–155, doi: 10.1016/j.icarus.2010.01.010.

Zorzano, M. P., Vázquez, L., and Jiménez, S. (2009). Retrieval of ultraviolet spectral irradiance from filtered photodiode measurements. *Inverse Probl.*, 25 (11), 115023, doi: 10.1088/0266-5611/25/11/115023.

Zurek, R. W. and C.B. Leovy (1981). Thermal tides in the dusty Martian atmosphere: a verification of theory. *Science*, 213(4506), 437–439.